Mathematical Problems in Engineering

Mathematics in Utilizing Remote Sensing Data for Investigating and Modelling Environmental Problems

Lead Guest Editor: Hasi Bagan
Guest Editors: Ram Avtar, Hajime Seya, and Huade Guan

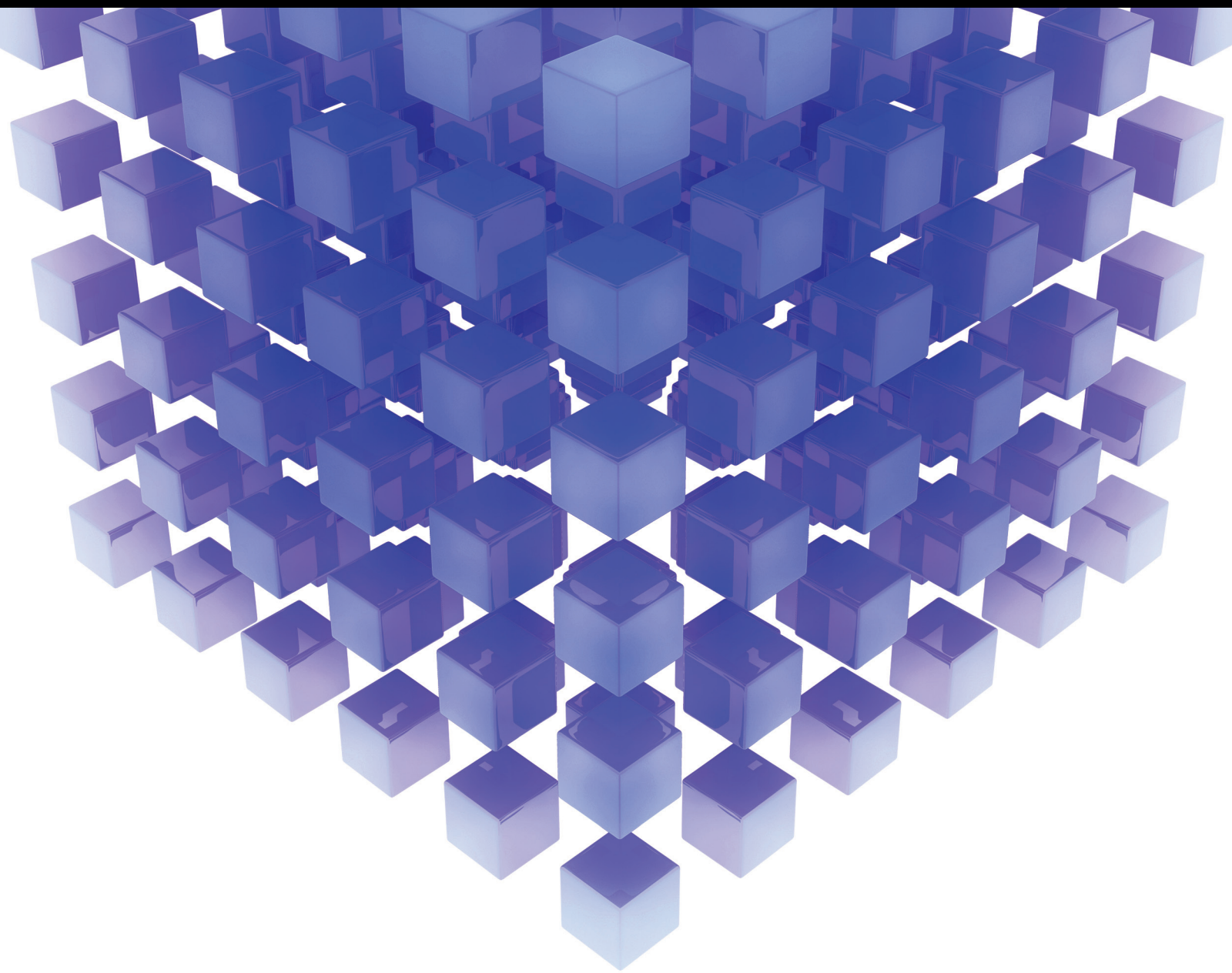

Mathematics in Utilizing Remote Sensing Data for Investigating and Modelling Environmental Problems

Mathematical Problems in Engineering

Mathematics in Utilizing Remote Sensing Data for Investigating and Modelling Environmental Problems

Lead Guest Editor: Hasi Bagan
Guest Editors: Hajime Seya and Huade Guan

Editorial Board

Contents

Hindawi
Mathematical Problems in Engineering
Volume 2017, Article ID 7430658, 3 pages
https://doi.org/10.1155/2017/7430658

Editorial

Mathematics in Utilizing Remote Sensing Data for Investigating and Modelling Environmental Problems

Hasi Bagan,[1,2] Ram Avtar,[3] Hajime Seya,[4] and Huade Guan[5]

[1] *Institute of Urban Studies, Shanghai Normal University, Shanghai 200234, China*
[2] *Center for Global Environmental Research, National Institute for Environmental Studies, Tsukuba, Japan*
[3] *United Nations University, Tokyo, Japan*
[4] *Hiroshima University, Higashihiroshima, Japan*
[5] *Flinders University, Adelaide, SA, Australia*

Correspondence should be addressed to Hasi Bagan; hasi.bagan@nies.go.jp

Received 8 June 2017; Accepted 8 June 2017; Published 27 August 2017

Remote sensing data have already proven useful for environmental monitoring in a timely, detailed, and cost-effective manner to assist various planning and management activities. Remotely sensed data collected over a span of years can be used to identify and characterize both natural and anthropogenic changes over large areas of land at a variety of spatial and temporal scales [1–3]. As climate change and population growth place increasing pressures on many parts of the world, improved methods for monitoring urban growth across a range of spatial and temporal scales will be vital for understanding and addressing the impacts of urbanization on our natural resources [4, 5]. With the advance of machine learning algorithms and computing facilities, many investigations on their real applications are taking place. Combining remote sensing data and mathematics techniques to quantitatively analyze environmental change is a topic growing in importance [6]. The meaningful interpretation of remote sensing data and in situ observations require implementation and analysis using advanced mathematics and statistical techniques.

The objective of this special issue is to provide a snapshot of status, potentials, challenges, and achievements of mathematical application in using remote sensing data to address environmental issues. This special issue includes thirteen papers that cover four major topics: image processing methods, land use/land cover change analysis, land degradation, urbanization, and vegetation cover. A brief description of these 13 works is detailed below.

(i) "Multisensor Fusion of Landsat Images for High-Resolution Thermal Infrared Images Using Sparse Representations" by H. S. Jin and D. Han investigates a method of fusing Landsat panchromatic and thermal infrared images using a sparse representation (SR) technique. Their results show that the proposed method improves spatial resolution and preserves the thermal properties of basic LST data for use with environmental problems.

(ii) "A Subpixel Matching Method for Stereovision of Narrow Baseline Remotely Sensed Imagery" by N. Ma et al. proposes a subpixel image matching approach based on improved phase correlation through the analysis of narrow baseline remotely sensed imagery stereovision.

(iii) In order to assess the feasibility of the BeiDou Navigation Satellite System reflected signals (BeiDou-R) in detecting oil slicks, the paper by Y. Zhang et al. performs a BeiDou-R coastal simulation experiment on the oil slick distribution of an oil pipeline explosion accident. Their analysis reveals that oil slicks can be detected within a radius of less than 5 km around the specular reflection point for BeiDou-R coastal simulation.

(iv) With using grey relational analysis, "Analysis of the Spatial Variation of Soil Salinity and Its Causal Factors in China's Minqin Oasis" by T. Qian et al. evaluates

the factors that affect soil salinity and investigates the interactions among them in China's Minqin Oasis. The factors are ranked based on the significance of their impacts on soil salinity for different land use and cover types. They find that the main factors that affect soil salinity in the region's sparse grassland are groundwater salinity and vegetation cover.

(v) Population increase, excessive land development, overgrazing, and collection of fuel wood have been the main driving forces in Horqin's desertification process. "A Detailed and High-Resolution Land Use and Land Cover Change Analysis over the Past 16 Years in the Horqin Sandy Land, Inner Mongolia" by X. Bai et al. presents a detailed and high-resolution (30 m) land cover change analysis over the past 16 years in Ongniud Banner, western part of the Horqin Sandy Land. The land cover classification was performed by combining multiple features calculated from the Landsat archive products using the Support Vector Machine (SVM) based supervised classification approach. This study implies increasing demand of water and indicates that the conservation of water resources is crucial for protecting the sensitive ecological zones in the Horqin Sandy Land.

(vi) "Analysis of Drought Characteristics in Xilingol Grassland of Northern China Based on SPEI and Its Impact on Vegetation" by S. Tong et al. explores the spatial and temporal dynamics of SPEI and NDVI over the Xilingol grassland and investigates the impact of drought on the NDVI in Xilingol grassland during the growing season.

(vii) The detection of decreasing vegetation cover is very important due to its impact on ecosystems. "Detection of Decreasing Vegetation Cover Based on Empirical Orthogonal Function and Temporal Unmixing Analysis" by D. Xu et al. applied a new method of integrated empirical orthogonal function (EOF) and temporal unmixing analysis (TUA) to detect the vegetation decreasing cover in Jiangsu Province of China.

(viii) Monitoring and mapping of urban growth and developing effective urban planning strategies require spatiotemporal extent and expansion trends of cities. The Beijing-Tianjin-Hebei Region (Jing-Jin-Ji) is a core source for China's rapid economic growth. "Dynamic Changes Analysis and Hotspots Detection of Land Use in the Central Core Functional Area of Jing-Jin-Ji from 2000 to 2015 Based on Remote Sensing Data" by Y. Li et al. uses GIS spatial analysis and grid technologies to study the dynamic changes, hotspot regions, and driving forces in land use of the central core functional area of Jing-Jin-Ji. The results indicate that the level of land use was very uneven in the central core functional area of Jing-Jin-Ji.

(ix) "Dynamic Changes of Typical Blowouts Based on High-Resolution Data: A Case Study in Hulunbuir Sandy Land, China" by Y. Yang et al. studies the dynamic changes of typical blowouts within the past decade which were analyzed via multiperiod high-resolution remote sensing images. RTK was used to repeatedly measure the blowouts to obtain their high-precision 3D terrain data in 2010, 2011, and 2012.

(x) The distribution of cities around the world broadly corresponds to the brightness distribution of DMSP nighttime lights. "Evaluating Urbanization and Spatial-Temporal Pattern Using the DMSP/OLS Nighttime Light Data: A Case Study in Zhejiang Province" by P. Xu et al. using DMSP/OLS night-lighting data, mutation detection, regression analysis, and spatial analysis methods to analyze the urbanization in Zhejiang province, China.

(xi) The study of spatial planning for urban development is very important due to its impact on urban ecosystems. "Implications of a Spatial Multicriteria Decision Analysis for Urban Development in Ulaanbaatar, Mongolia" by P. Myagmartseren et al. illustrates how multicriteria decision analysis and geographical information systems can be used for more effective urban planning. This study shows the effect of using poor elevation data and how a sensitivity analysis can be applied to yield further information, spot weighting weaknesses, and assess the quality of the criteria.

(xii) "An Integrated Field and Hyperspectral Remote Sensing Method for the Estimation of Pigments Content of Stipa Purpurea in Shenzha, Tibet" by B. Kong et al. investigates the typical hyperspectral variables sensitive to chlorophyll content of Stipa purpurea and established the estimation model of chlorophyll.

(xiii) "Hierarchical Sea-Land Segmentation for Panchromatic Remote Sensing Imagery" by L. Ma et al. proposed a fully automatic sea-land segmentation approach for practical use with a hierarchical coarse-to-fine procedure. They compared the proposed method with other state-of-the-art methods with real images under complex backgrounds and conducted quantitative comparisons. The experimental results show that proposed method outperforms all other methods and proved being computationally efficient.

We wish this special issue would inspire more ideas in utilizing mathematics and statistical techniques in the study of earth system (land, ocean, and atmosphere) environments.

Acknowledgments

We would like to take this opportunity to sincerely thank all of the authors and peer reviewers for their efforts devoted to this special section.

Hasi Bagan
Ram Avtar
Hajime Seya
Huade Guan

References

[1] K. M. Bergen, T. Zhao, V. Kharuk et al., "Changing regimes: forested land cover dynamics in central Siberia 1974 to 2001," *Photogrammetric Engineering and Remote Sensing*, vol. 74, no. 6, pp. 787–798, 2008.

[2] C. Gómez, J. C. White, and M. A. Wulder, "Optical remotely sensed time series data for land cover classification: a review," *ISPRS Journal of Photogrammetry and Remote Sensing*, vol. 116, pp. 55–72, 2016.

[3] J. van Vliet, D. A. Eitelberg, and P. H. Verburg, "A global analysis of land take in cropland areas and production displacement from urbanization," *Global Environmental Change*, vol. 43, pp. 107–115, 2017.

[4] H. Bagan and Y. Yamagata, "Land-cover change analysis in 50 global cities by using a combination of Landsat data and analysis of grid cells," *Environmental Research Letters*, vol. 9, no. 6, Article ID 064015, 2014.

[5] C. Bren d'Amour, F. Reitsma, G. Baiocchi et al., "Future urban land expansion and implications for global croplands," *Proceedings of the National Academy of Sciences*, p. 201606036, 2016.

[6] D. J. Lary, A. H. Alavi, A. H. Gandomi, and A. L. Walker, "Machine learning in geosciences and remote sensing," *Geoscience Frontiers*, vol. 7, no. 1, pp. 3–10, 2016.

Hindawi
Mathematical Problems in Engineering
Volume 2017, Article ID 4787054, 10 pages
https://doi.org/10.1155/2017/4787054

Research Article

An Integrated Field and Hyperspectral Remote Sensing Method for the Estimation of Pigments Content of Stipa Purpurea in Shenzha, Tibet

Bo Kong,[1] Bing He,[1] Huan Yu,[2] and Yu Liu[2]

[1]*Institute of Mountain Hazards and Environment, Chinese Academy of Sciences, Chengdu 610041, China*
[2]*College of Earth Sciences, Chengdu University of Technology, Chengdu 610059, China*

Correspondence should be addressed to Bing He; hebing@imde.ac.cn

Received 28 November 2016; Revised 20 March 2017; Accepted 7 May 2017; Published 22 June 2017

Academic Editor: Huade Guan

Stipa purpurea is the representative type of alpine grassland in Tibet and the surviving and development material for herdsmen. This paper takes Shenzha County as the research area. Based on the analysis of typical hyperspectral variables sensitive to chlorophyll content of Stipa purpurea, 10 spectral variables with significant correlation with chlorophyll were extracted. The estimation model of chlorophyll was established. The photosynthetic pigment contents in the Shenzha area were calculated by using HJ-1A remote sensing images. The results show that (1) there are significant correlations between chlorophyll content and spectral variables; in particular, the coefficient of Chlb in Stipa purpurea with RVI is the largest (0.728); (2) 10 variables are correlated with chlorophyll, and the order of correlation is Chlb > Chla > Chls; (3) for the estimation of Chla, the EVI is the best variable. RVI, NDVI, and VI2 are suitable for Chlb; RVI and NDVI are also suitable for the estimation of Chls; (4) the mean estimated content of Chla in Stipa bungeana is about 4.88 times that of Chlb, while Cars is slightly more than Chlb; (5) the distribution of Chla is opposite to Chlb and Chls content in water area.

1. Introduction

Stipa purpurea, distributed in northern Tibet, is the most important and largest ecological system and the survival and development materials for herdsmen [1, 2]. At the same time, Stipa purpurea grassland known as alpine biological germplasm resources has unique species diversity and high biodiversity conservation value. Due to the severe natural conditions in northern Tibet, the ecological system of Stipa purpurea grassland is extremely fragile and the antidisturbance ability is poor [3, 4]. Once the grassland vegetation is destroyed, it is difficult to recover. Photosynthetic pigment content, as an effective plant health indicator for the detection of photosynthesis and disease pollution [5, 6], can be estimated and analyzed by remote sensing. This will be useful not only for analyzing the growth and health status of Stipa purpurea grassland, but also for reflecting the succession of Stipa purpurea community. It could play an important role in regulating and improving the environment of Qinghai-Tibet plateau or even the whole Eurasia.

The nutritional status of plants is closely related to pigment content and compositions in vegetation biochemical parameters. Chlorophyll is such kind of vegetation biochemical parameter and closely related to nitrogen, protein, water, and others. When the grassland is damaged, the chlorophyll content will be reduced, which can indirectly reflect the physiological condition of the grassland under external stress. Chlorophyll can absorb light and convert it into electrical energy, while carotenoid has the function of preventing chlorophyll photooxidation besides collecting and transmitting light energy [7]. The traditional quadratic survey of chlorophyll has some shortcomings such as sparse sampling points and measurement difficulties in large scale, which leads to low reliability of analysis results. The hyperspectral remote sensing provides the possibility for estimating photosynthetic pigment contents in grassland [8, 9] and

is important for the estimating of photosynthetic capacity, species identification, production dynamic observation, and precision fertilization [10, 11].

At present, hyperspectral remote sensing has made progress in monitoring vegetation pigment contents, and some hyperspectral chlorophyll indices have been proposed by maximizing the reflection information of vegetation and minimizing the influence of external factors (e.g., aerosol, soil background, and nonphotosynthetic materials) [12–20]. For example, Horler et al. [12] studied the relationship between vegetation spectrum and chlorophyll content and analyzed the role of red edge position (wavelength of vegetation derivative spectrum near 700 nm) for the assessment of chlorophyll concentration. The contents of biochemical components (chlorophyll, lignin, nitrogen, cellulose, etc.) of 12 kinds of leaves were computed by using the first-order derivative reflectance spectroscopy and absorption characteristics method. Blackburn [15] proposed two new indices for estimating the pigment concentrations of four deciduous broad-leaved species at different wilting stages by using a simple ratio of specific pigment simple index and a normalized difference index of specific pigments. Richardson et al. [17] used traditional extraction techniques to measure chlorophyll a (Chla), chlorophyll b (Chlb), and total chlorophyll content (Chls) of 100 paper birch leaves and found that some indices based on reflectance, such as the chlorophyll NDI, were much better indicators of chlorophyll content than some of the more commonly used indices, such as λRE or NDVI. Dash and Curran [18] proposed a new index called the MERIS terrestrial chlorophyll index (MTCI) using data in three red/NIR wavebands centered at 681.25, 708.75, and 753.75 nm, and the MTCI appeared to be a most suitable index for the estimation of chlorophyll content with Medium Resolution Imaging Spectrometer (MERIS) data. The MERIS index is now a standard level-2 product of European Space Agency.

The above-mentioned indices can be classified into four types [21], single spectral index, normalized spectral index, ratio spectral index, and multiband spectral index, and can obtain very fine vegetation physiological conditions and environmental stress differences by their unique fine spectral characteristics. But, the majority of hyperspectral chlorophyll indices were developed for crops [22] or forests other than grassland [23]. Nichol and Grace [24] found that several previously published indices performed relatively poorly and yielded low coefficients, and some ecologically important species remain to be explored, despite their "applicability" across many species types [25]. Especially in alpine grassland, the hyperspectral estimation model for pigment content of Stipa purpurea community is rarely reported.

The objectives of this paper are (1) to take the sparse grass group of Stipa purpurea community as the target in alpine grassland and analyze its canopy and community spectral characteristics; (2) to extract spectral information and establish the correlation with pigments content; and (3) to analyze the spatial distribution of pigments content of Stipa purpurea in Shenzha. The remainder of this paper describes the field experiment, spectral analysis, and characteristics and the Stipa purpurea mapping results. The specific methods

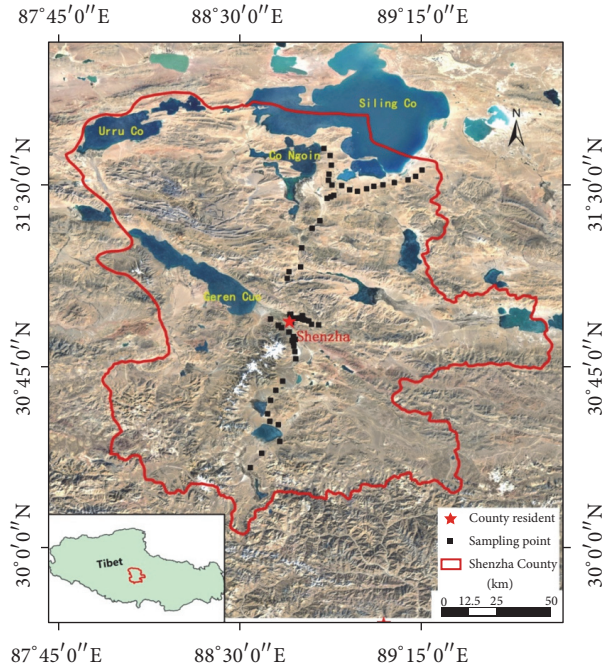

Figure 1: The study area and schematic plot of sample point.

are as follows: (1) the hyperspectral characteristic variables were selected by spectral analysis, and the spectral data were processed by statistical method; (2) correlation analysis was carried out and the sensitive parameters were selected to establish the pigments content and spectral characteristics of the estimation model; (3) in order to reflect the distribution and succession of Stipa purpurea community, the maps are produced and analyzed by GIS tools.

2. Materials and Methods

2.1. Study Area. Shenzha County is located in the middle of Tibet, southwest of Naqu area. The average elevation of this area is 4750 m. The annual average temperature is below 0°C, and the highest temperature is 10°C every year in July-August. The minimum temperature is −40°C. The Stipa purpurea grassland is well developed in Shenzha, and it is widely distributed in slopes, hills, rivers, and lakes terraces and lake plains, which are well drained below 4900 m, forming a large grassland community. This region has vast grassland and abundant water resources, which is one of the traditional pastoral areas in Tibet. As a result of long-term overgrazing, some good grasslands have been significantly degraded, such as Stellera chamaejasme Linn, Morina kokonorica Hao, and other poisonous grass.

2.2. Spectral Data Acquisition. The selection of quadratic sampling location is very important for field spectrum acquisition process. The selected target must be representative and can truly reflect the average characteristics. In this paper, the field experiment locations are shown in Figure 1. Each location is a typical Stipa purpurea community in northern Tibet plateau of Shenzha. A total of 9 sampled plots

Figure 2: Field experiment.

(0.5 m × 0.5 m) were selected randomly, and 60 test units were measured. The spectral reflectance of Stipa purpurea was measured by SVC HR-1024 portable spectrometer. The spectral range of this spectrometer is from 350 nm to 2500 nm and the number of channels is 1024. In order to show the best growth status of alpine grassland, field experiments are seasoned between August and September 2015, which is the growth season of Stipa purpurea community in Shenza area. The weather is sunny, without wind or with very little wind. The measurement time is controlled between 11:00 and 14:00. In the measurement, a single vegetation type was selected. The sensor head of spectrometer is down vertically, the field angle is 4°, the height of the grass canopy is about 20 cm, the coverage is nearly 100%, and the diameter is about 5.2 cm. Four sampling points were selected randomly in each plot for spectral determination, and the mean value was taken as the repeat spectral reflectance value. In order to reduce the impact of atmospheric changes, plots and reference whiteboard was measured alternately (as shown in Figure 2). At each sample point, GPS, grass height, and coverage were recorded at the same time.

2.3. Remote Sensing Data and Its Preprocessing. The HJ-1A hyperspectral imager (HSI) product was downloaded from July to August 2015 from China Centre for Resources Satellite Data and Application, with ground width of 50 km, spatial resolution of 100 m, and 128 bands ranging from 450 nm to 950 nm. The hyperspectral data was selected according to the growing season of Stipa purpurea in study area. The principle of data selection is to remove the image covering the same area with a larger sampling time or poor quality, thus reducing the error caused by mismatch between the ground sampling and satellite monitoring time. Finally, 46 images were selected; 13 images contain quadratic samples. And then these images were postprocessed such as band fusion, geometric correction, and projection conversion.

2.4. Determination of Photosynthetic Pigments. In order to extract photosynthetic pigments of alpine grassland, the optical density was measured by spectrophotometry at the wavelength of 663 nm, 647 nm, 537 nm, and 470 nm. According to Lambert-Beer law, The Chla, Chlb, Chls, and Carotenoids (Cars) were calculated. Each process was repeated three times, and the average value was taken as the photosynthetic pigment content. A total of 70 samples were determined, and four photosynthetic pigment contents were determined for each sample.

$$\begin{aligned}
&\text{Chla} = 0.137A_{663} - 0.000897A_{537} - 0.003046A_{647},\\
&\text{Chlb} = 0.024A_{647} - 0.004305A_{537} - 0.005507A_{663},\\
&\text{Chls} = \text{Chla} + \text{Chlb},\\
&\text{Cars}\\
&= \frac{\left(A_{470} - \left(17.1 \times \left(\text{Chl}_a + \text{Chl}_b\right) - 9.479 \times \text{Anthocyanin}\right)\right)}{119.26},\\
&\text{Anthocyanin} = 0.0817A_{537} - 0.00697A_{647} - 0.002228A_{663}.
\end{aligned} \tag{1}$$

2.5. Feature Parameter Extraction of Hyperspectral Data. In order to explore the characteristics of canopy reflectance spectrum of Stipa purpurea, some useful narrow bands were selected from hyperspectral bands for remote sensing information extraction. The aboveground biomass was modeled by using hyperspectral data and various transformations, such as red, yellow, and blue optical parameters, vegetation index, green reflection peak, and red light absorption valley. The spectral data of the experimental units were smoothed and deaveraged four times. The parameters such as the position, area, vegetation index, and derivative of the spectra were calculated (as shown in Table 1). The linear and nonlinear regression equations were established by comparing these spectral variables with the light and pigment contents, and the optimal estimation model of one or more variables was preliminarily screened.

2.6. Regression Method. A stepwise regression analysis method was used to determine the biomass-related spectral variable equation, and the measured biomass and spectral variable value was then input. The output result was a series of multivariate linear equations containing different spectral variables, as well as the corresponding determination coefficient (R^2), and test value (F). The stepwise regression model was as follows:

$$Y = a_0 + a_1x_1 + a_2x_2 + \cdots + a_ix_i + \cdots, \tag{2}$$

where x_i is the spectral variable value; Y is the biomass estimation value; a_0 is a constant item; and a_i represents the partial regression coefficient.

Table 1: High spectral characteristic parameter selection.

Types	Name	Abbreviation	Calculation formula	Literature
Spectral area and location parameters	Blue margin value	D_b	Maximum of first derivative spectrum in 490 to 520 nm wavelength	Elvidge et al., 1995
	Blue margin area	SD_b	Integration of first derivative in 490 to 520 nm wavelength	Elvidge et al., 1995
	Yellow margin value	D_y	Maximum of first derivative spectrum in 560 to 640 nm wavelength	Elvidge et al., 1995
	Yellow margin area	SD_y	Integration of first derivative in 560 to 640 nm wavelength	Elvidge et al., 1995
	Red margin value	D_r	Maximum of first derivative spectrum in 670 to 760 nm wavelength	Elvidge et al., 1995
	Red margin area	SD_r	Integration of first derivative in 670 to 760 nm wavelength	Pu et al., 1993
	Green peak reflectance	R_g	Maximum of band reflectance in 520 to 560 nm wavelength	Elvidge et al., 1995
	Green peak area	SD_g	Area of original spectrum in 520 to 560 nm wavelength	Elvidge et al., 1995
	Red valley reflectance	R_r	Minimum of band reflectance in 650 to 690 nm wavelength	Elvidge et al., 1995
Ratio parameters of spectral area and location	Ratio between green peak reflectance and red valley reflectance	VI1	$\frac{\rho_g}{\rho_r}$	Gitelson et al., 1996
	Normalization value of green peak reflectance and red valley reflectance	VI2	$\frac{\rho_g - \rho_r}{\rho_g + \rho_r}$	Gitelson et al., 1996
	Ratio between red margin area and blue margin area	VI3	$\frac{SD_r}{SD_b}$	Gitelson et al., 2003
Vegetation indices	Ratio vegetation index	RVI	$\frac{\rho_{NIR}}{\rho_{Red}}$	Jordan, 1969
	Normalized difference vegetation index	NDVI	$\frac{\rho_{NIR} - \rho_{Red}}{\rho_{NIR} + \rho_{Red}}$	Rouse, 1973
	Enhanced vegetation index	EVI	$\frac{\rho_{NIR} - \rho_{Red}}{\rho_{NIR} + C_1\rho_{Red} - C_2\rho_B + L}(1 + L)$	Liu, 1995
	Again normalized difference vegetation index	RDVI	$\sqrt{NDVI \times (\rho_{NIR} - \rho_{Red})}$	Richardson, 1992

3. Results and Analysis

3.1. Hyperspectral Analysis of Stipa Purpurea. Grassland vegetation, atmosphere, water, soil, and other factors form a comprehensive reflection spectrum of grassland. The reflectance is affected by many factors, such as grassland population, type, vegetation water content, vegetation coverage, air condition, and soil condition. Therefore, the spectrum analysis of Stipa purpurea is the basis of remote sensing monitoring of forage resources in Tibetan plateau, and its spectral characteristics are the integrated responses of Stipa purpurea and its habitat conditions.

It can be seen from Figure 3 that the overall trend of 5 different coverages of Stipa purpurea samples is consistent, although the spectral reflectance is varying. The blue-band with the largest water penetration is located in the chlorophyll absorption zone of green plants between 490 and 520 nm. It shows that blue-band is sensitive to the chlorophyll concentration and is helpful for the identification of plant

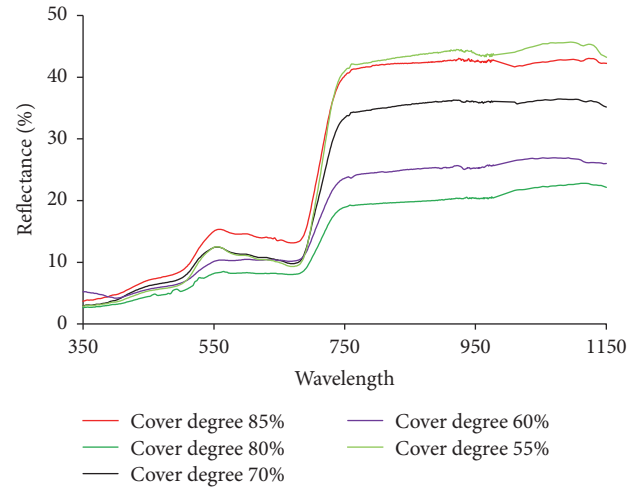

Figure 3: Comparison of different coverage of Stipa purpurea spectral reflectance curve.

Table 2: The correlation coefficient of Stipa pigment content and spectral variables.

	Characteristic variables	Chla	Chlb	Chls	Cars
Spectral location variable	D_b	−.409*	−.407*	−.377*	−0.007
	D_y	−0.016	−0.007	−0.038	−0.157
	D_r	−.424*	−.398*	−.417*	0.015
	R_g	−.579**	−.578**	−.556**	−0.053
	R_r	−.589**	−.592**	−.571**	−0.035
Spectral area variable	SD_b	−0.414*	−.404*	−.395*	−0.098
	SD_y	−0.315	−0.322	−0.32	0.038
	SD_r	0.123	0.124	0.094	−0.09
	SD_g	−.583**	−.584**	−.561**	−0.06
Vegetation variable	RVI	.707**	.728**	.694**	0.14
	NDVI	.594**	.607**	.571**	0.026
	EVI	.606**	.623**	.584**	0.075
	RDVI	.661**	.679**	.644**	0.09
VI variable	VI1	.597**	.627**	.609**	0.131
	VI2	.569**	.594**	.578**	0.104
	VI3	.626**	.630**	.585**	0.045

Note. * and ** indicate significant levels at 0.05 and 0.01, respectively.

stress. This conclusion is consistent with Jin et al.'s research [26]. The green reflectance of healthy grass between 490 and 520 nm is sensitive to grass reflectance, and it could be used to identify grassland type and plant productivity state. At the same time, the green band reflection peaks also increase with the lift of coverage and growth conditions. The sharp rising portion between the red and the near-infrared bands of high reflectance is located in the vicinity of the red edge of 700–750 nm. In the decreasing process of coverage, the red edge of the spectrum will shift to the long wave direction, and the offset is about 10~40 nm. The near-infrared band is located in the meadow high reflection area (760–900 nm). The spectral characteristics are controlled by the cell structure of the grassland and are sensitive to the change of the grassland type, density, and growth force. The higher the vegetation height, the coverage, and the productivity, the higher the reflectance is. The canopy reflectance is usually between 20% and 40%, which is due to the multiple reflection and scattering of the internal tissue structure of plant leaves and is mainly determined by biomass and leaf area index.

3.2. Data Analysis. The hyperspectral data after transformation were correlated with pigments content and the results are shown in Table 2. There are significant correlations between chlorophyll content and spectral characteristic variables; in particular, the correlation coefficient of chlorophyll content with green peak reflectance, red valley reflectance, green peak area, RVI, NDVI, EVI, RDVI, VI1, VI2, and VI3 reached 0.01 significant level. The correlation coefficient of Chlb of Stipa purpurea and RVI is the largest value of 0.728. The correlation coefficient of Chla, Chlb, and Chls to RVI, EVI, RDVI, and VI3 is 0.6. The correlation coefficient between carotenoid content and 16 characteristic variables is generally low, which indicates that the spectral characteristic variables of Stipa purpurea are correlated with chlorophyll, and the chlorophyll content could be estimated by using the characteristic variables with good correlation.

3.3. Model Construction and Verification. In many studies, hyperspectral remote sensing data is used to estimate the chlorophyll content. The main method was to find the bands relation to chlorophyll content by regression method. In high spectral narrow band data, the green band uses 553 nm reflectivity, the red band uses 670 nm reflectivity, the near-infrared band uses 801 nm reflectivity to carry on the inversion parameter operation, and the result is valid. This is due to the fact that 553 nm and 670 nm are used to determine the most responsive narrow band position according to R_g, R_r two parameters; 801 nm is used to screen out the narrow band at near-infrared band according to many experts in the grassland vegetation index parameters [26]. The regression models of chlorophyll and band combination are shown in Table 3.

Based on the analysis of typical hyperspectral variables sensitive to chlorophyll content of Stipa purpurea, 10 variables with significant correlation with chlorophyll were extracted in Table 3, and SPSS22.0 was used to analyze Chla, Chlb, and Chls. We analyzed the linear, quadratic, logarithmic, and exponential models and selected the higher coefficient of determination of Chla and Chlb and total chlorophyll as the basis for the modeling of Stipa purpurea (as shown in Figure 4). The observed data were randomly selected and divided into two groups: one for the training samples ($n = 30$) is used to establish the regression relationship.

As shown in Table 4, all the regression equations R^2 are tested by 0.01 significance and varied between 0.623 and 0.708 with an average value of 0.658. For the Chla content estimation, the best fitting model is EVI variable parabola equation, R^2 is 0.708, F-test value is 31.9, and the estimated standard error is small; for Chlb, the best fitting model is the parabolic equation of RVI, NDVI, and VI2 variables, the F-test value is large, and the standard error is small. For the estimation of Chls, the best fitting model is also the parabolic equation of RVI and NDVI, R^2 value is 0.644, and F test value reached 12.79.

3.4. Spatial Pattern Analysis. The best models for Chla, Chlb, and Chls estimation were obtained and validated by correlation coefficient model (as shown in Table 3, Figure 4). The hyperspectral raster data can be directly used to calculate the spatial results. In the calculation process, the green band uses 553 nm reflectivity which is 38 band of HJ-1A image, 670 nm reflectivity as red band which is 70 band of HJ-1A image, and 801 nm reflectivity as the near-infrared band. Finally, EVI parameters of Chla, RVI value of Chlb, and EVI parameters of Chls were calculated and substituted into the estimation model, respectively. The photosynthetic pigment contents in Shenzha area were estimated by HJ-1A images.

The contents of Chla, Chlb, and Chls in Shenzha area are shown in Figure 5. The Chla is in the range of 0–30 mg/g. The

Table 3: Estimation model and evaluation index of the photosynthetic pigment content of Stipa purpurea.

Variable	Model	Model function	Training sample (n = 30)		Validation sample (n = 20)	
			R^2	F	R^2	SEE
R_g	Chla	$y = 18.941e^{-0.101x}$	0.360	15.755	0.337	0.318
	Chlb	$y = 4.9395e^{-0.134x}$	0.421	20.358	0.400	0.734
	Chls	$y = 0.0483x^2 - 2.031x + 24.361$	0.402	9.086	0.358	3.226
R_r	Chla	$y = 0.0498x^2 - 1.8608x + 20.157$	0.522	14.737	0.486	3.415
	Chlb	$y = 0.0103x^2 - 0.4021x + 4.3275$	0.430	21.154	0.410	0.950
	Chls	$y = 0.0685x^2 - 2.3681x + 23.633$	0.484	12.686	0.446	2.996
SD_g	Chla	$y = 3E-05x^2 - 0.0524x + 22.071$	0.384	8.409	0.338	3.877
	Chlb	$y = 19.434e^{-0.003x}$	0.425	20.706	0.405	0.731
	Chls	$y = 4E-05x^2 - 0.0554x + 24.53$	0.401	9.053	0.357	3.229
RVI	Chla	$y = 0.0087x^2 + 2.4105x - 1.2277$	0.655	25.575	0.629	2.903
	Chlb	$y = 0.3113x^2 - 1.4038x + 2.2996$	0.712	33.423	0.691	0.687
	Chls	$y = 0.1029x^2 - 1.1332x + 11.11$	0.701	29.367	0.662	1.713
NDVI	Chla	$y = 80.457x^2 - 55.9x + 13.24$	0.686	29.554	0.663	2.766
	Chlb	$y = 29.211x^2 - 21.795x + 4.5795$	0.653	25.415	0.627	0.755
	Chls	$y = 140.84x^2 - 110.27x + 24.82$	0.612	21.281	0.583	2.600
EVI	Chla	$y = 9.7705x^2 - 13.358x + 8.1238$	0.710	32.995	0.688	0.864
	Chlb	$y = 3.5428x^2 - 5.4181x + 2.6148$	0.702	31.812	0.680	0.700
	Chls	$y = 20.154x^2 - 44.399x + 32.094$	0.556	16.913	0.523	2.034
RDVI	Chla	$y = 3.2447x^2 - 1.5165x + 2.8664$	0.659	26.097	0.634	2.884
	Chlb	$y = 3.114x^2 - 5.8428x + 3.3762$	0.699	31.412	0.677	0.703
	Chls	$y = 6E-06x^2 - 0.0098x + 11.83$	0.655	25.682	0.630	1.792
VI1	Chla	$y = 7.6192x^2 - 2.3606x - 1.567$	0.579	18.593	0.525	3.285
	Chlb	$y = 13.379x^2 - 27.295x + 14.61$	0.583	18.839	0.552	0.828
	Chls	$y = 47.726x^2 - 96.932x + 53.56$	0.436	10.454	0.395	3.133
VI2	Chla	$y = 127.15x^2 + 17.461x + 3.7539$	0.589	19.320	0.558	3.167
	Chlb	$y = 127.15x^2 + 17.461x + 3.75$	0.589	19.349	0.559	0.822
	Chls	$y = 337.33x^2 - 10.643x + 4.124$	0.444	10.784	0.403	3.112
VI3	Chla	$y = 436.67x^2 - 617.11x + 220.8$	0.668	27.196	0.644	2.877
	Chlb	$y = 0.0378x^2 - 0.3662x + 1.507$	0.552	16.652	0.519	0.858
	Chls	$y = 0.2864x^2 - 3.8448x + 17.188$	0.549	16.415	0.515	2.804

Table 4: Stepwise regression models of photosynthetic pigment in Stipa purpurea with enhanced spectral variables (with VIF = 35, R^2 is the coefficient of determination, F is the value of F distribution, and P is the significant level).

Soil properties	Regression models	R^2	F	P
Chla	$y = 0.466 - 9.17$EVI	0.708	31.9	0.000
Chlb	$y = 12.69 + 11.22$RVI $- 6.57$NDVI $+ 0.027$VI2	0.623	48.36	0.000
Chls	$y = 0.902 + 0.741$RVI $+ 1.866$NDVI	0.644	12.79	0.000

Chla values in bare soil and alpine steppe region are low, the Siling Co. and Kering Co. are up to 30 mg/g, and the alpine swamp meadow near lake is 18 mg/g. The range of Chlb is 0–15 mg/g. The Chlb values in the alpine swamp meadow and alpine meadow near Kering Co. are 6–10 mg/g and in the alpine grassland are varied from 10 to 15 mg/g. The Chls is between 7 and 50 mg/g, and its spatial distribution is similar to Chlb. The above results indicate that the distribution of Chla is opposite to Chlb and total chlorophyll. Chlb determines the distribution pattern of Chls in the water area, but the Chlb value is lower than the Chla. The Chls in the wetland is between 15 and 25 mg/g, while the chlorophyll in the alpine steppe and alpine desert steppe is lower than that in the dry soil condition.

3.5. Photosynthetic Pigment Analysis. The Chla and Chlb are the most studied parameters in photosynthetic pigments content. The lutein, carotenoids, and other photosynthetic

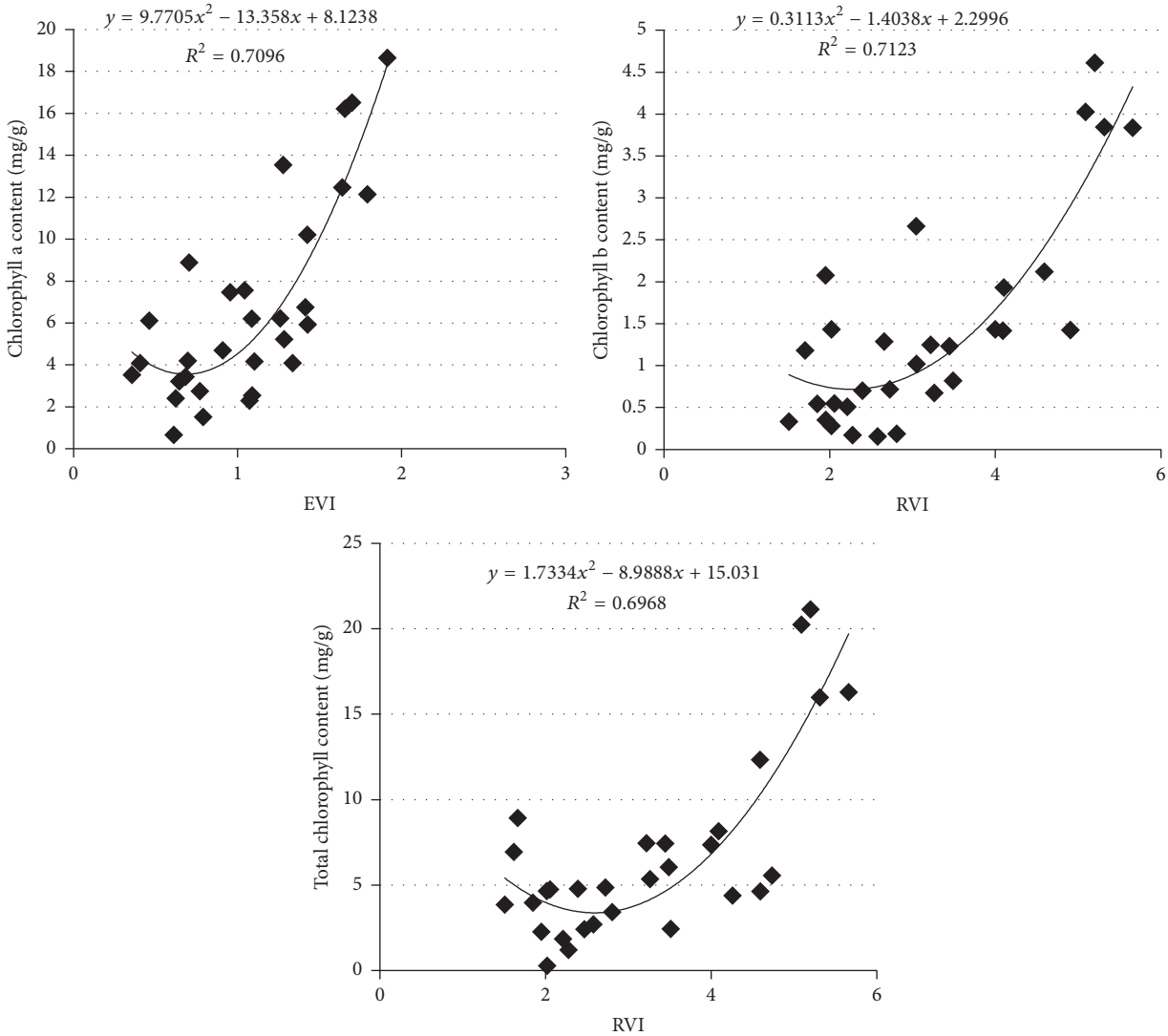

Figure 4: Results of the optimal estimation model of the photosynthetic pigment of Stipa purpurea.

Table 5: The correlation coefficient between different pigments.

pigment	Chla	Chlb	Chls	Cars
Chla	1	0.8597	0.9886	0.7540
Chlb	0.8597	1	0.9266	0.5126
Chls	0.9886	0.9266	1	0.7060
Cars	0.7540	0.5126	0.7060	1

pigments are not only the composition of light-emitting pigment. Under the external stress they are more involved in the leaves of yellow Cyclin and other metabolic pathways. The correlation coefficients of the pigment content of Stipa grandis were correlated with each other by 0.01. In particular, the correlation coefficient between the Chla and Chls is 0.98 (Table 5), indicating that the trend of change between different pigments is consistent, and the response of different pigments in the spectral characteristic parameters are similarity (Table 3), such as Chla, Chla, and Chls of RVI. In single factor model, R^2 of RVI is higher than 0.65, and R_g and SD_g are both lower than 0.42. It is shown that the characteristic parameters are consistent with the simulation of the photosynthetic pigment content. Some parameters are related to all the pigment correlations, and some are independent. However, in the stepwise regression model, not all parameters with higher correlation with the pigment can iterate into the equation but rather enter the equation in the form of complementary effects. Several similar parameters are excluded from the model operation (Table 4). The spectral parameters of the hyperspectral remote sensing image are calculated by comparing the band of the characteristic parameters involved in the regression model with the band of the hyperspectral image of HJ-1A and then are substituted into the regression model. The results showed the spatial distribution of Chla, Chlb, and Chls (Figure 5).

The chlorophyll content of Shenzha County was calculated by the spatial distribution data of photosynthetic pigments (Table 6). The mean estimated value content of Chla

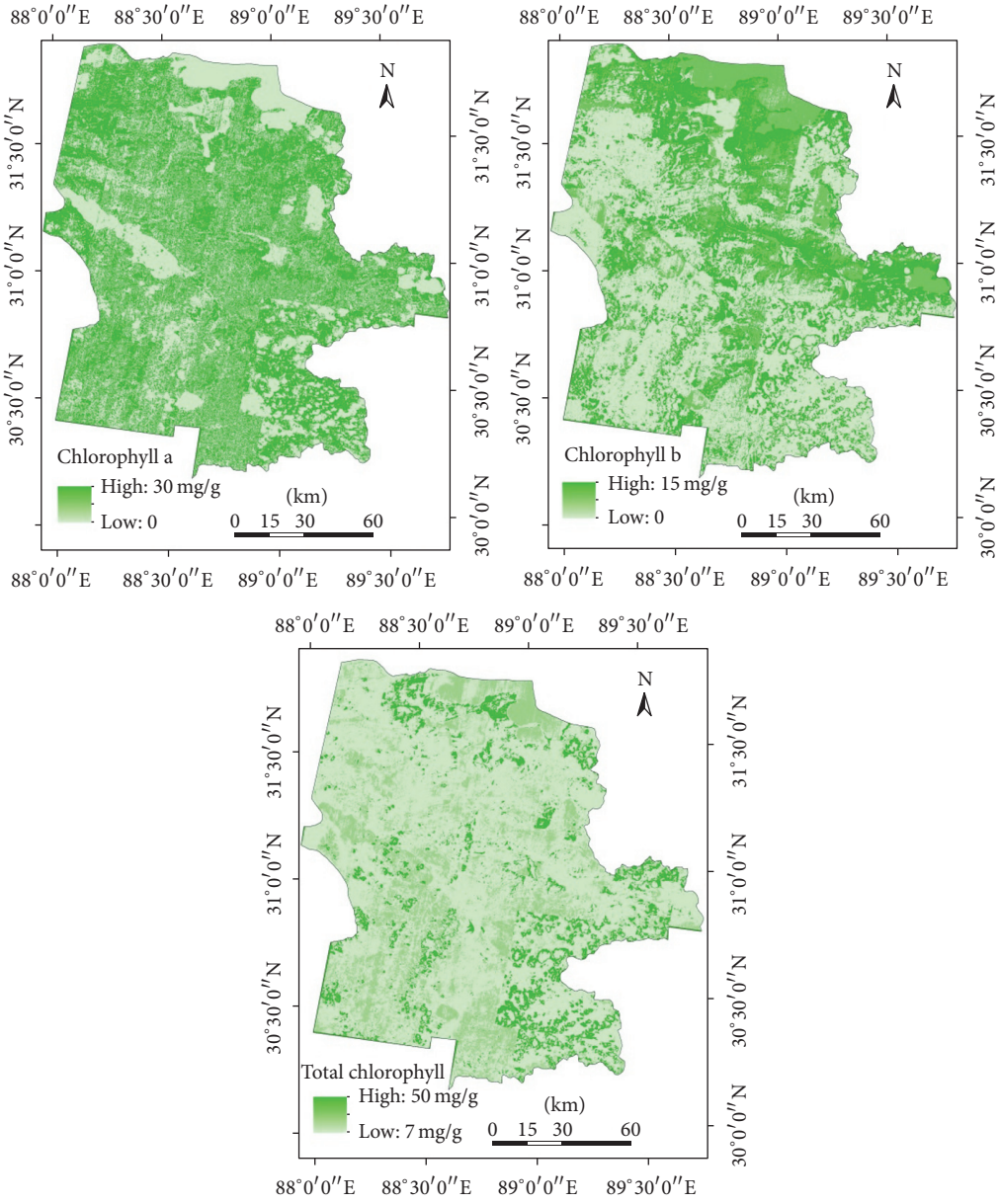

Figure 5: The map of photosynthetic pigment content.

Table 6: The chlorophyll content of Shenzha County (mg/g).

Pigment	Maximum measured value	Maximum estimated value	Minimum measured value	Minimum estimated value	Average measured value	Mean estimated value	Estimated standard deviation	Relative error (%)
Chla	31.5	29.5	1.22	0.65	10.4	9.12	7.86	1.57
Chlb	17.2	14.9	0.40	0.01	2.50	1.87	2.07	7.24
Chls	54.6	48.5	0.96	0.29	12.8	9.23	10.7	6.95

in Stipa bungeana is about 4.88 times that of Chlb, while Cars is generally slightly more than Chlb, so chlorophyll a plays a dominant role in absorption. The chlorophyll content of the measured sample was slightly higher than that of the spatial estimation, because the change of photosynthetic pigment in the community of Stipa purpurea occurred in the alpine steppe region with low soil water content, and the change of the pigment in the lake and water was small. Some of the images of the snow-covered area (seasonal snow) affect the actual monitoring of photosynthetic pigments, so the estimate is slightly lower, but the estimated relative error is small, below 7.24%.

4. Conclusion

Based on the correlation between ground measured spectral characteristics and photosynthetic pigments, R_g, R_r, SD_g, RVI, NDVI, EVI, RDVI, VI1, VI2, and VI3 characteristic parameters with the correlation level of 0.01 and ground photosynthetic pigments are used to establish single factor equations and select the appropriate spectral characteristic parameters. In these parameters, R^2 of R_g, R_r, and SD_g are less than 0.42, so these three parameters do not participate in the next step budget. The three spectral inversion models of Chla, Chlb, and Chls were established by using RVI, NDVI, EVI, RDVI, VI1, VI2, and VI3. Finally, the spatial distribution pattern of Chla, Chlb, and Chls was obtained by using the scale push method and HJ-1A remote sensing image, and the characteristic parameter band in the model was mapped to the band in the hyperspectral remote sensing image. The relative error is small, and the monitoring and investigation of the grassland growth and health status of large-scale area in high altitude and alpine region are realized by using the spatial estimation value and the ground measured value.

(1) In the fitting analysis of pigments content and hyperspectral parameters, 670 nm is used as the red band, 801 nm as the near-infrared band, and 553 nm as the green band to construct pigments content inversion model. Among the 16 spectral parameters, 10 parameters are correlated with chlorophyll, and the correlation order is Chlb > Chla > Chls. The best correlation index between Chla, Chlb, and Chls is RVI, and the correlation coefficients are 0.707, 0.728, and 0.694, respectively. The results indicate that the estimation of the chlorophyll content of Stipa purpurea is more feasible by using spectral characteristic variables.

(2) The chlorophyll estimation model of Stipa purpurea was established by using 10 extremely significant correlation spectral parameters. The estimation model of Chla is based on vegetation index EVI, estimation of Chlb is based on RVI, NDVI, and VI2, Chls model is based on RVI and NDVI, and the coefficient of determination (R^2) of fitted equation is 0.6. The relative error of the model estimation is small, which is below 7.24%, indicating that the model is feasible in the region.

(3) The distribution of Chla is opposite to Chlb and Chls in the water area. Chlb in water area determines the distribution pattern of Chls, but Chlb value is lower than Chla; thus, the Chls in wetlands near lakes is 15–25 mg/g. The Chls of alpine steppe and alpine desert steppe is mainly affected by Chla in dry soil condition.

(4) The proposed method in this paper can effectively estimate the pigments content of Stipa purpurea in Shenzha, Tibet. The results could reflect the distribution and succession pattern of Stipa purpurea community. However, there are some errors in estimation model for pigment content based on hyperspectral vegetation physiological parameters. This is due to the fact that the vegetation type, growth stage, growth condition, and the signal-to-noise ratio of the spectrometer itself will influence the establishment of statistical model.

Conflicts of Interest

The authors declare that they have no conflicts of interest.

Acknowledgments

This research is supported by the National Natural Science Funds of China (41301094); the Hundred Young Talents Program of the Institute of Mountain Hazards and Environment (SDSQB-2015-02); the Lead Strategic Project of the Chinese Academy of Sciences (XDB03030507); the 973 National Projects (2015CB452706); the Open Fund for Spatial Information Technology Key Lab Bases of the Ministry of Land and Resources of China (KLGSIT2014-06).

References

[1] X. M. Zhou, Q. J. Wang, Y. Q. Zhang, X. Q. Zhao, and Y. P. Lin, "Quantitative analysis of vegetation succession in alpine meadow under different grazing intensity," *Journal of Plant Ecology and Botany*, vol. 11, no. 4, pp. 276–285, 1987.

[2] M. J. Duan, Q. Z. Gao, Y. F. Wan et al., "Effect of grazing on community characteristics and species diversity of stipa purpurea alpine grassland in northern tibet," *Acta Ecologica Sinica*, vol. 30, no. 14, pp. 3892–3900, 2010.

[3] D. Lu, Y. Zhao, R. Han, L. Wang, and P. Qin, "The complete chloroplast genome sequence of the Purple Feathergrass Stipa purpurea (Poales: Poaceae)," *Conservation Genetics Resources*, vol. 8, no. 2, pp. 101–104, 2016.

[4] P. P. Yue, X. F. Lu, R. R. Ye et al., "Distribution of Stipa purpurea steppe in the northeastern qinghai-xizang plateau (China)," *Russian Journal of Ecology*, vol. 42, no. 1, pp. 50–56, 2011.

[5] D. Filella and J. Peñuelas, "The red edge position and shape as indicators of plant chlorophyll content, biomass and hydric status," *International Journal of Remote Sensing*, vol. 15, no. 7, pp. 1459–1470, 1994.

[6] A. C. Madeira, A. Mendonça, and M. E. Ferreira, "Relationship between spectroradiometric and chlorophyll measurements in green beans," *Communications in Soil Science and Plant Analysis*, vol. 31, no. 5-6, pp. 631–643, 2000.

[7] A. A. Gitelson, G. P. Keydan, and M. N. Merzlyak, "Three-band model for noninvasive estimation of chlorophyll, carotenoids, and anthocyanin contents in higher plant leaves," *Geophysical Research Letters*, vol. 33, no. 11, Article ID L11402, 2006.

[8] M. J. Gallardo, J. P. Staforelli, P. Meza, I. Bordeu, and S. Torres, "Characterization of Chromobacterium violaceum pigment through a hyperspectral imaging system," *AMB Express*, vol. 4, no. 4, pp. 2–9, 2014.

[9] M. Gupta, P. K. Srivastava, S. Mukherjee, and G. Sandhya Kiran, "Chlorophyll retrieval using ground based hyperspectral data from a tropical area of india using regression algorithms," in *Remote Sensing Applications in Environmental Research*, vol. 4, pp. 177–194, 2014.

[10] F. Flores-de-Santiago, J. M. Kovacs, and F. Flores-Verdugo, "The influence of seasonality in estimating mangrove leaf

chlorophyll-a content from hyperspectral data," *Wetlands Ecology and Management*, vol. 21, no. 3, pp. 193–207, 2013.

[11] D. Haboudane, J. R. Miller, N. Tremblay, P. J. Zarco-Tejada, and L. Dextraze, "Integrated narrow-band vegetation indices for prediction of crop chlorophyll content for application to precision agriculture," *Remote Sensing of Environment*, vol. 81, no. 2-3, pp. 416–426, 2002.

[12] D. N. H. Horler, J. Barber, and A. R. Barringer, "Effects of heavy metals on the absorbance and reflectance spectra of plants," *International Journal of Remote Sensing*, vol. 1, no. 2, pp. 121–136, 1980.

[13] A. A. Gitelson, C. Buschmann, and H. K. Lichtenthaler, "The chlorophyll fluorescence ratio F735F700 as an accurate measure of the chlorophyll content in plants," *Remote Sensing of Environment*, vol. 69, no. 3, pp. 296–302, 1999.

[14] D. A. Sims and J. A. Gamon, "Relationships between leaf pigment content and spectral reflectance across a wide range of species, leaf structures and developmental stages," *Remote Sensing of Environment*, vol. 81, no. 2-3, pp. 337–354, 2002.

[15] G. A. Blackburn, "Quantifying chlorophylls and carotenoids at leaf and canopy scales: An evaluation of some hyperspectral approaches," *Remote Sensing of Environment*, vol. 66, no. 3, pp. 273–285, 1998.

[16] J. G. P. W. Clevers and L. Kooistra, "Using hyperspectral remote sensing data for retrieving total canopy chlorophyll and nitrogen content," in *Proceedings of 3rd Workshop on Hyperspectral Image and Signal Processing: Evolution in Remote Sensing, WHISPERS 2011*, June 2011.

[17] A. D. Richardson, S. P. Duigan, and G. P. Berlyn, "An evaluation of noninvasive methods to estimate foliar chlorophyll content," *New Phytologist*, vol. 153, no. 1, pp. 185–194, 2002.

[18] J. Dash and P. J. Curran, "Evaluation of the MERIS terrestrial chlorophyll index (MTCI)," *Advances in Space Research*, vol. 39, no. 1, pp. 100–104, 2007.

[19] J. Delegido, L. Alonso, G. González, and J. Moreno, "Estimating chlorophyll content of crops from hyperspectral data using a normalized area over reflectance curve (NAOC)," *International Journal of Applied Earth Observation and Geoinformation*, vol. 12, no. 3, pp. 165–174, 2010.

[20] P. Chen, D. Haboudane, N. Tremblay, J. Wang, P. Vigneault, and B. Li, "New spectral indicator assessing the efficiency of crop nitrogen treatment in corn and wheat," *Remote Sensing of Environment*, vol. 114, no. 9, pp. 1987–1997, 2010.

[21] W. M. Yong and X. M. Wang, "Progress on grassland chlorophyll content estimation by hyperspectral analysis," *Progress in Geography*, vol. 35, no. 1, pp. 25–34, 2016.

[22] A. Bannari, K. S. Khurshid, K. Staenz, and J. W. Schwarz, "A comparison of hyperspectral chlorophyll indices for wheat crop chlorophyll content estimation using laboratory reflectance measurements," *IEEE Transactions on Geoscience and Remote Sensing*, vol. 45, no. 10, pp. 3063–3074, 2007.

[23] G. Le Maire, C. François, and E. Dufrêne, "Towards universal broad leaf chlorophyll indices using PROSPECT simulated database and hyperspectral reflectance measurements," *Remote Sensing of Environment*, vol. 89, no. 1, pp. 1–28, 2004.

[24] C. J. Nichol and J. Grace, "Determination of leaf pigment content in Calluna vulgaris shoots from spectral reflectance," *International Journal of Remote Sensing*, vol. 31, no. 20, pp. 5409–5422, 2010.

[25] G. L. Jin, J. Z. Zhu, H. L. Liu, S. M. Tang, and C. H. Wang, "Study on physiology/ecology adaptation of main plant in degraded seriphidiumtransiliense desert rangeland," *ActaAgrectirSinica*, vol. 19, no. 1, pp. 26–30, 2011.

[26] H. A. Jin, D. W. Liu, K. S. Song, Z. M. Wang, F. Li, and H. J. Liu, "Comparing the performance of broad-band and narrow-band vegetation indices for estimation of soybean LAI," *System Sciences and Comprehensive Studies in Agriculture*, vol. 23, no. 4, pp. 503–508, 2007.

Hindawi
Mathematical Problems in Engineering
Volume 2017, Article ID 2183585, 16 pages
https://doi.org/10.1155/2017/2183585

Research Article

Dynamic Changes Analysis and Hotspots Detection of Land Use in the Central Core Functional Area of Jing-Jin-Ji from 2000 to 2015 Based on Remote Sensing Data

Yafei Li,[1] Gaohuan Liu,[2] and Chong Huang[2]

[1]*Civil Aviation University of China, Tianjin 300300, China*
[2]*Institute of Geographic Sciences and Natural Resources Research, CAS, Beijing 100101, China*

Correspondence should be addressed to Yafei Li; commissioner@126.com

Received 4 January 2017; Revised 11 March 2017; Accepted 2 April 2017; Published 3 May 2017

Academic Editor: Hasi Bagan

The article uses GIS spatial analysis and grid technologies to study the dynamic changes, hotspot regions, and driving forces in land use of the central core functional area of Jing-Jin-Ji. The research results are as follows: from 2000 to 2015, the main types of land use in the central core functional area of Jing-Jin-Ji are cultivated land, woodland, and built-up land. In the period of 2005–2010, the transfer between built-up land and cultivated land was frequent. The dynamic degree of single land use in unused land was highest. It also finds out that the dynamic degree of the integrated land use from 2005 to 2010 was higher. The center of gravity transfer of the dynamic degree of integrated land use was concentrated in research area. As for the hotspots, their number and scope are increasing, and the positions located in the edge of original main urban area and developed transportation network. The main characteristics of land use dynamic change in the study area are the rapid decrease of cultivated land area and rapid growth of built-up land. The spatial agglomeration of economic factors caused by human activities has an important influence on the spatial and temporal dynamic changes of land use.

1. Introduction

Land, the carrier of human activities, is one of the most important natural resources and offers physical space for human being to live in and carry out social, economic, and political activities. Land use/cover change (LUCC) is a key basis for studying natural resource management, climate change [1–4], and urban planning and also a major impact factor for environmental assessment [5, 6]. It is closely connected with population migration and economic activities [7]. LUCC, therefore, has been a heated topic for geoscience [8] and also a core subject cosupported by International Geosphere Biosphere Programme (IGBP) and International Human Dimensions Programme (IHDP). The high precision land use dynamic change detection can provide basic data for the research of interaction relationship between human being and the nature [9–13].

Entering the 21st century, all regions have been experiencing rapid LUCC as the scope of human activities expands and land use intensity grows on a continuous basis [14, 15]. Detection of dynamic change features and hotspots for land use is of great significance. That is how land resource can be better managed and used efficiently in the long run. At the same time, it also offers basic data for the study of human-nature interaction. For this reason, LUCC research of varying spatial scales has drawn wide attention at home and abroad [16–25].

Today, most research efforts focus on the process and driving mechanism of land use change and how land use change influences and feeds back to ecology and environment [26–28]. The research scale ranges from the globe to regions, and the researchers have obtained plentiful research achievement over the years [29–35]. Hotspots detection is an important research method to discover the active regions of regional development [36]. It can help to highlight regions sensitive to land use change, which is of critical importance for authorities, such as land and resources administration and urban planning department, to set up future land use strategy. For the time being, the research on land use change

seldom involves hotspots detecting [37–42]; furthermore, no attention has been paid to the Beijing-Tianjin-Hebei Region in China. At the same time, land use research on the Beijing-Tianjin-Hebei Region rarely analyzes the process and driving factors of land use change in detail.

The main research methods of land use dynamic change in previous papers included land use dynamic index, transfer matrix, and driving force analysis. [17, 19, 26, 30–33]. Most of the previous researches were based on the land use classification map to calculate the intensity and scope of land use change, which rarely referred to spatial variation characteristics and hotspots analysis of land use dynamic change. The spatial transfer pattern of land use dynamic change was seldom mentioned, so the spatial evolution characteristics of regional land use dynamic change cannot be studied completely and deeply. In this article, from the perspective of spatial feature of land use dynamic change, the spatial characteristics of land use dynamic change were analyzed thoroughly using the map of land use transfer distribution, land use integrated dynamic index, the center of gravity of land use change and hotspots distribution of land use change on the basis of pervious researches. So, the research methods of this article were comprehensive and innovative in certain degree.

The Beijing-Tianjin-Hebei Region (Jing-Jin-Ji) is a core source for China's rapid economic growth. Particularly after 2000, this region has witnessed accelerating progress of urbanization and become a hotspot. However, the development level within the region varies greatly. The State Council of China has published *Plan of Coordinated Development for the Beijing-Tianjin-Hebei* to coordinate regional development and rearrange noncapital functions of Beijing. Under a structure of "One Core, Two Cities, Three Axes, Four Areas, and Multiple Nodes," the plan will promote order rearrangement of noncapital functions of Beijing and ultimately build a network space framework that combines major cities and functional zone platform of strategic importance. The "Four Areas" are, respectively, central core functional area [43–45], east coastal development area, south functional extension area, and northwest eco-conserving area. The central core functional area will be to undertake Beijing's noncapital functions and to accelerate the Beijing-Tianjin-Baoding interactive development. In the light of this, the central core functional area is key to Beijing-Tianjin-Hebei interactive development, in which land use strategy is a big question facing Beijing-Tianjin-Hebei land management department. This article follows the trend in LUCC research and answers to the demands by national key development planning strategy. Taking the central core functional area of Jing-Jin-Ji as the research object, this article utilized geographic information and geostatistics technologies, as well as classification data of remote sensing. Based on the spatial grid, the dynamic change characteristics of land use were analyzed to explore hotspots of land use change and their spatial relationships, and main driving factors of land use change are obtained in this article. It offers scientific basis and decision-making reference for the making of the land use policies, the rational use of land resources, and the optimization of land use structure, to better undertake Beijing's noncapital functions in the central core functional area.

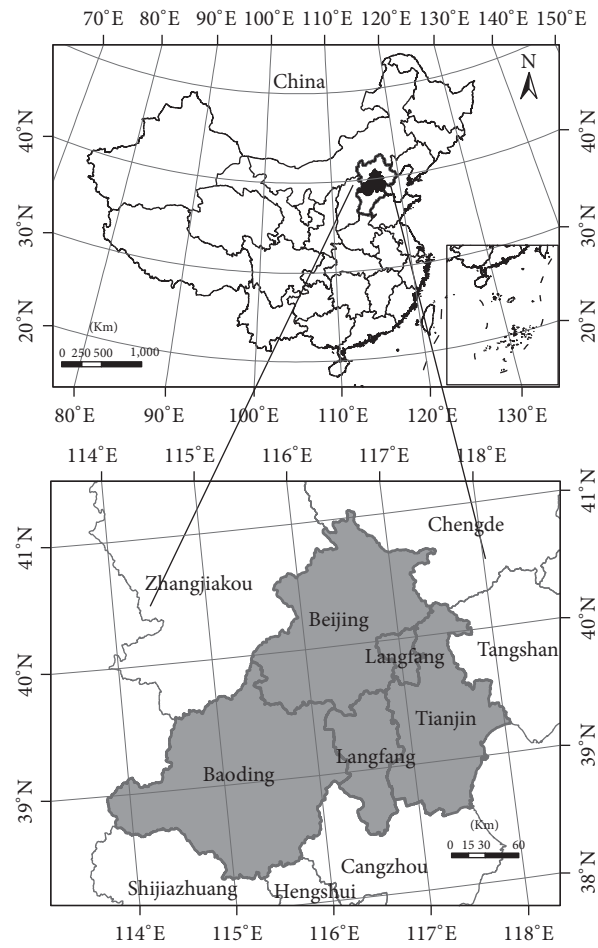

Figure 1: Location map of study area.

2. Study Area and Data Sources

The Jing-Jin-Ji region (113°11′E–119°45′E, 36°05′N–42°37′N), shown in Figure 1, covers an area of 218,000 km^2, about 2.27% of China. The region is located in North China Plain, Yanshan-Taihang Mountains, and the southeast side of Inner Mongolian Plateau. The region has mountains, hills, and plateaus in the northwest and broad plains in the middle and southeast, with the northwest part being higher than southeast part. The region has a typical continental monsoon climate with dry cold winter and hot rainy summer. The monthly average temperature is below 3°C, with the average temperature in July between 18°C and 27°C. The average annual precipitation is 524.4 mm [46]. The central core functional area of Jing-Jin-Ji includes Beijing, Tianjin as well as Baoding, and Langfang bordering Beijing and Tianjin. The central core functional area occupies an area of 57,000 km^2, about 27% of Beijing-Tianjin-Hebei Region, with a population of 52,706,000 (2015) or a population density of 924 people/km^2. In 2015, the area registered a GDP of 4.24 trillion yuan, becoming more developed than other areas in the region. Population aggregation effect is obvious, especially in Beijing and Tianjin. Arable land and forest land are two major land use categories in the target area; the area

of urban land expands very rapidly. In the background of regional coordinated development of Jing-Jin-Ji, Tianjin, Baoding, and Langfang will gradually undertake industrial transfer in Beijing, urban land and other construction lands will continue to expand, and land use structure will experience drastic changes. Given limited unused land in the region, making good use of land reserves will be a major direction for land development.

The research chose land use data and socioeconomic statistic data for analysis. The classification data of land use (30 m resolution) was provided by the Data Center for Resources and Environmental Sciences, Chinese Academy of Sciences (RESDC) in 2000, 2005, 2010, and 2015. The land use database was acquired by the rapid extraction of human-computer interaction based on remote sensing spectrum information. The Landsat TM images were interpreted to build the 30 m resolution land use database covering the whole of China from 2000 to 2015. While the Landsat TM data could not cover the whole of China or the quality of TM images was poor, the CCD multispectral data of HJ-1 could be as a supplement [47, 48]. In order to ensure the quality and consistency of data acquisition, the researchers examined the quality of each data and the process of data integration. Before the early development of land use database, the field investigation would be carried out to access to a large number of field investigation records and photos in the autumn of the north or in the spring of the south in China. The proportion of 10% counties of China were randomly selected to carry out accuracy verification of land use database. The accuracy of the comprehensive evaluation of land use type was more than 94.3%, which met the user mapping accuracy of 30 m resolution [47, 49].

The data, with the accuracy over 90%, met requirements for land use change analysis [49–51]. Based on IGBP LUCC and the research objective, a land use classification system (Tier I) was adopted. The system included 6 categories: arable land, forest land, grassland, water body, built-up land, and unused land. To increase understanding of regional land use characteristics, field investigations and interviews were also conducted in cities like Beijing, Tianjin, and Langfang. Socioeconomic statistic data were collected from China Social Economic Statistical Yearbook (2015) to discuss human factors driving land use change in the target area.

3. Research Method

This study adopted single dynamic index of land use, integrated dynamic index of land use, and land use transfer matrix to measure the temporal and spatial change characteristics of land use. The single dynamic index of land use can quantitatively be used to describe the change speed of regional land use [52, 53], which played an important role in comparing the regional differences of land use change and analyzing the change trend of land use [54]; the formula is

$$K = \frac{u_b - u_a}{u_a} \times \frac{1}{T} \times 100\%. \quad (1)$$

In this formula, u_b, u_a are the area of a certain land use category at the end and beginning moment of the research, respectively, and T is length of the research period.

The integrated dynamic index of land use is the transfer rate among land categories during the research period [55], and it can reflect the overall change of all land categories in the study area during the research period [56, 57]; the formula is

$$K_{\text{total}} = \frac{\sum_{i=1}^{n} \left| u_{bi} - u_{ai} \right|}{2 \sum_{i=1}^{n} u_{ai}} \times \frac{1}{T} \times 100\%. \quad (2)$$

In this equation, u_{bi} and u_{ai} are the area of a certain land use category at the end and beginning moment of the research, respectively, T is the duration of the study, and n is the quantity of land use categories and is equal to 6 in this study. When T is year(s), K_{total} is the annual integrated change rate of area change of all land use categories.

The land use transfer matrix can reveal the land use structure at a certain point in time and quantitatively describe the dynamic process of the mutual transformation between land categories at the end and beginning of the research period and show the transferred-in and transferred-out information of each land category [58]. Based on the land use data of the research area in three time periods and four time points from 2000 to 2015, with the support of relevant spatial analysis modules of ArcGIS10.3 and ENVI5.3, this article conducted spatial analysis and statistics of the land use data of four periods to obtain the transfer matrixes of land use in three time periods, namely, 2000–2005, 2005–2010, and 2010–2015, and then contrasted the quantity and structural characteristics of land use change during 15 years. At the same time, the spatial distribution maps of land use transfer were obtained in three time periods by ENVI 5.3 postclassification processing module to analyze the spatial variation and features of land use transfer and explore the active regions of land use change during 15 years in the research region.

The center of gravity is the average x- and y-coordinate of all the features in the study area. It is useful for tracking changes in the distribution or for comparing the distributions of different types of features. The center of gravity is given as

$$X = \frac{\sum_{i=1}^{n} x_i}{n}, \qquad Y = \frac{\sum_{i=1}^{n} y_i}{n}. \quad (3)$$

In the equation, x_i and y_i are the coordinate for feature i and n is equal to the total number of features.

The Weighted center of gravity extends to the following:

$$X_w = \frac{\sum_{i=1}^{n} w_i x_i}{\sum_{i=1}^{n} w_i}, \qquad Y_W = \frac{\sum_{i=1}^{n} w_i y_i}{\sum_{i=1}^{n} \sum_{i=1}^{n} w_i}. \quad (4)$$

In the equation, w_i is the weight at feature i.

Hierarchical hotspot detection is one of the global clustering test methods, which is used to determine if there is

clustering in the studied area and obtain the hotspots in a "Pyramid" type multilayer space based on a certain rule [58]. In the process of hierarchical hotspot detection, the "limit distance" of a "cluster unit" is defined and compared with the distance of spot pair in each space. When it is less than the limit distance, this spot will be included in the cluster unit [37, 39, 58, 59]. The method of Nearest Neighbor Hierarchical Clustering is used to cluster the hotspots of land dynamic change; the main calculation formula is as follows.

The mean random distance was defined as

$$d_{\mathrm{NN(ran)}} = 0.5\sqrt{\frac{A}{N}}. \tag{5}$$

In the equation, A is the area of the region and N is the number of incidents and the standard error of the mean random distance is

$$\mathrm{SE}_{d(\mathrm{ran})} \cong \sqrt{\frac{(4-\pi)\,A}{4\pi N^2}} = \frac{0.26136}{\sqrt{N^2/A}}. \tag{6}$$

In the equation, A is the area of the region and N is the sample size (number of incidents). The confidence interval around that distance is defined as

$$\text{Confidence interval} = d_{\mathrm{NN(ran)}} \pm t * \mathrm{SE}_{d(\mathrm{ran})}. \tag{7}$$

In the equation, t is the t-value associated with a probability level in Student's t-distribution.

The approximate lower limit of this confident interval is

$$\text{lower limit of confidence interval} = d_{\mathrm{NN(ran)}} - t * \mathrm{SE}_{d(\mathrm{ran})} \cong 0.5\sqrt{\frac{A}{N}} - t\sqrt{\frac{(4-\pi)\,A}{4\pi N^2}} \tag{8}$$

and the upper limit of this confidence interval is

$$\text{upper limit of confidence interval} = d_{\mathrm{NN(ran)}} + t * \mathrm{SE}_{d(\mathrm{ran})} \cong 0.5\sqrt{\frac{A}{N}} + t\sqrt{\frac{(4-\pi)\,A}{4\pi N^2}}. \tag{9}$$

The confidence interval defines a probability for the distance between any pair of points.

For hierarchical clustering analysis, the number of spots in the cluster unit is specified to strengthen the clustering rules of elements. In this article, the "limit distance" was set to 30 km and the number of spots in the cluster unit was defined as 5 according to many tests. It also needed to provide a grid of the research region and determine the size of grid according to the accuracy and completeness of land use change, which, therefore, needed to be determined by repeated tests. The research region was eventually divided into 189 grids with the size of 20 km × 20 km by reference to other researchers' research results [37, 39, 60, 61]. The integrated dynamic index and the center of gravity of the integrated dynamic index of land use of each grid were, respectively, calculated in ArcGIS. The hotspots of land use dynamic change of the research region in three different time periods from 2000 to 2015 were obtained by use of the hotspots detection tool in Crimestat software (Crimestat 5.2), which were combined with other data to analyze the causes of formation of land use hotspots.

The center of gravity and hotspots analysis both can reflect the dynamic change tendency of land use intensity. The difference is that the gravity is the core point of dynamic change of regional land use, while the hotspots analysis reveals the core regions of land use dynamic change. At some point, there is only one point of gravity, but the one or several hotspots regions can be obtained from hotspots analysis. In general, gravity analysis can be used to analyze the transfer trend of regional land use dynamic change, which can reflect the transfer process of land use dynamic change intensity. The hotspots analysis can determine where land use change is more severe during the research period. The combination of two methods can be used to reflect the transfer characteristic of land use dynamic change intensity and also to obtain the hotspots regions of land use change.

4. Research Results and Analysis

4.1. Analysis of Land Use Quantity and Spatial Characteristics in Central Core Functional Area of Jing-Jin-Ji. Based on the land use spatial classification data of the four periods in the research region, the spatial distribution map of land use in different periods was produced (Figure 2), and the statistical tables of land use in the corresponding years (Table 1) were also produced to analyze the quantitative and spatial characteristics of land use changes. It can be seen that the main land categories were arable land, forest land, and built-up land, among which, the arable land was the largest, mainly distributed in the eastern and southern plains of the research region, including the southeastern part of Beijing, Langfang, northern and southern parts of Tianjin, and eastern part of Baoding, which was mainly distributed in rural settlements and around the city, with a great degree of fragmentation. The area of arable land accounts for over 45% of the total area of the studied area, but the arable land was decreasing gradually from about 50% in 2000 to 45% in 2015, a decrease of nearly 5% and a significant decline in the quantity of arable land. This was mainly due to the rapid expansion of urban areas, especially around the main urban areas of Beijing and Tianjin, where part of the arable land was occupied.

The forest land was mainly distributed in the northwest mountain area of the research region, including the northwest part of Beijing and the western part of Baoding, with a concentrated contiguous distribution and small degree of fragmentation. From 2000 to 2015, the area of forest land was relatively stable and had less fluctuation, accounting for about 20% of the total area, which was mainly related to the national policy of the Closed Forest Project in China. In order to prevent dust weather, many State-Level Greening Projects have been started in the mountain area of Hebei, Beijing, and other places since the 1980s, which have been basically completed by 2000. In order to ensure the quality of The Shelter Forests, the state strictly limited changes of forest land, making the forest land area relatively stable.

Although the area of built-up land was less than that of arable land and forest land, the relative change was more

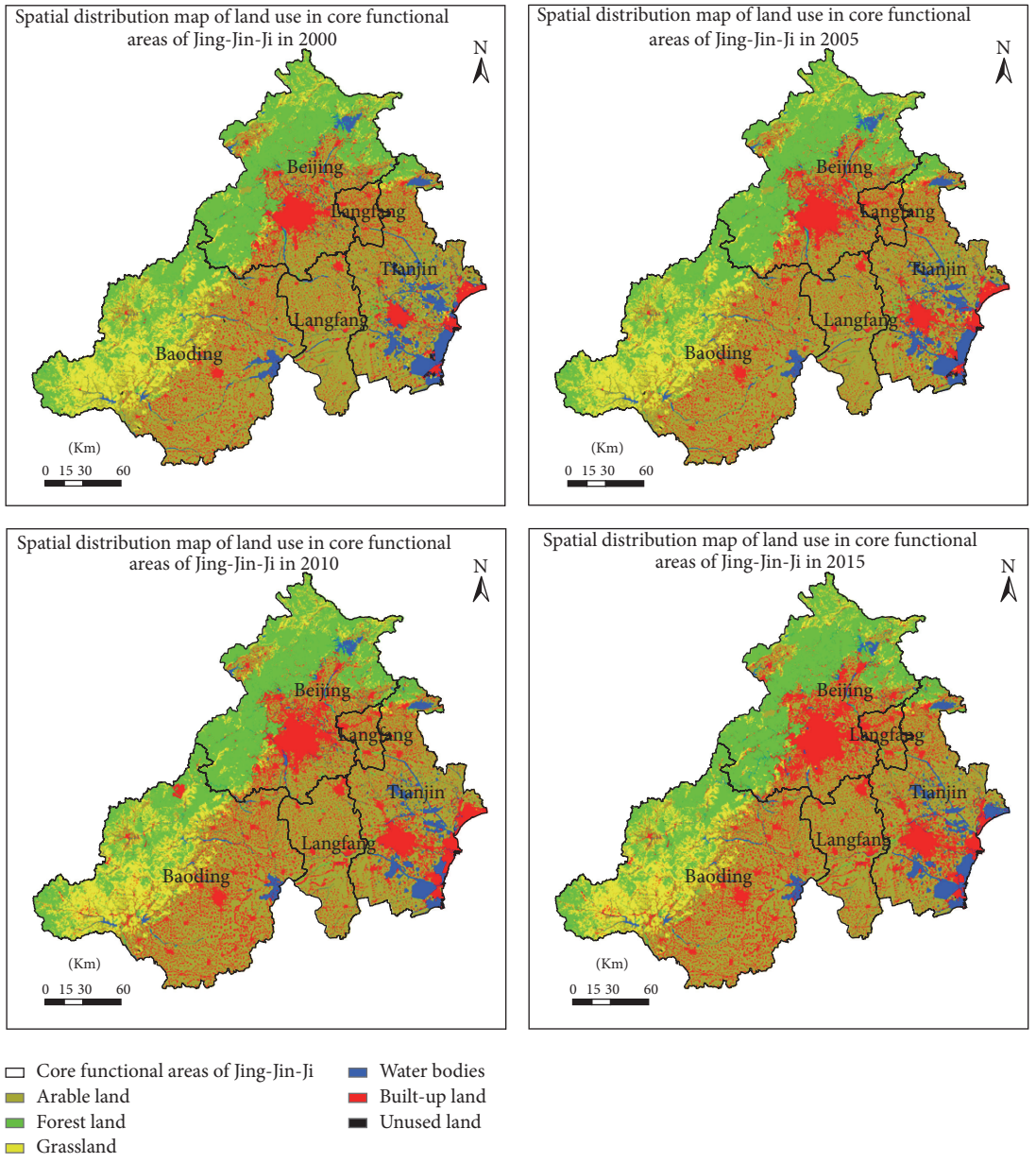

Figure 2: Spatial distribution map of land use in central core functional area of Jing-Jin-Ji from 2000 to 2015.

Table 1: Land use type structure in central core functional area of Jing-Jin-Ji.

Land category		2000	2005	2010	2015
Arable land	Area (km^2)	27964.13	27300.68	26496.46	25612.27
	Proportion (%)	49.39	48.22	46.80	45.24
Forest land	Area (km^2)	11761.77	11731.70	11547.78	11520.04
	Proportion (%)	20.77	20.72	20.40	20.35
Grass land	Area (km^2)	6638.89	6593.44	6340.99	6135.64
	Proportion (%)	11.73	11.65	11.20	10.84
Water body	Area (km^2)	3160.18	2942.69	2440.62	2644.09
	Proportion (%)	5.58	5.20	4.31	4.67
Built-up land	Area (km^2)	6987.65	7963.80	9774.07	10688.97
	Proportion (%)	12.34	14.07	17.26	18.88
Unused land	Area (km^2)	102.68	82.97	13.28	12.77
	Proportion (%)	0.18	0.15	0.02	0.02

intense, with an increasing trend year by year from 2000 to 2015. From the space viewpoint, this type of land was mainly distributed in the plain area of the studied area, and the expanded region was mainly in the surrounding area of the original built-up land. The southern area of the main urban area of Beijing, the surrounding area of the main Tianjin urban area, and Binhai New Area were the regions expanding faster than other areas. In terms of quantity, the area of built-up land accounted for less than 20% of the regional area and showed a rapid increasing trend year by year, from 12.34% in 2000 to 18.88% in 2015, an increase of nearly 6.5%. There was the most rapid increasing area in all the land categories, reflecting the rapid urbanization in the past 15 years.

4.2. Analysis of Land Use Transfer Features of the Central Core Functional Area of Jing-Jin-Ji

4.2.1. Analysis of Quantity and Structural Characteristics of Land Use Transfer. The land use transfer matrix in the studied region in periods of 2000–2005, 2005–2010, 2010–2015, and 2000–2015 was shown in Tables 2–5. As shown in Tables 2–5, the main land category transferred from arable land during 2000–2005 was built-up land, with an area of 806.65 km^2, accounting for about 3% of the arable land area in 2000, and the main transferred-in land category was water area, with an area of 154.34 km^2. In 2005–2010, there were no changes in the categories of transferred-out land, but the transferred-out area increased rapidly, which amounted to 2,038.14 km^2, with an increase of nearly 2.5 times, accounting for 7% of the arable land area in 2005, and the main transferred-in land categories were built-up land and water area, and about 3% of the land was transferred from built-up land. In 2010–2015, the main categories of transferred-out land did not change, but the transferred-out area decreased to 1,390.92 km^2, reaching a decrease of about 31%, accounting for 5.2% of the arable area in 2010, and the main transferred-in land categories were built-up land and forest land. Overall, from 2000 to 2015, the main transferred-out land categories from arable land were built-up land, and the main transferred-in land categories were built-up land, water body, and forest land, but the transferred-out area was far more than the transferred-in area, so the area of arable land was decreasing year by year. It can be seen that most of the transferred-out arable land was transferred into built-up land, which supported the need of economic development in this area.

In 2000–2005, the area of transferred-in and transferred-out from forest land was relatively small, and the forest land was relatively stable. The main transferred-out land categories from 2005 to 2010 were built-up land and arable land, accounting for 2.4% of the total forest land area in 2005. The transferred-in land categories were arable land and water body, with a relatively small area. During 2010–2015, the main transferred-out land categories were arable land and built-up land, accounting for 3.5% of the total area of forest land in 2010, and the main transferred-in land categories were arable land and grassland, with less differences of transferred-in area and transferred-out area. Therefore, from 2000 to 2015, the area of forest land was relatively stable, with less transferred-in and transferred-out area. The land categories used to make up for the loss of forest land were arable land and grassland.

The transferred-out area from built-up land in 2000–2005 was small, with only 24.7 km^2, but the transferred-out area was 1,000 km^2. The transferred-in land categories were mainly arable land and water body, of which the arable land accounted for 80% of transferred-in area, being the main source of increasing built-up land. During 2005 to 2010, the trend was obviously different from the previous stage. The transferred-out area increased significantly, and its land category was arable land, accounting for 10.3% of built-up land. Besides, the main transferred-in land category was also arable land, which increased significantly to about 2,038.14 km^2, accounting for about 20% of the built-up land in 2010. It indicated that the transfer between arable land and built-up land was frequent in this period, and the urbanization and arable land consolidation were carried out at the same time, but the area of built-up land increased more rapidly. During 2010 to 2015, the speed of transferred-in and transferred-out land slowed down, the main transferred-out land categories were the arable land and water body, and the transferred-in land was still arable land, with the area of 1,390.92 km^2. From 2000 to 2015, the area of built-up land increased significantly. The main transferred-out land categories were the arable land and water body, and the main transferred-in land categories were the arable land, forest land, grassland, and water body, indicating that the most active land categories of the research region were the arable land and built-up land. The mutual conversion between them led to the increase of built-up land and the decrease of other land categories, especially the arable land, reflecting the drastic urbanization of the research region.

Grassland, water body, and unused land had less transferred-in and transferred-out area, and the trends in the three periods were very similar.

The transferred-out land category from grassland was mainly built-up land, and its main transferred-in land category was arable land. The main transferred-in and transferred-out land categories of water body were both arable land. The main transferred-out land categories of unused land were arable land and built-up land, and the transferred-out area was relatively less.

From the above statistics, the arable land and built-up land were the most active land categories. When other land categories changed, most of them were exchanged with these two land categories, which were mainly transferred-out area, relating to the speed of regional economic development and the national policy of arable land protection. The area of forest land was relatively stable, and it had less interaction with other land categories. The change of water body was closely related to the arable land, which was mainly due to the convenient conversion between arable land and water area. That is to say, after the conversion of arable land into water body, it could be used for aquaculture and salt pond. When the farming efficiency declined, it was also easy for the farmers to transform the water body into arable land, and this conversion often occurred in farmland. The studied area was located in relatively developed region, so its unused land area

Table 2: Transfer matrix of land use in central core functional area of Jing-Jin-Ji from 2000 to 2005, unit (km^2).

2000	2005					
	Arable land	Forest land	Grass land	Water body	Built-up land	Unused land
Arable land	27111.26	15.53	2.47	28.21	806.65	0
Forest land	9.28	11712.87	0.3	1.84	37.47	0
Grass land	9.14	2.27	6579.75	9.63	38.09	0
Water body	154.34	0.31	8.53	2894.69	102.04	0.26
Built-up land	16.57	0.71	2.36	5.06	6962.94	0
Unused land	0.08	0	0.02	3.27	16.61	82.7

Table 3: Transfer matrix of land use in central core functional area of Jing-Jin-Ji from 2005 to 2010, unit (km^2).

2005	2010					
	Arable land	Forest land	Grass land	Water body	Built-up land	Unused land
Arable land	24989.07	63.59	14.55	189.62	2038.14	1.29
Forest land	148.18	11408.17	8.18	19.72	145.44	0
Grass land	85.4	25.85	6297.12	19.39	163.14	1.9
Water body	412.19	42.91	1.95	2144.7	339.3	0.56
Built-up land	822.56	4.94	12	51.81	7071.5	0.28
Unused land	35.83	0.04	6.42	15.13	16.28	9.23

Table 4: Transfer matrix of land use in central core functional area of Jing-Jin-Ji from 2010 to 2015, unit (km^2).

2010	2015					
	Arable land	Forest land	Grass land	Water body	Built-up land	Unused land
Arable land	24797	151.54	47.37	108.43	1390.92	1.2
Forest land	252.74	11098.72	18.67	28.62	149.03	0
Grass land	72.08	154.34	6035.11	9.72	69.72	0.02
Water body	133.13	17.29	5.43	2195.42	89.35	0
Built-up land	356.88	97.29	28.77	301.86	8989.7	0.13
Unused land	0.45	0.85	0.28	0.03	0.24	11.43

Table 5: Transfer matrix of land use in central core functional area of Jing-Jin-Ji from 2000 to 2015, unit (km^2).

2000	2015					
	Arable land	Forest land	Grass land	Water body	Built-up land	Unused land
Arable land	23572.01	153.25	62.23	278.32	3891.41	2.48
Forest land	333.78	11097.02	29.75	36.19	263.00	0.00
Grass land	154.34	182.26	6001.50	40.62	257.61	1.92
Water body	630.27	58.74	9.74	2079.10	380.82	0.43
Built-up land	882.46	25.59	25.27	191.52	5862.11	0.05
Unused land	36.20	0.89	6.39	17.96	33.29	7.87

was relatively small, which was often used as arable land or built-up land.

4.2.2. Analysis of Spatial Pattern Distribution of Land Use Transfer. The spatial pattern distribution of land use transfer from 2000 to 2015 was shown in Figure 3. During the three periods, there were obvious spatial differences in the research region. In 2000–2005, the transferred land of the studied area was located around the main urban area of Beijing and Tianjin, with the arable land and water body converted to built-up land. From 2005 to 2010, the active area of land transfer was located in the southeastern region, especially Tianjin Binhai New Area, whose main categories of land transfer were built-up land transferred from the arable land and the water body. From 2010 to 2015, the active area of land transfer was located in the outskirts of the main urban area of Beijing, and the process of land transfer was that built-up land was transferred from other land categories. In short, from 2000 to 2015, the land use transfer area was located in the middle and southeast part and centered in the surrounding regions of main urban areas of Beijing, main urban area of Tianjin, Tianjin Binhai New Area, Langfang, and Baoding.

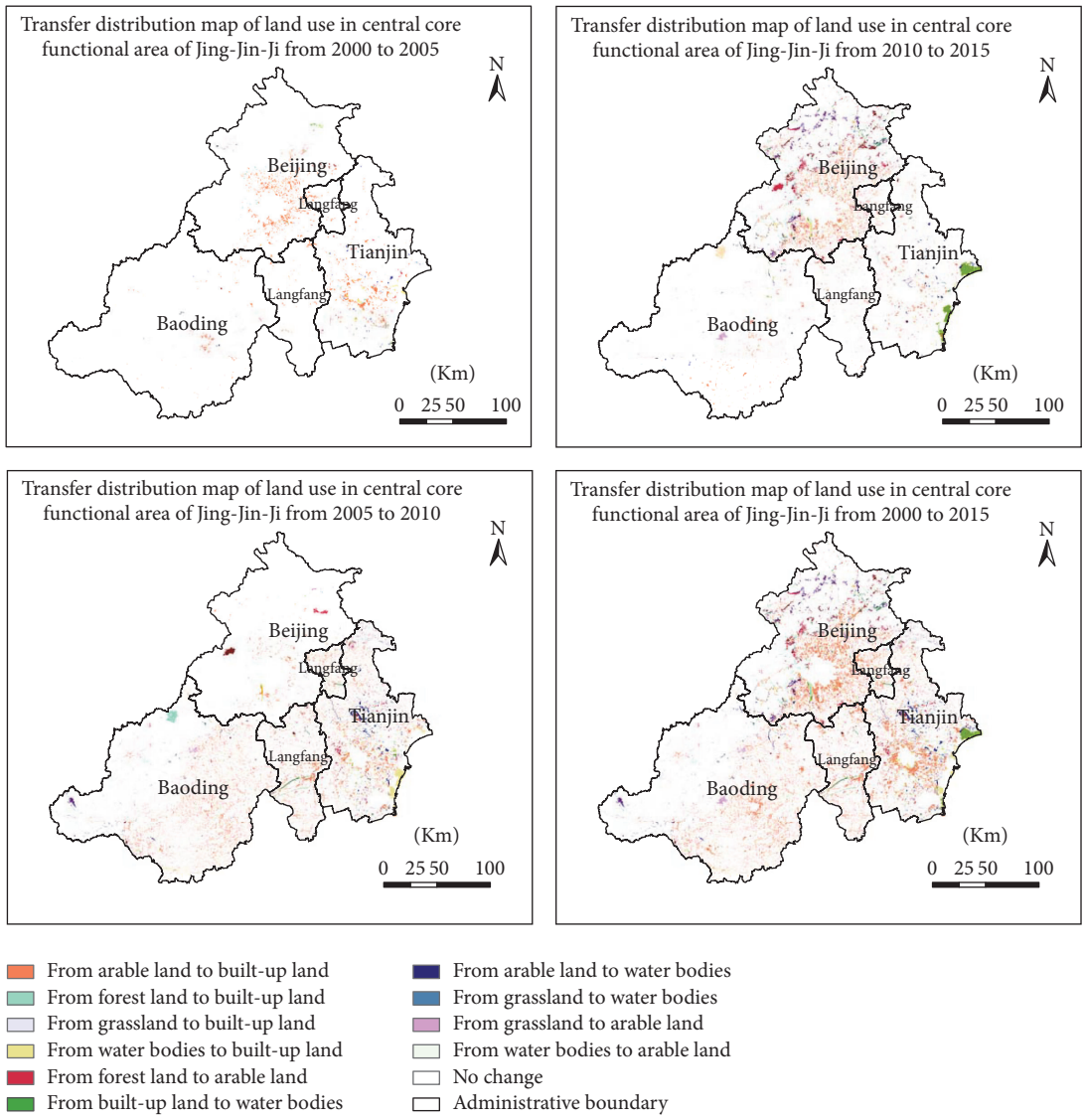

Figure 3: Transfer spatial map of land use in central core functional area of Jing-Jin-Ji from 2000 to 2015.

The main categories of land transfer were arable land and built-up land.

It can be seen that the land transfer regions of these three periods were closely linked with the economic development and National Policies of Jing-Jin-Ji. Beijing, as the key city in the central core functional area of Jing-Jin-Ji, has been developing rapidly since 2000 with the opportunity of hosting the Olympic Games, and its economic level and population scale have been expanding. But because of the single-center circle-mode urban planning, the size of the city kept expanding continuously. As shown in Figure 3, the active area of land transfer in Beijing continues to expand, which have expanded outwards beyond the sixth-ring road, reflecting the rapid expansion of Beijing's city size. The other land use categories have been rapidly transferred to built-up land. Tianjin Binhai New Area started to be planned into the National Development Strategy in 2005 and became the National New District with the key support of development and opening. Correspondingly, from 2005 to 2010, Tianjin Binhai New Area entered the high-speed development stage, promoting large-scale frequent land transfer. In the past 15 years, the land transfer scale of Baoding and Langfang has been relatively small, with the active areas mainly concentrated in the main urban area and the surrounding towns. There has not been a large-scale land transfer, providing a land space to undertake Beijing's noncapital function.

4.3. Analysis of Dynamic Change of Land Use in the Core Functional Area of Jing-Jin-Ji. According to formula (1), the single dynamic degree of the research region in 2000–2015 was calculated. As shown in Table 6, the largest single dynamic degree of land use in the studied area was the unused land in the former two periods, which was −3.84% and −16.8%, respectively, indicating that the urban area developed rapidly in these two periods and occupied the unused land for economic activities, resulting in rapid depletion of unused

Table 6: The single land use dynamic degree in central core functional area of Jing-Jin-Ji from 2000 to 2015.

Land category	2000–2005		2005–2010		2010–2015		2000–2015	
	Change area (km^2)	Dynamic degree (%)	Change area (km^2)	Dynamic degree (%)	Change area (km^2)	Dynamic degree (%)	Change area (km^2)	Dynamic degree (%)
Arable land	−663.46	−0.47	−804.21	−0.59	−884.19	−0.67	−2351.86	−0.56
Forest land	−30.06	−0.05	−183.92	−0.31	−27.74	−0.05	−241.72	−0.14
Grass land	−45.44	−0.14	−252.45	−0.77	−205.35	−0.65	−503.25	−0.51
Water body	−217.48	−1.38	−502.07	−3.41	203.47	1.67	−516.09	−1.09
Built-up land	976.16	2.79	1810.27	4.55	914.90	1.87	3701.32	3.53
Unused land	−19.71	−3.84	−69.68	−16.80	−0.51	−0.78	−89.91	−5.84

land region and intense dynamic changes. In these two periods, the forest land had the lowest single dynamic degree of land use, only −0.05% and −0.31%. Influenced by the national natural forest protection measures, the area of forest land was relatively stable and the dynamic change was less. In the period of 2010–2015, the built-up land had the largest single dynamic degree of land use, which was 1.87%, followed by that of water body, which was 1.67%. It means that the change trend of water body was different from that of the previous two periods. The dynamic degree changed from negative to positive indicated that the water area gradually increased in this period.

Overall, from 2000 to 2015, the unused land had the largest single dynamic degree of land use, up to −5.84%, followed by built-up land, which was 3.53%. The dynamic change trends of these two land categories were on the contrary, indicating that, with the deepening of urbanization in the studied area, the unused land decreased sharply and the built-up land increased rapidly.

The changing tendency of single dynamic degree of land use showed that there were great differences of land categories in different periods. The dynamic degree of arable land and grassland was negative, the absolute value of which was increasing year by year (except for the dynamic degree of grassland in 2010–2015), indicating that the area of arable land and grassland decreased year by year, but the speed was increased. The dynamic degree of the forest land was relatively low, but the dynamic degree of the water body changed greatly, which was similar to dynamic degree of the arable land in the first two periods. The dynamic degree became positive, changing from annual decrease in the first two periods to annual increase in the third period, as shown in Figure 3. This was mainly because the original built-up land was transferred into water body in Tianjin Binhai New Area near Bohai Sea region, which might be related to the industrial policy and sea level changes. The changing trends of dynamic degree of built-up land and unused land were similar, showing the trend which is an increase first and later a decrease, but the change direction of the dynamic degree was opposite. The dynamic degree of unused land in 2005–2010 was over 4 times of that in 2000–2005, reflecting an acceleration of urbanization of the studied area and a rapid decrease of the unused land. Compared with situation between 2000–2005 and 2010–2015, the speed of urbanization

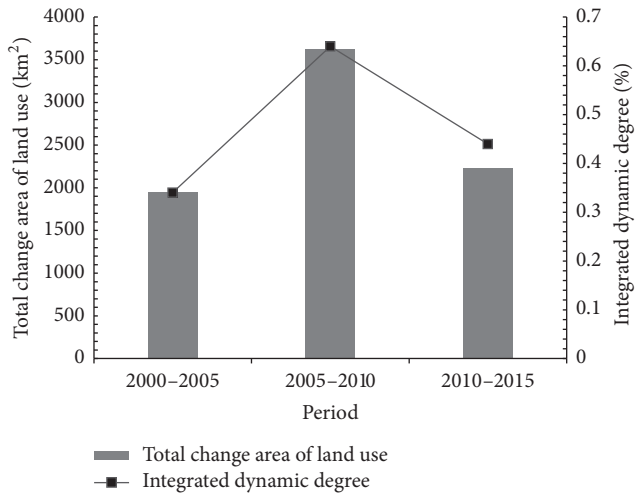

Figure 4: The change map of integrated dynamic degree of land use in central core functional area of Jing-Jin-Ji from 2000 to 2015.

construction was the fastest in 2005–2010, and the built-up land increased rapidly.

According to formula (2), the integrated dynamic degree of the studied area in 2000–2015 was calculated. As shown in Figure 4, the integrated dynamic degree of land use in 2005–2010 was 0.64%, much higher than that in 2000–2005 and 2010–2015, which was nearly twice of the dynamic degree of land use in 2000–2005, indicating that the economic activity of the studied area was active and the conversion of land type was more frequent in this period. The total amplitude of land use change was similar to that in 2000–2005, which was about 2000 km^2 in 2010–2015. The integrated dynamic degree of land use was 30% higher than that in 2000–2005, which indicated that the land transfer was more rapid in 2010–2015, and the land use change was more intense.

4.4. Analysis on Hotspot Area in Dynamic Change of Land Use in the Central Core Functional Area of Jing-Jin-Ji. In order to analyze the regional hotspots of land use dynamic change, the research region was divided into 189 grid regions, and the integrated dynamic degree of land use in every grid was calculated. Then, the spatial analysis tools of ArcGIS were used to produce the spatial distribution of integrated dynamic

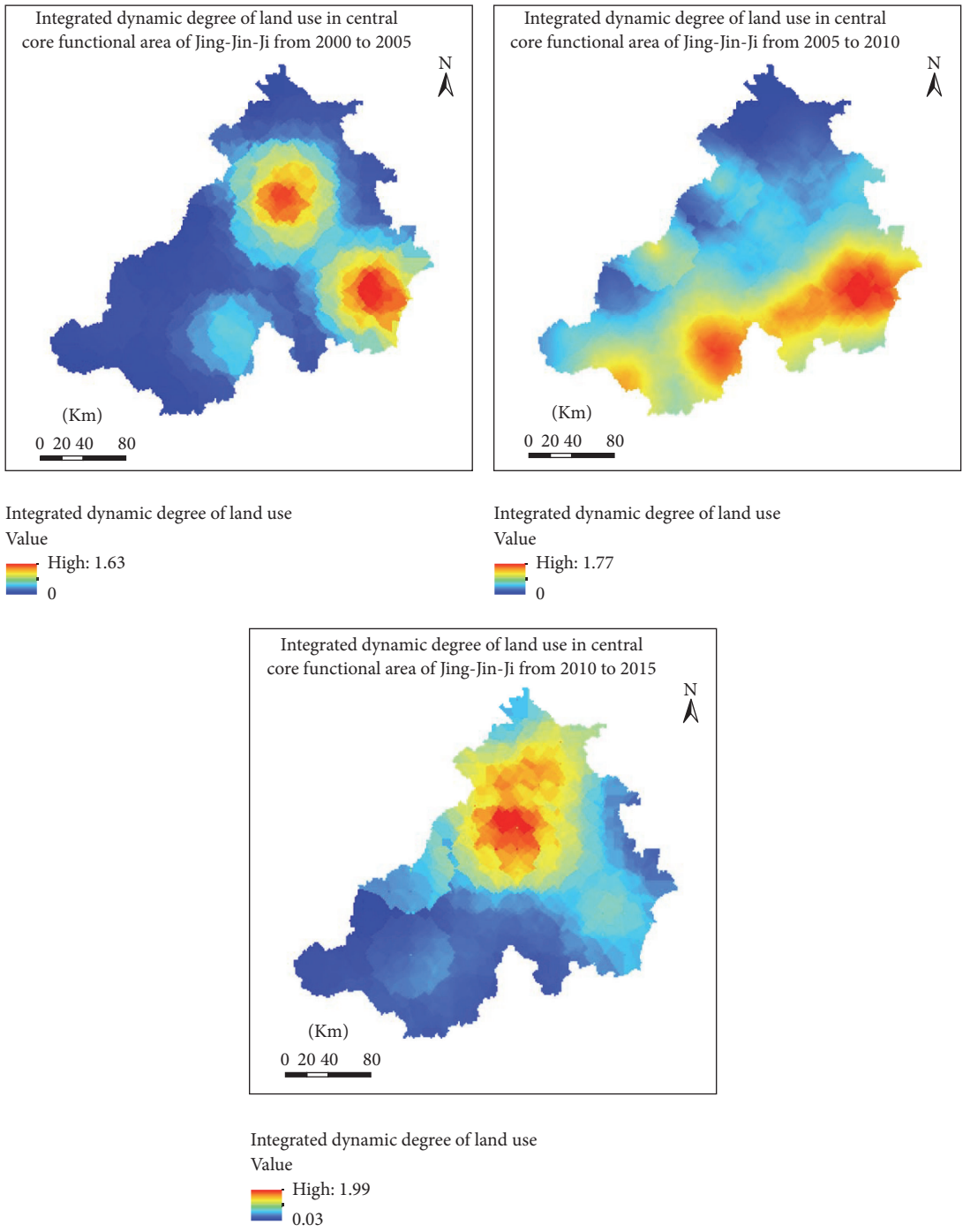

Figure 5: The spatial distribution map of integrated dynamic degree of land use in central core functional area of Jing-Jin-Ji from 2000 to 2015.

degree of land use in the studied area from 2000 to 2015. As shown in Figure 5, there were significant spatial differences of dynamic degree of land use during the three research periods. In 2000–2005, the area with the larger dynamic change of land use was located in the central and eastern part of the studied area, and the western and northern areas were less varied. In 2005–2010, the dynamic change of land use was relatively average. Except for the small part regions in the northern and western, the dynamic changes of land use were great in most areas, especially the eastern and southern part. In 2010–2015, the regions with the larger dynamic change of land use were located in the north and the central regions.

The center of gravity analysis could be used to reflect the regional transfer of the integrated dynamic degree of land use over the three periods. Based on data of the 189 grids and ArcGIS spatial statistical tool, the center of

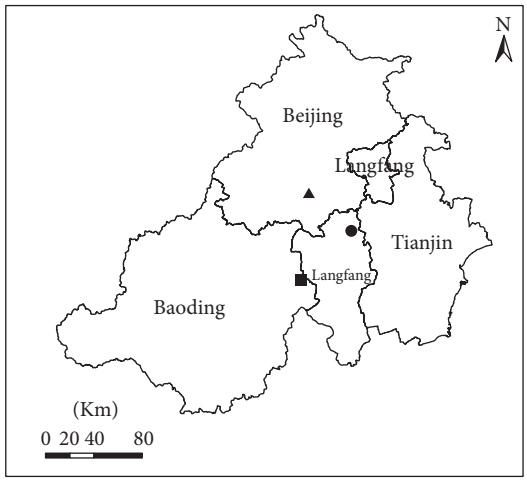

Figure 6: The gravity center transfer spatial distribution map of integrated dynamic degree of land use in central core functional area of Jing-Jin-Ji from 2000 to 2015.

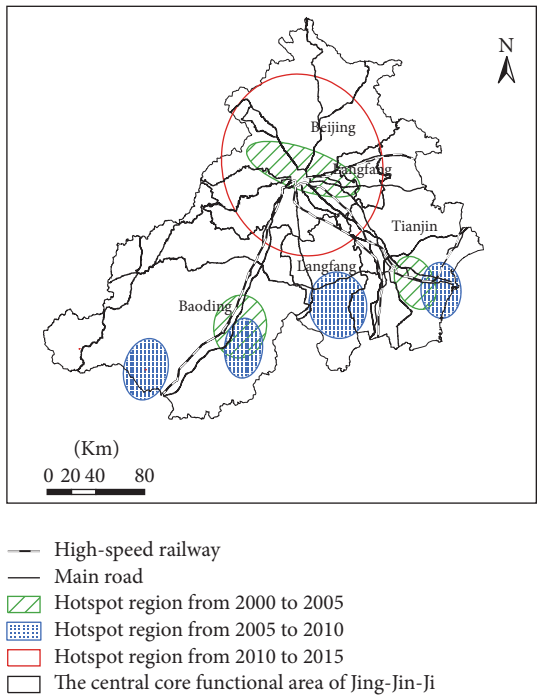

Figure 7: The hot spots map of dynamic changes of land use in central core functional area of Jing-Jin-Ji from 2000 to 2015.

gravity change map in the research region was obtained in 2000–2015. As shown in Figure 6, the center of gravity of land use dynamic change was located in the central region of the studied area, which was close to the geometric center. The center of gravity of the three periods was located in north of Langfang, west of Langfang, and south of Beijing, respectively. In the first two periods, the center of gravity moved from northeast to southwest, reflecting the impetus of urbanization development to land use change in the southern region of the studied area, making the south region hotspots. In the third period, the center of gravity migrated from south to north, which reflected that the south of Beijing became the hotspots of land use dynamic change in the studied area.

In order to further identify the land use hotspots in the target area, the Crimestat 5.2 was used to carry out hotspots analysis on integrated dynamic degree of land use of 189 grids in the three periods, and hotspots distribution map was obtained, as shown in Figure 7. In 2000–2005, there were three land use hotspots, which were located around the main urban areas of Beijing, Tianjin, and Baoding, respectively. In 2005–2010, there were four hotspots, which were all located in the south of the research region, including Tianjin Binhai New Area, main urban area of Langfang, and south and west of Baoding downtown. In 2010–2015, the hotspots were mainly located in Beijing and the junction of Beijing-Tianjin. The hotspots obtained by Crimestat 5.2 was similar to that of spatial distribution map of integrated dynamic degree of land use, but more exact, which could mutually verify the accuracy of the land use hotspots in the studied area.

Transportation is the main driving force of land use change. With the improvement of regional traffic conditions, especially the construction of high-speed railway and expressway, the land use situation along the traffic can be changed, as shown in Figure 7. In 2000–2015, the hotspots of land use dynamic change in the research region were mainly distributed along the high-speed railway and expressway. Beijing had a unique traffic conditions because the country's major transport routes have been going through Beijing, so Beijing's land use hotspots were distributed along the traffic lines, with the main urban area of Beijing as the center. Tianjin's land use hotspots were located along the Jing-Jin intercity railway and the Jing-Jin expressway. The Beijing-Tianjin intercity railway was the earliest intercity railway in China. It has strengthened the economic links and population flows between Beijing and Tianjin and promoted land development along the road. The land use hotspots of Langfang were located between Beijing-Guangzhou Railway, G112, and Beijing-Fuzhou High-Speed Railway, with excellent traffic environment. The land use hotspots of Baoding were located along the Beijing-Zhuhai Expressway and Beijing-Shijiazhuang High-Speed Railway. The two traffic arteries went through the hotspots of the eastern side of Baoding. All of these indicated that the traffic was an important factor affecting the dynamic change of land use in the research region.

In addition to transportation, economy, population, and policy were also main reasons of the gravity transfer and hotspots migration of land use dynamic change. Beijing and Tianjin were the most developed areas in the research region. From 2000 to 2015, the GDP increased more than 3 times in Beijing and Tianjin (Figure 9). Economic development was bound to increase investment in fixed assets and related projects, which would accelerate regional land use change. The increase of population was also the reason for the land

use dynamic change and formation of hotspots. Beijing, as the capital of China, has a huge attraction to the surrounding population. From 2000 to 2015, the population of Beijing has increased nearly 5 million, and Tianjin was also similar about population. So, the center of gravity transferred around the southern of Beijing and northern of Tianjin, and the hotspots of land use change were mainly concentrated in Beijing and Tianjin during the research period, especially 2000–2005 and 2010–2015.

National and regional development policies were also important factors in the hotspots formation of land use dynamic change. Since 2004, the Chinese government has formulated a series of policies and measures for the development of Jing-Jin-Ji, including *Regional Planning of Jing-Jin-Ji Metropolitan, Regional Planning of Beijing Capital Circle, Coordinated Development of Urban Planning of Jing-Jin-Ji, and Urban and Rural Spatial Development Planning of Jing-Jin-Ji*. These policies put forward the development strategy of the research region, formulated the development direction, and accelerated the land use dynamic change to form some hotspots regions. For example, Beijing-Tianjin intercity high-speed railway has promoted the economic development of the Beijing-Tianjin corridor, including Fengtai in Beijing, Langfang in Hebei, and Wuqing in Tianjin. The development of Tianjin Binhai New Area has made the land use change rapidly, and capital new airport has made the regional land development change actively, such as Daxing in Beijing, Langfang in Hebei, and Wuqing in Tianjin.

5. Conclusion and Discussion

5.1. Conclusion. The central core functional area of Jing-Jin-Ji is the key area of coordinated development of Jing-Jin-Ji, which is also a hotspot region of land use dynamic change. This article analyzed the quantitative and spatial characteristics of land use dynamic change in the support of four periods of land use classification distribution map from 2000 to 2015, based on land use dynamic index, land use transfer matrix, and hotspots detection. The trend of land use dynamic change and the hotspots of land use change were also detected in the research area. The results showed that arable land was the largest area in the studied area, accounting for 45% of the total area, which was mainly distributed in the east and south of the research region, and the area of arable land decreased year by year from 2000 to 2015. The transferred-out land was mainly used as built-up land. Forest land was the second largest area, which was intensively distributed in the northwest mountain area, and the area was basically stable. The built-up land was relatively active, the area of which increased rapidly with an increase of nearly 7%. The main transferred-in land categories were arable land and water body. From the spatial distribution of land use transfer, the main area of land use transfer continuously switched from around the main urban area of Beijing and Tianjin in 2000–2005 to the southeast regions of the research area in 2005 to 2010 and then to suburb away from the main urban area of Beijing in 2010–2015.

In 2005–2010, there was the highest integrated dynamic degree of land use in the studied area, which was 0.64%, much higher than that of 2000–2005 and 2010–2015, and was twice as high as integrated dynamic degree of land use in 2000–2005, showing that the land categories transformation was more frequently. The region with large integrated dynamic degree of land use in 2000–2005 was in the middle and east part of the research area, and there was less change on the west and north part of the research area. The center of gravity of land use of the research area transferred from northeast to southwest and then to north. In 2000–2005, there were three hotspots of land use dynamic change, which were located around the main urban areas of Beijing, Tianjin, and Baoding, respectively. In 2005–2010, there were four hotspots, which were all located in the south of the studied area, including Tianjin Binhai New Area, main urban area of Langfang, and south and west of Baoding downtown. In 2010–2015, the hotspots were mainly located in Beijing and the junction of Beijing-Tianjin. The area of the hotspots expanded gradually, reflecting the accelerating urbanization process in the research region.

In brief, the rapid decrease of arable land area and the sharp increase of built-up land area were the main characteristic of the dynamic change of land use in the research region. From 2000 to 2015, the net transferred-out area of arable land increased year by year and reached 884.63 km^2 in 2010–2015, accounting for 3.5% of the arable land in 2015. In 2000–2005, 790.08 km^2 (net area) arable land (after deducting the area transferred from built-up land) transferred to built-up land, followed by 1,215.58 km^2 and 1,034.04 km^2 in the subsequent two periods. In 2005–2010, the net area of arable land accounted for 12% of built-up land. Since 2000, the area of arable land has shown an irreversible decrease trend, which on one hand has met the demand of land for urban expansion but on the other hand has reduced the least cultivated areas and food security of the target area. China implements the fundamental policy of "requisition-compensation balance." Therefore, the region should, on the premise of maintaining the existing farmland scale, improve the productivity of arable land, ensure the grain security, and protect the regional ecological environment.

In 2000–2010, the dynamic degree of land use increased, indicating that the intensity of land use change was increasing during this period, which reflected the impact of urbanization development on land use. With the constant deepening of people's attention to the ecological environment and the proposal of integrative development strategy for Jing-Jin-Ji, the government has carried out a series of land use planning and conducted reasonable planning of urban development in order to avoid waste and idling of land resources, which was the main reason for the decline of land use dynamic degree in 2010–2015.

In the research region, the intensity and area of hotspots in land use dynamic change increased, but the change range of the center of gravity was small. In terms of quantity, it covered the most land use hotspots in the period of 2005–2010, and there were 4 regions. In terms of area, there was the largest area of land use hotspots in the period of 2010–2015. The center of gravity transferred in the central region of the studied area. The hotspots analysis of land use could help to develop reasonable land use policy and realize rational

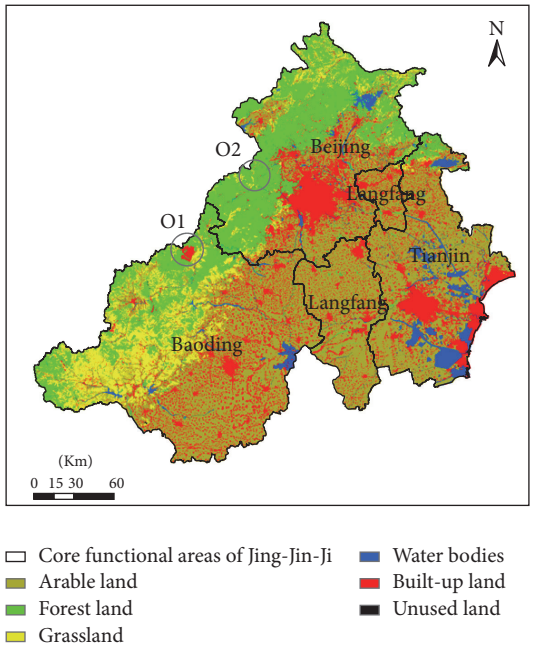

Figure 8: The error classification map of land use in central core functional area of Jing-Jin-Ji in 2010.

exploitation and sustainable utilization of land resources in Jing-Jin-Ji.

5.2. Discussion

5.2.1. Land Use Data. The land use data used in this article comes from the Environmental Science Data Center of the Chinese Academy of Sciences. The accuracy of land use classification is as high as 94.3%, which meets the research needs. However, since the classification accuracy is obtained at the national scale, there might exist differences for different research regions. According to test, the accuracy of land classification was relatively high in most of the research region. But as shown in Figure 8, part of the region was classified wrongly, which marked the wrongly classified regions with circles. In the land use classification map of 2010, O1 was classified into built-up land, and O2 was classified into forest land, while in the land use classification maps of the other three periods, O1 was forest land and O2 was arable land (Figure 2). These two regions were in the mountainous area of the northwest Jing-Jin-Ji, so it was impossible for them to change abruptly without large-scale man-made interference. The classification data was believed wrong initially. After looking into the high-resolution image (Google Earth) of the relevant location, it was confirmed that O1 and O2 were classified wrongly. Before analyzing land use transfer, dynamic degree, and hotspots, these two wrong classifications had been corrected.

5.2.2. Exploration Method of Active Regions of Land Use. According to the above study methods and conclusions, the spatial distribution of land use transfer, the spatial distribution of integrated dynamic degree of land use, and the exploration of land use hotspots have illustrated the active regions of land use change from the different views. The spatial distribution of land use transfer showed the regions and categories of land use transfer in the studied area. The spatial distribution of integrated dynamic degree of land use reflected the spatial variation characteristics of land use transfer speed. The exploration of hotspots of land use could obtain the hotspots of land use dynamic change. The results of these three analysis methods could be mutually verified to reflect the active regions of land use in the studied area.

5.2.3. Driving Force of Land Use Change. The central core functional area of Jing-Jin-Ji is the key area for Beijing to carry out noncapital function in Jing-Jin-Ji coordinated development. Since 2000, with the development of economy, land use category has changed greatly in each city but the development way was more extensive. After the coordinated development of Jing-Jin-Ji for the National Strategy, land use would develop with the direction of unified planning and scientific utilization. In the whole process, the human factor played a decisive role in the land use change. Therefore, when analyzing the driving force of land use change, it should start from the human factors, mainly including population, economics, and policy.

As one of three core engines of China's economic development, Jing-Jin-Ji region plays an important role in national economic system. The GDP and population size of the research region in 2000–2015 were shown in Figure 9, showing that economic gap between the studied areas was relatively large, of which economic levels of Beijing and Tianjin were much higher than those of Langfang and Baoding; however, the growth trend was basically the same. In 2000, economic level of each city started to grow rapidly with the average annual growth rate of about 10%. The economics gap was prerequisite for the integration of Jing-Jin-Ji; it was possible to ease Beijing's noncapital function. Population size was also expanding, but with the restriction on population size of large cities, the average annual population growth showed stage characteristics. Compared to 2000–2005 and 2010–2015, it was the stage with rapid population growth in 2005–2010. Correspondingly, it had relatively high land use dynamic degree and the most hotspots in 2005–2010, which showed that population aggregation could promote the process of regional urbanization and significantly increase the area of built-up land.

From the policies point of view, on the one hand, some national and local ecological protection projects have been promulgated since 2000, mainly including *Grain for Green Project*, *Sand Dust Source Control Project in Beijing and Tianjin*, and *Three North Forest Protection Project*. These projects have promoted the protection of the ecological environment in Jing-Jin-Ji region, relatively stabilized the regional forest land area, and achieved a slight increase in some regions (such as Beijing). On the other hand, Jing-Jin-Ji coordinated development has been developed into National Strategy, the issue of *Outline of the Plan for Jing-Jin-Ji Coordinated Development* provided policy guidance for Jing-Jin-Ji coordinated development, and it would have more detailed polices introduced in the future. Land is the key

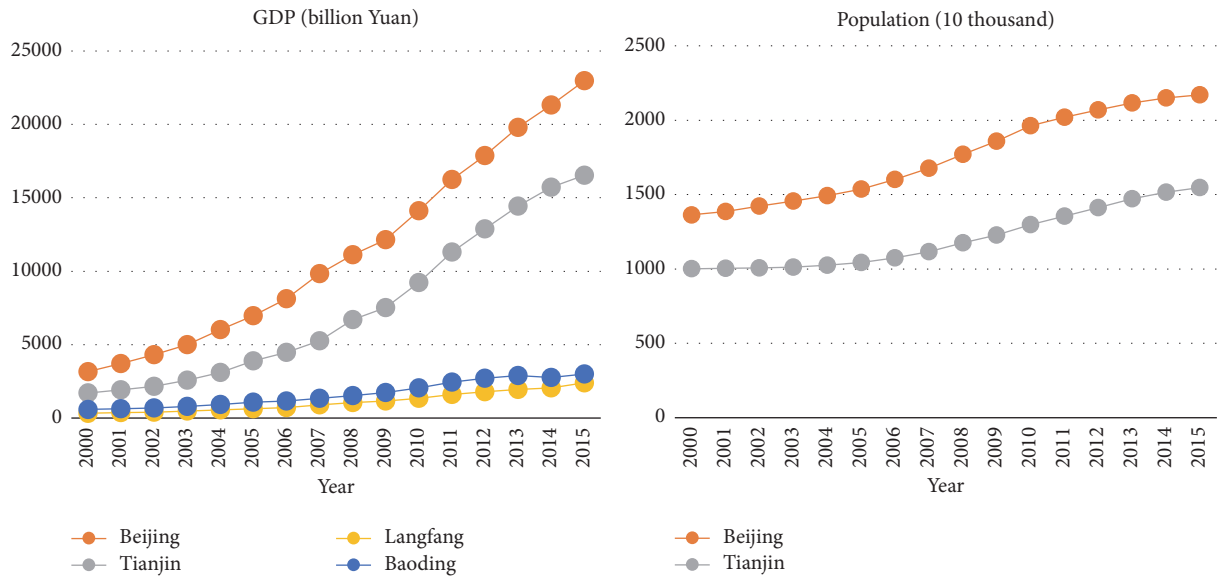

Figure 9: The change trend map of population and GDP in central core functional area of Jing-Jin-Ji from 2000 to 2015.

factor for Jing-Jin-Ji coordinated development, and how to utilize the land resources rationally and plan the quantity and distribution of each land category is the key to land policy. Therefore, the policies of Jing-Jin-Ji coordinated development would be also the important driving force of land use dynamic change in the future.

5.3. Outlook. The central core functional area of Jing-Jin-Ji takes the important responsibility of noncapital functions of Beijing. Both the outflow of industry and personnel need land resource as the carrier. To reasonably plan and comprehensively arrange the land resources of central core functional area of Jing-Jin-Ji is of great importance to the realization of Jing-Jin-Ji coordinated development. Therefore, research on land use status, dynamic change, and transfer characteristics of the research region provided decision reference for land use policies-making of this region, having great significance. In this article, the authors deeply researched the land use status and dynamic changes of the central core functional area of Jing-Jin-Ji; however, the mechanism and simulation of land use dynamic changes of the region were not involved. We will increase the prediction simulation of land use in the research region and set up different development scenarios to forecast the dynamic change characteristics of land use and hotspots in order to improve the support of policy-making departments in the future. In addition, the main data used in this research is the existing data of land use distribution. Remote sensing images can be used to update and validate land use data in the future.

Based on the results of this article, we can see that the level of land use was very uneven in the central core functional area of Jing-Jin-Ji. It is necessary to formulate some land policies which are suitable for the characteristics of regional land use change. The regional land use efficiency should be improved under the premise of protecting arable land. From the view of land use distribution, the built-up land was mainly concentrated in Beijing and Tianjin, which was expanding rapidly, especially Beijing (Figures 2 and 3). In the context of integration of Jing-Jin-Ji, the land management department should formulate land policies to restrict the expansion rate of built-up land in Beijing, control the increase of built-up land, and encourage the conversion of stock built-up land into ecological land. At the same time, the industries that need occupy the larger area land should be transferred to the other regions, such as Langfang and Baoding. From the point of view of hotspots of land use, the hotspots were located in the areas along the main road and supported by national policies, such as Binhai New Area (Figures 5 and 7). Therefore, in order to promote the balanced and efficient development of regional land use, the land management department should provide adequate land recourse for the transportation infrastructure to improve the regional accessibility, promote the development of industries along the traffic, and guide the reasonable population aggregation, so that we can achieve the purpose of easing Beijing's noncapital functions and promoting the coordinated development of Jing-Jin-Ji. Finally, when the departments formulate the land development strategies, it is important to focus on the regions in which land use changes severely (Figure 3). If necessary, the land management department should limit the rate of land use transfer in the violent area of land use change in order to ensure adequate reserve land.

Conflicts of Interest

The authors declare that there are no conflicts of interest regarding the publication of this paper.

Acknowledgments

This study was supported by the National Natural Science Foundation of China (41501430, U1633124, 41271546, and

61603396) and Natural Science Foundation of Tianjin (Youth Project: Simulation of the Impact of Airport Construction on Regional Ecological Environment Change and Urbanization in Jing-Jin-Ji.)

References

[1] E. F. Lambin, H. J. Geist, and E. Lepers, "Dynamics of land-use and land-cover change in tropical regions," *Annual Review of Environment and Resources*, vol. 28, pp. 205–241, 2003.

[2] J. Feddema, K. Oleson, G. Bonan et al., "A comparison of a GCM response to historical anthropogenic land cover change and model sensitivity to uncertainty in present-day land cover representations," *Climate Dynamics*, vol. 25, no. 6, pp. 581–609, 2005.

[3] I. C. Bohnet, B. Roberts, E. Harding, and K. J. Haug, "A typology of graziers to inform a more targeted approach for developing natural resource management policies and agricultural extension programs," *Land Use Policy*, vol. 28, no. 3, pp. 629–637, 2011.

[4] Y. Tsai, A. Zia, C. Koliba, G. Bucini, J. Guilbert, and B. Beckage, "An interactive land use transition agent-based model (ILUTABM): endogenizing human-environment interactions in the Western Missisquoi Watershed," *Land Use Policy*, vol. 49, pp. 161–176, 2015.

[5] A. Wahid, *Geo-Environmental Assessment and Landuse Planning for Coastal Plains*, Lap Lambert Academic Publishing, 2011.

[6] M. Li, J. Wu, and X. Deng, "Land use change and soil carbon sequestration in China: where does it pay to conserve?" *Regional Environmental Change*, pp. 1–13, 2016.

[7] Y. Li, Y. Liu, H. Long, and W. Cui, "Community-based rural residential land consolidation and allocation can help to revitalize hollowed villages in traditional agricultural areas of China: Evidence from Dancheng County, Henan Province," *Land Use Policy*, vol. 39, pp. 188–198, 2014.

[8] X. B. Li, "A review of the international researches on land use/land cover change," *Acta Geographica Sinica*, vol. 6, pp. 553–558, 1996.

[9] N. C. Gautam and G. C. Chennaiah, "Land-use and land-cover mapping and change detection in Tripura using satellite LANDSAT Data," *International Journal of Remote Sensing*, vol. 6, no. 3-4, pp. 517–528, 1985.

[10] Q. Weng, "Land use change analysis in the Zhujiang Delta of China using satellite remote sensing, GIS and stochastic modelling," *Journal of Environmental Management*, vol. 64, no. 3, pp. 273–284, 2002.

[11] H. J. König, J. Schuler, U. Suarma et al., "Assessing the impact of land use policy on urban-rural sustainability using the FoPIA approach in Yogyakarta, Indonesia," *Sustainability*, vol. 2, no. 7, pp. 1991–2009, 2010.

[12] K. Swangjang and V. Iamaram, "Change of land use patterns in the areas close to the airport development area and some implicating factors," *Sustainability*, vol. 3, no. 9, pp. 1517–1530, 2011.

[13] G. Sen, M. M. Bayramoglu, and D. Toksoy, "Spatiotemporal changes of land use patterns in high mountain areas of northeast turkey: a case study in maçka," *Environmental Monitoring and Assessment*, vol. 187, no. 8, article no. 515, pp. 1–14, 2015.

[14] M. Al-shalabi, B. Pradhan, L. Billa, S. Mansor, and O. F. Althuwaynee, "Manifestation of Remote Sensing Data in Modeling Urban Sprawl Using the SLEUTH Model and Brute Force Calibration: a Case Study of Sana'a City, Yemen," *Journal of the Indian Society of Remote Sensing*, vol. 41, no. 2, pp. 405–416, 2013.

[15] S. L. Tuck, C. Winqvist, F. Mota, J. Ahnström, L. A. Turnbull, and J. Bengtsson, "Land-use intensity and the effects of organic farming on biodiversity: a hierarchical meta-analysis," *Journal of Applied Ecology*, vol. 51, no. 3, pp. 746–755, 2014.

[16] C. Su, B. Fu, Y. Lu et al., "Land use change and anthropogenic driving forces: a Case Study in Yanhe River Basin," *Chinese Geographical Science*, vol. 21, no. 5, pp. 587–599, 2011.

[17] K. Zhang, Z. Yu, X. Li, W. Zhou, and D. Zhang, "Land use change and land degradation in China from 1991 to 2001," *Land Degradation and Development*, vol. 18, no. 2, pp. 209–219, 2007.

[18] D. R. Thielen, J. J. San José, R. A. Montes, and R. Lairet, "Assessment of land use changes on woody cover and landscape fragmentation in the Orinoco savannas using fractal distributions," *Ecological Indicators*, vol. 8, no. 3, pp. 224–238, 2008.

[19] J. Y. Liu, W. H. Kuang, Z. X. Zhang et al., "Spatiotemporal characteristics, patterns and causes of land use changes in china since the late 1980s," *Acta Geographica Sinica*, vol. 69, pp. 3–14, 2014.

[20] R. E. Kennedy, P. A. Townsend, J. E. Gross et al., "Remote sensing change detection tools for natural resource managers: Understanding concepts and tradeoffs in the design of landscape monitoring projects," *Remote Sensing of Environment*, vol. 113, no. 7, pp. 1382–1396, 2009.

[21] Minakshi, R. Chaurasia, and P. K. Sharma, "Landuse/land cover mapping and change detection using satellite data—a case study of Dehlon block, district Ludhiana, Punjab," *Journal of the Indian Society of Remote Sensing*, vol. 27, no. 2, pp. 115–121, 1999.

[22] H. Chen, S. Yan, Z. Ye, H. Meng, and Y. Zhu, "Utilization of urban sewage sludge: Chinese perspectives," *Environmental Science and Pollution Research*, vol. 19, no. 5, pp. 1454–1463, 2012.

[23] M. R. Altaweel, L. N. Alessa, A. D. Kliskey, and C. E. Bone, "Monitoring land use: capturing change through an information fusion approach," *Sustainability*, vol. 2, no. 5, pp. 1182–1203, 2010.

[24] M. C. Hansen and T. R. Loveland, "A review of large area monitoring of land cover change using Landsat data," *Remote Sensing of Environment*, vol. 122, pp. 66–74, 2012.

[25] G. Han, J. Chen, C. He et al., "A web-based system for supporting global land cover data production," *Journal of Photogrammetry & Remote Sensing*, vol. 103, pp. 66–80, 2015.

[26] C. Z. Li, F. L. Yu, J. Liu et al., "Research on land use/cover change and its driving force in midstream of the heihe mainstream basin during the past 20 years," *Journal of Natural Resources*, pp. 353–363, 2011.

[27] F. J. Gao, G. P. Lei, F. H. Yang et al., "Eco-security evaluation before and after Grain for green in project mudangjiang city," *Transaction of the CSAE*, vol. 28, pp. 206–214, 2012.

[28] Y. Y. Li, J. X. Chang, Y. M. Wang et al., "Spatiotemporal responses of runoff to land use change in wei river basin," *Transaction of the CSAE*, vol. 32, pp. 232–238, 2016.

[29] H. Delile, L. Schmitt, N. Jacob-Rousseau, L. Grosprêtre, G. Privolt, and F. Preusser, "Headwater valley response to climate and land use changes during the Little Ice Age in the Massif Central (Yzeron basin, France)," *Geomorphology*, vol. 257, pp. 179–197, 2016.

[30] J. Y. Liu, Z. X. Zhang, X. L. Xu et al., "Spatial patterns and driving forces of land use change in china in the early 21st century," *Acta Geographica Sinica*, vol. 64, pp. 1411–1420, 2009.

[31] Y. R. Zou, Z. X. Zhang, Q. B. Zhou et al., "Land use change dynamics spatial pattern in ecotone between agriculture and animal husbandry and its driving force analysis," *Journal of Natural Resources*, vol. 18, pp. 222–227, 2003.

[32] M. Güler, T. Yomralioğu, and S. Reis, "Using landsat data to determine land use/land cover changes in samsun, turkey," *Environmental Monitoring and Assessment*, vol. 127, no. 1–3, pp. 155–167, 2007.

[33] X. D. Du, X. B. Jin, X. Yang H et al., "Spatial pattern of land use change and its driving force in Jiangsu Province," *International Journal of Environmental Research & Public Health*, vol. 11, pp. 3215–3232, 2014.

[34] J. Marull, J. Pino, E. Tello, and M. J. Cordobilla, "Social metabolism, landscape change and land-use planning in the Barcelona Metropolitan Region," *Land Use Policy*, vol. 27, no. 2, pp. 497–510, 2010.

[35] S. Balaselvakumar, E. V. R. College, and P. Sujatha, "Landuse and landcover change detection in lalgudi block, tiruchirappalli district - using remote sensing and GIS techniques," *International Journal of Engineering Research and Applications*, vol. 5, pp. 108–117, 2015.

[36] W. H. Yu, T. H. Ai, M. Yang et al., "Detecting 'Hot spots' of facility POIs Based on kernel density estimation and spatial autocorrelation technique," *Geomatics and Information Science of Wuhan University*, vol. 41, pp. 221–227, 2016.

[37] L. Zhang, G. F. Yang, and J. P. Liu, "The dynamic change and Hot spots of land use in Fushun city," *Scientia Geographica Sinica*, vol. 34, pp. 185–191, 2014.

[38] F. J. Gao, L. Q. Ma, Shan. M. P. et al., "Land use/cover change and hot spots analysis in muling city of helongjiang province," *Areal Research and Development*, vol. 35, pp. 126–130, 2016.

[39] C. Y. Guo, "Land use transiton and hotspots detection in yongcheng city base on the grid scale," *China Land Sciences*, vol. 30, pp. 43–51, 2016.

[40] P. Singh and K. Khanduri, "Land use and land cover change detection through remote sensing gis technology: case study of pathankot and dhar kalan tehsils, Punjab," *International Journal of Geomatics & Geosciences*, pp. 839–846, 2010.

[41] S. Khan, S. Qasim, R. Ambreen, and Z. Syed, "Spatio-temporal analysis of landuse/landcover change of district pishin using satellite imagery and GIS," *Journal of Geographic Information System*, vol. 8, no. 3, pp. 361–368, 2016.

[42] H. J. Geist, "Change or collapse? A theoretical approach to global environmental change and landuse in rainforest and arid zone hotspots," *Geographische Zeitschrift*, vol. 94, no. 3, pp. 143–159, 2006.

[43] S. B. Hao and H. W. Wang, "Spatial structure research of urban agglomeration in Jing-Jin-Ji," *Inquiry into Economic Issues*, vol. 6, pp. 105–111, 2015.

[44] D. J. Fu, *Construction of the Four Major Functional Areas Based on Integration of Jing-Jin-Ji Region*, Minzu University of China, 2015.

[45] X. F. Gong, "Development driving force of Jing-Jin-Ji region," *The World of Real Estate*, vol. 8, pp. 86–89, 2015.

[46] D. Meng, "Analysis of spatial-temporal change of NDVI and its climatic driving factors in Beijing-Tianjin-Hebei metropolis circle from 2001 to 2013," *Journal of Geo-Information Science*, vol. 17, pp. 1001–1007, 2015.

[47] J. Liu, Z. Zhang, X. Xu et al., "Spatial patterns and driving forces of land use change in China during the early 21st century," *Journal of Geographical Sciences*, vol. 20, no. 4, pp. 483–494, 2010.

[48] Z. X. Zhang, X. L. Zhao, X. Wang et al., *Remote Sensing Monitoring of Land Use in China*, Star Maps Publishing, Beijing, China, 2012.

[49] J. Y. Liu, M. L. Liu, D. F. Zhuang, Z. X. Zhang, and X. Z. Deng, "Study on spatial pattern of land-use change in China during 1995–2000," *Science China Earth Science*, vol. 46, no. 4, pp. 373–384, Ser. D 2003.

[50] J. Y. Liu, J. Y. Zhan, and X. Z. Deng, "Spatio-temporal patterns and driving forces of urban land expansion in china during the economic reform era," *Ambio*, vol. 34, pp. 450–455, 2005.

[51] J. Liu, Q. Zhang, and Y. Hu, "Regional differences of China's urban expansion from late 20th to early 21st century based on remote sensing information," *Chinese Geographical Science*, vol. 22, no. 1, pp. 1–14, 2012.

[52] S. Y. Wang, J. Y. Liu, Z. X. Zhang et al., "Analysis on spatial-temporal features of land use in China," *Acta Geographica Sinica*, vol. 56, pp. 631–639, 2001.

[53] D. J. Redo, T. M. Aide, M. L. Clark, and M. J. Andrade-Núñez, "Impacts of internal and external policies on land change in Uruguay, 2001–2009," *Environmental Conservation*, vol. 39, no. 2, pp. 122–131, 2012.

[54] L. Yi, Z. X. Zhang, X. Wang et al., "Spatial-temporal change of major reserve resources of arable land in China in recent 30 years," *Transaction of the CSAE*, vol. 29, pp. 1–12, 2013.

[55] H. P. Zhao, Y. H. Zhu, K. N. Wu et al., "Study on the method for the demarcation of urban-rural fringe based on land use dynamic indicator," *China Land Sciences*, vol. 26, pp. 60–65, 2012.

[56] J. Y. Liu, Z. X. Zhang, D. F. Zhuang et al., "A study on the spatial-temporal dynamic changes of landuse and driving forces analyses of China in the 1990s," *Geographical Research*, vol. 22, pp. 1–12, 2003.

[57] P. Pfaffenbichler, G. Emberger, and S. Shepherd, "The integrated dynamic land use and transport model MARS," *Networks and Spatial Economics*, vol. 8, no. 2-3, pp. 183–200, 2008.

[58] J. F. Wang, *Spatial Data Analysis Tutorial*, Science Press, 2010.

[59] V. De Oliveira and M. D. Ecker, "Bayesian hot spot detection in the presence of a spatial trend: application to total nitrogen concentration in Chesapeake Bay," *Environmetrics*, vol. 13, no. 1, pp. 85–101, 2002.

[60] Q. Pan, X. B. Jin, and Y. K. Zhou, "Gridding reconstruction of land use pattern in Jiangsu province in the mid-qing dynasty," *Acta Geographica Sincia*, vol. 70, pp. 1449–1462, 2015.

[61] M. Meroni, D. Fasbender, F. Kayitakire et al., "Early detection of biomass production deficit hot-spots in semi-arid environment using FAPAR time series and a probabilistic approach," *Remote Sensing of Environment*, vol. 142, pp. 57–68, 2014.

Hindawi
Mathematical Problems in Engineering
Volume 2017, Article ID 9206963, 17 pages
https://doi.org/10.1155/2017/9206963

Research Article

Dynamic Changes of Typical Blowouts Based on High-Resolution Data: A Case Study in Hulunbuir Sandy Land, China

Yi Yang,[1,2] Chao Guan,[1] and Eerdun Hasi[1]

[1]*College of Resources Science & Technology, Beijing Normal University, Beijing 100875, China*
[2]*National Computer Network Emergency Response Technical Team/Coordination Center of China, Shanghai 201315, China*

Correspondence should be addressed to Chao Guan; gc471603869@126.com

Received 30 November 2016; Revised 29 January 2017; Accepted 15 February 2017; Published 21 March 2017

Academic Editor: Hasi Bagan

Blowouts are an important ground indication of wind-sand activity in the Hulunbuir grassland. They include two basic geomorphologic units, erosion depression and sand deposition, and three typical morphological types: saucer type, trough type, and compound type. In this study, the dynamic changes of typical blowouts within the past decade were analyzed via multiperiod high-resolution remote sensing images. RTK was used to repeatedly measure the blowouts to obtain their high-precision 3D terrain data in 2010, 2011, and 2012. Short-term dynamic changes in 3D blowout morphology were carefully analyzed to discover the following. (1) From 2002 to 2012, the depressions of typical blowouts exhibited downwind extension and lateral expansion trends, as they continuously grew in size. Regarding the sand deposition zones, those of the saucer blowout grew continuously, while those of the trough and compound blowouts fluctuated between growth and contraction. (2) The erosion depression of saucer blowouts eroded downward and spread horizontally; that of trough blowouts first accumulated then eroded but also spread horizontally. The erosion depression of compound blowouts exhibited horizontal spreading accompanied with bottom accumulation. The sand deposition zones of all three types of blowouts exhibited decreasing length with increasing width and height.

1. Introduction

As one of the main Aeolian landforms of sandy grasslands, the formation and development of blowouts are also the main driving factors driving landscape patterns heterogeneity. Blowouts are created by a variety of factors including wind conditions, precipitation, air temperature, and vegetation coverage; their root causes are the enhanced surface erosion capability of sandstorms and decreased erosion resistance at the surface soil layer. Damage to surface soil and vegetation leads to the direct exposure of sandy materials to wind erosion, which is the direct impetus of a blowout [1–4]. Research on sandy grassland blowouts in China has been concentrated mainly in the Hulunbuir Sandy Land. Dong and Ya [5] and Feng and Wang [6], for example, have found through satellite remote sensing monitoring that the sandy land of Hulunbuir grassland is dominated by grassland desertification accounting for 99% of the total desertification area. Further, the land desertification is rapidly expanding. Nie et al. [7] assert that the human destruction of grassland vegetation and surface soil is the direct cause of desertification. Zan and Sun [8] found that the vegetation status generally improved between 1982 and 2006 in the eastern part of the Hulunbuir grassland but deteriorated in the western part. Sand belt degradation was particularly obvious in the southern part, where vegetation slightly degraded. Zhang et al. [9] and Man et al. [10] surveyed the small vegetation communities of bare, semibare, and fixed blowouts and their corresponding sand deposition zones in the Hulunbuir grassland to find that the coverage of small vegetation communities in three types of blowouts and sand deposition zones are altogether smaller than those of the native *Stipa grandis* community, having decreased in the order of fixed blowouts, semibare blowouts, and bare blowouts. Du et al. [11] forecasted the landscape pattern development in their study area from 2012 to 2020 via CA-Markov model and found that the grassland area of Hulunbuir

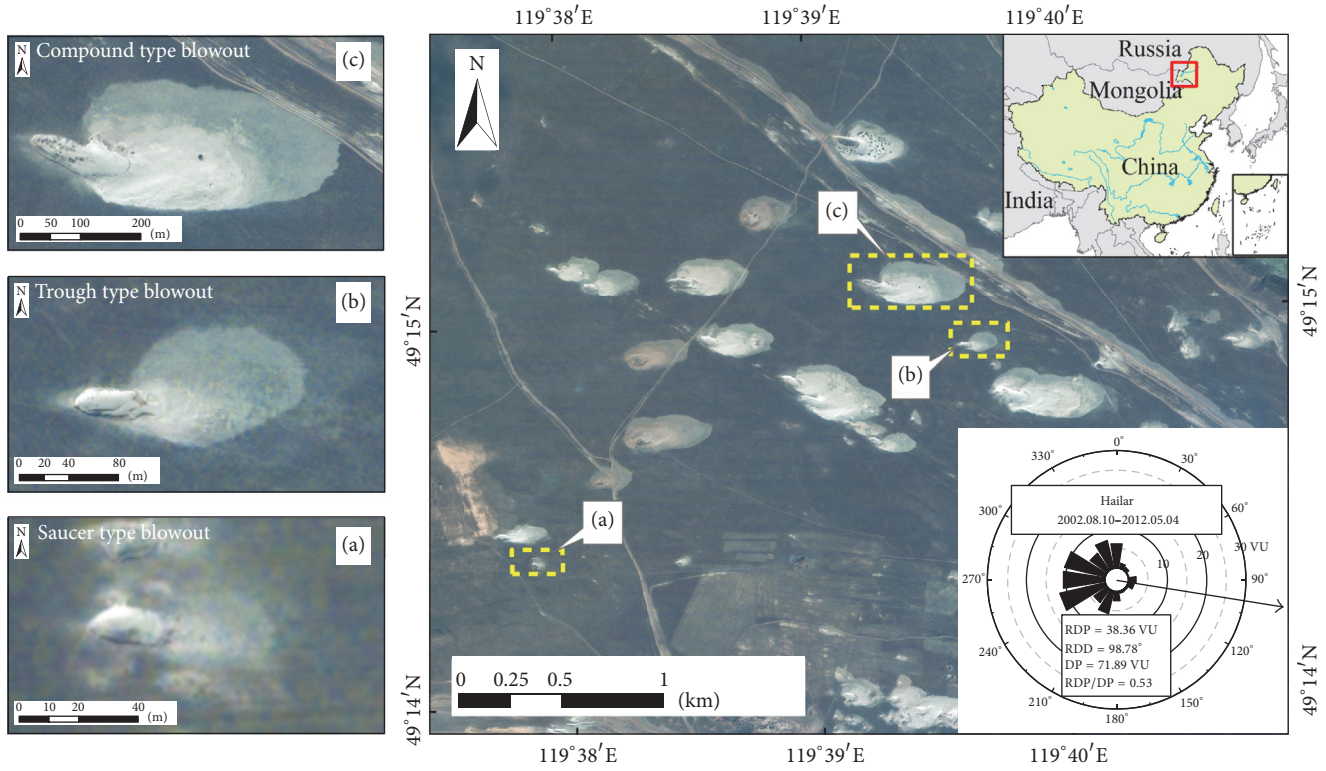

Figure 1: Location of the study area of the Hulunbuir Sandy Land: three different types of blowouts are regarded as the research objects; they are saucer blowout (a), trough blowout (b), and compound blowout (c), respectively, whose size increases sequentially. Meteorological data are obtained from Hailar Meteorological Station. The data includes daily maximum wind velocity and wind direction from 2002 to 2012. Fryberger's Drift Potential Index [12] is used to calculate the total drift potential (DP), resultant drift potential (RDP), and resultant drift direction (RDD); the formula is $DP = U^2(U - U_t)t$. Since U is required to be the average wind velocity, while data in this paper is the maximum wind velocity, conversion is performed by regarding the empirical value of 8.8 studied by Fang et al. [13] as the parameter, that is, $DP_{max} = 8.8DP_{average}$. The prevailing wind direction in the study area is northwesterly; the RDP value is less than 200 VU, indicating of a low wind energy environment [12]. The basemap is QuickBird satellite image of the Hulunbuir Sandy Land in 2002.

decreased while the area of other land cover types increased. Despite these valuable contributions to the literature, there has been little research on the dynamic variation of typical blowouts based on high-precision morphometry combined with remote sensing image analysis. In the present study, we analyzed the dynamic changes in typical sandy grassland blowouts by obtaining relevant morphological through high-precision remote sensing images and RTK measurements. The results presented here may provide scientific basis for the rational utilization of grasslands and for the effective prevention and control of desertification therein.

2. Overview of Study Area and Research Objects

The study area is located in the border area between Hailar City and Old Barag Banner of Inner Mongolia Autonomous Region (Figure 1). The area is a flat grassland north of the eastern Hailar Sand Belt section and south of the Hailar River, with an elevation of 620–630 m, on which blowouts are scattered. Zonal vegetation is dominated by *Stipa grandis*, *Stipa krylovii*, and *Cleistogenes squarrosa*. In Aeolian sand covered areas, there are also psammophytes such as *Agriophyllum squarrosum*. Zonal soil is sandy chestnut soil, with a caliche depth of 0.1–0.3 m, whose parent material is grey fluviolacustrine sands of Hailar Group [1].

Depending on the morphological characteristics, the blowouts in the study area were divided into simple blowouts and compound blowout. Simple blowouts can be subdivided into two types: saucer blowout and trough blowout. In general, trends of dynamic changes vary for different types and sizes of blowouts. Saucer blowouts are generally in the early stage, which are small in size. Trough blowouts are in the middle stage, which are moderate in size. Compound blowouts are in the mature stage, which have large size and complex morphology. Thus, typical saucer blowout (Figure 1(a)), trough blowout (Figure 1(b)), and compound blowout (Figure 1(c)) (with size increasing sequentially) are selected to discuss the processes and causes of their dynamic changes.

2.1. Simple Blowouts. Saucer blowouts are small in scale and shallow in depth, which are mainly in disc, semidisc, or oval shape. There are one or more air outlets on the depressions and soil layer exposed in a "crescent" shape around their

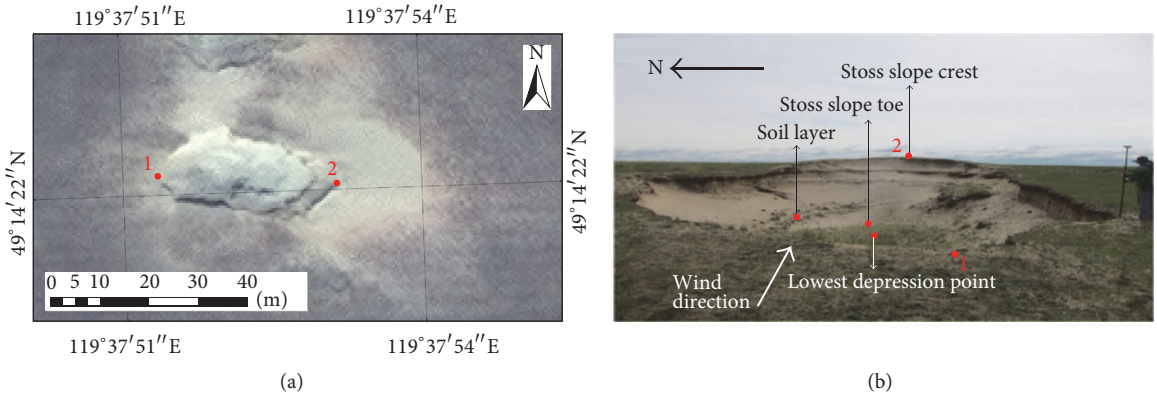

Figure 2: Morphological characteristics of saucer blowout ((a) WorldView2 data, 2012; (b) Field photographs, 2012).

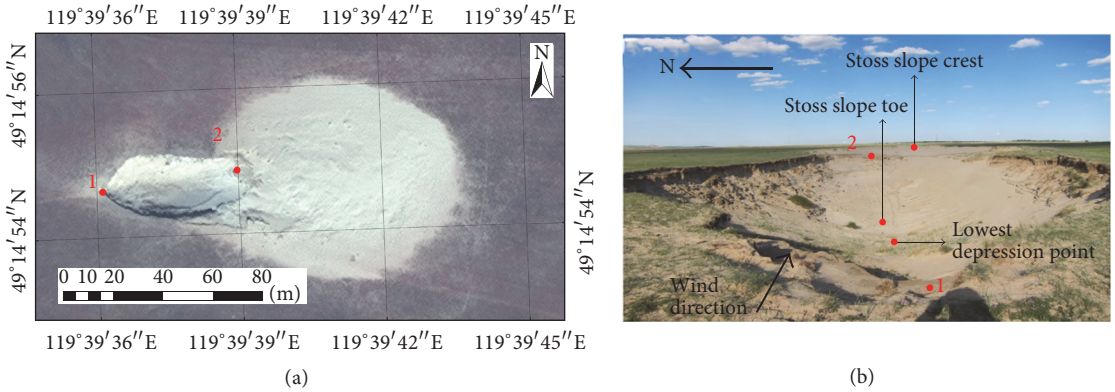

Figure 3: Morphological characteristics of trough blowout ((a) WorldView2 data, 2012; (b) Field photographs, 2012).

rear edge. Inside the depressions, northern walls are relatively gentle, while southern walls are relatively steep. Sand depositions are small in area and thickness, which thinned gradually along with outward spreading (Figure 2).

The trough blowout, per its namesake, forms in a trough-like shape with steep depression sidewalls and a deep bottom. Its sidewalls are prone to collapse, after which they are deposited on the bottom of erosion depressions at a natural angle of repose. There is "crescent" soil layer exposure around the rear edge of the erosion depressions. The sand depositions are large in area, with short and steep stoss slope, round top, and thick deposition that extends and thins gradually along the prevailing wind direction. When the bottom of a large-scale trough blowout is eroded to reach the wet sand layer of erosion datum or the clay layer, with strong antiwind erosion capability in the sand layer, the erosion is impeded from flattening the depression bottom (Figure 3).

2.2. Compound Blowouts. Compound blowouts are complex and varied in morphology. Their formation processes can be roughly divided into three categories: (1) compound blowouts formed by the expansion and joining of simple blowouts during their development (Figure 4(a)); (2) compound blowouts formed by the activation of fixed blowouts that have been superimposed on the original depressions or their edges (Figure 4(b)); and (3) secondary blowouts and parabolic dunes generated by wind erosion in the sand deposition zone of large-scale blowouts (Figure 4(c)). In this paper, the typical compound blowouts shown in Figure 4(c) were selected as the research object.

3. Data and Methods

The data used in the study are QuickBird images taken in 2002, 2004, and 2009 as well as WorldView2 images from 2012 (Table 1). Pretreatment of the images is as follows: firstly, panchromatic images are orthorectified with the ground control points; these ground control points are selected on the basis of field measurements using Leica 1230 differential GPS. They include the geometric center of nebkhas in the depression, the inflection points of buildings, and typical trees; the ground control points are evenly distributed within the study area, and the number of points is increased in areas around blowouts. Secondly, image enhancement for more precise extraction of blowout morphological parameters. We chose WGS84 as our data coordinate system; the UTM projection zone was 50 with a central meridian of 117°E.

Our ground survey of blowout morphology in the study area was carried out primarily with a Leica 1230 differential GPS system. Its nominal planar precision is 10 mm + 1 ppm

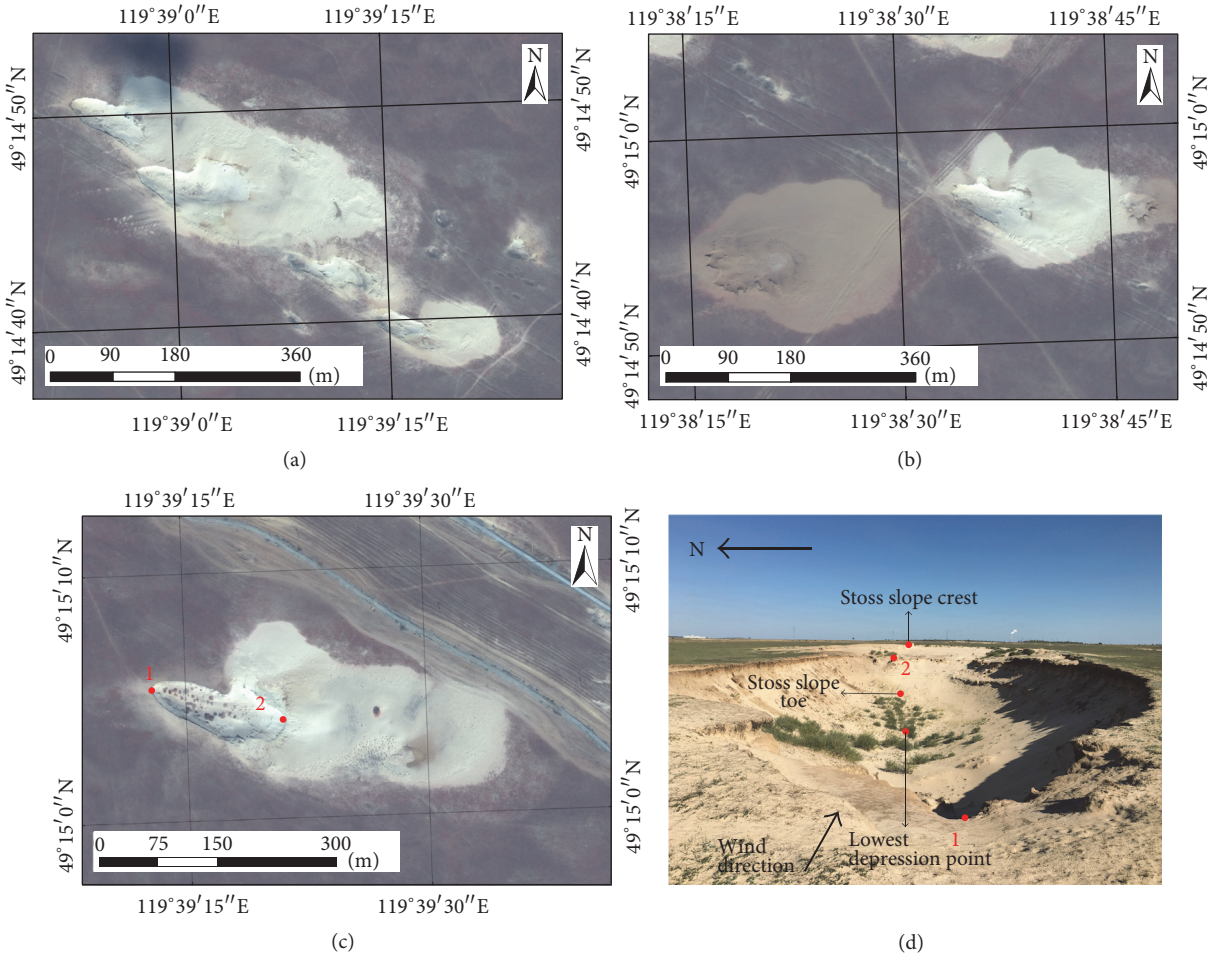

Figure 4: Compound blowouts ((a), (b), (c) WorldView2 data, 2012; (d) Field photographs, 2012).

Table 1: Remote sensing image parameters.

Type	Time	Mean cloudiness
QuickBird	2002.08.10	<10%
	2004.05.22	<10%
	2009.04.09	<10%
WorldView2	2012.05.04	<20%

and its vertical precision is 20 mm + 1 ppm. Measurements were taken in May 2010, September 2011, and June 2012. The collected three-period high-precision differential GPS data were imported into the ArcGIS 9.3 software. The main processing steps were as follows: (1) the outer blowout boundary, erosion depression zone boundary, and sand deposition zone boundary were outlined according to the point names in the attribute table, and the area and morphological parameters of the erosion depression and sand deposition zones were calculated; (2) DEM data of blowouts were generated by Kriging spatial interpolation; (3) on the basis of regional DEM, the interpolation of region was cut utilizing the outer blowout boundary to obtain the DEM data within the scope of blowouts. The volume and 3D morphological parameters of the erosion depression and sand deposition zones were calculated using ArcGIS 9.3's Area and Volume Statistic tool; (4) contour lines were generated based on the DEM data to analyze the overall elevation changes of blowouts; (5) longitudinal profiles of blowouts and transverse profiles of erosion depressions and sand deposition zone were created using ArcGIS 9.3's Interpolate Shape tool to obtain the profile change map for different regions of blowouts; (6) based on the profile change map, the dynamic changes of characteristic parts were statistically analyzed.

4. Results

4.1. Dynamic Change of Typical Blowouts. Figure 5 presents the morphological changes of different blowout types from 2002 to 2012. Saucer blowouts were the smallest in area and exhibited the lowest variation in amplitude. Within the ten-year study period, the erosion depression zone was dominated by the expansion of rear depression edges along the long axis of depression. The sand deposition zone, on the other hand, experienced southwestward expansion from 2002 to 2004 and then decreased in area from 2004 to 2009, showing contraction towards the erosion depression zone;

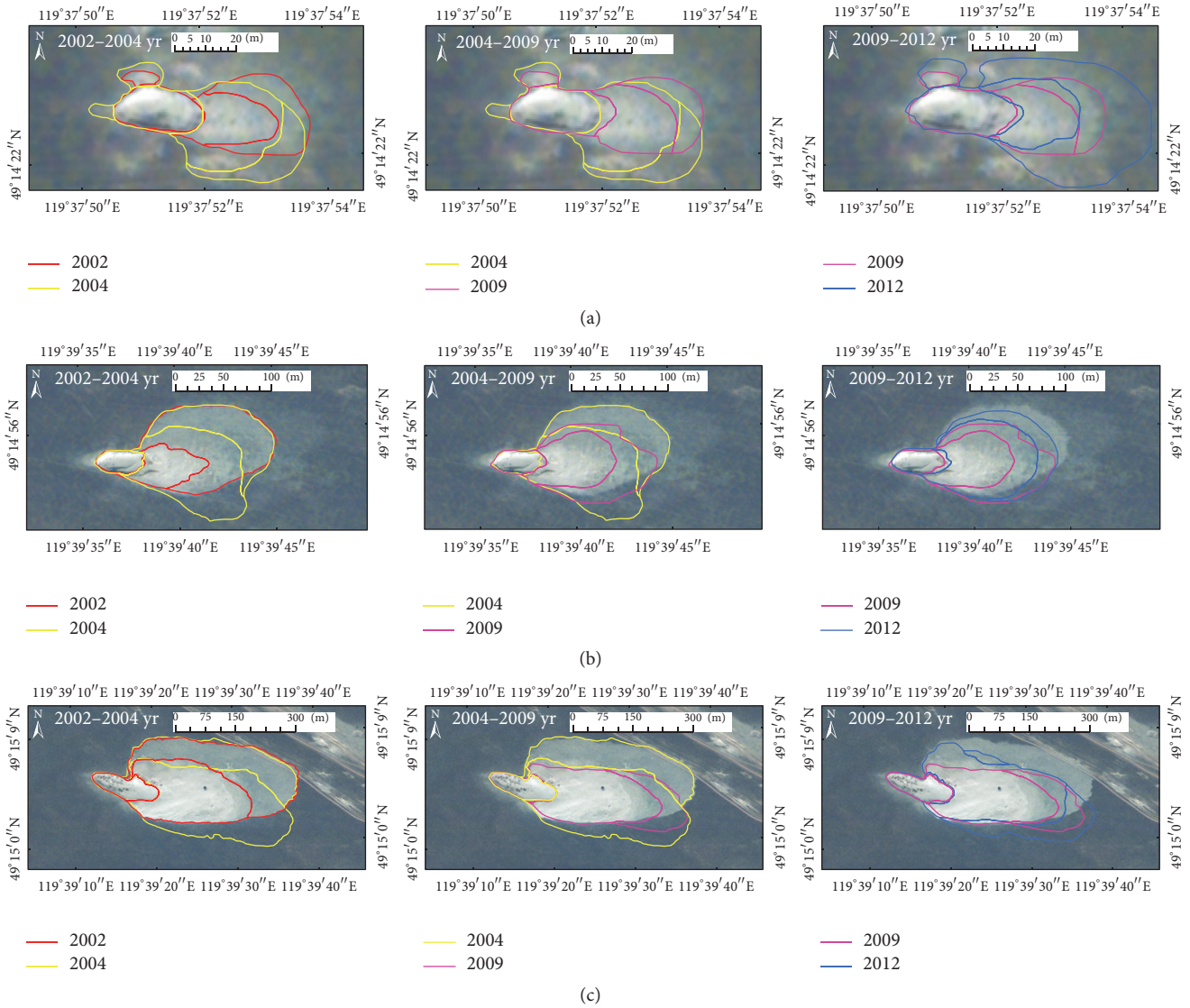

FIGURE 5: Morphological changes of different blowout types ((a) saucer blowout, (b) trough blowout, and (c) compound blowout; QuickBird images, 2002).

again in 2012, the zone expanded northwestward. Trough blowouts varied in amplitude to a lesser extent than compound blowouts.

From 2002 to 2004, erosion in the depression zone occurred mainly around the eastern edge and manifested as an expansion of the depression along the long axes. The sand deposition zone expanded rapidly to the surroundings, primarily towards the southwest. The sand drift zone was partially transformed into a sand deposition zone which expanded outward towards the northeast in the sand deposition zone. From 2004 to 2009, the eastern edge of the erosion depression zone expanded considerably and the soil layer moved forward along the prevailing wind direction due to erosion; the sand deposition zone and sand drift zone diminished due to the interannual compound blowout variations.

From 2009 to 2012, expansion in the erosion depression zone occurred mainly around the southeastern edge, while the sand deposition zone expanded to the north and east. The compound blowout changed most significantly within the ten-year study period. From 2002 to 2004, erosion in the depression zone occurred mainly in the northeastern and eastern edges, while the soil layer exposed around the eastern edge moved forward along the long axis of depression due to wind erosion. The sand deposition zone expanded eastward and southeastward due to prevailing west and northwesterly winds. Sand drift zone was transformed into sand deposition zone along with the accumulation of sand materials.

From 2004 to 2009, erosion in the compound blowout depression zone occurred mainly in the southeastern and northeastern edges, primarily exhibiting increased width of depression. Vegetation fixation strengthened due to the abrupt decrease in resultant drift potential from 2004 to 2009, thus leading to the rapid reduction of sand deposition and sand drift zones during that period which contracted in the

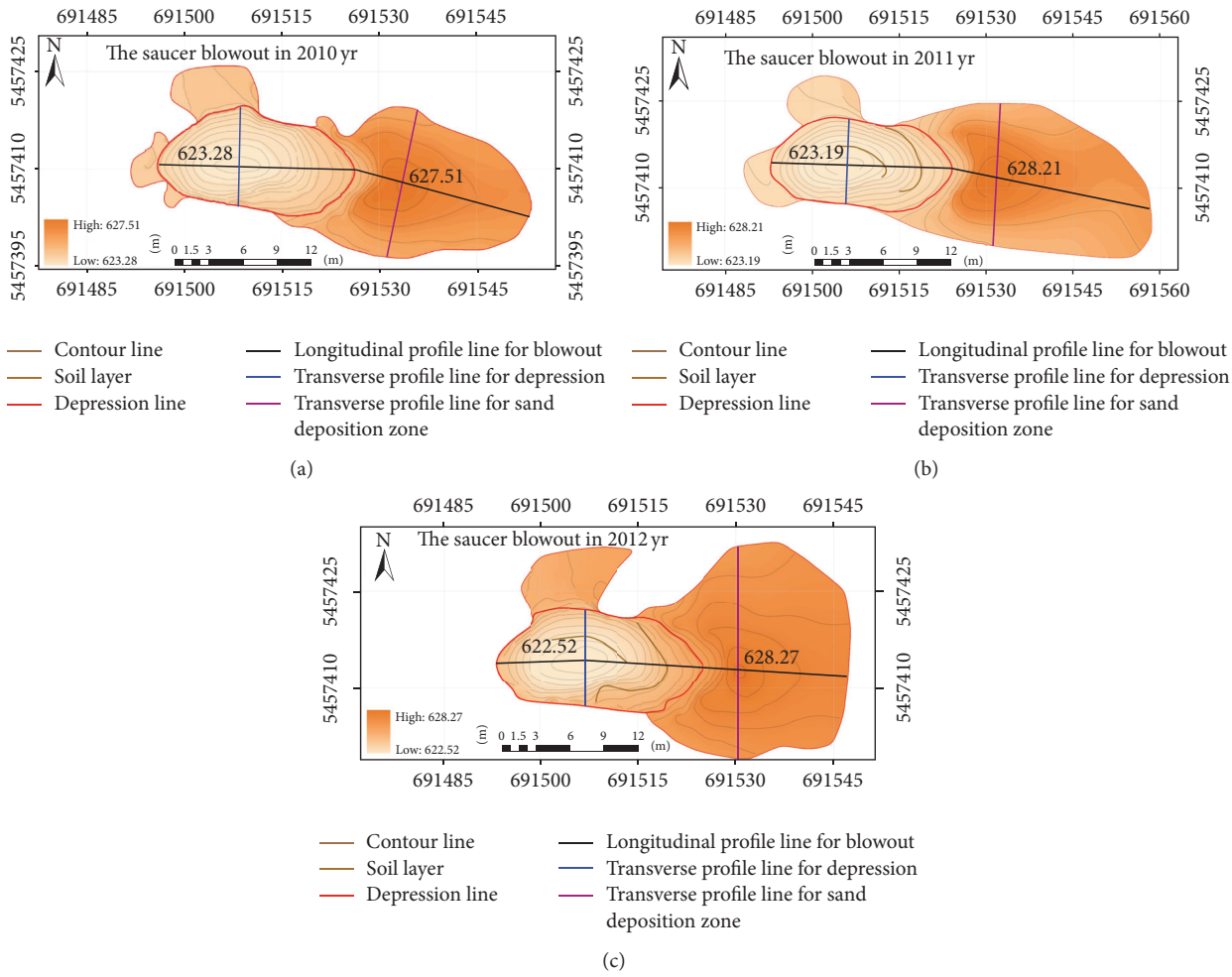

Figure 6: DEM variations of saucer blowout from 2010 to 2012.

erosion depression zone direction. From 2009 to 2012, major eroded sites in the depression zone formed the northeastern, eastern, and southeastern edges; the length and width of the depression continued to increase. The sand deposition zone expanded northward and eastward, while the sand drift zone expanded at the southern part of the sand deposition zone.

4.2. Dynamic Change of Typical Blowouts Based on RTK Ground Survey

4.2.1. Morphological Changes of Saucer Blowout. As shown in Figure 6, the tested saucer blowout erosion depression zone was discoid with the depression opening in the WNW prevailing wind direction. The depression elevation was more stable compared to that that of the trough blowout. Northern, southern, and eastern edges of the depression were similar in slope. There were two layers of crescent soil layer exposure at the bottom and northeastern edges of the depression which retreated due to abrasion. The sand deposition zone was fan-shaped with a convex stoss slope and gradually decreasing lee slope elevation towards the surrounding areas. A new air outlet was formed on the northern edge of the depression as airflow entered it and generated a vortex due to the shallow saucer blowout, ultimately forming a small-scale, fan-shaped sand deposition zone at the northern part of the depression.

Table 2 lists the changes in various saucer blowout zone areas from 2010 to 2012. Overall, the areas of erosion depression and sand deposition zones increased; the growth amplitude was far higher for the sand deposition zone (44.4%) than the erosion depression zone (6.3%). From 2010 to 2011, the area of the erosion depression zone increased by 19.4 m^2 with a relative growth amplitude of 5.3%, exceeding that of the 2011 to 2012 period (0.9%). The area of the sand deposition zone increased sharply with a relative growth amplitude from 2010 to 2011 (43.7%) far greater than that from 2011 to 2012 (0.5%), similar to the interannual growth trend of the erosion depressions. These results indicate that the expansion amplitude of the saucer blowout area from 2010 to 2011 was greater than that from 2011 to 2012.

Table 3 lists the changes in saucer blowout morphological parameters. The length, width, depth, and volume of the blowouts presented continuous growth trends. The growth rate of depression length was 0.7 $m \cdot a^{-1}$, with small growth amplitude (4.5%), while width growth rate was 0.5 $m \cdot a^{-1}$

Table 2: Changes in saucer blowout area (unit: m^2).

Zone	2010	2011	2012	Variation of area	Variation amplitude
Erosion depression zone	362.7	382.1	385.5	22.8	6.3%
Sand deposition zone	669.6	962.0	967.1	297.5	44.4%
Total area	1,032.3	1,344.1	1,352.6	320.3	31.0%

Table 3: Changes in morphological parameters for saucer blowout erosion depression zone.

Morphological parameter	2010	2011	2012	Variation quantity	Variation amplitude
Length (m)	31.1	31.4	32.5	1.4	4.5%
Width (m)	14.8	15.5	15.8	1.0	6.8%
Depth (m)	3.5	3.7	3.8	0.3	8.6%
Volume (m^3)	558.0	559.6	571.4	13.4	2.4%

Table 4: Changes in morphological parameters for saucer blowout sand deposition zone.

Variable	2010	2011	2012	Variation quantity	Variation amplitude
Length (m)	27.6	35.1	22.3	−5.3	−19.2%
Width (m)	23.7	25.6	33.6	9.9	41.8%
Height (m)	2.8	2.9	3.1	0.3	10.7%
Volume (m^3)	1,162.8	1,741.7	1,723.1	560.3	48.2%

with large growth amplitude (6.8%). Depression depth slowly increased with growth amplitude of 8.6%; depression volume also continuously increased, with a growth amplitude of 2.4% and a growth rate of 6.7 $m^3 \cdot a^{-1}$.

Table 4 lists the changes in morphological parameters for the saucer blowout sand deposition zone. The length of the sand deposition zone first increased then decreased with an overall reduction amplitude of 19.2%. The length increased from 2010 to 2011 with relative growth amplitude of 27.2%. From 2011 to 2012, the length decreased sharply by 12.8 m with a relative reduction amplitude of 36.5%. Width, on the other hand, continued to increase at a rate of 5 $m \cdot a^{-1}$. The height of the sand deposition zone also continued to increase at a flat growth rate. The total volume of the sand deposition zone fluctuated, increasing to 1,741.7 m^3 (relative growth amplitude of 49.8%) in 2011, and then decreased slowly to 1,723.1 m^3 (relative reduction amplitude of 1.1%) in 2012. The volume and length of the sand deposition zone showed the same variation trends and did not increase as width and height increased.

To further investigate these morphological parameters using 3D GPS data, we studied the profile variations of blowouts and changes in the movement of various characteristic parts between 2010 and 2012 by extracting longitudinal blowout profiles and transverse erosion depressions and sand deposition zone profiles. We first draw layers of the longitudinal and transverse profile lines and then cut the DEM of saucer blowout according to the respective layers using the Interpolate Shape tool in ArcGIS 9.3's 3D Analyst module. Profile graphs were generated using the Create Profile Graph tool. As shown in Figure 7, the geomorphic units of saucer blowout consisted of an air inlet, erosion depression bottom, rear depression edge, and the windward and lee slopes of the sand deposition zone. The saucer blowout depressions had gentle slopes; the slope of the front edge was between 14 and 16°. The depression bottom was relatively flat. The slope of the rear edge was smaller than that of the front edge (8–10°). There was crescent soil layer exposure at the top of the rear depression edge, and the stoss slope of the sand deposition zone was concave. The slope of the middle section was relatively gentle, between 10 and 12°. The stoss slope was steeper, between 29 and 31°. The lee slope of sand deposition zone was concave and with gradually decreasing elevation along the long axis of the blowouts.

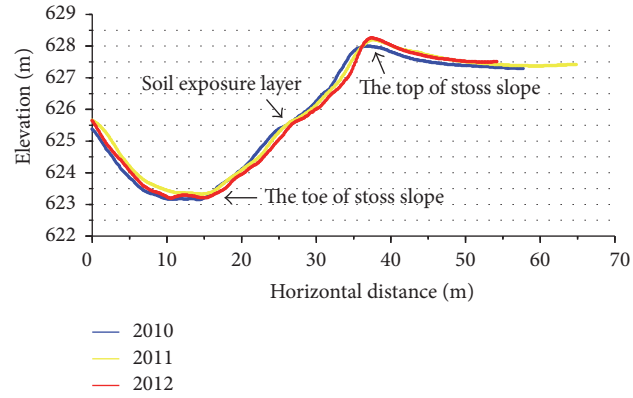

Figure 7: Longitudinal profile variations of saucer blowout from 2010 to 2012.

As shown in Figure 7, the depression gradually deepened while the rear depression edge and stoss slope of the sand deposition zone were subject to apparent wind erosion. The soil layer moved forward along the long axis of the depression due to erosion and the stoss slope crest elevation increased due to the accumulation of sand materials.

Table 5: Changes in various characteristic points of saucer blowout (unit: m).

	Stoss slope toe		Soil layer		Stoss slope crest	
	Horizontal distance	Elevation	Horizontal distance	Elevation	Horizontal distance	Elevation
2010	14.3	623.4	24.8	625.6	36.2	628.1
2011	15.2	623.4	26.3	625.6	37.1	628.2
2012	15.3	623.2	27.0	625.5	37.3	628.3
Variations	1.0	−0.2	2.2	−0.1	1.1	0.2

To obtain the annual changes in horizontal distance and elevation of each characteristic part for the saucer blowout, the slopes of all points on the profile line were calculated. Then, the range of characteristic parts was determined based on Figure 7. Within this range, the second derivatives of all points were calculated, and the point with the largest slope change within this region was obtained, which was precisely the characteristic point of the characteristic part (Figure 7). The horizontal distance (the distance from the air inlet to the characteristic point) and elevation of the characteristic point were recorded. By this way, the horizontal migration distance and elevation values of stoss slope toe, soil layer, stoss slope crest, and lowest depression point in various years were obtained as shown in Table 5.

Table 5 shows where the stoss slope toe of the blowouts moved forward by 1.0 m along the long axis of the depression due to wind erosion, with an annual mean movement of 0.5 m·a^{-1} and elevation reduction of 0.2 m. From 2010 to 2011, the slope toe moved forward by 0.9 m, showing much faster movement than 2011-2012. Soil layer at the rear edge of the erosion depression moved forward by 2.2 m along the long axis as a result of severe wind erosion attributed to terrain uplift, airflow compression, and continuously increasing wind speed, with an annual mean movement of 1.1 m·a^{-1}. From 2010 to 2011, the soil layer moved by 1.5 m; that is, it moved much faster than it did in 2011-2012 (0.7 m). Soil layer elevation was relatively stable from 2010 to 2011 and decreased by 0.1 m from 2011 to 2012. The stoss slope crest increased overall due to airflow dispersion and reduced wind speed. Its horizontal forward movement was 1.1 m and its annual mean movement was 0.6 m·a^{-1}. There was also greater migration distance from 2010 to 2011 (0.9 m) than that from 2011 to 2012 (0.2 m). Its elevation steadily increased with an overall increase of 0.2 m.

The transverse depression profiles (Figure 8) show where the northern and southern slopes of erosion depressions were asymmetrical. The northern slopes were relatively gentle (18–20°), whereas the southern slopes were relatively steep (23–25°). The depression bottoms were smooth. From 2010 to 2012, the depressions formed an erosion pattern and elevations of the northern slopes, southern slopes, and bottoms decreased as a result of wind erosion. The southern slopes were gentle, so they became the air outlet after the airflow formed a vortex in the blowouts, thereby resulting in the fan-shaped sand deposition zone in the northern part of the depression.

Figure 9 shows the sand deposition zone transverse profile variations. Accumulation was common throughout this

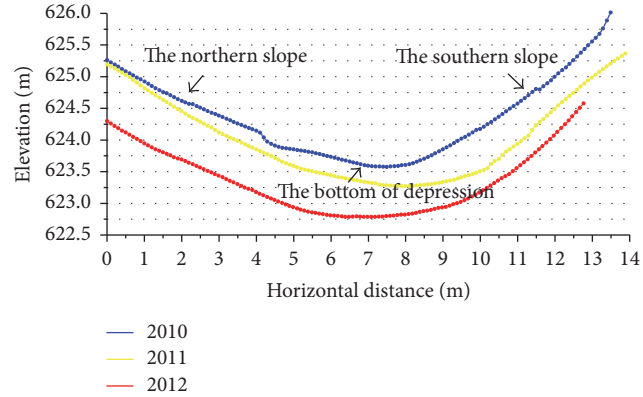

Figure 8: Transverse profile variations of saucer blowout erosion depression zone from 2010 to 2012.

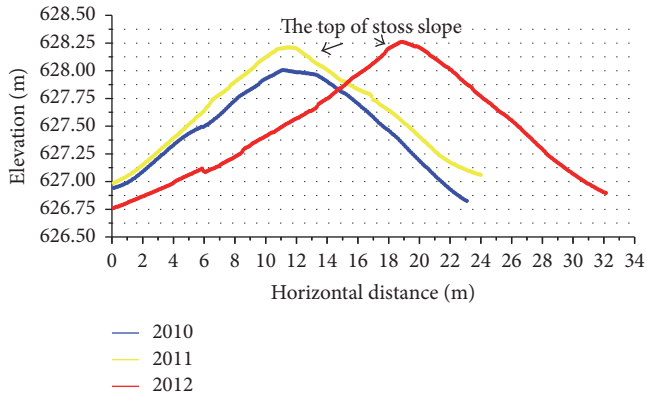

Figure 9: Transverse profile variations of saucer blowout sand deposition zone from 2010 to 2012.

zone. The stoss slope crest was the highest in elevation and spread to the surrounding areas with gradually decreasing elevation. From 2010 to 2012, the sand deposition zone continued to grow in height, while moving gradually southward due to the influence of the prevailing wind direction. The stoss slope crest increased by 0.2 m in elevation and moved horizontally southward by 7.3 m at a rate of 3.6 m·a^{-1} from 2010 to 2012. It moved by 1.0 m from 2011 to 2012 and then by as much as 6.3 m from 2011 to 2012. The southern boundary of the deposition zone also expanded southward, moving by 0.9 m from 2010 to 2011 by 8.0 m from 2011 to 2012.

4.2.2. Morphological Changes of Trough Blowout. Based on our field survey and DEM data analysis (Figure 10), trough

Table 6: Changes in trough blowout area (unit: m^2).

Zone	2010	2011	2012	Variation of area	Variation amplitude
Erosion depression zone	1,254.4	1,257.5	1,360.9	106.5	8.5%
Sand deposition zone	4,831.4	6,079.8	6,562.3	1,730.9	35.8%
Total area	6,085.8	7,337.3	7,923.2	1,837.4	30.2%

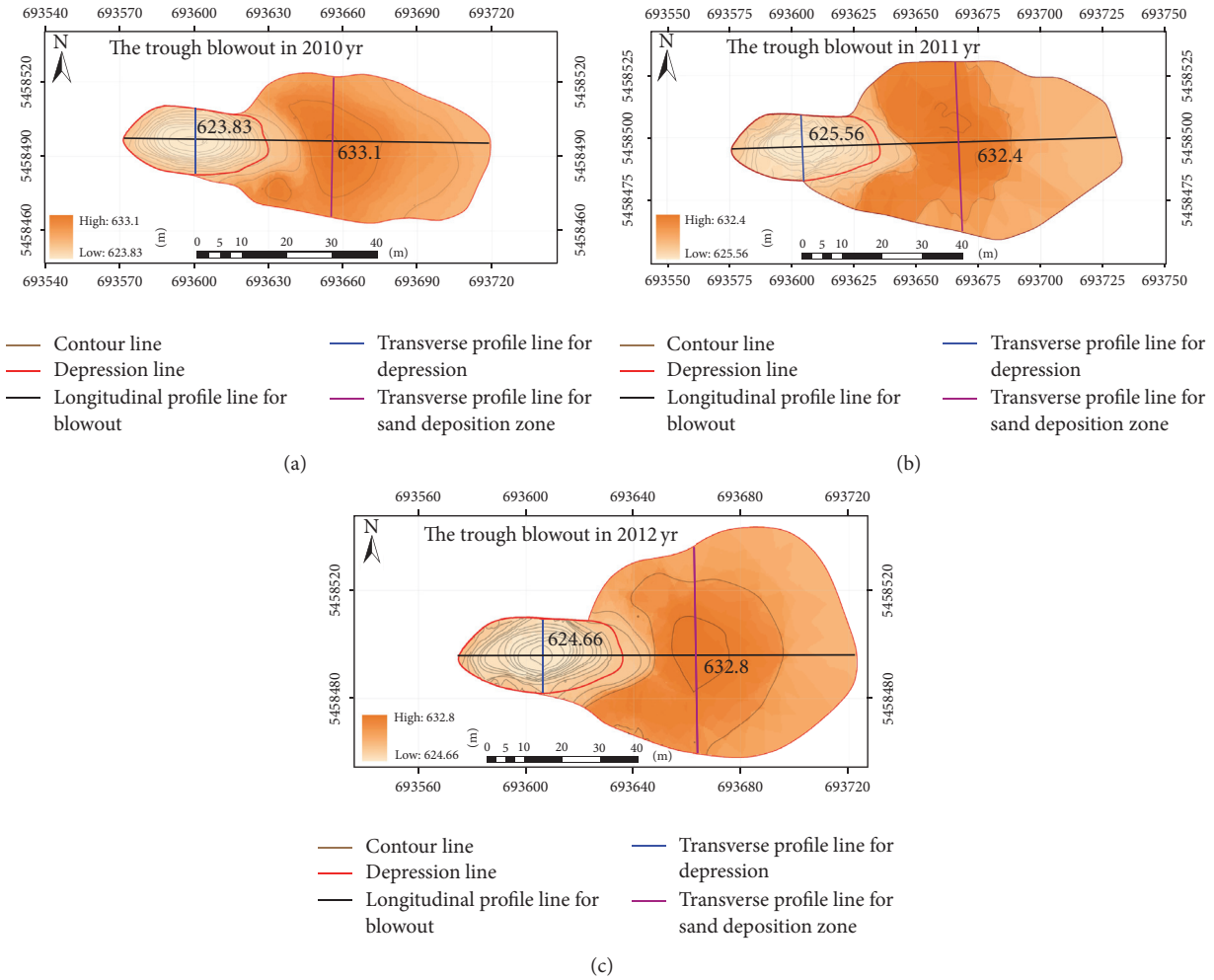

Figure 10: DEM variations of trough blowout from 2010 to 2012.

blowouts occurred in the erosion depression zone and the sand deposition zone. The erosion depression zone was oblong in shape with its opening facing westward, which is consistent with the prevailing wind direction. The elevation of the depression changed substantially over the study period. The northern and southern edges were relatively steep; the northeastern edge expanded due to wind erosion and the stoss slope at the eastern edge was concave. Crescent soil layer exposure occurred and retreated due to abrasion, thereby enabling the erosion depression zone to develop along the long axis of depression. The sand deposition zone had a convex stoss slope and a lee slope that gradually decreased in elevation.

Table 6 describes the changes in trough blowout area. The trough blowout's erosion depression zone area was generally more stable than that of the sand deposition zone from 2010 to 2012; their variation amplitudes were 8.5% and 35.8%, respectively, with respective growth rates of 53.3 $m^2 \cdot a^{-1}$ and 865.5 $m^2 \cdot a^{-1}$. The area of the sand deposition zone increased by 1,248.4 m^2 from 2010 to 2011, showing relative growth amplitude of 25.8%; from 2011 to 2012, its relative growth amplitude was only 8.0%.

Table 7 lists the changes in trough blowout morphological parameters: those of erosion depressions altogether increased, as did volume. The length and width of the depression continually increased, with similar growth amplitudes of 5.3% and 5.1%, respectively. The depth of the depression decreased from 6.5 m in 2010 to 6.0 m in 2011 and then increased to 7.0 m in 2012. Depression volume fluctuated in a similar pattern, suggesting that it was controlled by the

Table 7: Changes in morphological parameters for trough blowout erosion depression zone.

Morphological parameter	2010	2011	2012	Variation quantity	Variation amplitude
Length (m)	60.9	61.1	64.1	3.2	5.3%
Width (m)	27.2	27.4	28.6	1.4	5.1%
Depth (m)	6.5	6.0	7.0	0.8	12.9%
Volume (m^3)	4,022.3	3,960.7	5,055.1	1,032.8	25.7%

Table 8: Changes in morphological parameters for trough blowout sand deposition zone.

Morphological parameter	2010	2011	2012	Variation quantity	Variation amplitude
Length (m)	90.2	98.8	86.6	−3.6	−4.0%
Width (m)	60.5	72.4	85.5	25.0	41.3%
Height (m)	2.4	2.8	2.9	0.5	20.8%
Volume (m^3)	7,564.1	13,089.3	13,303.2	5,739.1	75.9%

changes in depression depth rather than increasing with the increase in length and width.

As shown in Table 8, the length of the trough blowout sand deposition zone was fairly stable with a reduction amplitude of only 4.0%. The length increased from 90.2 m in 2010 to 98.8 m in 2011 and then decreased again to 86.6 m. Its width grew continuously at a rate of 12.5 $m \cdot a^{-1}$. The length-width ratio was close to 1 : 1, indicating that the sand deposition zone in the trough blowout gradually became fan-shaped. Its height increased by 0.5 m with a growth amplitude of 20.8%. The volume of the sand deposition zone increased at a rate as high as 2,869.6 $m^3 \cdot a^{-1}$ and amplitude of 75.9%.

The longitudinal profiles of trough blowouts and transverse profiles of their depressions and sand deposition zones were extracted with the same analytical method as that used to extract the saucer blowout profiles. As shown in Figure 11, the front edge of erosion depressions was relatively steep with slopes between 16 and 20°. The depression was smooth on the bottom, which was covered with a small range of psammophyte vegetation. Crescent soil layer exposure was present at the rear upper part of the depression affected by wind erosion. In 2011 and 2012, the stoss slope of the sand deposition zone migrated along the long axis due to wind erosion, and a section of soil layer scarp appeared. The stoss slope of the sand deposition zone was convex in shape ranging within 5–7° with a rounded crest. Its elevation decreased with the prevailing wind direction, which transited towards the grass basement.

From 2010 to 2012, the trough blowout erosion depression zone first grew and then shrank, whereas the sand deposition zone first shrank and then grew. From 2010 to 2011, the front edge, bottom, and lower rear part of depression all showed an accumulation trend, while, from 2011 to 2012, the depression deepened due to erosion. The upper rear part of the depression presented an erosion pattern. The soil layer moved forward along the long axis of the depression due to wind erosion; the stoss slope of the sand deposition zone was also eroded by wind. The elevation of the stoss slope crest first decreased then increased.

Table 9 shows the variation trends of various characteristic points in the trough blowout. The horizontal distance of

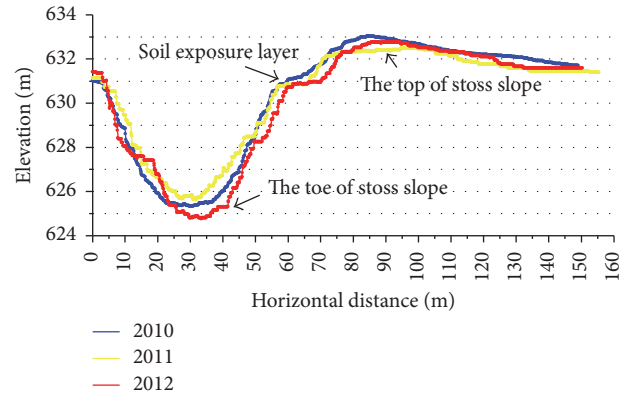

Figure 11: Longitudinal profile variations of trough blowout from 2010 to 2012.

the stoss slope toe first decreased and then increased, which is attributed mainly to the accumulation of sand materials at the depression bottom from 2010 to 2011. From 2011 to 2012, the slope toe was dominated by erosion, with horizontal movement of 5.7 m and elevation decrease of 0.3 m. The soil exposure layer continued to move forward along the long axis of the depression at a rate of 3.2 $m \cdot a^{-1}$, while its elevation remained fairly stable. The elevation of the stoss slope crest first decreased by 0.7 m from 2010 to 2011 and then increased by 0.4 m from 2011 to 2012; it decreased overall by 0.3 m during these years. This was mainly because the depressions were in an accumulation pattern from 2010 to 2011. The sand materials transported to the sand deposition zone diminished in size, and the original sand deposition zone decreased in elevation as a result of wind erosion. From 2011 to 2012, large amounts of sand materials were transported to the sand deposition zone as the depression was severely eroded by wind, resulting in increased elevation of the slope crest in the sand deposition zone.

Figure 12 shows the transverse profile variations of the trough blowout sand deposition zone, which first shrank and then grew over the study period. The elevation of its stoss slope crest decreased by 0.4 m from 2010 to 2011 and

Table 9: Variations of various characteristic trough blowout points (unit: m).

	Stoss slope toe		Soil layer		Stoss slope crest	
	Horizontal distance	Elevation	Horizontal distance	Elevation	Horizontal distance	Elevation
2010	35.3	625.6	55.1	630.6	82.3	633.1
2011	32.0	625.7	56.8	630.8	92.4	632.4
2012	41.0	625.3	61.5	630.9	85.3	632.8
Variations	5.7	−0.3	6.4	0.3	3.0	−0.3

Table 10: Changes in area of compound blowout (unit: m^2).

Zone	2010	2011	2012	Variation of area	Variation amplitude
Erosion depression zone	8,259.1	8,439.9	8,442.9	183.8	2.2%
Sand deposition zone	41,866.8	46,774.2	49,881.1	8,014.3	19.1%
Total area	50,125.9	55,214.1	58,324.0	8,198.1	16.4%

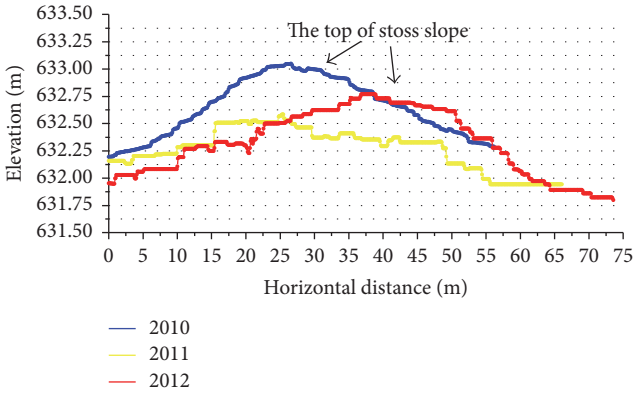

Figure 12: Transverse profile variations of trough blowout sand deposition zone between 2010 and 2012.

increased by 0.2 m from 2011 to 2012, showing an overall rise of 0.2 m. The horizontal distance of the stoss slope crest moved northward by 3.9 m from 2010 to 2011 and moved southward by 14.0 m from 2011 to 2012, presenting an overall southward movement of 10.1 m.

4.2.3. Morphological Changes of Compound Blowout. We divided the compound blowout as-measured into the erosion depression zone and sand deposition zone based on our field survey and DEM data analysis (Figure 13). The erosion depression zone was oblong in shape and opened towards the WNW prevailing wind direction. The elevation of the depression changed considerably during the study period. The northern and southern edges were relatively steep; the northeastern edge was expanded due to wind erosion and the stoss slope at the eastern edge was concave. Crescent soil layer exposure was present and retreated due to abrasion, thereby enabling the erosion depression zone to develop along the long axis. The sand deposition zone expanded to the southeast. The stoss slope of this zone was convex, while the middle part of the lee slope deviated southeastward. Secondary blowout with low elevation appeared at the sand deposition zone due to differential erosion, behind which a parabolic dune developed with its own stoss slope and slope crest. Sand materials reaccumulated, resulting in increased elevation.

Table 10 describes variations in the measured area of compound blowouts. Various blowout zones mainly exhibited morphological expansion. The variation amplitude was greatest in the sand deposition zone. The area of the erosion depression zone increased by 183.8 m^2 with a growth amplitude of 2.2% and growth rate of 91.1 $m^2 \cdot a^{-1}$. From 2010 to 2011, the area increased by 180.8 m^2 with a relative growth amplitude of 2.1%; from 2011 to 2012, the area increased by 3 m^2 with a relative growth amplitude of only 0.04%. In other words, the expansion of the depression area slowed down. The area of the sand deposition zone increased by 8014.3 m^2, showing a growth amplitude of 19.1% and growth rate of 4007.2 $m^2 \cdot a^{-1}$. From 2010 to 2011, the area increased by 4907.4 m^2 with a relative growth amplitude of 11.7%, while, from 2011 to 2012, the area increased by 3106.9 m^2 with a relative growth amplitude of 6.6%. The decrease in growth amplitude suggests slowed growth overall in the sand deposition zone. The total area increased by 8198.1 m^2 (16.4%). From 2010 to 2011, the area increased by 5088.2 m^2 with a growth amplitude of 10.1%, while, from 2011 to 2012, the area increased by 3109.9 m^2, with a growth amplitude of 5.6%. These area variations altogether indicate that various blowout zones increased in area while their growth rates decreased.

Table 11 lists the changes in morphological parameters for the compound blowout erosion depression zone. The length, width, and volume of the erosion depressions increased, while the depth gradually decreased, indicating morphological expansion with simultaneous shallowing. The length of the depression increased by 1.5 m with a 2.5 $m \cdot a^{-1}$ growth rate and growth amplitude of 0.8% from 2010 to 2011, while, from 2011 to 2012, the length increased by 3.5 m with a relative growth amplitude of 2.0%. The width of the depression increased by 1.6 m at a growth rate of 1.3 $m \cdot a^{-1}$ and growth amplitude of 2.2% from 2010 to 2011; the growth amplitude decreased to 1.4% from 2011 to 2012 as the width increased by 1.0 m. The depth of the depression decreased by 0.9 m from 2010 to 2011 with a relative reduction amplitude of 8.4%; it decreased by only 0.2 m from 2011 to 2012 with a relative

Table 11: Changes in morphological parameters for compound blowout erosion depression zone.

Morphological parameter	2010	2011	2012	Variation quantity	Variation amplitude
Length (m)	171.3	172.8	176.3	5.0	2.9%
Width (m)	71.5	73.1	74.1	2.6	3.6%
Depth (m)	10.7	9.8	9.6	−1.1	−10.3%
Volume (m^3)	31,975.4	34,231.1	34,415.5	2,440.1	7.6%

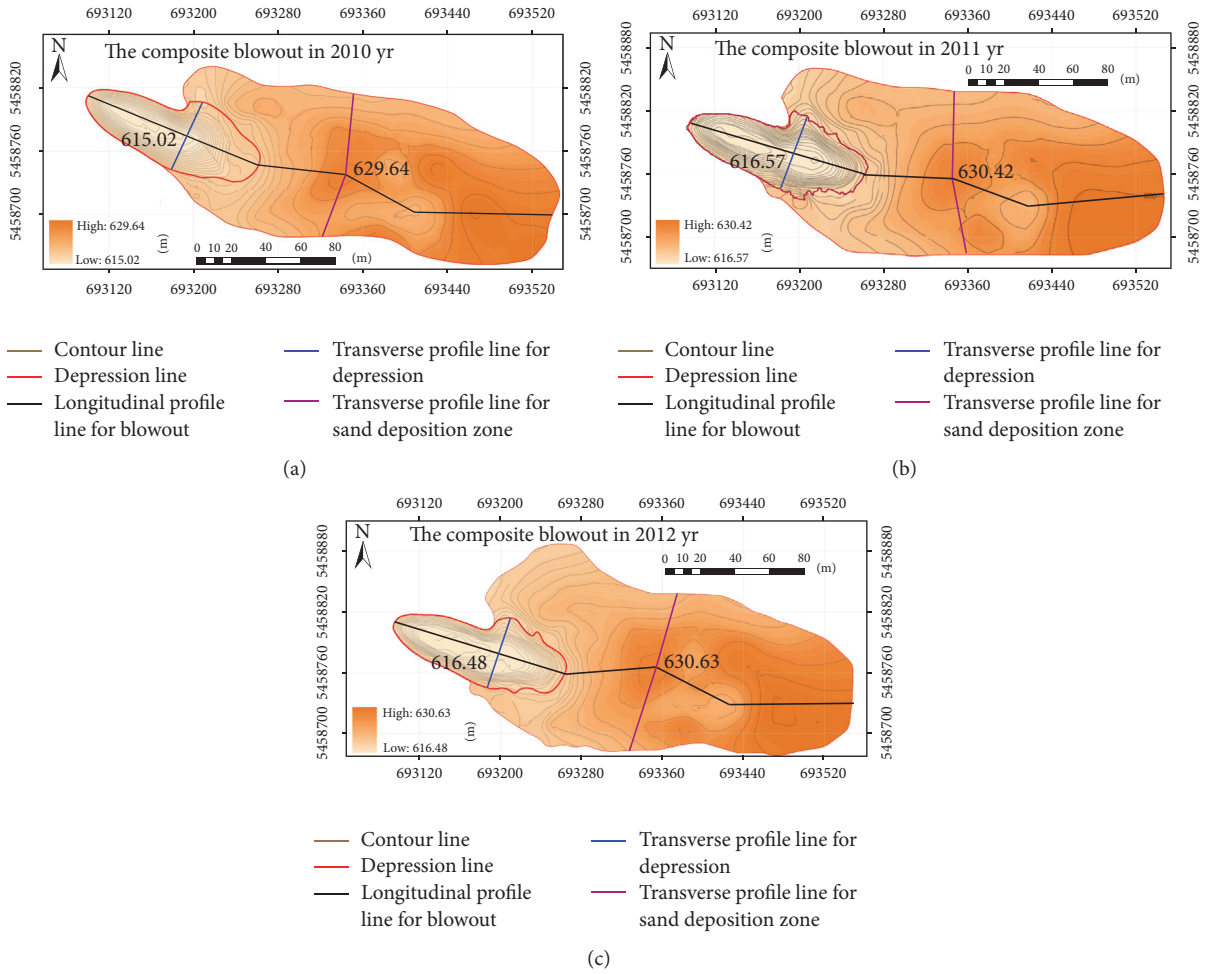

Figure 13: DEM variations of compound blowout from 2010 to 2012.

reduction amplitude of 2.0%, presenting an overall decrease of 1.1 m with decreased reduction amplitude and reduced accumulation rate. The total volume of erosion depression increased by 2440.1 m^3 with a growth amplitude of 7.6%.

Table 12 lists the changes in the sand deposition zone morphological parameters. The length of this zone decreased while its width, height, and total volume all increased over the study period. The length decreased by 3.5 m with a reduction rate of 1.8 $m{\cdot}a^{-1}$ and reduction amplitudes of 0.2% from 2010 to 2011 and 1.0% from 2011 to 2012. The width changed substantially, increasing by 36.8 m with a growth rate of 18.4 $m{\cdot}a^{-1}$. Its relative growth amplitude was 15.8% from 2010 to 2011 and 7.4% from 2011 to 2012. These results suggest that the growth amplitude of sand deposition zone width was large when the reduction amplitude of length was small; conversely, when the reduction amplitude of length was large, the growth amplitude of width was small. The zone developed into a fan shape due to these changes. The volume growth rate of the sand deposition zone was 39310.9 $m^3{\cdot}a^{-1}$, indicating large amounts of sand accumulation in the zone during the study period having led to the rapid growth in volume.

The longitudinal profiles shown in Figure 14 indicate that the compound blowout behaved similarly to the trough blowout in terms of basic geomorphologic units, with the exception of secondary blowouts and parabolic dunes in the sand deposition zone. The front edge of the erosion depression was relatively steep with slopes between 16 and 20°. *Salix psammophila* shrubs grew abundantly at the bottom

Table 12: Changes in morphological parameters for compound blowout sand deposition zone.

Morphological parameter	2010	2011	2012	Variation quantity	Variation amplitude
Length (m)	290.3	289.6	286.8	−3.5	−1.2%
Width (m)	150.7	174.5	187.5	36.8	24.4%
Height (m)	6.4	6.7	7.3	0.9	14.1%
Volume (m^3)	175,913.1	223,245.9	254,534.9	78,621.8	44.7%

Table 13: Variations of various characteristic compound blowout points (unit: m).

	Stoss slope toe		Soil layer		Stoss slope crest		Recession	
	Horizontal distance	Elevation	Horizontal distance	Elevation	Horizontal distance	Elevation	Horizontal distance	Elevation
2010	93.9	616.5	144.0	624.5	247.9	629.0	325.8	627.4
2011	127.4	617.6	166.1	624.9	256.2	629.5	330.8	628.2
2012	132.2	617.9	171.0	625.2	251.5	629.6	333.3	628.3
Variations	38.3	1.4	27.0	0.7	3.6	0.6	7.5	0.9

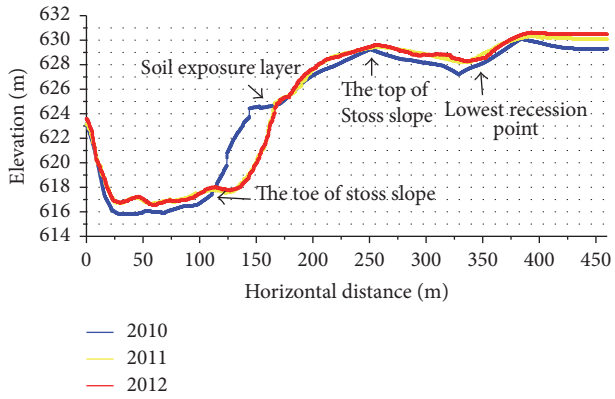

Figure 14: Longitudinal profile variations of compound blowout from 2010 to 2012.

of depression, resulting in a concave-convex curve at the depression bottom. The rear edge of the depression was concave with slopes between 14 and 16°. There was crescent soil layer exposure at the rear upper part of the depression due to wind erosion. The stoss slope of the sand deposition zone was convex with slopes between 4 and 7°. Again, as-affected by wind erosion, small recessions appeared at the lee slope accompanied by reduced elevation and soil exposure. Sand materials also accumulated behind the lee slope with dunes in the stoss slope, again resulting in increased elevation.

As shown in Figure 14, the depth of the compound blowout depression bottom gradually decreased from 2010 to 2012. The rear edge of the depression was severely eroded from 2010 to 2011 but less severely so from 2011 to 2012. From 2010 to 2011, the sand deposition zone exhibited an overall accumulation trend. Sand materials accumulated intensely from 2010 to 2011 but less intensely from 2011 to 2012. Small recessions behind the sand deposition zone developed similarly with an increase in elevation. The horizontal distances and elevations of stoss slope toe, soil exposure layer, stoss slope crest, and lowest recession point in various years were measured as reported in Table 13. From 2010 to 2012, the stoss slope toe moved 38.3 m along the long axis as a result of wind erosion and increased by 1.4 m in elevation, indicating that the erosion depression expanded along the long axis due to accumulated sand materials. The increase in horizontal distance was much greater from 2010 to 2011 than from 2011 to 2012 at 33.5 m and 4.8 m, respectively, suggesting that wind erosion was more severe from 2010 to 2011. The soil layer exposed at the rear tail edge of the erosion depression moved horizontally by 27.0 m, while its elevation increased only 0.7 m. The movement distance for the period from 2010 to 2011 was much greater than that from 2011 to 2012, at 22.1 m and 4.9 m, respectively, with a movement rate of 13.5 $m \cdot a^{-1}$. The crest of the stoss slope moved 3.6 m along the long axis and increased 0.6 m in elevation. The elevation for this characteristic point was fairly stable from 2011 to 2012 but increased by 0.5 m from 2010 to 2011. The lowest recession point of the lee slope moved by 7.5 m along the long axis of the blowout at 5.0 m and 2.5 m, from 2010 to 2011 and from 2011 to 2012, respectively; that is, the change was more dramatic from 2010 to 2011. An overall increase of 0.9 m in elevation was also observed.

The transverse profiles of the rear depression edge (Figure 15) indicate that the northern and southern slopes of the depression were asymmetrical. The northern slopes were relatively gentle (6–10°), whereas the southern slopes were rather steep (20–24°). There was also a scarp caused by soil layer exposure at the southern slope. From 2010 to 2012, the bottom of the depression widened from 17.1 m to 36.3 m at a 19.2 m total increase. The elevation of the depression bottom increased and the depression depth became shallower. For this reason, the length of the northern depression slope decreased from 28.5 m in 2010 to 23.3 m in 2012. The southern slope changed similarly. As the southern slope toe was eroded by wind, the soil layer collapsed to generate new collapse surfaces, thereby steepening the slope.

Figure 16 presents the transverse profile variations for the compound blowout sand deposition zone, which was convex and north-south asymmetrical. The southern section of the sand deposition zone was concave and featured secondary blowouts. The elevation of the stoss slope crest increased by 0.6 m from 2010 to 2012 and its crest moved southward by

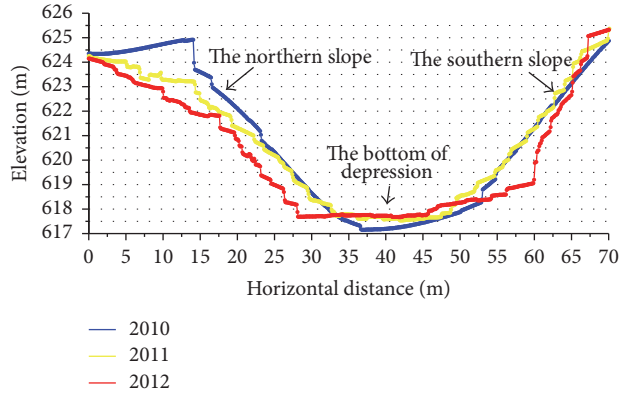

Figure 15: Transverse profile variations for compound blowout erosion depression zone from 2010 to 2012.

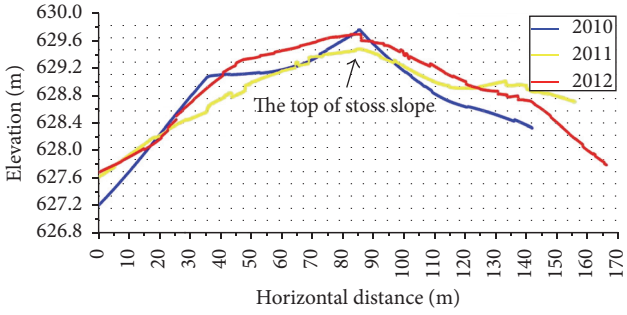

Figure 16: Transverse profile variations for sand deposition zone of compound blowout from 2010 to 2012.

29.6 m at a speed of 14.8 m·a^{-1}. The change was sizable from 2010 to 2011 at a movement of 29.5 m but minimal from 2011 to 2012 with a movement of only 0.1 m. The boundary of sand deposition zone also moved southward by 24.1 m from 2010 to 2012 at a speed of 12.1 m·a^{-1}.

5. Discussion

The shape and variation trends in the trough blowout were dependent mainly on wind entering the blowouts and accelerating continuously in the depressions due to funneling effect. There was no large-scale shrub coverage at the depression bottom, so the wind-drift sands were not effectively intercepted and thus caused severe erosion of the southern slopes, northern slopes, and depression bottom [14, 15]. Shallow depressions and gentle slopes at the southern and northern edges also allowed airflow to form a vortex which blew out from the relatively gentle northern edge to form a new air outlet, thereby leading to the appearance of a small fan-shaped sand deposition zone at the northern part of the depression. Airflow compressed from the stoss slope toe due to the effect of topographic uplift. Wind speed continued to increase and caused severe erosion of the rear depression edge and soil layer, causing the soil layer to gradually disappear along the prevailing wind direction. In the lee slope, the airflow dispersed and wind gradually decelerated to weaken the transportation of sand materials, thereby resulting in gradual deposition of sands in the sand deposition zone. The zone was also found to be controlled primarily by northwest winds. After the sands were transported to the sand deposition zone, they moved southwestward along the prevailing wind direction; thus, slope crest of the zone moved southward and the zone boundary expanded to the south.

The erosion depression zone of the trough blowout first increased then decreased, likely due to weakened wind intensity from 2010 to 2011 having transported less sand material into the blowout. The wind's sand transporting ability weakened due to abatement. The lack of sand source caused the original sand deposition zone to decrease in elevation. From 2011 to 2012, large amounts of sand materials were transported to the sand deposition zone as the depressions were severely eroded by wind, thereby resulting in increased elevation of the zone's slope crest. The soil layer exposed at the rear depression edge moved forward along the long axis of the erosion depression as a result of continuous erosion attributed to elevated terrain, compressed airflow, and strengthened wind at the site.

The formation of the compound blowout can be attributed to the westerly and northwesterly prevailing wind directions in the area. When the wind entered the blowouts, the *Salix psammophila* shrubs grown at the depression bottom intercepted the wind-drifted sand materials causing them to accumulate continuously and result in ever shallower depth of depression. The shrubs also played a role in shunting wind-drift sands [16, 17] so that the airflow moved forward towards the rear depression edge along the northern and southern slopes to undercut them, thereby continuously increasing the depression width (Figure 17(a)) [18]. The sand materials severely eroded the soil layer at the rear depression edge beginning at the stoss slope toe due to the effects of terrain uplift, compressed airflow, and continuously accelerating wind after drifting, causing the soil layer to move along the long axis of blowout [19, 20]. The wind decelerated after reaching the stoss slope crest where sand materials were deposited.

At the lee slope, airflow gradually dispersed, wind decelerated, and large amounts of sands accumulated in the sand deposition zone. Secondary blowouts appeared at the southern part of the lee slope due to wind erosion per the large coverage area of the compound blowout's sand deposition zone (Figure 17(b)). Parabolic dunes developed behind it [21]. Wind speed increased due to funneling in the recessed areas, where erosion was severe. Wind continued to accelerate at the stoss slope of the dunes and picked up large amounts of sand materials. On the lee slope of the dunes, sand materials deposited to continuously increase the elevation of the sand deposition zone. To this effect, the emergence of parabolic dunes led the depositional trend at the compound blowout's sand deposition zone and increased the elevation of the dune-side lee slope rather than gradually reducing the sand materials along the long axis. This is the primary difference between this zone and other simple blowout sand deposition zones.

It can be seen from the analysis of repeatedly measured ground high-precision GPS data that the trends of dynamic

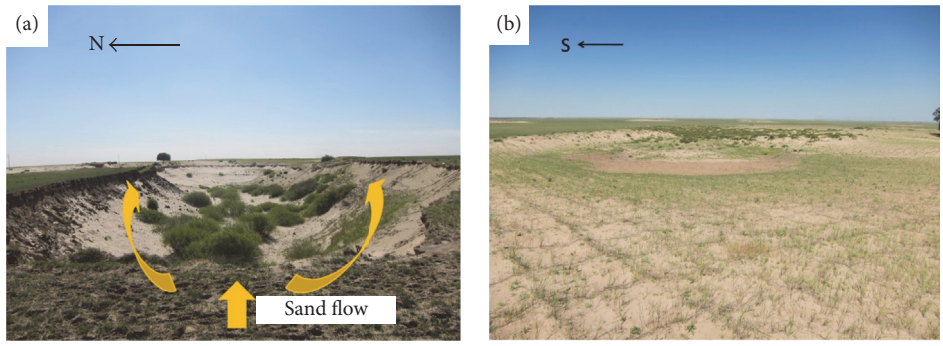

(a) (b)

Figure 17: Field photographs of compound blowout ((a) vegetation and airflow at the erosion depression, 2012; (b) secondary blowouts in the sand deposition zone, 2012).

changes varied for different types and sizes of blowouts from 2010 to 2012. As the smallest blowout selected, the length, width, and depth of the saucer blowout's erosion depression zone all experienced continuous increase, which appeared as a changing process of continuous erosion. The sand deposition zone, on the other hand, experienced a process of continuous deposition, thereby resulting in persistent increase in the elevation of its stoss slope crest. This was mainly because the saucer blowout had small form and shallow depression depth, so that the base level of erosion failed to reach the groundwater level. Therefore, the erosion depression zone presented a continuous erosion pattern, while the sand deposition zone was in a continuous deposition process. Compared to the saucer blowout, trough blowout had larger size and more complicated variation. Its erosion depression zone exhibited a first deposition then erosion process. This was probably due to the sidewall collapse between 2010 and 2011, which led to deposition of some sand materials at the bottom of depression. Moreover, wind's energy to transport sand materials in the erosion depression weakened, thereby causing increased depth of the depression during this stage. Because there was no sand source, and the sands in the original sand deposition zone was affected by wind erosion, the elevation decreased. Between 2011 and 2012, the depression was subject to strong wind erosion, so that substantial sand materials were transported into the sand deposition zone, thereby causing increased elevation of slope crest for the zone. Compound blowout had the largest and deepest sand depression zone. The length and width of the zone continued to increase, but the depression depth decreased gradually. This was mainly because the erosion depression zone was eroded to the groundwater level, so that the soil moisture content was high enough to develop large-scale *Salix psammophila* shrubs. Besides, vegetation itself had a role in intercepting and shunting wind-drift sands, which allowed continuous deposition of sand materials to result in the shallower depth of depression. Moreover, its shunting effect led the airflow to advance towards the rear edge of the depression along the northern and southern slopes to undercut these slopes, thereby continuously increasing the depression width. In addition, the sand deposition zone of the compound blowout was once again subject to wind erosion due to its large size to develop secondary blowouts.

Within the study area, road was one of the main factors inducing the development of blowouts. Due to the automobile roller compaction, the surface vegetation of sandy grasslands was damaged, and the soil layer was exposed. By the undercutting effect of strong wind, the loose soil layer on the road was subject to strong wind erosion to develop into blowouts. Extensive beaded blowouts were developed within the study area, which belonged to a type of road blowouts (Figure 4(a)). The authors statistically analyzed the road area (Table 14) in 1959, 2002, 2004, 2009, and 2012 to find that the area increased by 488,581 m^2 in total, which was an increase of 23.5%. Meanwhile, with the development of animal husbandry, the pressure of grassland habitat in the study area has been exacerbating. Overgrazing resulted in degradation of grasslands and exposure of surface soil layer, which easily facilitated the formation of bare areas under wind erosion. From a cause analysis perspective, the desertification of Hulunbuir grassland was the result of the combined action of natural and human factors. The arid or semiarid climatic environment is the prerequisite for desertification, whereas the human destruction of grassland vegetation and surface soil layer is the direct cause of desertification. Therefore, engineering desertification control measures such as straw checkerboard barriers and vegetation planting, as well as policies such as rational development of grassland resources and rational road construction are the primary means of controlling the blowout expansion.

6. Conclusion

From 2002 to 2012, the erosion depressions of saucer, trough, and compound blowouts in the study area extended along the downwind direction, while expanding laterally and continually increasing in size. The saucer blowout area increased in the sand deposition zone, while areas of trough and compound blowouts first increased, then decreased, and then increased again over the study period: their area markedly increased from 2002 to 2004, decreased to the minimum from 2004 to 2009, and then increased again from 2009 to

Table 14: Variations in area of roads (unit: m^2).

Year	1959	2002	2004	2009	2012
The area of roads	2,080,425	2,282,358	2,312,852	2,505,163	2,569,006

2012. Changes in the sand drift zone were rather complex. The trough blowout continued to decrease until reaching the minimum in 2012. Compound and saucer blowouts continued to decrease from 2002 to 2009, reached their respective minima in 2009, and then increased again from 2009 to 2012.

Our analysis of 3D data from repeated ground surveys indicates that the saucer blowout is the smallest in scale of all three blowout types, though it is in a period of active development. From 2010 to 2012, its erosion depression exhibited a downward erosion and horizontal expansion trend. Its sand deposition zone, conversely, presented an accumulation pattern. Its length decreased while its width and slope crest elevation increased. Sands deposited in the southeasterly direction due to the influence of resultant drift potential. The trough erosion depression increased in length and width and expanded horizontally, but its depth increased first and then decreased (i.e., first accumulated and then eroded). Its sand deposition zone exhibited the opposite pattern (first erosion and then accumulation). Its length decreased and its width increased, while its apex elevation first decreased and then increased. The erosion depression of the compound blowout expanded horizontally as-affected by northwestern and western winds; its area, length, and width continually increased over the study period. As *Salix psammophila* shrubs at the bottom of the depression intercepted the wind-drifted sand materials, they continued to accumulate at the depression bottom resulting in ever shallower depression depth. In the sand deposition zone, sand materials continued to accumulate, thereby resulting in continuous elevation of the slope crest. We also observed the development of secondary blowouts and parabolic dunes.

Conflicts of Interest

The authors declare that they have no conflicts of interest.

Acknowledgments

This research was supported by "the National High Technology Research and Development Program of China (Grant no. 2016YFC0500805)" and the National Natural Science Foundation of China Project "Formation and Deformation of Reticulate Dune Patterns in Hobq Desert (Grant no. 41671002)." The authors are grateful to Liu Dan and Zhou Yanguang for their assistance in the field.

References

[1] D. P. Zhang, X. K. Wang, E. D. Hasi et al., "HulunBuir sandy grassland blowouts I geomorphology, classification, and significances," *Journal of Desert Research*, vol. 26, no. 6, pp. 894–902, 2007.

[2] D. P. Zhang, H. W. Sun, X. K. Wang et al., "HulunBuir sandy grassland blowouts II: process of development and landscape evolution," *Journal of Desert Research*, vol. 27, no. 1, pp. 20–24, 2007.

[3] D. P. Zhang, X. K. Wang, R. L. Hu et al., "HulunBuir Sandy grassland blowouts III influence of soil layer and micro-relief," *Journal of Desert Research*, vol. 27, no. 1, pp. 25–31, 2007.

[4] D. P. Zhang, X. K. Wang, H. W. Sun et al., "HulunBuir Sandy grassland blowouts IV influence of human activities," *Journal of Desert Research*, vol. 27, no. 2, pp. 214–220, 2007.

[5] J. L. Dong and J. Ya, "Analysis on the changes of land desertification in hulunbeier sandy land area over the last 10 years," in *Forest Resources Management*, pp. 39–43, 2002.

[6] J. M. Feng and T. Wang, "Study on the actualty and historical evolution of desertification in the HulunBuir grasslands," *Arid Land Geography*, pp. 356–360, 2004.

[7] H. G. Nie, L. P. Yue, W. Yang et al., "Present situation, evolution trend and causes of Sandy desertification in Hulunbuir steppe," *Journal of Desert Research*, vol. 25, no. 5, pp. 635–639, 2005.

[8] G. S. Zan and T. Sun, "Vegetation cover change on Hulun Buir grassland," *Forest Resources Management*, no. 1, pp. 44–48, 2011.

[9] P. Zhang, E. D. Hasi, S. Wang, and S. Zhang, "Zonation of vegetation on depositional area of blowout in Hulun Buir grassland," *Journal of Natural Resources*, vol. 23, no. 2, pp. 237–244, 2008.

[10] L. Man, E. D. Hasi, P. Zhang et al., "Micro-community characteristics of vegetations on blowouts and depositional areas of HulunBuir Grassland, Inner Mongolia," *Chinese Journal of Applied Ecology*, vol. 19, no. 10, pp. 2177–2181, 2008.

[11] H. S. Du, E. D. Hasi, Y. Yang et al., "Land-cover landscape changes of blowouts distribution in the HulunBuir Grassland," *Journal of Arid Land Resources and Environment*, pp. 129–134, 2013.

[12] S. G. Fryberger and G. Dean, "Dune forms and wind regime," in *A Study of Global Sand Seas*, E. D. McKee, Ed., pp. 137–169, U.S. Geological Survey Publications Warehouse, 1979.

[13] Y. J. Fang, J. F. Zhao, Y. P. Guo et al., "Magnitude deviations of sand drift potential calculation in the 'FRYBERGER' model: a case of the Taklimakan Desert," *Arid Land Geography*, no. 1, pp. 95–112, 2015.

[14] P. D. Jungerius, J. V. Witter, and J. H. van Boxel, "The effects of changing wind regimes on the development of blowouts in the coastal dunes of The Netherlands," *Landscape Ecology*, vol. 6, no. 1-2, pp. 41–48, 1991.

[15] P. A. Gares and K. F. Nordstrom, "A cyclic model of foredune blowout evolution for a leeward coast: Island Beach, New Jersey," *Annals of the Association of American Geographers*, vol. 85, no. 1, pp. 1–20, 1995.

[16] J. S. Olson, "Lake michigan dune development 2. Plants as agents and tools in geomorphology," *The Journal of Geology*, vol. 66, no. 4, pp. 345–351, 1958.

[17] E. C. Hu, X. J. Wang, and W. J. Zhang, "Analysis on spatial pattern of blowouts in otindag sandy grassland based on ALOS data," *Desert and Desertification*, vol. 33, no. 3, pp. 662–667, 2013.

[18] C. H. Hugenholtz and S. A. Wolfe, "Morphodynamics and climate controls of two aeolian blowouts on the northern Great

Plains, Canada," *Earth Surface Processes and Landforms*, vol. 31, no. 12, pp. 1540–1557, 2006.

[19] G. S. Fraser, S. W. Bennett, G. A. Olyphant et al., "Windflow circulation patterns in a coastal dune blowout, south coast of Lake Michigan," *Journal of Coastal Research*, vol. 14, no. 2, pp. 451–460, 1998.

[20] M.-L. Byrne, "Seasonal sand transport through a trough blowout at Pinery Provincial Park, Ontario," *Canadian Journal of Earth Sciences*, vol. 34, no. 11, pp. 1460–1466, 1997.

[21] P. A. Hesp and R. Hyde, "Flow dynamics and geomorphology of a trough blowout," *Sedimentology*, vol. 43, no. 3, pp. 505–525, 1996.

Hindawi
Mathematical Problems in Engineering
Volume 2017, Article ID 9745264, 9 pages
https://doi.org/10.1155/2017/9745264

Research Article

Analysis of the Spatial Variation of Soil Salinity and Its Causal Factors in China's Minqin Oasis

Tana Qian,[1] Atsushi Tsunekawa,[1] Tsugiyuki Masunaga,[2] and Tao Wang[3]

[1]*Arid Land Research Center, Tottori University, 1390 Hamasaka, Tottori City 680-0001, Japan*
[2]*Life and Environmental Science, Shimane University, 1060 Nishikawatsu, Matsue City 690-8504, Japan*
[3]*Key Laboratory of Desert and Desertification, Northwest Institute of Eco-Environment and Resources, Chinese Academy of Sciences, 320 West Donggang Road, Lanzhou 730000, China*

Correspondence should be addressed to Tana Qian; qian.tana@gmail.com

Received 30 November 2016; Accepted 26 January 2017; Published 15 March 2017

Academic Editor: Hajime Seya

Land salinization and water resource deterioration negatively affect irrigated agriculture in arid and semiarid areas by limiting the area of arable land and reducing crop yields. The spatial variation of soil salinity is affected by many factors, and their interactions are complex. In this study, we utilized grey relational analysis to evaluate the factors that affect soil salinity in China's Minqin Oasis and the interactions among them and then ranked the significance of their impacts on soil salinity for different land use and cover types. The data used in this study include data obtained from soil chemical analyses based on field sampling in 2015 and hydrological data obtained from local government agencies. We found that the main factors that affect soil salinity in the region's sparse grassland are groundwater salinity and vegetation cover; the least important factor was the distance to the nearest irrigation canal. For cropland, the most important factors were the distance to irrigation canals and hydrological factors. By accounting for these factors, it should be possible to manage the region's limited natural water and soil resources more efficiently, while allowing remediation of existing salinized land and helping to maintain sustainable agriculture in this arid land.

1. Introduction

In arid northwestern China, a severe water scarcity and growing soil salinization are closely related problems that are strongly affecting agricultural development and sustainability. These problems are especially severe in oasis ecosystems, where the water scarcity and soil salinization have caused an unrepairable loss of productive land within the past few decades and have threatened the sustainability of agriculture and ecosystem stability [1–3].

The Shiyang River Basin, which lies east of the Hexi Corridor in Gansu Province, has been one of China's most important traditional agricultural regions since 121 BC. The Shiyang River is the region's primary water resource. It flows from glacial headwaters in the Qilian Mountains to its lower reaches, in a region called the Minqin Oasis, which is surrounded by both gobi (gravel) deserts and sandy deserts [4]. Since the late 1950s, China's government has promoted increased agricultural practices to support the region's rapid population growth. This has led to a large expansion of cultivation, accompanied by deforestation and reclamation of the region's grasslands. The requirement for irrigation of crops in this arid region has expanded rapidly. Together, these changes have contributed to the degradation of oasis ecosystem services such as freshwater provision and desertification control [5, 6].

Due to a lack of long-term water resources planning in the Shiyang River Basin, the distribution of water resources between the river's middle and lower reaches is heavily unbalanced, with excessive withdrawals of water upstream of the oasis [7]. In addition, the water supply to the Minqin Oasis is controlled by management of the giant upstream Honyashan Reservoir and the construction of an extensive network of irrigation canals. According to data from the Gansu Shiyang River Basin Administrative Bureau, the surface runoff flowing into the Minqin Oasis from the upper

and middle reaches of Shiyang River has decreased rapidly, from 4.931×10^8 m^3 per year in the 1960s to 1.218×10^8 m^3 per year in the 2000s. To meet the high water demand of the Minqin Oasis, groundwater became the primary water resource to support large-scale irrigation, which led to excessive extraction of the groundwater. This, in turn, has had serious environmental consequences, such as strong mineralization of the groundwater, increasing depth to the groundwater table, and rapid salinization of soils [8]. The depth to groundwater in the oasis has increased at an average rate of 0.47 m per year since 1981 [9].

Furthermore, the increasing depth to the groundwater table has caused an increase in the concentrations of dissolved minerals in the groundwater [8]. The reuse of saline water for crop irrigation, combined with poor drainage systems, has exacerbated the problem and degraded the hydrological ecosystem. The average total dissolved solids (TDS) content of groundwater in the Minqin Oasis reached 6 g/L, with maximum of over 10 g/L [9]. According to China's national standards for drinking-water quality, the maximum concentration level is 1000 mg/L.

In addition, due to the persistent water scarcity and mineralization, many branches of the Shiyang River have gradually dried out and communities of natural vegetation have become seriously degraded or have disappeared [10]. The natural bush communities and man-made shrub plantations fix the region's abundant deposits of sand and provide windbreaks that reduce the erosive power of the wind; the loss of this vegetation due to a lack of sufficient water increases the risk of desertification. In addition, the wetland vegetation that once grew in large areas of the oasis has declined as the wetlands have dried out. These problems have been exacerbated by an improved system of irrigation canals, which has also contributed to increases in the depth to the groundwater table both by increasing water withdrawals and by reducing groundwater recharge; unlike the previously unlined canals, the concrete-lined canals lose relatively little water into the surrounding soil [9]. The effects of the processes leading to degradation of vegetation in the oasis have ultimately resulted in increased sandy desertification [11].

Damage to the environment has been extensive and represents a serious threat to the sustainability of social and economic development in the Minqin Oasis. In agriculture, saline irrigation water not only restricts the growth of all crops other than those with high salt-tolerance and drought-tolerance, but also aggravates the formation of secondary salinization, which results from salt accumulation in the soil under the strong evaporation produced by the dry atmosphere. Irrigation in Minqin Oasis farmland is controlled by canals lined with cement cobble and concrete to improve irrigation efficiency. However, in contrast with the original unlined canals, this leads to reduced groundwater recharge and contributes to the deepening groundwater table [4]. Flood and furrow irrigation are widely used in the Minqin Oasis, and together they exacerbate the process of secondary salinization. Unfortunately, there is insufficient freshwater available to leach the accumulated salt below plant rooting depth throughout the oasis.

As a result of these factors, the land area that is experiencing severe secondary salinization has increased in the oasis. The average salt content of the soil is up to 16.7 g/kg [11]. More than 59% of the irrigated agricultural land has been abandoned because of the combination of water scarcity and the adverse effects of secondary salinization [12]. From 2005 to 2011, the local government organized emigration of two subvillages in Huqu District, with a total population of 1868 (1000 people for 2005, 250 people for 2006, 534 people for 2007, and 84 people for 2011), which has suffered from a growing water scarcity, sand invasion, and soil salinization [9]. Since the 1960s, 2.52×10^4 km^2 of farmland in the oasis has been abandoned [5]. However, the low income of the farmer households who were forced to emigrate and the sustainability of water usage in their resettlement area remain important social, economic, and environmental issues [13].

Because of its severity, land salinization has received much attention from researchers. Although the salinization is affected by many factors [1], the interaction among the factors responsible for different types and intensities of salinization of different land use and cover types is still inadequately understood. To provide this information, we began a study of the Minqin Oasis. Our main objectives were to (a) analyze the spatial variability of soil salinity, (b) analyze the factors that affect soil salinity, and (c) rank the importance of these factors based on land use and cover types. To accomplish these goals, we applied the technique of grey relational analysis to the field survey data, supported by geographical information system (GIS) tools. We also took advantage of government statistical records and remote sensing data in our statistical analysis and relational factor analysis.

2. Methods

2.1. Study Area. The Huqu region is located on the downstream alluvial plain of the Shiyang River Basin, in the northern part of the Minqin Oasis. The terrain is relatively flat, with an elevation that ranges from 1254 to 1376 m asl. It covers an area of 1430 km^2 and is located between 38°42′N and 39°10′N and between 103°19′E and 103°49′E (Figure 1(a)). The region is surrounded by the Badan Jaran Desert to the west and north and by the Tengger Desert to the east. The region has a temperate continental arid climate, with a mean annual temperature of 7.8°C (monthly means range from −8.6°C in January to 21.8°C in August). Total annual precipitation averages 110 mm, but the potential evaporation ranges between 2000 and 2600 mm. The mean annual wind speed is 2.8 m/s, but the highest wind speed can reach 23 m/s, and winds strong enough to entrain sand occur 139 days per year on average [9].

The main soil types are grey-brown desert soil, sandy soil, solonchak, meadow soil, and anthropogenic-alluvial soil [4]. The main soil type in croplands is a silty clay or a sandy silt. The major crops include cereals (spring wheat, summer maize) and cash crops (cotton, melon, and fennel). Native vegetation includes drought-resistant shrubs, salt-resistant shrubs, and perennial sand-loving herbaceous plants (e.g., *Elaeagnus angustifolia*, *Populus euphratica*, *Salix purpurea,*

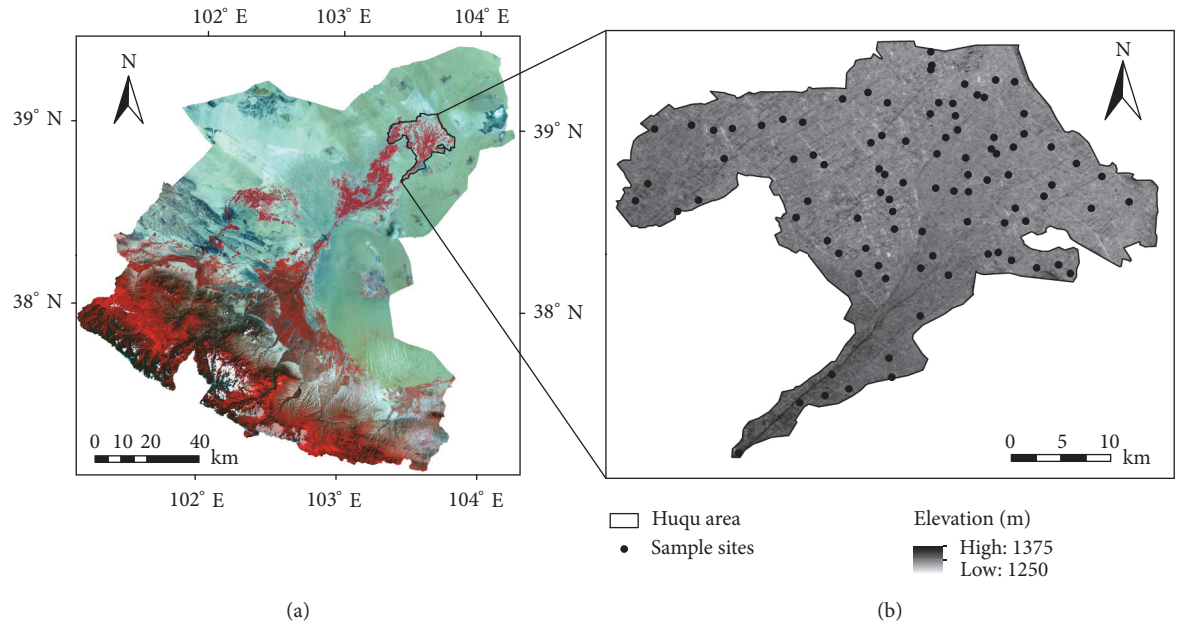

Figure 1: The location of the study area (the Huqu region) within Shi Yang River Basin. (b) Locations of the 94 soil samples analyzed in the present study.

and *Agriophyllum squarrosum*) [14]. Because most of the grassland area in the oasis was suitable for cultivation, very little natural grassland remains; however, sparse grassland has developed where cultivated land was abandoned for more than decades.

We chose the Huqu region as our study area because of the existence of both the original salt accumulation (primary salinization) and irrigation-caused salt accumulation (secondary salinization). The area has been suffering from severe ecological problems for decades, including high mineralization of groundwater, salinization, and desertification characterized by sand invasion, as well as from social and economic pressures caused by ecological emigration and cropland abandonment.

2.2. Soil Sampling and Laboratory Analysis. The field dataset was obtained during April 2015, when the salt concentration in surface soils reaches its maximum in this region. In April, the low precipitation combines with a high evaporation rate to cause salt from deeper soil layers to migrate upwards and accumulate near the surface of the soil [15]. We obtained 94 surface soil samples (Figure 1(b)) to a depth of 10 cm from unused land (9 samples from shrubland, 5 samples from abandoned land, 46 samples from sparse grassland, and 13 samples from saline wasteland) and cropland (used to grow wheat, sunflower, alfalfa, goji berry, and fennel). The sites were selected based on the results of previous soil salinity studies and Google Earth images, and each sample site represented an area of 90 m × 90 m. For each sample point, we combined five topsoil samples into a single composite sample, which we used to represent the value of the soil chemical parameters at that site. The location of each sample point was recorded with a MAP64SJZ GPS receiver (Garmin, Olathe, KS, USA) and we photographed the site. The characteristics of the soil surface, the land use and cover types surrounding the site, and the vegetation cover were recorded in a field notebook. We also consulted local farmers to learn about historical land use and cover types.

Soil moisture was assessed during the soil sample collection. The samples were sealed into weighed, empty specimen boxes and their total weights were measured. When we returned to the laboratory, we opened the boxes and oven-dried the samples for 24 hours at 105°C together with the boxes. We calculated the soil moisture content (SMC) as a percentage of the dry soil weight.

For the chemical analysis, the samples were air-dried, crushed, and passed through a 1 mm sieve to remove large particles and plant residues. To quantify the soil salinity, we measured the electrical conductivity ($EC_{1:5}$) in deionized distilled water at 1 : 5 g/mL soil : water ratio. We calculated the frequency distribution of these values and several associated parameters: the mean, median, standard deviation, skewness, kurtosis, range, and maximum and minimum values. We used version 23 of the SPSS software (http://www.ibm.com/analytics/us/en/technology/spss/) for our statistical analysis.

We also measured the soil pH. To make the pH measurements better reflect the water content of the soil under field conditions, we used a 1 : 1 g/mL soil solution [16].

2.3. GIS and Map Preparation. Maps of the distribution of soil $EC_{1:5}$ were prepared to visualize the results at the 94 sample sites. We used version 10.2.1 of the ArcView software (http://www.esri.com). We also visualized the layout of the irrigation canal network, depths to the water table, and TDS data for the water using ArcView. Additional data included an ASTER Global Digital Elevation Model (ASTER GDEM)

Table 1: Definitions of the affecting factors for the reference series (soil $EC_{1:5}$).

Affecting factor	Definition	Measurement
X_i (1)	Elevation of the sample site	Distance above mean sea level
X_i (2)	Distance to the nearest irrigation canal	The distance between the sample point and the nearest canal
X_i (3)	Compound topographic index (CTI)	Defined in Section 2.3
X_i (4)	Vegetation cover	The % coverage of the soil by vegetation
X_i (5)	Groundwater level	Distance from the ground surface to the top of the groundwater table
X_i (6)	Groundwater salinity	Total dissolved salt content in the groundwater

acquired from https://gdex.cr.usgs.gov/gdex/ at a 30-m resolution. To describe the topographic characteristics of the sample sites, we derived the compound topographic index (CTI), which is widely used in hydrology and terrain-related applications, from the DEM data [17]. CTI is a compound index that is calculated using two primary topographic attributes [18]; it is also known as the steady-state wetness index when it is used to quantify the catenary landscape position [19]. We used the following equation to calculate the CTI values:

$$\mathrm{CTI} = \ln\left(\frac{\alpha}{\tan\beta}\right), \tag{1}$$

where α represents the catchment area per pixel, and β represents the slope gradient. Low CTI values represent small catchments, steep slopes, and upper catenary positions. High CTI values represent large catchments, gentle slopes, and lower catenary positions with a higher capacity for water accumulation and wetness [20].

2.4. Grey Relation Analysis. A grey relationship is a relationship among different types of data series often with different units of measurement when there is considerable uncertainty and an unsatisfactory sample size [21]. Grey relational analysis (GRA) is a way to identify the key factors that control a system and quantify the influence that each factor exerts on a reference variable [22]. It is often applied in studies that have an insufficient sample size and uncertainty about whether the data is truly representative [21, 23]. The basic idea behind GRA is to compute the strength of the relationship between variables by examining the degree of proximity for certain geometrical figures or the degree of correlation between curves [22]. In this study, we employed GRA to quantify the influence of several factors on the soil salinity of the 94 samples from the Huqu area.

In GRA, the original data series are divided into two types of series: a reference series that will be compared with all other variables and one or more affecting series (one per variable that potentially affects the values in the reference series). The grey strength of the relationship is calculated to represent the relative proximity of two series. A discrete sequence of ranks can then be generated, with the ranks depending on the strengths of each factor's relationship to the reference series. If the strength of the relationship for one affecting series is higher than that of the others, the former series is considered to have a greater influence than the others on the reference series [24].

The first step in GRA is to generate the reference series and the affecting series. Since the range of values and the units of measurement in one data series may differ from those in other series, the original data are first normalized by dividing each value by the mean value in the series, thereby producing a range of values from 0 to 1, and are then used to calculate the grey relational coefficient between the reference series and the affecting series [25]. The reference series is represented as $x_0(k) = x_0(1), x_0(2), \ldots, x_0(n)$, where k is the number of sample data, with $k \in (1, 2, \ldots, n)$, and n is the number of factors. Each affecting series is represented as $x_i(k) = x_i(1), x_i(2), \ldots, x_i(n)$, where i represents the affecting series. In this study, we used the soil $EC_{1:5}$ (dS/m) as the reference series. Based on our review of the research literature and the mechanisms of salinization, as well as based on data availability, we selected six affecting factors for use as the affecting series (Table 1).

The grey relational coefficient for two series, $\zeta_i(k)$, can be calculated as follows:

$$\zeta_i(k) = \frac{\Delta_{\min} + \zeta\Delta_{\max}}{\Delta_{0i}(k) + \zeta\Delta_{\max}}, \tag{2}$$

where $\Delta_{0i}(k) = \|x_0(k) - x_i(k)\|$ is the absolute difference between the reference factor $x_0(k)$ and the corresponding affecting factor $x_i(k)$; ζ represents a grey parameter with a value between 0 and 1, and that is often assigned a value that equaled 0.5, a value that is commonly used [26]; and $\Delta_{\min}$ and $\Delta_{\max}$ represent the smallest and biggest values, respectively, among all of the $\Delta_{0i}(k)$ values.

The grey relational grade, γ_i, for the relationship between each affecting series $x_i(k)$ and the reference series $x_0(k)$ can be calculated by averaging the grey relational coefficient corresponding to each affecting factor:

$$\gamma_i = \frac{1}{n}\sum \zeta_i(k). \tag{3}$$

The ranking of the affecting factors is then conducted based on the computed grey relational grades. As mentioned earlier, a higher value of the grey relational grade indicates a stronger relationship between the two series and suggests that the corresponding affecting factor is closer to the reference series than other affecting factors [27].

3. Results and Discussion

3.1. Statistical Analysis. Figure 2 shows the frequency distribution and descriptive statistics for $EC_{1:5}$ of the cropland and

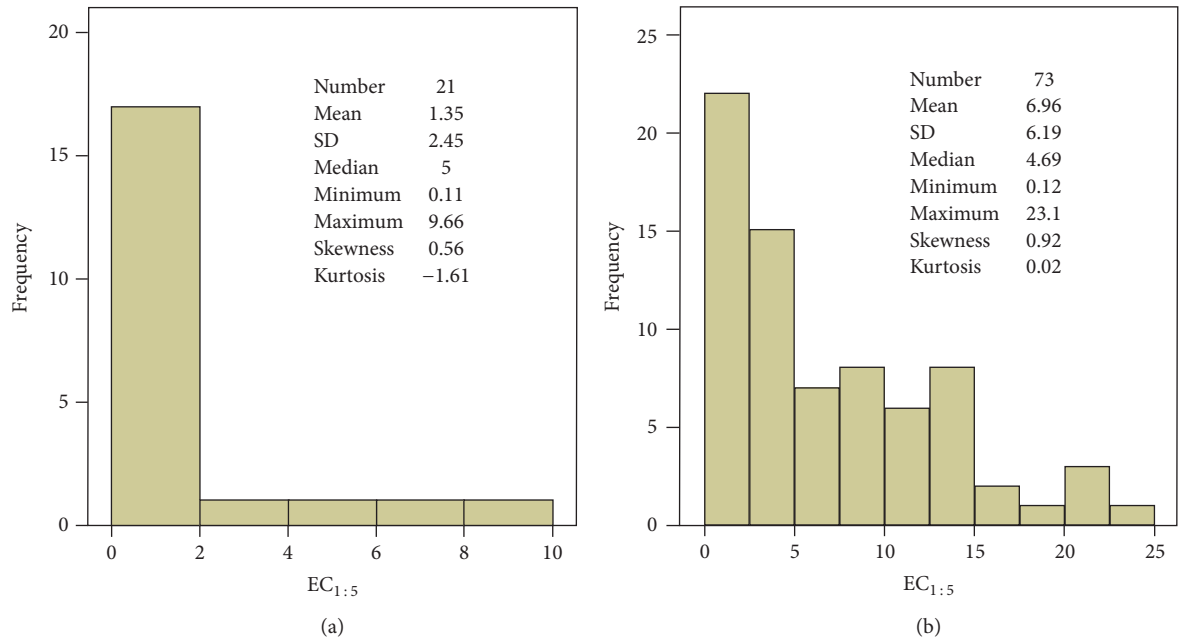

FIGURE 2: Histograms of $EC_{1:5}$ values for samples from (a) cropland ($n = 21$) and (b) all other land types ($n = 73$) and their associated descriptive statistics.

other land types. 21 soil samples were collected from cropland during the spring, which explains why many samples have a low $EC_{1:5}$ value. 73 soil samples were collected from other land types (shrubland, abandoned land, sparse grassland, and saline wasteland). Figure 2 also shows wide variation in the $EC_{1:5}$ data, with values ranging from 0.11 to 23.1 dS/m (two orders of magnitude).

To understand the spatial distribution of the salinity levels, we mapped the distribution of soil $EC_{1:5}$ using ArcView based on equal interval method (Figure 3). As the distribution map shows, most of the samples with high $EC_{1:5}$ were distributed at the margins of the oasis, but some were distributed in the center; in contrast, the samples with lower $EC_{1:5}$ were distributed throughout the oasis.

3.2. Differences in Soil Salinity among the Different Land Use and Cover Types. To further explore the characteristics of the distribution of the soil $EC_{1:5}$ values in the Huqu area in relation to the land management in the study area, we classified the 94 samples into the five main land use and cover types: cropland, shrubland, abandoned land, sparse grassland, and saline wasteland. Table 2 summarizes the measured values of the various properties of the soil samples.

The coefficient of variation (CV) is the ratio of the standard deviation to the mean and is often used as a general index of variability among the samples [28]. A CV value lower than 0.1 (10%) indicates low variability, whereas a CV value higher than 1.0 (100%) indicates high variability; intermediate values have moderate variability [29]. Table 2 shows that the CV values of $EC_{1:5}$ for cropland and shrubland were highly variable, with CV values greater than 1.0, which suggests that $EC_{1:5}$ and its distribution pattern are strongly

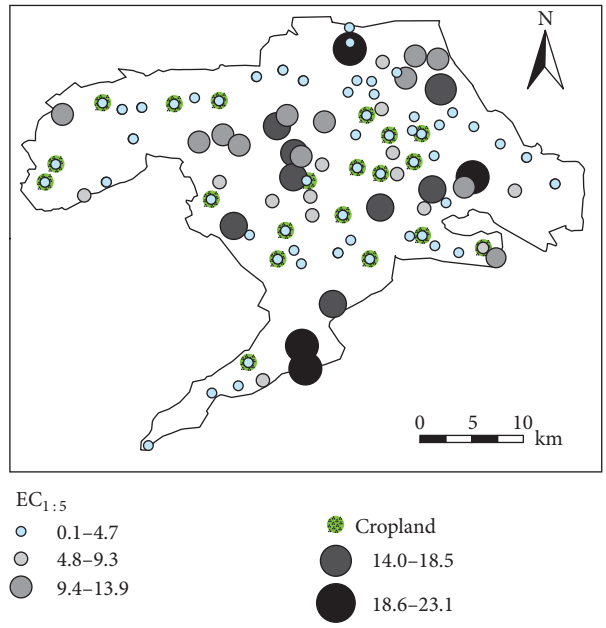

FIGURE 3: Map of the distribution of $EC_{1:5}$ values for the 94 soil samples.

influenced by human driving factors such as irrigation and farming activities as well as by the irrigation canal system. Despite regular irrigation, some of the cropland soil $EC_{1:5}$ values reached 9.66 dS/m, which indicates the existence of a secondary salinization problem. The shrubland is mainly artificial and has resulted from a local policy to replace cropland with shrubs to combat desertification. The low

Table 2: Descriptive statistics for the soil parameters, by land use and cover class (LUCC)[a].

LUCC (sample size)	Parameters	Range	Mean	SD	CV	LUCC description
Cropland (21)	$EC_{1:5}$ (dS/m)	0.11–9.66	1.35	2.39	1.77	This class includes land covered with crops (e.g., fennel, cotton, alfalfa, wheat, maize, sunflower, and goji berry), newly cultivated land, and fallow land.
	$pH_{1:1}$	7.82–8.76	8.32	0.24	0.03	
	SMC (%)	0.86–13.81	7.15	2.77	0.39	
	GW salinity (g/L)	2.11–27.39	14.59	6.09	0.42	
	GW table depth (m)	5.32–32.33	18.61	7.99	0.43	
Shrubland (9)	$EC_{1:5}$ (dS/m)	0.12–14.89	3.23	4.45	1.38	Land with woody vegetation, with a total shrub cover that exceeds 10% of the surface. Some of this land resulted from a local policy of replacing cropland with shrubs to combat desertification.
	$pH_{1:1}$	8.05–8.99	8.38	0.31	0.04	
	SMC (%)	1.47–6.03	3.19	1.61	0.50	
	GW salinity (g/L)	9.68–27.91	15.53	6.38	0.41	
	GW table depth (m)	7.17–29.95	18.47	8.34	0.45	
Abandoned land (5)	$EC_{1:5}$ (dS/m)	0.21–1.41	0.99	0.41	0.42	Land has been abandoned for 5 to 20 years, with vegetation cover <5%.
	$pH_{1:1}$	7.96–8.83	8.35	0.3	0.04	
	SMC (%)	1.54–4.55	2.66	1.07	0.40	
	GW salinity (g/L)	10.06–18.44	13.22	3.45	0.26	
	GW table depth (m)	10.89–28.78	20.05	6.66	0.33	
Sparse grassland (46)	$EC_{1:5}$ (dS/m)	0.15–21.44	6.18	5.01	0.81	Land has been abandoned for more than 20 years. Dominated by grasses and salt-tolerant grasses, with vegetation cover of 5% to 20%.
	$pH_{1:1}$	7.89–8.75	8.34	0.22	0.03	
	SMC (%)	0.93–10.18	4.08	2.14	0.52	
	GW salinity (g/L)	6.51–23.27	14.12	4.19	0.30	
	GW table depth (m)	7.18–36.05	22.70	6.33	0.28	
Saline wasteland (13)	$EC_{1:5}$ (dS/m)	8.28–23.10	14.6	5.12	0.35	Land with a salt crust at the soil surface. Dominated by natural salt-tolerant grasses, with vegetation cover >20%. Naturally salt-affected areas are distributed at the margins of the oasis.
	$pH_{1:1}$	7.88–8.58	8.36	0.22	0.03	
	SMC (%)	3.91–14.96	8.87	3.09	0.35	
	GW salinity (g/L)	7.55–19.97	11.20	3.39	0.30	
	GW table depth (m)	6.76–29.42	15.80	8.29	0.52	

[a]SMC represents the soil moisture content as a percentage of the dry soil weight. GW represents the groundwater.

Table 3: Grey relational grade (γ) and the resulting ranking for each affecting factor.

Reference factor	Affecting factor	Definition	γ	Ranking	Relationship[a]
X_0 $EC_{1:5}$	X_i (2)	Distance to irrigation canals	0.814	1	Positive
	X_i (6)	Groundwater salinity	0.810	2	Negative
	X_i (3)	CTI	0.804	3	Positive
	X_i (1)	Elevation of the sample site	0.801	4	Negative
	X_i (5)	Groundwater level	0.798	5	Negative
	X_i (4)	Vegetation cover	0.771	6	Negative

[a]Positive relationships mean that a high value of the affecting factor increased $EC_{1:5}$; negative relationships mean that a high value decreased $EC_{1:5}$.

Table 4: Grey relational grade (γ) for each affecting factor and the resulting ranking for the two main land use and cover types.

Reference factor	Affecting factor	Definition	γ	Ranking	Relationship[a]
		Cropland			
X_0 $EC_{1:5}$	X_i (2)	Distance to irrigation canals	0.847	1	Positive
	X_i (5)	Groundwater level	0.787	2	Negative
	X_i (3)	CTI	0.783	3	Positive
	X_i (1)	Elevation of the sample site	0.780	4	Negative
	X_i (6)	Groundwater salinity	0.777	5	Positive
	X_i (4)	Vegetation cover	0.760	6	Negative
		Sparse grassland			
X_0 $EC_{1:5}$	X_i (6)	Groundwater salinity	0.755	1	Positive
	X_i (4)	Vegetation cover	0.742	2	Positive
	X_i (1)	Elevation of the sample site	0.714	3	Negative
	X_i (5)	Groundwater level	0.711	4	Positive
	X_i (3)	CTI	0.708	5	Negative
	X_i (2)	Distance to irrigation canals	0.662	6	Negative

[a]Positive relationships mean that a high value of the affecting factor increased $EC_{1:5}$; negative relationships mean that a high value decreased $EC_{1:5}$.

soil moisture content of the shrubland provides evidence of a water scarcity problem. This is consistent with previous research, which showed that shrubs have died in large areas because the groundwater level fell below the level their roots can reach. The maximum $EC_{1:5}$ value of shrubland reached 14.89 dS/m, which indicated large amounts of salt accumulation in the topsoil as a result of a high evaporation rate combined with low rainfall and mineralization of the groundwater.

The CV values of $EC_{1:5}$ for abandoned land, sparse grassland, and saline wasteland were moderate (between 0.1 and 1.0). These land use and cover types were less strongly affected by human activities. Abandoned land was defined as land that had been abandoned for 5 to 20 years, and sparse grassland has been abandoned for more than 20 years and has begun to develop a grassland ecosystem. The majority of the soil $EC_{1:5}$ values for abandoned land were lower than those for sparse grassland, which indicated that soil salinity increased with increasing duration of abandonment. Compared with sparse grassland, the salinity level and moisture content of soils in the abandoned land were lower.

The CV values for SMC for all land use and cover types showed moderate variability (0.1 to 1.0). The $pH_{1:1}$ of the soil of the study areas ranged from 7.82 to 8.99 (slightly alkaline), and its low CV values (<0.1) indicated slight variation. The mean $pH_{1:1}$ for all land use and cover types was greater than 8, which indicated most of the soil samples are weakly alkaline. The high groundwater salinity (>11 g/L) content and deep groundwater table depth (>15 m) indicated poor water quality and poor access to water, and their low CV values indicate moderate spatial variability.

3.3. Impact Factors. Many factors, including soil factors, hydrological factors, management factors, and other factors, affected the soil salinization process and its spatial distribution in the Huqu area. Interactions among these factors are complex [30]. Based on the calculated value of the grey relational grade (γ), we determined the order of each affecting factor for all 94 samples combined. As shown in Table 3, these values range from 0 to 1, and we obtained the following ranking of the factors based on the grey relational grades: distance to the nearest irrigation canal > groundwater salinity > CTI > elevation of the sample site > groundwater level > vegetation cover.

Analyzing the grey relationships between the affecting factors and soil $EC_{1:5}$ for specific land use and cover types will help us to better understand the interaction between these factors and the salinization processes. To do this, we selected the two main land use and cover types and applied GRA to their affecting factors (Table 4).

Table 4 shows the calculated grey relational grades for the affecting factors for cropland and sparse grassland. For the cropland soil samples, the distance to the nearest irrigation canals was the most important factor for soil $EC_{1:5}$ and had a positive relationship with soil $EC_{1:5}$. The greater the distance between the sample sites and the canal, the higher the soil $EC_{1:5}$ content. This is because the use of fresh river water as an irrigation source, coupled with the drainage system, greatly, decreased salt accumulation in the topsoil. In contrast, the groundwater salinity had a negative relationship with soil $EC_{1:5}$, which was mainly because farmers combined fresh river water with groundwater to irrigate the croplands. The higher groundwater salinity is, the less amount of it can be used for irrigation, and the more river water must be consumed for irrigation, leading to accelerated salt leaching and reducing the salt accumulation in the soil. Some samples were taken from the margins of the oasis, where the groundwater salinity was strongly affected by highly saline desert groundwater. In addition, the groundwater table depth was at least 5.3 m (Table 2) in those areas with high groundwater salinity. Because this large distance interrupts the capillary rise of water from the groundwater table to the soil surface, salt movement from the groundwater into the topsoil was reduced [31]. The vegetation cover had the weakest impact on the soil $EC_{1:5}$ of cropland, mainly because little vegetation had developed at the beginning of the growing season, when we obtained our soil samples.

For sparse grassland, distance to the nearest canal was the weakest affecting factor. This was mainly because the sparse grassland was close to a natural condition because of low intervention by human activities (i.e., after abandonment for more than 20 years). The groundwater salinity had a strong positive relationship with soil $EC_{1:5}$ for sparse grassland, which indicated that local-scale hydrological factors affected the distribution and variation of surface soil salinity. The sparse grassland had been abandoned for more than 20 years, and most of the sparse grassland had suffered from secondary salinization. Some of the land has been abandoned for more than 40 years; severe adverse effects of intensive agricultural practices during the 1950s and 1960s made the land unsuitable for cultivation. Excessive groundwater extraction for irrigation caused a rapid deepening of the groundwater table and mineralization of the groundwater. The use of groundwater with a high salt content, coupled with strong evaporation, accelerated salt accumulation in the topsoil. This caused rapid degradation of productive land and, eventually, abandonment of this land. The soil $EC_{1:5}$ values in this land could reach as high as the values in saline wasteland. The vegetation cover was the second-strongest affecting factor due to dense growth of halophytes in salt-affected areas [32].

4. Conclusions

Salt-affected soils were distributed throughout the Huqu area. Most of the cropland had relatively low soil salinity, but several samples had high $EC_{1:5}$, which indicates a high potential for secondary salinization. The saline wasteland had some of the highest salinity values and was concentrated mainly at the margin of the oasis, where there was no irrigation. Secondary salinized land was mainly located in areas of sparse grassland inside the oasis. The CV values of soil $EC_{1:5}$ for cropland and shrubland were greater than 1.0, which indicates that soil $EC_{1:5}$ and its distribution were strongly influenced by human activities.

Land use practices also strongly influenced the distribution of salt-affected soils. The abandoned cropland had low salinity, but the long-abandoned cropland (which became sparse grassland) tended to have high salinity, sometimes reaching values as high as those in saline wasteland. In addition, transforming cropland to shrubland could result in further land degradation in Huqu area; due to the water scarcity and poor water quality, this change led to higher $EC_{1:5}$ and lower SMC. Improved management should focus on these lands to prevent further degradation.

The distance to the nearest irrigation canal was the most important factor for determining the salinity of cropland. The access to fresh river water and good drainage, combined with a deep groundwater table, prevented salt accumulation in the topsoil. However, the use of highly saline water and improper drainage and soil management will increase the risk of secondary salinization in irrigated soils. Therefore, proper irrigation methods, an improved drainage system, and effective soil management will be necessary to prevent non-salinized cropland from undergoing secondary salinization and to remediate existing salinized cropland.

The small sample size in this study may have made the data less reliable. However, the use of GRA should have mitigated this problem. Nonetheless, obtaining more and better data on water and soil properties would improve the ability to support management of the water and soil resources of the Minqin Oasis, particularly if combined with remote sensing and GIS techniques to improve our ability to detect the distribution of salt-affected soils over larger areas.

Competing Interests

The authors declare that there is no conflict of interests regarding the publication of this paper.

Acknowledgments

The authors would like to thank International Platform for Dryland Research and Education, Tottori University, for financial support; Professor Xue Xian, Professor Wang Ninglian, Dr. Huang Cuihua, Dr. Liao Jie, and Dr. Luo Jun from Northwest Institute of Eco-Environment and Resources, CAS, for providing them with the equipment and the assistance in the field; the Minqin Bureaus of Water Resources Management for providing hydrological data; Professor Kitamura Yoshinobu and Professor Fujimaki Haruyuki from Tottori University for the useful advices and equipment; Geoff Hart for helpful advice on early version of this paper. The Landsat dataset is provided by Environmental and Ecological Science Data Center for West China, National Natural Science Foundation of China (http://westdc.westgis.ac.cn).

References

[1] P. Rengasamy, "World salinization with emphasis on Australia," *Journal of Experimental Botany*, vol. 57, no. 5, pp. 1017–1023, 2006.

[2] W. Genxu and C. Guodong, "Water resource development and its influence on the environment in arid areas of China-the case of the Hei River basin," *Journal of Arid Environments*, vol. 43, no. 2, pp. 121–131, 1999.

[3] C. Tian and H. Zhou, "The proposal on control of soil salinization and agricultural sustainable development in the 21st century in Xinjian," *Arid Land Geography*, vol. 23, no. 2, pp. 177–181, 2000.

[4] S. Danfeng, R. Dawson, and L. Baoguo, "Agricultural causes of desertification risk in Minqin, China," *Journal of Environmental Management*, vol. 79, no. 4, pp. 348–356, 2006.

[5] Y. Ma, S. Fan, L. Zhou, Z. Dong, K. Zhang, and J. Feng, "The temporal change of driving factors during the course of land desertification in arid region of North China: the case of Minqin County," *Environmental Geology*, vol. 51, no. 6, pp. 999–1008, 2007.

[6] R. T. Munang, I. Thiaw, and M. Rivington, "Ecosystem management: tomorrow's approach to enhancing food security under a changing climate," *Sustainability*, vol. 3, no. 7, pp. 937–954, 2011.

[7] G. Schneier-Madanes and M. F. Courel, *Water and Sustainability in Arid Regions: Bridging the Gap between Physical and Social Sciences*, Springer, Dordrecht, The Netherlands, 2009.

[8] D. K. Vajpeyi, M. Bondes, A. M. Buainain et al., *Climate Change, Sustainable Development, and Human Security: A Comparative Analysis*, Lexington Books, 2013.

[9] Local Chronicles Office of Minqin County, *Annals of Shi Yang River*, Wuwei Guangxin Kemao Printing Co. Ltd, 2014.

[10] Z. L. Huo, S. Y. Feng, S. Z. Kang, S. J. Cen, and Y. Ma, "Simulation of effects of agricultural activities on groundwater level by combining FEFLOW and GIS," *New Zealand Journal of Agricultural Research*, vol. 50, no. 5, pp. 839–846, 2007.

[11] J. Ma and H. Wei, "The ecological and environmental problems caused by the excessive exploitation and utilization of groundwater resources in the Minqin Basin, Gansu province," *Arid Zone Research*, vol. 20, no. 4, pp. 261–265, 2002.

[12] C. Guo, L. Wang, F. Han et al., "Studies of soil physical property on different abandoned lands in the Minqin Oasis, downstream of the Shiyang River," *Agricultural Science & Technology*, vol. 16, no. 5, pp. 1014–1018, 2015.

[13] Y. Li, D. López-Carr, and W. Chen, "Factors affecting migration intentions in ecological restoration areas and their implications for the sustainability of ecological migration policy in arid Northwest China," *Sustainability*, vol. 6, no. 12, pp. 8639–8660, 2014.

[14] S. Kang, X. Su, L. Tong et al., "The impacts of human activities on the water-land environment of the Shiyang River basin, an arid region in northwest China," *Hydrological Sciences Journal*, vol. 49, no. 3, p. 427, 2004.

[15] A. A. Elnaggar and J. S. Noller, "Application of remote-sensing data and decision-tree analysis to mapping salt-affected soils over large areas," *Remote Sensing*, vol. 2, no. 1, pp. 151–165, 2010.

[16] G. W. Thomas, D. L. Sparks, A. L. Page et al., *Soil pH and Soil Acidity. Sparks D Methods of Soil Analysis. Part II*, Soil Science Society of America, 1996.

[17] K. J. Beven and M. J. Kirkby, "A physically based, variable contributing area model of basin hydrology," *Hydrological Sciences Bulletin*, vol. 24, no. 1, pp. 43–69, 1979.

[18] I. D. Moore, R. B. Grayson, and A. R. Ladson, "Digital terrain modelling: a review of hydrological, geomorphological, and biological applications," *Hydrological Processes*, vol. 5, no. 1, pp. 3–30, 1991.

[19] P. E. Gessler, O. A. Chadwick, F. Chamran, L. Althouse, and K. Holmes, "Modeling soil–landscape and ecosystem properties using terrain attributes," *Soil Science Society of America Journal*, vol. 64, no. 6, pp. 2046–2056, 2000.

[20] T. R. Marthews, S. J. Dadson, B. Lehner, S. Abele, and N. Gedney, "High-resolution global topographic index values for use in large-scale hydrological modelling," *Hydrology and Earth System Sciences*, vol. 19, no. 1, pp. 91–104, 2015.

[21] J. L. Deng, *A Course in Grey Systems Theory*, Press of Huazhong University of Science and Technology, Wuhan, China, 1990.

[22] Y. Lin and S. F. Liu, "A systemic analysis with data (II)," *International Journal of General Systems*, vol. 29, no. 6, pp. 1001–1013, 2000.

[23] S. F. Liu and J. Forrest, "The current development status on Grey System Theory," *Journal of Grey System*, vol. 19, no. 2, pp. 111–123, 2007.

[24] J. L. Deng, "Introduction to Grey System Theory," *The Journal of Grey System*, vol. 1, no. 1, pp. 1–24, 1989.

[25] C. L. Lin, "Use of the Taguchi Method and Grey Relational Analysis to optimize turning operations with multiple performance characteristics," *Materials and Manufacturing Processes*, vol. 19, no. 2, pp. 209–220, 2004.

[26] N. Tosun, "Determination of optimum parameters for multi-performance characteristics in drilling by using grey relational analysis," *The International Journal of Advanced Manufacturing Technology*, vol. 28, no. 5, pp. 450–455, 2006.

[27] S. F. Liu and Y. Lin, *Grey Information: Theory and Practical Applications*, Springer, London, UK, 2006.

[28] L. P. Wilding and L. R. Drees, "Spatial variability and pedology," *Developments in Soil Science*, vol. 11, pp. 83–116, 1983.

[29] P. Adhikari, M. K. Shukla, and J. G. Mexal, "Spatial variability of electrical conductivity of desert soil irrigated with treated wastewater: implications for irrigation management," *Applied and Environmental Soil Science*, vol. 2011, Article ID 504249, 11 pages, 2011.

[30] M. Aslam and S. A. Prathapar, "Strategies to mitigate secondary salinization in the Indus Basin of Pakistan: a selective review," Tech. Rep. 97, IWMI, 2006.

[31] H. Solomon, Y. Kitamura, Z. Li et al., "Classification of salinization processes in Luohui Irrigation Scheme, China—part of water management research to prevent salinization in semiarid land," *Journal of Arid Land Studies*, vol. 15, no. 2, pp. 89–105, 2005.

[32] Z. F. Chang, H. Liu, M. Zhao, F. Han, S. Zhong, and J. Tang, "A primary study on the process of formation and succession of desert vegetation in Minqin," *Journal of Arid Land Resources and Environment*, vol. 21, no. 7, pp. 116–124, 2007.

Hindawi
Mathematical Problems in Engineering
Volume 2017, Article ID 4728425, 8 pages
https://doi.org/10.1155/2017/4728425

Research Article

Hierarchical Sea-Land Segmentation for Panchromatic Remote Sensing Imagery

Long Ma,[1] Nouman Q. Soomro,[2] Jinjing Shen,[3] Liang Chen,[1] Zhihong Mai,[1] and Guanqun Wang[1]

[1]*Beijing Key Laboratory of Embedded Real-Time Information Processing Technology, Beijing Institute of Technology, Beijing 100081, China*
[2]*Department of Software Engineering, Mehran University of Engineering and Technology, SZAB Campus, Khairpur 66020, Pakistan*
[3]*Institute of Information Engineering, Chinese Academy of Sciences, Beijing 100093, China*

Correspondence should be addressed to Liang Chen; chenl@bit.edu.cn

Received 15 November 2016; Accepted 31 January 2017; Published 12 March 2017

Academic Editor: Ram Avtar

Automatic sea-land segmentation is an essential and challenging field for the practical use of panchromatic satellite imagery. Owing to the temporal variations as well as the complex and inconsistent intensity contrast in both land and sea areas, it is difficult to generate an accurate segmentation result by using the conventional thresholding methods. Additionally, the freely available digital elevation model (DEM) also difficultly meets the requirements of high-resolution data for practical usage, because of the low precision and high memory storage costs for the processing systems. In this case, we proposed a fully automatic sea-land segmentation approach for practical use with a hierarchical coarse-to-fine procedure. We compared our method with other state-of-the-art methods with real images under complex backgrounds and conducted quantitative comparisons. The experimental results show that our method outperforms all other methods and proved being computationally efficient.

1. Introduction

Sea-land segmentation is a promising yet very challenging area of research in the field of image segmentation and used in a wide range of remote sensing applications such as ship detection, reconnaissance/investigation on surface of water, and oil spilling detection, just to name a few [1]. Compared to SAR imagery, panchromatic remote sensing images are free from high-level speckle and have fine-drawn information even for small targets and hence make this sort of images ideal for sea-land segmentation. Moreover, the easily interpreted characteristic makes researchers gradually draw their attention to high-resolution panchromatic imagery for applications of ship detection and classification [2, 3]. However, sea-land segmentation using panchromatic remote sensing images, so far, has attracted less attention in the literature, despite containing rich information and possible impact on a wide range of applications. In this paper, we attempt to narrow down this gap to utilize the maximum advantages of panchromatic remote sensing images.

Digital elevation model (DEM) can plausibly be used to obtain the sea-land mask; however, both the freely available and paid DEMs are low in quality and resolution (the spatial resolution varies from approx. 1 km to 12 m) in contrast to the high-resolution imagery acquired by on-orbit panchromatic payloads nowadays [4, 5]. Moreover, when integrating the DEM into the practical real time systems, the consumption of storage resource becomes huge. As a result, automatic sea-land segmentation is an essential and meaningful application of panchromatic satellite images. Work of automatic sea-land can broadly be divided into three categories: thresholding based segmentation, edge-based segmentation, and classification based methods. Based on the theory of 2D maximum entropy (ME) and genetic algorithm, Li et al. [1] developed an improved thresholding algorithm to extract water areas. Zhang and Li [6] presented a thresholding method (T) based

on minimum class mean absolute deviation. In [7], Mao et al. proposed an improved Chan-Vese (CV) model under the constraint of extracting edge information which is calculated by dual tree complex wavelet transform (DT-CWT). Aktaş et al. [8] put forward an edge-aware segmentation and preserved the shoreline boundaries by using steerable filters. Since both the thresholding- and edge-based segmentation methods are sensitive to noise as well as the complicated distribution of intensity and texture on land and shoreline borders, denoising is commonly used as the preprocessing step prior to segmentation. However, this preprocessing may largely destroy the integrity of coastal line. To address this problem, classification based methods are gaining popularity recently on the basis of intensity, texture, statistical characteristics, and other low level features. A set of gray level cooccurrence matrix (GLCM) features in four directions was employed in [9]. Dai et al. [10] introduced a multilevel local pattern histogram (MLPH) to classify water area class from TerraSAR-X images. Xia et al. [11] used local binary patterns (LBP) features to obtain the integrated feature map for sea-land segmentation.

Sea-land segmentation provides a rough interpretation of the scene, though less focused on minute details but much higher on processing efficiency. The existing thresholding- and edge-based methods suffer from the deficiency in illumination variations leading to oversegmentation. However, the classification based algorithms usually have a higher computational complexity due to the complex feature extraction and the subsequent classification. To tackle all these problems, we propose a fast algorithm for sea-land segmentation by combining modified Otsu's method [12] with homogeneous texture and intensity features. As we demonstrate, compared with state-of-the-art methods, our hierarchical method reasonably distributes the computational resources and presents a promising segmentation performance.

The rest of the paper is organized as follows. The outline of the proposed hierarchical segmentation method is given in Section 2. Experimental results are discussed in Section 3. In Section 4, we draw the conclusion.

2. Hierarchical Sea-Land Segmentation

Unlike the multispectral and natural-colored images, the panchromatic images lack useful help of color information or spectral metric, that is, normalized difference water index (NDWI) for sea-land segmentation. In addition, the complicated distributions of intensity and texture make it arduous to segment an integrated land mask because of the various land cover types. Ships, isles, clouds, and other scattered resources in shore may also affect the extraction of water information from sea because they partially cover the water area.

In this paper, the overall work is divided into two stages: a coarse segmentation stage and a fine segmentation stage. The main part of sea/land is separated out by using homogenized features in the coarse stage. Then, the subsequent fine stage refines the shoreline boundaries, to be obtained from coarse segmentation, by means of Otsu's method. Under this strategy, the computing resources are reasonably assigned resulting in spatially consistent results. The overall flowchart is shown in Figure 1. In the following subsections, we discuss our work in more detail.

2.1. Coarse Segmentation Stage. As shown in Figure 1, the coarse segmentation stage comprises three steps: homogeneous feature extraction (HFE), local threshold segmentation (LTS), and fusion and false alarm removal (F-FAR). It is easy to notice the fact that most of the sea surfaces are in a calm and peaceful state and show regular gray values and textures. However, the ships, isolated isles, and waves may destroy the integrity of water, whereas the shadows of mountains and buildings existing on land may act as the complicated disturbances because they become obstructions in getting the information required for land detection. In addition, the commonly existing clouds with various kinds and sizes make it a big challenge for consistent segmentation. From this perspective, we replace the original spatial information with the homogeneous features to characterize the land and sea. The features used here are intensity and texture.

2.1.1. Homogeneous Feature Extraction (HFE). HFE consisted of intensity feature extraction and texture feature extraction. They are defined in detail in subsections below.

(a) Intensity Feature Extraction. Let $I_{M\times M}$ represent the input image. We divide $I_{M\times M}$ into n equal blocks with the size of $H\times H$, that is, $[I_1, I_2, I_3, \ldots, I_n]$. To utilize the correlation between the regions, the overlapped width between adjacent blocks is set as $H/2$, and the standard deviation of each block can be calculated according to

$$\sigma_k = \sqrt{\frac{\sum_{i=1}^{H}\sum_{j=1}^{H}\left(f_k(i,j)-\mu_k\right)^2}{H\times H}}. \tag{1}$$

Let $f_k(i, j)$ denote the intensity value of the pixel (i, j) in block k, whereas μ_k represents the mean value of all pixels in block k. Then for each block the pixel is labeled uniformly according to

$$L_k = \begin{cases} 1, & \left|f_k(i,j)-c_k\right| \le t\sigma_k, \\ 0, & \left|f_k(i,j)-c_k\right| > t\sigma_k, \end{cases} \tag{2}$$

where c_k means the center pixel intensity value in block k and t is an experimental threshold, which is 2.97 in this paper.

Afterwards, a homogeneous intensity value is defined and used to represent each block. First, the numbers of "0" and "1" labels are counted, respectively. Then, compare the label numbers of "0" and "1." If pixels "1" are in the majority, then assign the mean intensity values of all pixels "1" to the present block; otherwise, the mean intensity values of pixels "0" are used for assigning instead. Last, repeatedly calculate all blocks to get the homogeneous intensity feature vector $\bar{\mathbf{I}}_{\text{in}} = [\hat{I}_{\text{in},1}, \hat{I}_{\text{in},2}, \hat{I}_{\text{in},3}, \ldots, \hat{I}_{\text{in},n}]$.

(b) Texture Feature Extraction. Gradient information always offers a basic and direct way to characterize texture features. In this paper, we combine gradient information with calculation of integral image to represent the homogeneous texture

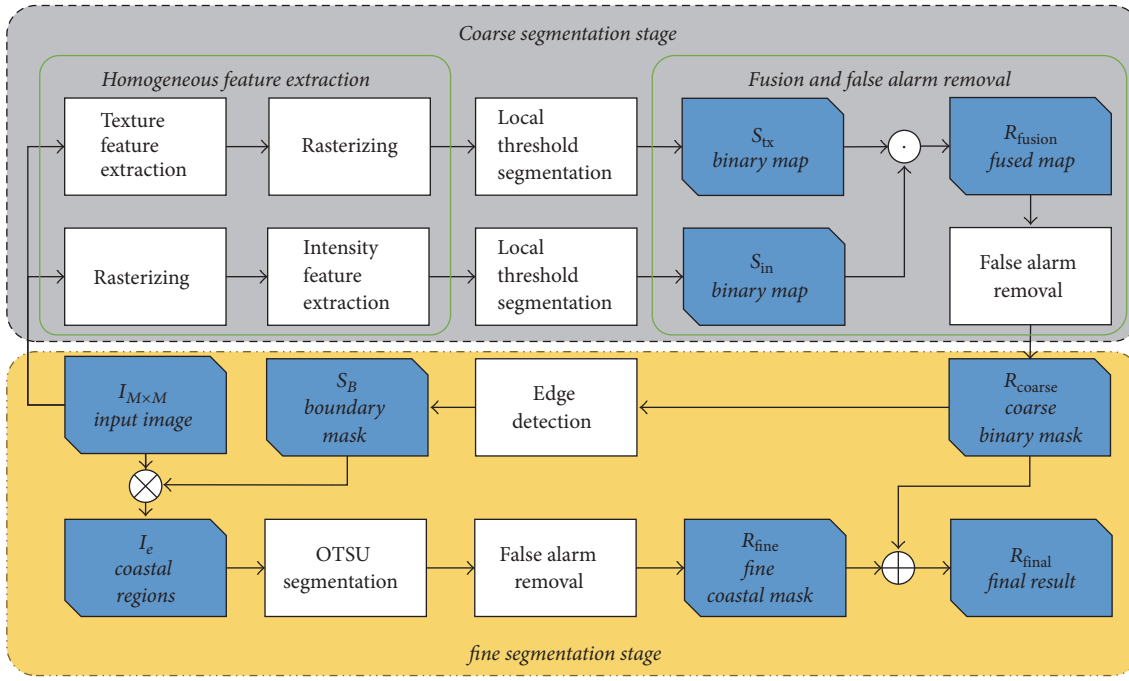

Figure 1: Flowchart of the proposed method.

feature. For the input image $I_{M\times M}$, the gradient map $G(i, j)$ is calculated on the basis of the vertical gradient $G_V(i, j)$ and the horizontal gradient $G_H(i, j)$. The gradient values in image boundaries are set as 0.

$$\begin{aligned} G_H(i, j) &= \left|I(i+1, j) - I(i, j)\right|, \\ G_V(i, j) &= \left|I(i, j+1) - I(i, j)\right|, \\ G(i, j) &= G_H(i, j) + G_V(i, j). \end{aligned} \tag{3}$$

The integral image $G_{\mathrm{IN}}(i, j)$ of the gradient map $G(i, j)$ is generated according to

$$\begin{aligned} G_{\mathrm{IN}}(i, j) = {} & G(i, j) + G_{\mathrm{IN}}(i-1, j) + G_{\mathrm{IN}}(i, j-1) \\ & - G_{\mathrm{IN}}(i-1, j-1). \end{aligned} \tag{4}$$

Then, we divide $G_{\mathrm{IN}}(i, j)$ into n blocks with the size of $H \times H$. The mean gradient value of block k is determined by (5) and (6).

$$\begin{aligned} \mathrm{Block}(k) = {} & G_{\mathrm{IN}}\left(i_k + \frac{H}{2}, j_k + \frac{H}{2}\right) \\ & - G_{\mathrm{IN}}\left(i_k + \frac{H}{2}, j_k - \frac{H}{2}\right) \\ & - G_{\mathrm{IN}}\left(i_k - \frac{H}{2}, j_k + \frac{H}{2}\right) \\ & + G_{\mathrm{IN}}\left(i_k - \frac{H}{2}, j_k - \frac{H}{2}\right), \end{aligned} \tag{5}$$

$$\overline{G_{\mathrm{block}}}(k) = \frac{\mathrm{Block}(k)}{H \times H},$$

where (i_k, j_k) represents the coordinate of the center pixel in block k and Block(k) represents the sum value of gradients. Thus, the homogeneous texture feature vector $\bar{\mathbf{I}}_{\mathrm{tx}} = [\hat{I}_{\mathrm{tx},1}, \hat{I}_{\mathrm{tx},2}, \hat{I}_{\mathrm{tx},3}, \ldots, \hat{I}_{\mathrm{tx},n}]$ is generated, when these elements $\hat{I}_{\mathrm{tx},k} = \overline{G_{\mathrm{block}}}(k)$, $k = 1, 2, \ldots, n$, are obtained by computing within all n bocks. Subsequently, the homogenized n-dimensional intensity and texture features are generated and then used for the further coarse segmentation calculation to replace the original image information.

2.1.2. Local Threshold Segmentation (LTS). The traditional global thresholding based methods segment images according to the gray histogram using the optimal threshold. However, within the usage of remote sensing applications, the aforementioned disturbances in sea/land areas give a wide dynamic range in gray scale, which makes the conventional thresholding based method sensitive to the complex backgrounds. Considering this problem, local thresholding segmentation based on homogeneous features is proposed in this section. In contrast with conventional Otsu's method, this modified version maintains robustness to the noise interference and avoids the deficiency from backgrounds. The specific steps are illustrated below.

Step 1. For the previously obtained homogeneous feature vectors $\bar{\mathbf{I}}_i$ ($i = \mathrm{in}, \mathrm{tx}$), set the binary threshold T_i^* ($i = \mathrm{in}, \mathrm{tx}$) using Otsu's method.

Step 2. Label each block initially based on T_i^* using

$$M_{i,j} = \begin{cases} 1, & \hat{I}_{i,j} \geq T_i^*, \\ 0, & \hat{I}_{i,j} < T_i^*, \end{cases} \quad (i = \mathrm{in}, \mathrm{tx};\ j = 1, 2, \ldots, n). \tag{6}$$

Step 3. For one block region, we separate it uniformly into four subblocks. Hence, every subblock region with the size of $H/2 \times H/2$ is overlapped by four labeled blocks from different sides: upper left, upper right, lower left, and lower right.

Step 4. For each subblock, we accumulate all labels of overlapped blocks. If the total sum value is greater than 2, then we consider this half-block region as a land region; otherwise it is considered as a water region.

2.1.3. Fusion and False Alarm Removal (F-FAR). After the above subsection, the initial binary masks S_{in} and S_{tx} are generated with the same size as the input image, respectively. To incorporate the complementary information from these two results, we employ a simple strategy. Regions identified with water labels, from both S_{in} and S_{tx}, are considered as water regions as whole; the rest of areas are defined as land areas. We refer to this fusing result as R_{fusion}.

On one side, the cargo ships and scattered reefs in sea are outliers similar to land. On other side, green lands, shadows of clouds, mountains, and buildings existing on land have properties similar to water area. These types of local information seem to be a large obstruction in distinctively recognizing the water and land areas separately. To address these outliers, here, FAR is used. Detailed steps are given below.

Step 1 (remove false alarms in water areas). Perform morphological opening on R_{fusion} with a disk-shaped structuring element S_d whose size is defined in accordance with the size of the biggest merchant vessel as well as the image resolution. Specifically, for the 5-meter resolution images, the radius of S_d is set as 40 according to (7), because it is widely accepted that there is no ship larger in size than 400 meters.

$$\text{Radius}\{S_d\} = \frac{400}{2 \times \text{Resolution}\{I_{M\times M}\}}. \tag{7}$$

Step 2 (remove false alarms in land areas). Reverse the binary values, generated as a result of Step 1, and then process the reversed binary map using the same way as in Step 1. This step aims to counteract the "fading effects" to coastal boundary caused by opening operation of Step 1. Hence, the size of the disk-shaped structuring element used in this step should be the same as Radius$\{S_d\}$. Meanwhile, the false alarms on land can be removed somewhat.

Step 3 (inversion). Invert binary values of Step 2 result, to obtain the coarse binary mask R_{coarse}.

Herein, this practical and efficient FAR method preserves the sea-land boundary to the maximum extent while guaranteeing the FAR effects at the same time in contrast to a solely morphological opening or closing operation in similar applications. By applying above steps, the coarse segmentation stage is successfully completed.

2.2. Fine Segmentation Stage. The sea and land areas can roughly be separated from each other by coarse stage. However, considering the computing efficiency and the effectiveness, the block is the smallest processing unit used in the coarse stage, leading to a roughly defined binary mask. Aiming to get smoother and more accurate boundaries, we use the fine segmentation stage. In this stage, we extract the boundary area information from the original image with the help of R_{coarse} firstly. Then, the shoreline boundaries are refined and synthesized with the rough binary mask by using the thresholding method. We observed that although traditional thresholding methods may lead to excessive false alarms, the segmented boundaries are precise. And this is the reason why we use the thresholding method to refine the boundaries. The concrete details are as follows.

Step 1. Extract the sea-land boundary mask B_f by computing "XOR" between R_{coarse} and R'_{coarse}, which is acquired by eroding R_{coarse} with S_d.

Step 2. Dilate the detected boundary mask B_f. Here, the radius size of the structuring element S_r is $H/2$.

Step 3. Extract I_e according to B_f, the corresponding gray level information, from the input image $I_{M\times M}$.

Step 4. Original Otsu's method is applied to I_e, and the result is in terms of R_{ot}.

Step 5. As a complementary process, a morphological opening step using S_d is adopted upon R_{ot} to prevent the interferences caused by shoals and preserve the detailed harbor outlines to the great extent. Consequently, the refined result R_{fine} is generated.

Step 6. The final segmentation result R_{final} is calibrated by R_{fine} on the basis of R_{coarse}, which is elaborated by

$$R_{\text{final}}(i,j) = \begin{cases} R_{\text{coarse}}(i,j), & (i,j) \in B_f, \\ R_{\text{fine}}(i,j), & (i,j) \in B_f^c. \end{cases} \tag{8}$$

3. Experimental Results and Analysis

In this section, two experiments are designed to evaluate our purposed methods in terms of the segmentation accuracy as well as the calculating time cost. All images are taken from a panchromatic SPOT5 satellite with 5 m spatial resolution and the size of 4096×4096 pixels.

3.1. Parameter Selection. Based on the arguments mentioned above, the selection of block size H may influence the overall segmentation performance, including the homogeneous feature and sea-land boundary mask extraction in coarse and fine segmentation stage, respectively. Therefore, to select the best value of H, we conducted an experiment with dataset (a). In this dataset, various factors of interfering conditions existing in 100 images were considered such as partial cloud covers, shadows caused by constructions, diversified vessels, and isles. Performance was evaluated with widely

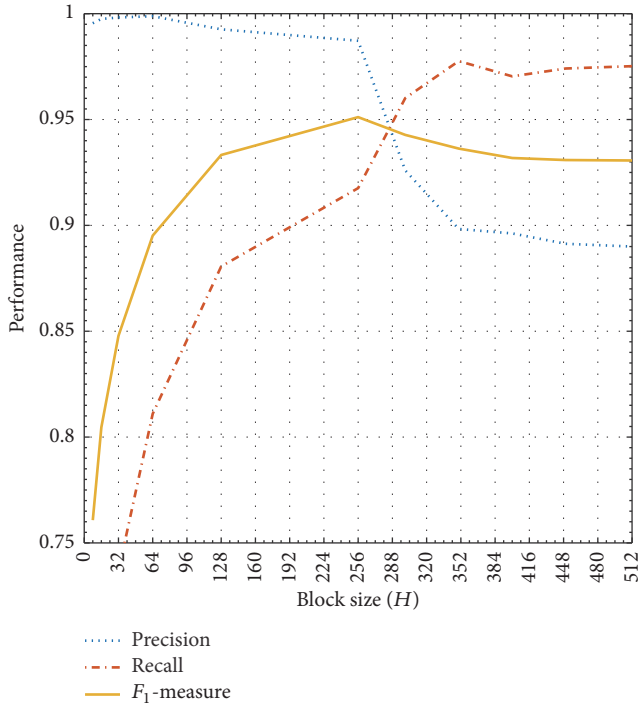

Figure 2: Precision, recall, and F_1-measure in different block sizes.

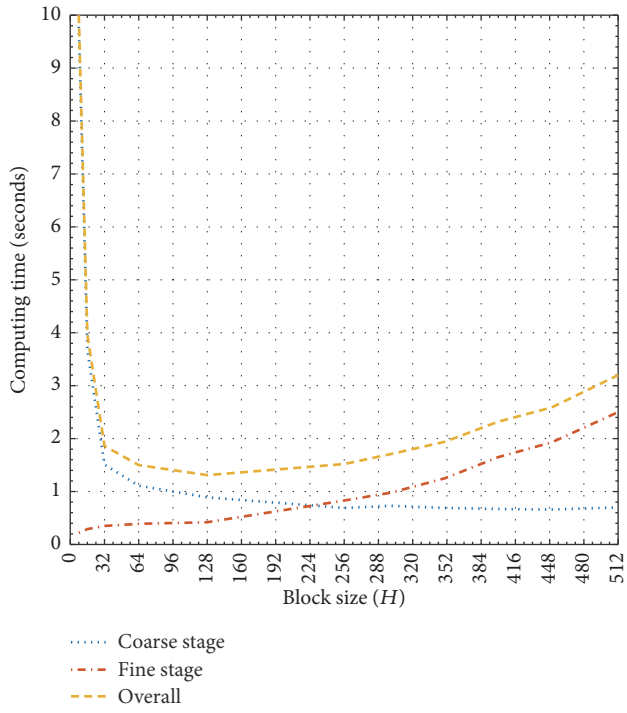

Figure 3: Computing time trends under different block sizes.

used precision (P), recall (R), and F_1-measure (F_1) and they are defined in the literature as

$$P = \frac{\sum_i \sum_j \mathrm{GT}(i,j) \cdot R_{\mathrm{final}}(i,j)}{\sum_i \sum_j R_{\mathrm{final}}(i,j)},$$
$$R = \frac{\sum_i \sum_j \mathrm{GT}(i,j) \cdot R_{\mathrm{final}}(i,j)}{\sum_i \sum_j \mathrm{GT}(i,j)}, \quad (9)$$
$$F_1 = \frac{2 \cdot P \cdot R}{P + R},$$

where GT means the ground truth and R_{final} denotes the binary mask obtained from the segmented result. It is well known that higher values of P, R, and F_1 present better results.

Figure 2 shows related results when the block size H varies from 8 to 512. The conclusions drawn from Figure 2 and the segmentation results are summarized here. First, it was wrongly assumed that smaller size blocks may lead to robust recognition but, contrary to this, result in a low recall. In most cases, the selection of small block is the main reason of high false alarm rates when encountered with interferences. This is because the smaller the block, the larger the possibility of being affected by contextual interferences. Second, a large H leads to a low precision because of the weak capabilities for detail recognition. Last, considering the overall performance indicated by F_1, 256 to 320 is a good range of H to obtain optimal performance.

Figure 3 illustrates the computation time of each substage and the overall process. From the perspective of computing efficiency, the increasing size of H decreases the processing load for homogenous feature extraction. However, it would increase the computational burden of morphology based method for sea-land boundary extraction in Section 2.2. As expected, in Figure 3, the coarse stage time decreases monotonically with the increase of H. And the fine stage time increases with the increasing H. Synthetically, the overall computational time-consuming curve shows a concave function characteristic.

Based on the discussion above, we assigned 288 to H in this paper to guarantee both effectiveness and efficiency.

3.2. Comparison with State of the Art. This section discussed the experiments to test our results under different complex background conditions and analyze our method by comparing the results with those of four approaches: ME [1], T [6], LBP [11] based algorithms, and the method in [13], which is referred to as ATI for short in this paper. The former three methods are state-of-the-art methods designed using different perspectives. Though ATI was not originally explored for the sea-land segmentation in remote sensing applications, its excellent robustness under various illuminated conditions made it a promising competitor. Working well on the temporal variations is a valuable treasure for this undertaken field. To give a comprehensive comparison, a dataset (b) containing five classes was taken. This dataset had total 200 panchromatic SPOT images varying from the ratio of sea-land coverage to background interference factors. Each class has 40 images, and it is shown in Figure 4 that the main characteristics of 5 classes from class (i) to class (v) can be summarized as less land with calm sea, less land with tides and waves of sea, half land with half water, less water with

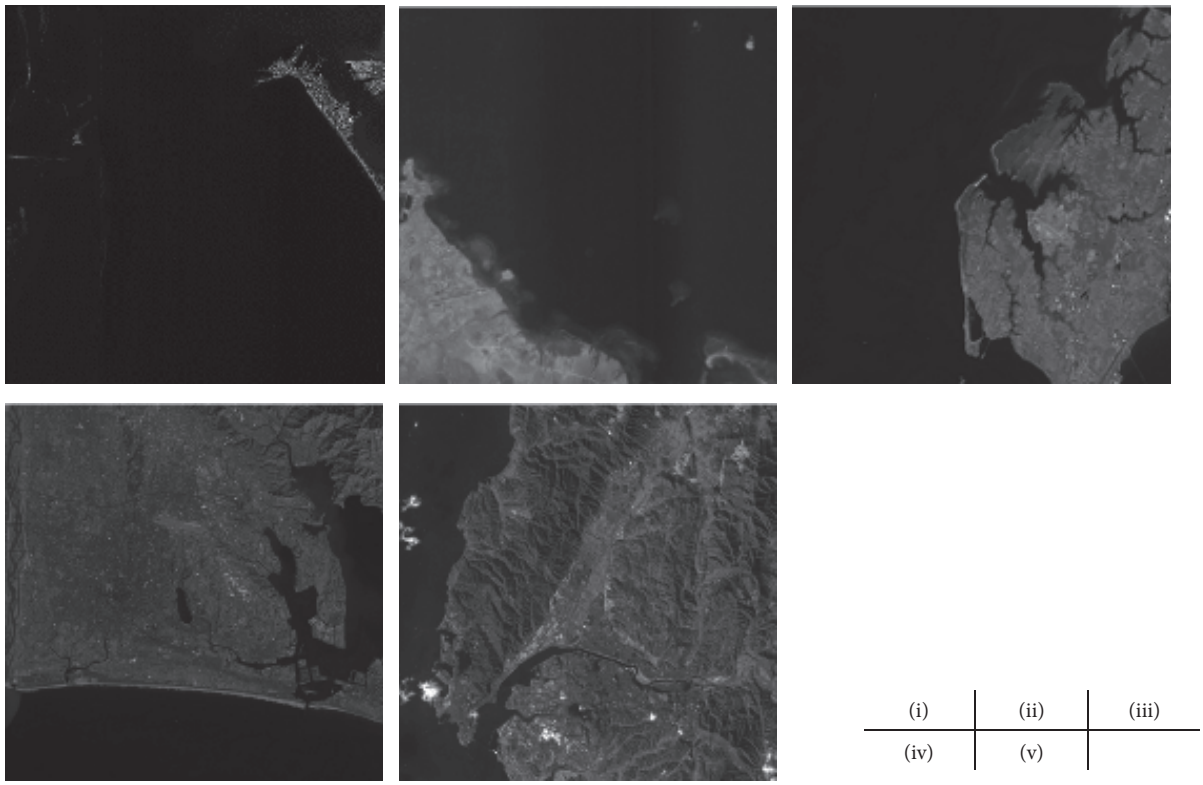

Figure 4: Samples of each class among dataset (b).

Table 1: Performance and time consumption comparison of different models.

	T	ME	ATI	LBP	Proposed
Class (i)					
F_1-measure	0.9864	0.9431	0.9852	0.9860	0.9864
False alarm rate	0.0064	0.0104	0.0031	0.0010	0.0019
Class (ii)					
F_1-measure	0.9728	0.9243	0.9633	0.9838	0.9704
False alarm rate	0.0131	0.0059	0.0648	0.0047	0.0023
Class (iii)					
F_1-measure	0.9577	0.9689	0.9423	0.9735	0.9781
False alarm rate	0.0799	0.0588	0.0965	0.0257	0.0249
Class (iv)					
F_1-measure	0.7768	0.7924	0.8145	0.9560	0.9623
False alarm rate	0.3642	0.3429	0.3026	0.0522	0.0304
Class (v)					
F_1-measure	0.4281	0.5692	0.6143	0.8557	0.9023
False alarm rate	0.7273	0.6010	0.5473	0.1950	0.1283
Average					
F_1-measure	0.8244	0.8396	0.8639	0.9510	0.9592
False alarm rate	0.2382	0.2036	0.2029	0.0557	0.0376
Time consumption	1.88	45.67	13.10	85.39	1.93

smooth land, and less water with rough land, respectively. The resultant samples are shown in Figure 5. First row in Figure 5 shows the manually labeled ground truth. Rows 2 to 5 show the results of ME, T, LBP, and ATI, respectively. And the last row shows the results of our proposed algorithm.

Additionally, to give a quantitative analysis, we used average values of F_1-measure and false alarm rate (FA) in the experiment defined by (10). We observed that high recall values can be obtained from all these competing methods; however FA values differ distinctively. As shown in Table 1,

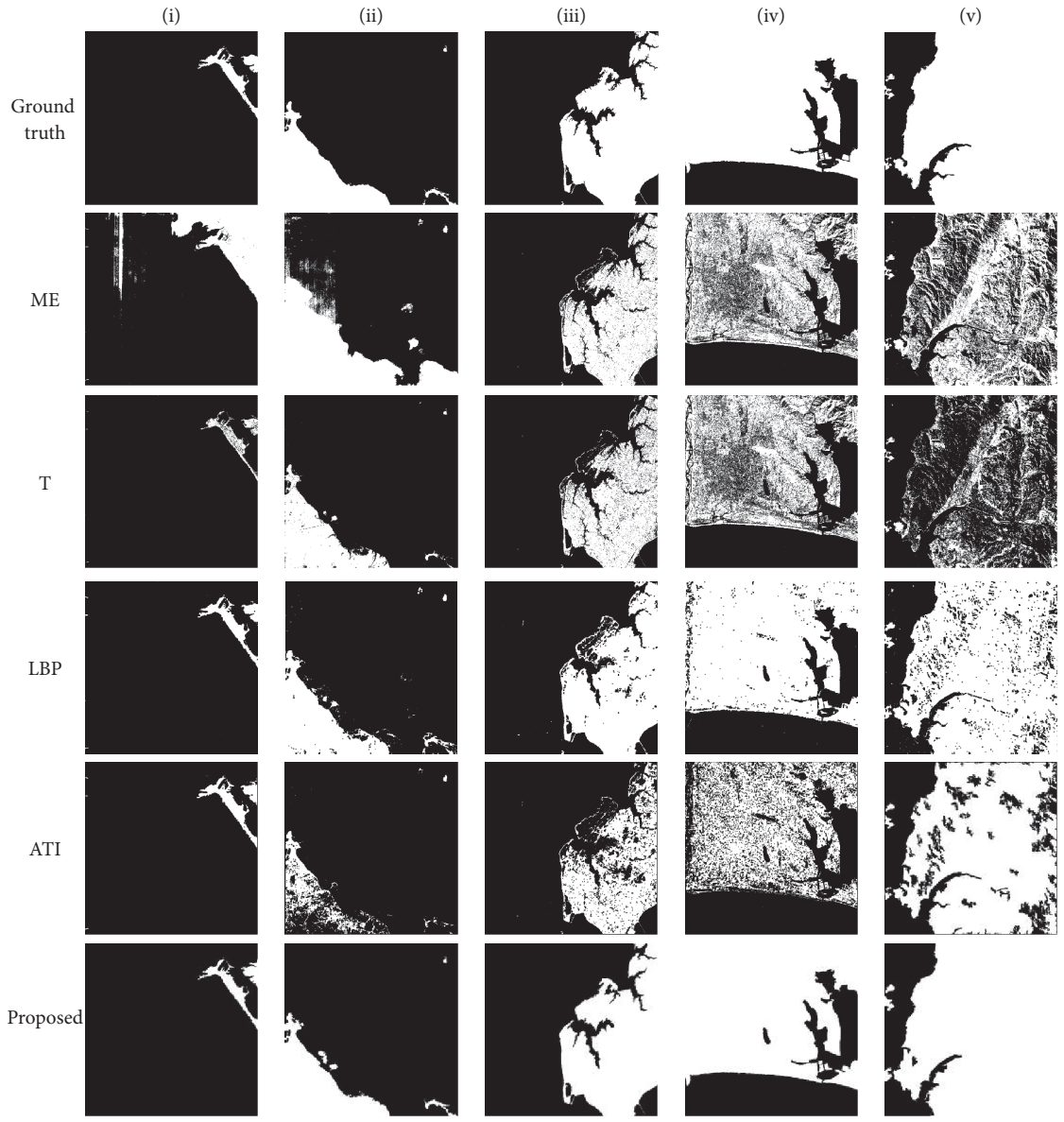

Figure 5: Comparison of segmentation results.

our method shows the highest F_1 and lowest FA values among all the methods.

$$\text{FA} = 1 - \text{Precision}. \tag{10}$$

Table 1 also illustrates the total execution time of these different algorithms on the abovementioned dataset (b). We used i5-3230M CPU and 8 GB RAM hardware and MATLAB R2016a software for these experiments. For the images with the size of 4096×4096 pixels, the average execution time of our proposed algorithm was 1.93 s. Time taken by our proposed method is little longer than the thresholding based method but drastically less than the other three methods. Promisingly, the performance of our method beats all other four methods. Overall, taking both the performance and execution time into consideration, our proposed method outperforms state of the art.

4. Conclusion

In this paper, a hierarchical sea-land segmentation method for panchromatic remote sensing imagery has been proposed and it provides a practical solution and can quickly be transformed from research to hardware implementation as it requires lower computational resources. Our work is divided into two stages and each stage addresses the different scenario instead of applying one whole procedure for every area. The coarse stage focuses on the main sea/land body segmentation giving out an initial result, and the successive fine stage refines the sea-land borders and brings on an ultimate result.

In comprehensive consideration of both performance and computing efficiency, our proposed algorithm outperforms the other four state-of-the-art methods.

Competing Interests

The authors declare that there is no conflict of interests regarding the publication of this paper.

Acknowledgments

This work was supported by the Chang Jiang Scholars Program under Grant no. T2012122 and the Hundred Leading Talent Project of Beijing Science and Technology under Grant no. Z141101001514005.

References

[1] Z. Li, X. Chen, P. Luo, and Y. Tian, "Water area segmentation of the Yangcheng Lake with SAR data based on improved 2D maximum entropy and genetic algorithm," in *Proceedings of the 2nd International Workshop on Earth Observation and Remote Sensing Applications (EORSA '12)*, pp. 263–267, Shanghai, China, June 2012.

[2] J. Tang, C. Deng, G.-B. Huang, and B. Zhao, "Compressed-domain ship detection on spaceborne optical image using deep neural network and extreme learning machine," *IEEE Transactions on Geoscience and Remote Sensing*, vol. 53, no. 3, pp. 1174–1185, 2015.

[3] F. Bi, B. Zhu, L. Gao, and M. Bian, "A visual search inspired computational model for ship detection in optical satellite images," *IEEE Geoscience and Remote Sensing Letters*, vol. 9, no. 4, pp. 749–753, 2012.

[4] K. A. Sambodo, "Semi-automatic ship detection using PI-SAR-L2 data based on rapid feature detection approach," *International Journal of Remote Sensing and Earth Sciences*, vol. 9, no. 2, pp. 112–118, 2014.

[5] G. Mattyus, "Near real-time automatic vessel detection on optical satellite images," in *Proceedings of the International Archives of the Photogrammetry, Remote Sensing and Spatial Information Sciences (ISPRS '13)*, vol. XL-1/W1, pp. 233–237, Hannover, Germany, May 2013.

[6] L. Zhang and A. Li, "Thresholding-based remote sensing image segmentation using mean absolute deviation algorithm," *Journal of Applied Remote Sensing*, vol. 8, no. 1, Article ID 083542, 2014.

[7] C. Mao, S. Wan, L. Yue, and Y. Xia, "A water/land segmentation algorithm based on an improved chan-vese model with edge constraints of complex wavelet domain," *Chinese Journal of Electronics*, vol. 24, no. 2, pp. 361–365, 2015.

[8] Ü. R. Aktaş, G. Can, and F. T. Y. Vural, "Edge-aware segmentation in satellite imagery: a case study of shoreline detection," in *Proceedings of the IAPR Workshop on Pattern Recognition in Remote Sensing (PRRS '12)*, Tsukuba, Japan, November 2012.

[9] W. Lv, Q. Yu, and W. Yu, "Water extraction in SAR images using GLCM and Support vector Machine," in *Proceedings of the IEEE 10th International Conference on Signal Processing (ICSP '10)*, pp. 740–743, IEEE, Beijing, China, October 2010.

[10] D. Dai, W. Yang, and H. Sun, "Multilevel local pattern histogram for SAR image classification," *IEEE Geoscience and Remote Sensing Letters*, vol. 8, no. 2, pp. 225–229, 2011.

[11] Y. Xia, S. Wan, P. Jin, and L. Yue, "A novel sea-land segmentation algorithm based on local binary patterns for ship detection," *International Journal of Signal Processing, Image Processing and Pattern Recognition*, vol. 7, no. 3, pp. 237–246, 2014.

[12] N. Otsu, "A threshold selection method from gray-level histograms," *IEEE Transactions on Systems, Man, and Cybernetics*, vol. 9, no. 1, pp. 62–66, 1979.

[13] D. Bradley and G. Roth, "Adaptive thresholding using the integral image," *Journal of Graphics Tools*, vol. 12, no. 2, pp. 13–21, 2011.

Hindawi
Mathematical Problems in Engineering
Volume 2017, Article ID 7901692, 14 pages
https://doi.org/10.1155/2017/7901692

Research Article

A Subpixel Matching Method for Stereovision of Narrow Baseline Remotely Sensed Imagery

Ning Ma,[1,2] Peng-fei Sun,[1] Yu-bo Men,[2] Chao-guang Men,[2] and Xiang Li[2]

[1]*College of Computer Science and Information Engineering, Harbin Normal University, Normal University Road 1, Harbin 150001, China*
[2]*College of Computer Science and Technology, Harbin Engineering University, Nantong Street 145, Harbin 150001, China*

Correspondence should be addressed to Chao-guang Men; menchaoguang@hrbeu.edu.cn

Received 24 August 2016; Revised 9 January 2017; Accepted 26 January 2017; Published 23 February 2017

Academic Editor: Ram Avtar

In this paper, an accurate and efficient image matching method based on phase correlation is proposed to estimate disparity with subpixel precision, which is used for the stereovision of narrow baseline remotely sensed images. The multistep strategy is adopted in our technical frame; thus the disparity estimation is divided into two steps: integer-pixel prematching and subpixel matching. Firstly, integer-pixel disparity is estimated by employing a cross-based local matching method. Then the relationship of corresponding points is established under the guidance of integer-pixel disparity. The subimages are extracted through selecting the corresponding points as the center. Finally, the subpixel disparity is obtained by matching the subimages utilizing a novel variant of phase correlation approach. The experiment results show that the proposed method can match different kinds of large-sized narrow baseline remotely sensed images and estimate disparity with subpixel precision automatically.

1. Introduction

Stereovision is an advanced task in remote sensing and photogrammetry [1]. The aim of stereovision is to estimate the disparity through matching two or more images of same scene in different views and extract digital elevation model (DEM) through the disparity [2]. Intuitively, the disparity represents the displacement vectors between corresponding pixels that horizontally shift from the left image to the right image [3]. The stereovision of narrow baseline remotely sensed imagery is a new research hotspot for stereovision in recent years [4]. Automatic subpixel image matching is the essential technique for narrow baseline stereovision [5]. We will brief review the stereovision with different baseline and subpixel image matching method in the remaining part of this section, respectively.

1.1. Principle of Stereovision. The process of DEM extracting can be represented by a stereovision model [6], as shown in Figure 1. B and H express the baseline and the altitude of a satellite. L and R are the left and right images captured by the satellite from different views; h represents the height of ground object to be measured. A and B are the 3D points of the real world scene, which are projected to the three 2D locations a, a', and b' in L and R. The 2D points of A and B in L are coincident; thus the disparity d of the two corresponding points a and a' equals the distance between a' and b' in R. D represents the mapping of d in the 3D scene; according to the similar triangles of geometry principle, the equation $D/B = h/(H - h)$ is established. Assume that the ground sample distance (GSD) of the sensed image is G (meters/pixel); the height h of ground object can be generated: $h = dG/(B/(H - h))$. Because the altitude of satellite is much larger than the height of ground object, that is, $H \gg h$, the height h can be approximated as $h \approx dG/(B/H)$. It can be known that the precision of h is proportional to the precision of disparity and GSD and is inversely proportional to the B/H ratio. In most real sensors, H and G are limited and fixed; therefore, only two aspects can be used to enhance the precision of h: (1) Improve the precision of disparity to subpixel level [7]; (2) increase the length of baseline, that is, increasing the B/H ratio. In traditional stereovision of remotely sensed imagery,

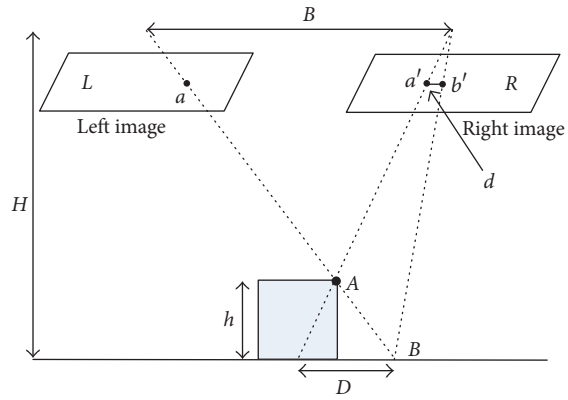

Figure 1: Stereovision model.

B/H ratio is usually set to about 1, called stereovision of wide baseline remotely sensed imagery. Even if the disparity precision is only up to the integer-pixel level, the DEM can be extracted accurately.

1.2. Comparison of Wide Baseline and Narrow Baseline Stereo. The stereovision of wide baseline remotely sensed imagery can not perform well in urban areas with dense buildings [8]. The captured process of the wide baseline remotely sensed image pair is shown in Figure 2(a). Due to the long baseline and large viewing angle, there is a large occlusion area and large geometric distortion between the images. In addition, the interval time of two imaging processes is long; the illumination condition has changed greatly. The above interference factors will lead to a high false matching rate in stereovision of wide baseline remotely sensed imagery. Therefore, it requires a lot of manual and postcorrection to extract DEM [9]. In order to solve this problem of DEM extraction in urban areas, stereovision of narrow baseline remotely sensed imagery technique has emerged and gradually become a new research focus in stereovision and remote sensing [10, 11]. The captured process of the narrow baseline remotely sensed image pair is shown in Figure 2(b). Due to the short baseline and small viewing angle, there is a small occlusion area and little geometric distortion between images. When $B/H \rightarrow 0$ (i.e., a very narrow baseline), then occlusions will be minimized, essentially because each image view becomes more geometrically similar. In addition, the interval time of two imaging processes is short; it can be considered that the illumination condition is similar to the same time. Due to above advantages, the stereovision of narrow baseline remotely sensed imagery is suitable for extracting DEM in the urban areas [8]. Two sets of simulated remotely sensed image pairs provided by Beijing Institute of Space Mechanics and Electricity are shown in Figure 3. Figure 3(a) is simulated wide baseline remotely sensed image pair with a B/H ratio of 1, and Figure 3(b) is simulated narrow baseline remotely sensed image pair with a B/H ratio of 0.05. From the comparison of Figures 3(a) and 3(b), we can see that the occlusion range and the geometric distortion of narrow baseline image pair are less, and there is a higher degree of similarity between left and right image. It is beneficial to improve the accuracy of image matching; thus fully automatic DEM extraction can be achieved through stereovision of narrow baseline remotely sensed imagery.

However the reduction of B/H ratio will inevitably lead to the reduction of precision for DEM extracting. If the stereovision of narrow baseline is going to extract the DEM as precise as the stereovision of wide baseline, the disparity needs to achieve $1/T$ pixel precision, where T is the ratio of wide baseline and narrow baseline [6]. For example, when B/H is 0.05, the precision of disparity needs to achieve 1/20 pixels to satisfy the DEM extraction. Therefore, the key technique for the stereovision of narrow baseline remotely sensed imagery is the high precision subpixel image matching [5, 7].

1.3. A Survey of Subpixel Image Matching Method. Automatic subpixel image matching is one of the most essential techniques in stereovision. It can be divided into three major categories: interpolation based method, fitting based method, and phase correlation method [12]. Interpolation based method includes the original image interpolation method and the matching cost interpolation method. The matching cost interpolation method is the representative algorithm, which combines the advantages of high efficiency and accuracy [13, 14]. The initial cost volume is interpolated by various interpolation function, and the subpixel disparity is estimated by searching the extremum of interpolated cost volume. At present, this method is usually used for the auxiliary system of driverless vehicles, robot navigation, and unmanned aerial vehicle. The original image interpolation method significantly increases the computing load, limits the possible precision to the chosen upsampling rate, and also may introduce interpolation artifacts [5]. The fitting based method generally postprocess the cost volume or disparity plane by fitting method to estimate the subpixel disparity. The cost volume fitting method fits the peak neighborhood of cost volume into a parabola; then the subpixel disparity is estimated by searching the extreme of parabola [15, 16]. The disparity plane fitting method models the disparity field by segmentation constraints, and subpixel disparity is obtained by fitting disparity plane [17–20]. The fitting based method is efficient, but the disparity precision is low. Phase correlation method provides high efficiency and accuracy via fast Fourier transform and other supplementary approaches under ideal conditions. In general, the main peak location of the inverse Fourier transform of the normalized cross-power spectrum was interpolated with the parabolic, Gaussian, and sinc functions to get the subpixel disparity [21–24].

In this paper, a subpixel image matching method based on phase correlation is proposed to estimate the disparity with subpixel precision for stereovision of narrow baseline remotely sensed imagery. The rest of this paper is organized as follows. The principle of phase correlation is introduced briefly in Section 2. A novel improved phase correlation method with subpixel precision is described in detail in Section 3. The complete algorithm is described in Section 4. Experimental evaluation is presented in Section 5. Finally, the paper is concluded in Section 6.

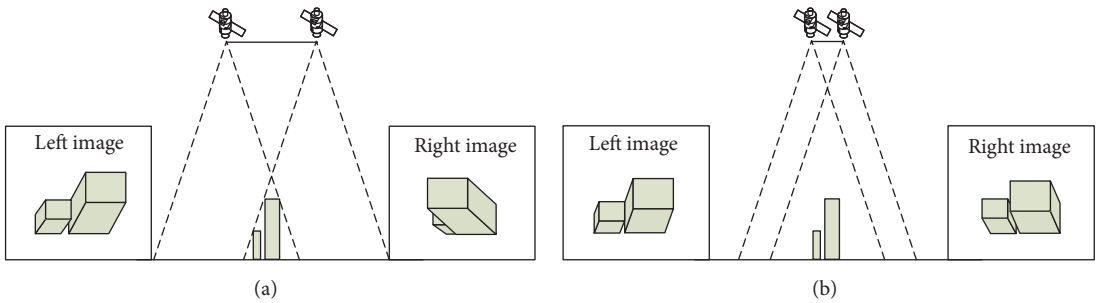

Figure 2: The captured process of the remotely sensed image pair. (a) Traditional wide baseline stereo configuration and (b) narrow baseline stereo configuration.

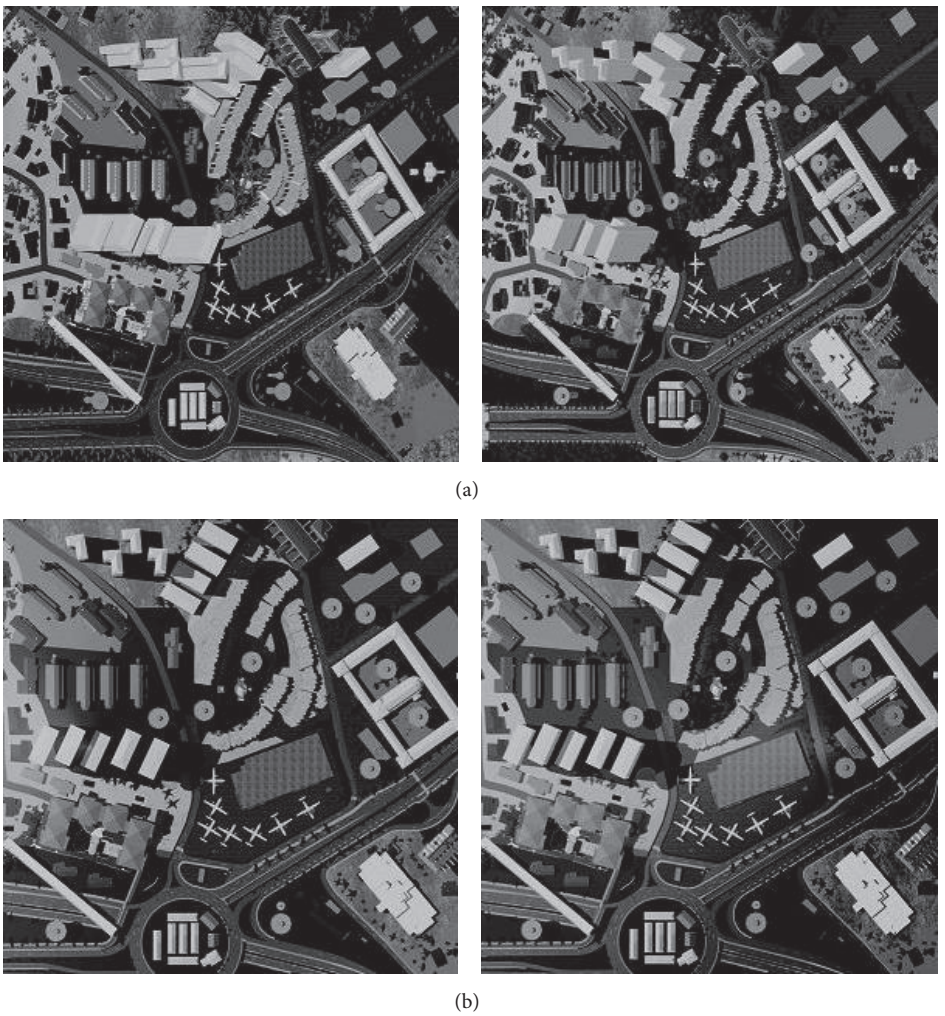

Figure 3: Two sets of simulated remotely sensed image pairs provided by Beijing Institute of Space Mechanics and Electricity. (a) Simulated wide baseline remotely sensed image pair with a B/H ratio of 1 and (b) simulated narrow baseline remotely sensed image pair with a B/H ratio of 0.05.

2. Phase Correlation

Phase correlation method is based on the well-known Fourier-domain shift property. This states that a translation between two images in the spatial domain will be expressed in the frequency domain as a linear phase difference between their Fourier transform [5]. Let f_1 and f_2 be two images with translation relationship, the size of image is $M \times N$, $f_1 = f(x, y)$, $f_2 = f(x + \Delta x, y + \Delta y)$, and $(\Delta x, \Delta y)$ are horizontal and vertical translations, respectively. Let $F_1(u, v)$

and $F_2(u, v)$ denote the 2D discrete Fourier transform (DFT) of two images:

$$F_1(u,v) = \frac{1}{MN}\sum_{x=0}^{M-1}\sum_{y=0}^{N-1} f(x,y)\exp\left(-j2\pi\left(\frac{ux}{M}+\frac{vy}{N}\right)\right), \quad (1)$$

$$F_2(u,v) = F_1(u,v)\exp\left(-j2\pi\left(\frac{u\Delta x}{M}+\frac{v\Delta y}{N}\right)\right),$$

where x and y are spatial domain variables, $x = 0, 1, 2, \ldots, M-1$, $y = 0, 1, 2, \ldots, N-1$. u and v are frequency domain variables, $u = 0, 1, 2, \ldots, M-1$, $v = 0, 1, 2, \ldots, N-1$. The normalized cross-power spectrum $Q(u, v)$ of two images is calculated as

$$Q(u,v) = \frac{F_1(u,v)F_2^*(u,v)}{\left|F_1(u,v)F_2^*(u,v)\right|} = \exp\left(-j2\pi\left(\frac{u\Delta x}{M}+\frac{v\Delta y}{N}\right)\right), \quad (2)$$

where $F_2^*(u, v)$ is complex conjugate of $F_2(u, v)$. The phase correlation $\mathrm{PC}(x, y)$ of two images is calculated by 2D inverse discrete Fourier transforms (IDFT) of $Q(u, v)$:

$$\mathrm{PC}(x,y) = F^{-1}(Q(u,v)) = \delta(x+\Delta x, y+\Delta y), \quad (3)$$

where $F^{-1}(\cdot)$ is IDFT function. $\delta(x + \Delta x,\ y + \Delta y)$ is a 2D pulse function which exists as peak at position $(\Delta x, \Delta y)$. The peak location $(\Delta x, \Delta y)$ corresponds to the translation between images.

Phase correlation is a common method to estimate the translation between images. Only phase information of images is utilized; thus it is almost not affected by noise and radiation difference and more robustness than spatial domain method. But the digital image is a discrete function whose Fourier transform is a discrete transform, so only the integer-pixel translation $(\mathrm{int}(\Delta x), \mathrm{int}(\Delta y))$ can be obtained by searching the peak location.

3. Improved Phase Correlation with Subpixel Precision

To estimate the subpixel translation, various algorithms have been proposed. In [23], Foroosh et al. achieved the subpixel estimation by approximating the Dirichlet function derived from the normalized cross-power spectrum. Nagashima et al. propose a fitting method to enhance the matching precision from integer-pixel level to subpixel level, which fits a curve surface by using the neighborhood data around phase correlation peak [21]. However, these methods only take into account the peak and its neighborhood; the distribution of phase correlation function is neglected; thus, the precision of translation estimation is low in stereovision of remotely sensed imagery. An improved phase correlation method used for subpixel estimation is designed in this section. The flow chart is shown in Figure 4. Due to the periodicity of DFT, an image can be considered to "wrap around" at an edge; therefore, discontinuities, which are not supposed to exist in real world, occur at every border in 2D DFT computation [21]. A 2D Hanning window function is applied to reduce the effect of discontinuities at image borders. The 2D Hanning window function is defined as

$$w(x,y) = \frac{1+\cos(\pi x/M)}{2}\frac{1+\cos(\pi y/N)}{2}. \quad (4)$$

The subpixel translation between two images can be obtained by downsampling high resolution images with integer-pixel translation. Therefore, the phase correlation of two images can be approximated by 2D sinc function:

$$\mathrm{PC}(x,y) \approx \frac{\sin(\pi(x+\Delta x))}{\pi(x+\Delta x)}\frac{\sin(\pi(y+\Delta y))}{\pi(y+\Delta y)}. \quad (5)$$

In theory, sinc function can approximate the distribution of phase correlation in ideal condition. However the phase correlation peak is decreased in remotely sensed images matching due to the interference of random noise, image aliasing, edge effects, and other influences. Therefore, the sinc function can not describe the distribution of phase correlation accurately. In our method, the sinc function is improved by introducing phase correlation coefficient:

$$\mathrm{PC}(x,y) \approx \alpha\frac{\sin(\pi(x+\Delta x))}{\pi(x+\Delta x)}\frac{\sin(\pi(y+\Delta y))}{\pi(y+\Delta y)}, \quad (6)$$

where α is the phase correlation coefficient, $\alpha \le 1$. When the translation is integer-pixel and there is no interference factor, $\alpha = 1$; when the translation is subpixel or there are interference factors, $\alpha < 1$. Due to this improved phase correlation method is applied to the stereovision of narrow baseline remotely sensed imagery, and the image pair is treated by epipolar rectification before matching. Thus, the phase correlation $\mathrm{PC}(x, y)$ can be separated in spatial domain, and a 1D function expression is given which only exists as translation in horizontal direction:

$$\mathrm{PC}_x(x) \approx \alpha\frac{\sin(\pi(x+\Delta x))}{\pi(x+\Delta x)}. \quad (7)$$

The peak position $(\Delta x, 0)$ is the translation which is expected to be estimated. To locate the high precision subpixel peak position, a peak evaluation method based on uniformly spaced sampling is proposed. Assume that p is the real peak position of sampled-data, as shown at the bottom left corner of Figure 4, and $p - k$ and $p + k$ are a pair of points located k pixels away from p. The phase correlation values $\mathrm{PC}_x(p - k)$, $\mathrm{PC}_x(p)$, and $\mathrm{PC}_x(p + k)$ of three sample points used for peak evaluation are satisfying the following relationship:

$$\alpha\frac{\sin(\pi(p-k+\Delta x))}{\pi(p-k+\Delta x)} = \mathrm{PC}_x(p-k) \quad (8a)$$

$$\alpha\frac{\sin(\pi(p+\Delta x))}{\pi(p+\Delta x)} = \mathrm{PC}_x(p) \quad (8b)$$

$$\alpha\frac{\sin(\pi(p+k+\Delta x))}{\pi(p+k+\Delta x)} = \mathrm{PC}_x(p+k). \quad (8c)$$

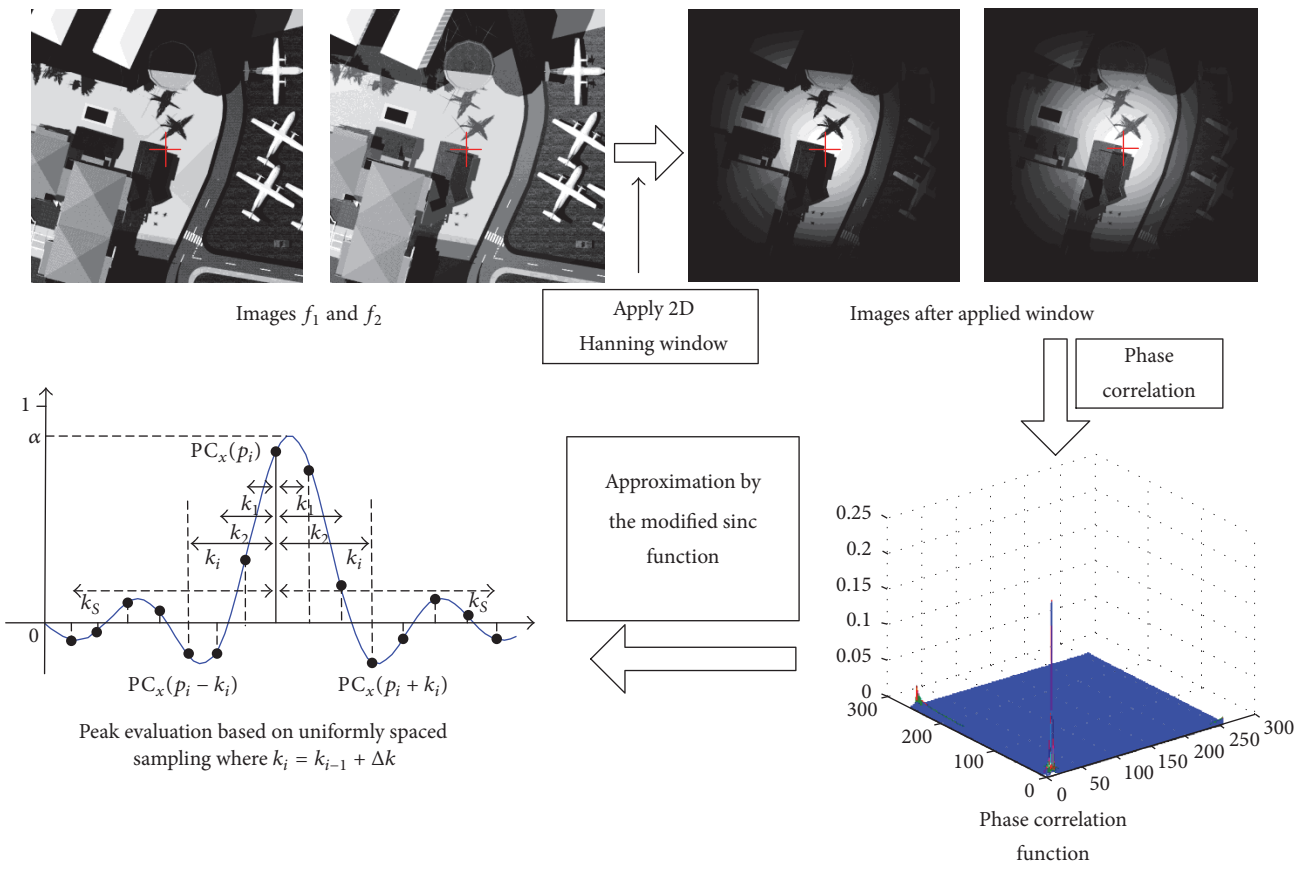

Figure 4: Flow chart of improved phase correlation image matching method.

Add (8c) to (8a); the above equation group can be rewritten as

$$\frac{\alpha}{\pi}\left(\sin\left(\pi\left(p+\Delta x\right)\right)\right) = \mathrm{PC}_x\left(p\right)\left(p+\Delta x\right) \tag{9a}$$

$$\begin{aligned}\frac{\alpha}{\pi}&\left(\sin\left(\pi\left(p-k+\Delta x\right)\right)+\sin\left(\pi\left(p-k+\Delta x\right)\right)\right)\\ &= \mathrm{PC}_x\left(p-k\right)\left(p-k+\Delta x\right)\\ &\quad+\mathrm{PC}_x\left(p+k\right)\left(p+k+\Delta x\right).\end{aligned} \tag{9b}$$

Equation (9b) can be rewritten by using the difference product formula:

$$\frac{\alpha}{\pi}\left(\sin\left(\pi\left(p+\Delta x\right)\right)\right) = \mathrm{PC}_x\left(p\right)\left(p+\Delta x\right) \tag{10a}$$

$$\begin{aligned}\frac{\alpha}{\pi}&\left(2\sin\left(\pi\left(p+\Delta x\right)\right)\cos\left(\pi k\right)\right)\\ &= \mathrm{PC}_x\left(p-k\right)\left(p-k+\Delta x\right)\\ &\quad+\mathrm{PC}_x\left(p+k\right)\left(p+k+\Delta x\right).\end{aligned} \tag{10b}$$

Add (10a) to (10b); the equation group ((10a) and (10b)) can be rewritten as

$$\begin{aligned}&\mathrm{PC}_x\left(p-k\right)\left(p-k+\Delta x\right)+\mathrm{PC}_x\left(p+k\right)\left(p+k+\Delta x\right)\\ &\quad=2\cdot\mathrm{PC}_x\left(p\right)\left(p+\Delta x\right)\cos\left(\pi k\right).\end{aligned} \tag{11}$$

The above equation can be expressed as a linear expression of Δx:

$$\begin{aligned}&\left(\mathrm{PC}_x\left(p-k\right)+\mathrm{PC}_x\left(p+k\right)-2\cdot\cos\left(\pi k\right)\mathrm{PC}_x\left(p\right)\right)\\ &\quad\cdot\Delta x\\ &\quad=2\cdot p\cdot\cos\left(\pi k\right)\mathrm{PC}_x\left(p\right)-\left(p-k\right)\mathrm{PC}_x\left(p-k\right)\\ &\qquad+\left(p+k\right)\mathrm{PC}_x\left(p+k\right).\end{aligned} \tag{12}$$

Through (12), the horizontal translation Δx with subpixel precision can be estimated:

$$\Delta x = \frac{2\cdot p\cdot\cos\left(\pi k\right)\mathrm{PC}_x\left(p\right)-\left(p-k\right)\mathrm{PC}_x\left(p-k\right)+\left(p+k\right)\mathrm{PC}_x\left(p+k\right)}{\mathrm{PC}_x\left(p-k\right)+\mathrm{PC}_x\left(p+k\right)-2\cdot\cos\left(\pi k\right)\mathrm{PC}_x\left(p\right)}. \tag{13}$$

To reduce the influence of noise, the peak evaluation is performed by selecting multiple sets of uniformly spaced sampled-data which are all the data on the x axis, and the least square is applied to solve the optimal translation. Assume that S sets of uniformly spaced sampled-data $(p_i - k_i, p_i, p_i - k_i)_{i \in S}$ are selected for peak evaluation; p_i, k_i are determined as follows: $p_1 = p_2 = \cdots = p_S = \arg\max_x \mathrm{PC}_x(x)$, $k_1 = 1$, $k_2 = k_1 + \Delta k, \ldots, k_S = k_{S-1} + \Delta k$, $(\Delta k = 1)$. Equation (12) can be rewritten as

$$\begin{bmatrix} a(p_1, k_1) \\ a(p_2, k_2) \\ \vdots \\ a(p_S, k_S) \end{bmatrix} \cdot \begin{bmatrix} \Delta x \\ \Delta x \\ \vdots \\ \Delta x \end{bmatrix} = \begin{bmatrix} b(p_1, k_1) \\ b(p_2, k_2) \\ \vdots \\ b(p_S, k_S) \end{bmatrix}, \tag{14}$$

where $a(p_i, k_i)_{i \in S} = \mathrm{PC}_x(p_i - k_i) + \mathrm{PC}_x(p_i + k_i) - 2 \cdot \cos(\pi k_i)\mathrm{PC}_x(p_i)$, and $b(p_i, k_i)_{i \in S} = 2 \cdot p_i \cdot \cos(\pi k_i)\mathrm{PC}_x(p_i) - (p_i - k_i)\mathrm{PC}_x(p_i - k_i) + (p_i + k_i)\mathrm{PC}_x(p_i + k_i)$. The objective of (14) is $\min(\sum_{i=1}^{S} |b(p_i, k_i) - a(p_i, k_i) \cdot \Delta x|^2)$. Assume that $A = [a(p_1, k_1), a(p_2, k_2), \ldots, a(p_S, k_S)]^T$ and $B = [b(p_1, k_1), b(p_2, k_2), \ldots, b(p_S, k_S)]^T$, then the horizontal translation Δx with subpixel precision can be obtained by solving the least square linear equation:

$$\Delta x = \left(A^T A\right)^{-1} A^T B. \tag{15}$$

4. Complete Subpixel Image Matching Algorithm

The input of our algorithm is rectified narrow baseline remotely sensed image pair, and output is the disparity with subpixel precision. Because the stability of phase correlation method is poor when the disparity search range is large [9], therefore, a multistep strategy is adopted in our technical frame, and the disparity estimation is divided into two steps: integer-pixel prematching and subpixel matching. The complete framework of our algorithm is shown in Figure 5. Firstly, integer-pixel disparity is estimated by employing an effective cross-based matching algorithm [25]. Then relationship of corresponding points is established under the guidance of integer-pixel disparity. The subimages are extracted through selecting the corresponding points as center. Finally, subpixel disparity is obtained by matching the subimages utilizing the improved phase correlation proposed in Section 3.

Assume that a narrow baseline remotely sensed image pair consists of left image L and right image R, which can be expressed as a classic stereo model $L(x, y) = R(x + d(x, y), y)$. The disparity $d(x, y)$ is used to describe the geometric position variation between L and R, which consists of two parts, integer-pixel disparity $d_z(x, y)$ and subpixel disparity $d_s(x, y)$; that is, $d(x, y) = d_z(x, y) + d_s(x, y)$. The details of our subpixel image matching algorithm are described as follows from step (a) to step (g).

(a) Assume (x_0, y_0) is the pixel which is to be matched. In the first step, the cross-based support window of (x_0, y_0) is defined. Firstly, an upright cross is established for (x_0, y_0). It consists of two orthogonal line segments: horizontal segment $\varphi_H(x_0, y_0)$ and vertical segment $\varphi_V(x_0, y_0)$. A quadruple $\{h^-, h^+, v^-, v^+\}$ denotes the left, right, up, and bottom arm length, respectively, and the length of each arm is determined by searching for the extreme point in that direction based on the color similarity. The upright cross skeleton is defined as

$$\begin{aligned} &\varphi_H(x_0, y_0) \\ &\quad = \{(x, y) \mid x \in [x_0 - h^-, x_0 + h^+],\ y = y_0\}, \\ &\varphi_V(x_0, y_0) \\ &\quad = \{(x, y) \mid x = x_0,\ y \in [y_0 - v^-, y_0 + v^+]\}. \end{aligned} \tag{16}$$

Then the cross-based support window $\varphi(x_0, y_0)$ is defined based on the upright cross skeleton. $\varphi(x_0, y_0)$ is a combination of each horizontal segment $\varphi_H(x, y)$ where (x, y) traverses over the vertical segment $\varphi_V(x_0, y_0)$. The formula of $\varphi(x_0, y_0)$ is defined as

$$\varphi(x_0, y_0) = \bigcup_{(x,y) \in \varphi_V(x_0, y_0)} \varphi_H(x, y). \tag{17}$$

(b) The matching cost of (x_0, y_0) is calculated. Firstly, the initial matching cost C_{x,y,d_z} of each pixel in the support window is calculated:

$$\begin{aligned} C_{x,y,d_z} = {} & (1 - \beta) \cdot \min\left(\left|L(x, y) - R(x + d_z, y)\right|, \tau_1\right) \\ & + \beta \\ & \cdot \min\left(\left|\nabla_x L(x, y) - \nabla_x R(x + d_z, y)\right|, \tau_2\right), \end{aligned} \tag{18}$$

where ∇_x is horizontal gradient, β balances the color and gradient terms, and τ_1, τ_2 are truncation values. Then the matching cost $C^A_{x_0,y_0,d_z}$ of (x_0, y_0) is aggregated:

$$C^A_{x_0,y_0,d_z} = \sum_{(x,y) \in \varphi(x_0, y_0)} C_{x,y,d_z}. \tag{19}$$

(c) The integer-pixel disparity $d_z(x_0, y_0)$ of (x_0, y_0) is estimated by winner-takes-all strategy:

$$d_z(x_0, y_0) = \arg\min_{d_z \in S_d} C^A_{x_0,y_0,d_z}, \tag{20}$$

where S_d is the searching range of disparity.

(d) The relationship of corresponding points is established under the guidance of integer-pixel disparity. Assume that the integer-pixel disparity of pixel (x_0, y_0) in L is $d_z(x_0, y_0)$; the corresponding point of (x_0, y_0) in R is $(x_0 + d_z(x_0, y_0), y_0)$.

(e) The subimages $L_s(x_0, y_0)$ and $R_s(x_0, y_0)$ with same size are extracted through selecting the corresponding points as the center. Because the selection of the two subimages is based on the guidance of the integer-pixel disparity, thus there is only a small range of horizontal translation between $L_s(x_0, y_0)$ and $R_s(x_0, y_0)$.

(f) The subpixel horizontal translation Δx between $L_s(x_0, y_0)$ and $R_s(x_0, y_0)$ is estimated by using the improved phase correlation method proposed in Section 3. The Δx is

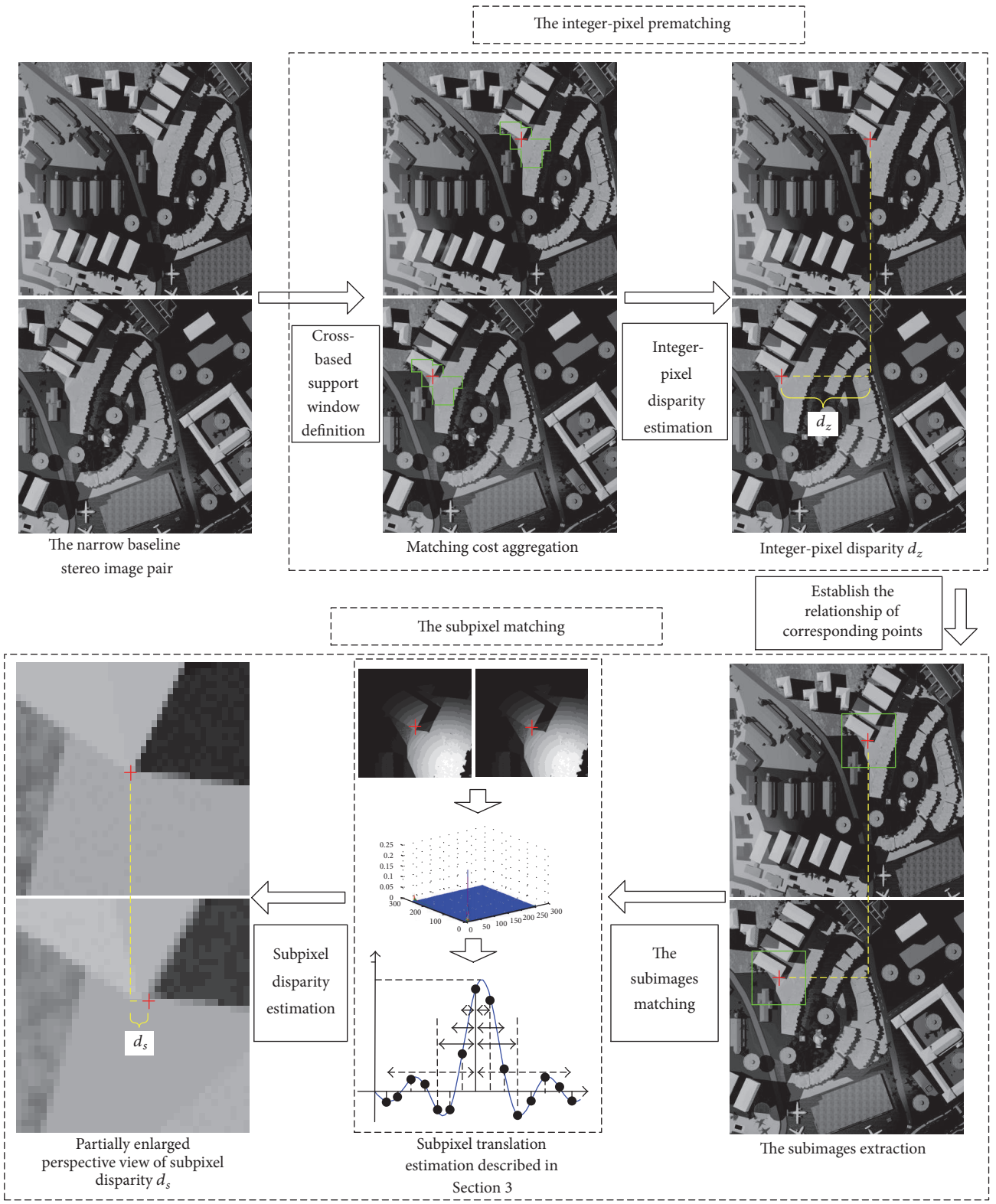

Figure 5: The complete framework of our subpixel image matching algorithm.

Table 1: General information of the test image pairs.

Test number	Data source	Image size	GSD (m)	Location	True disparity (pixels)
1	Pleiades	7590 × 6510	0.5	USA: Washington	8.738
2	SPOT-5	2050 × 2100	2.5	China: Beijing	8.738
3	SPOT-6	2015 × 1950	1.5	China: Beijing	8.738
4	WorldView-3	2000 × 2000	0.3	Spain: Madrid	8.738
5	GeoEye-1	3000 × 3000	0.4	Holland: Amsterdam	8.738
6	GF-2	4500 × 4750	0.8	China: Karamay	8.738

equivalent to the subpixel disparity $d_s(x_0, y_0)$ of the center pixel (x_0, y_0).

(g) Finally, the disparity result is obtained by combining the integer-pixel disparity and the subpixel disparity; that is, $d(x_0, y_0) = d_z(x_0, y_0) + d_s(x_0, y_0)$.

5. Experiments and Analysis

We test the proposed subpixel matching method for stereovision of narrow baseline remotely sensed imagery on a standard personal computer with Intel(R) Core(TM) i7 CPU, and the algorithm is implemented utilizing VS2010+OpenCV. The results analysis includes two aspects: precision analysis and complexity analysis. Constant parameter settings are used for all experiments. The parameters of this method are set as $\beta = 0.11$, $\tau_1 = 7/255$, and $\tau_2 = 2/255$.

5.1. Test on Simulated Narrow Baseline Remotely sensed Images Generated by Translation. To evaluate the matching precision of proposed method, six urban scenes of narrow baseline remotely sensed image pairs, including Pleiades, SPOT-5, SPOT-6, WorldView-3, and GF-2, are used to perform image matching. For each image pair, the original image is utilized as the reference image (often called the left image), and the original image is moved 8.738 pixels along the x-axis as the target image (called the right image). Thus the true disparity is known to be 8.738 pixels for all the matching points of each image pair. Table 1 shows the general information of the test image pairs used in these experiments.

Figure 6 shows the distribution of matched points for the test narrow baseline remotely sensed image pairs. Because the image size is different for each image pair, the step size of grid is different too. The step sizes of grid in Tests 1–6 are set to 540 × 540 pixels, 160 × 160 pixels, 180 × 180 pixels, 170 × 170 pixels, 300 × 300 pixels, and 380 × 380 pixels.

In order to evaluate the matching precision of our method quantitatively, interpolation based method [14], fitting based method [15], and traditional phase correlation method [23] are used to compare with our method. Root mean square error (RMSE) and mean error of matched points are used as the assessment indices to evaluate these methods. Figure 7 shows quantitative evaluation results for the four subpixel image matching methods. Here the traditional phase correlation is called traditional PC for short. Figure 8 shows statistical results of the quantitative evaluation. Figure 8(a) shows statistical results where the RMSE is less than or equal to 0.05 pixels. Figure 8(b) shows statistical results where the RMSE is greater than 0.05 pixels and less than 0.1 pixels. Figure 8(c) shows statistical results where the RMSE is greater than or equal to 0.1 pixels. From the experimental results, one can see that the two PC methods have a high matching precision, and the precision is better than that of interpolation method and fitting method. In addition, the matching precision is related to the spatial resolution of the images. High spatial resolution corresponds to a high matching precision. Because the peak evaluation method based on uniformly spaced sampling is designed to fit the phase correlation function, our method outperforms the traditional PC method, about 66% matched points of our method with RMSE less than or equal to 0.05 pixels.

5.2. Test on Simulated Narrow Baseline Remotely sensed Images. To evaluate the precision of DEM extraction by using the disparity estimated by our method, a simulated narrow baseline remotely sensed image pair provided by Beijing Institute of Space Mechanics and Electricity is used to perform image matching. The simulated narrow baseline remotely sensed image pair is generated by SE-WORKBENCH software. The attached parameters file of the image pair not only provides the true disparity, but also provides the true elevation of targets and buildings in the scene. Therefore, the precision of disparity and elevation estimated by our method can be evaluated carefully. Table 2 shows the general information of the test image pair used in these experiments. The B/H ratio of the image pair is 0.05, and spatial resolution is 0.3 meters/pixel. Overlap ratio of left and right images is 60%, and the overlap area includes 22 targets and 40 buildings. Figure 9 shows the simulated narrow baseline remotely sensed image pair and distribution of targets and buildings. Figure 9(a) is the image pair, Figure 9(b) is the distribution of targets, and Figure 9(c) is the distribution of buildings. The targets and buildings are marked with red numbers. Figure 10 shows the matching results. Figure 10(a) is the distribution of matched points for the buildings. Figure 10(b) is the distribution of matched points for the targets.

To evaluate the matching precision of our method quantitatively, interpolation based method [14], fitting based method [15], and traditional phase correlation method [23] are used to compare with our method. RMSE of disparity and mean elevation error are used as the assessment indices to evaluate the precision of four methods, where the elevation

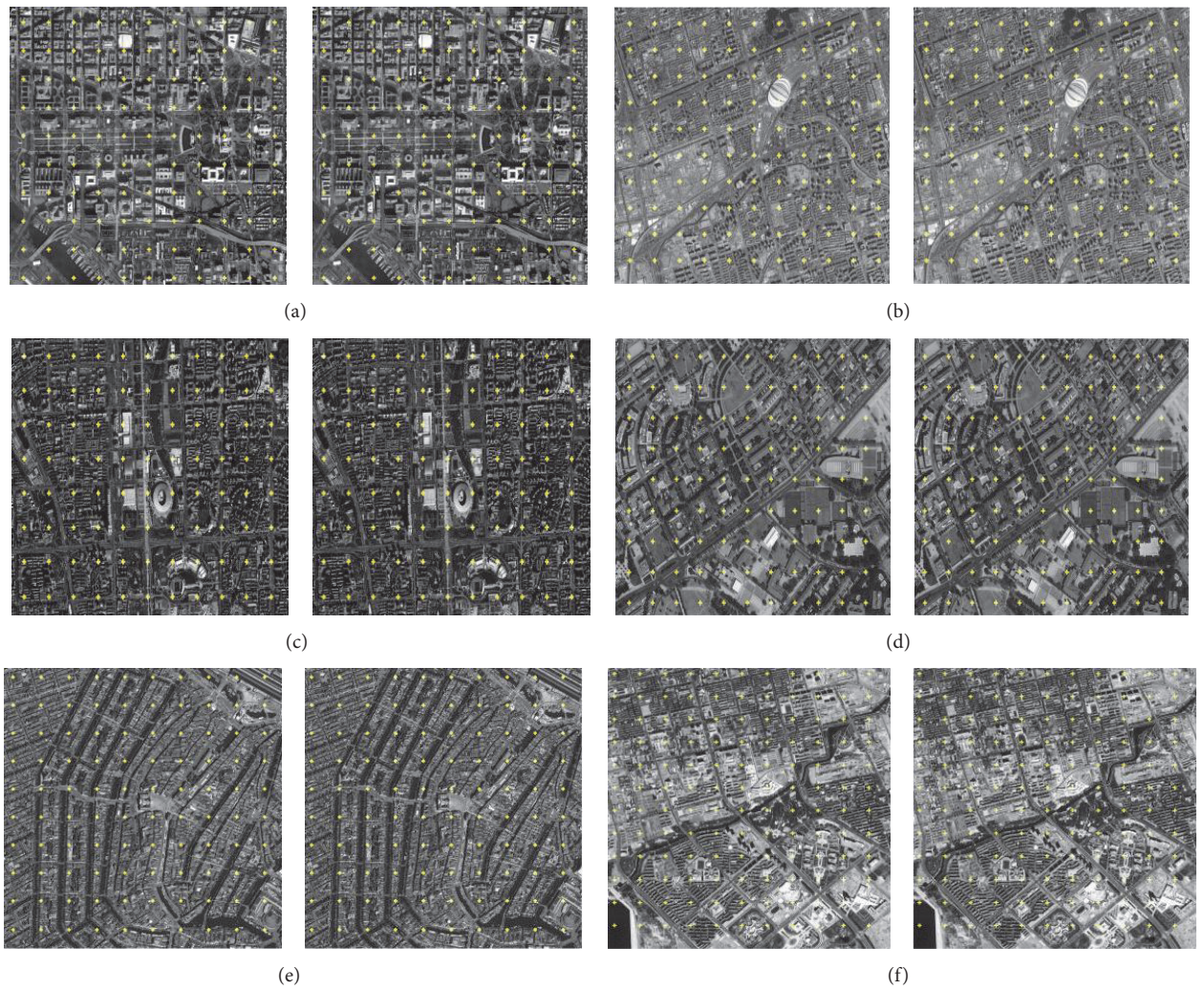

Figure 6: The distribution of matched points for the test narrow baseline remotely sensed image pairs. (a–f) are the results of Pleiades, SPOT-5, SPOT-6, WorldView-3, GeoEye-1, and GF-2 image pairs, respectively.

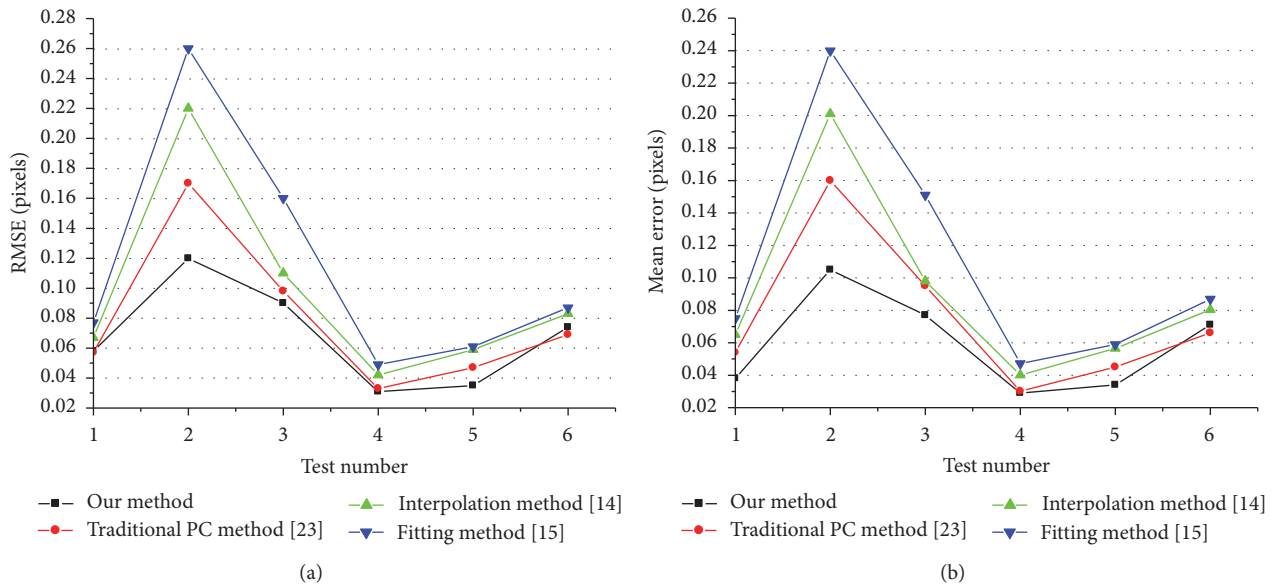

Figure 7: The quantitative evaluation results for the four subpixel image matching methods. (a) RMSE and (b) mean error.

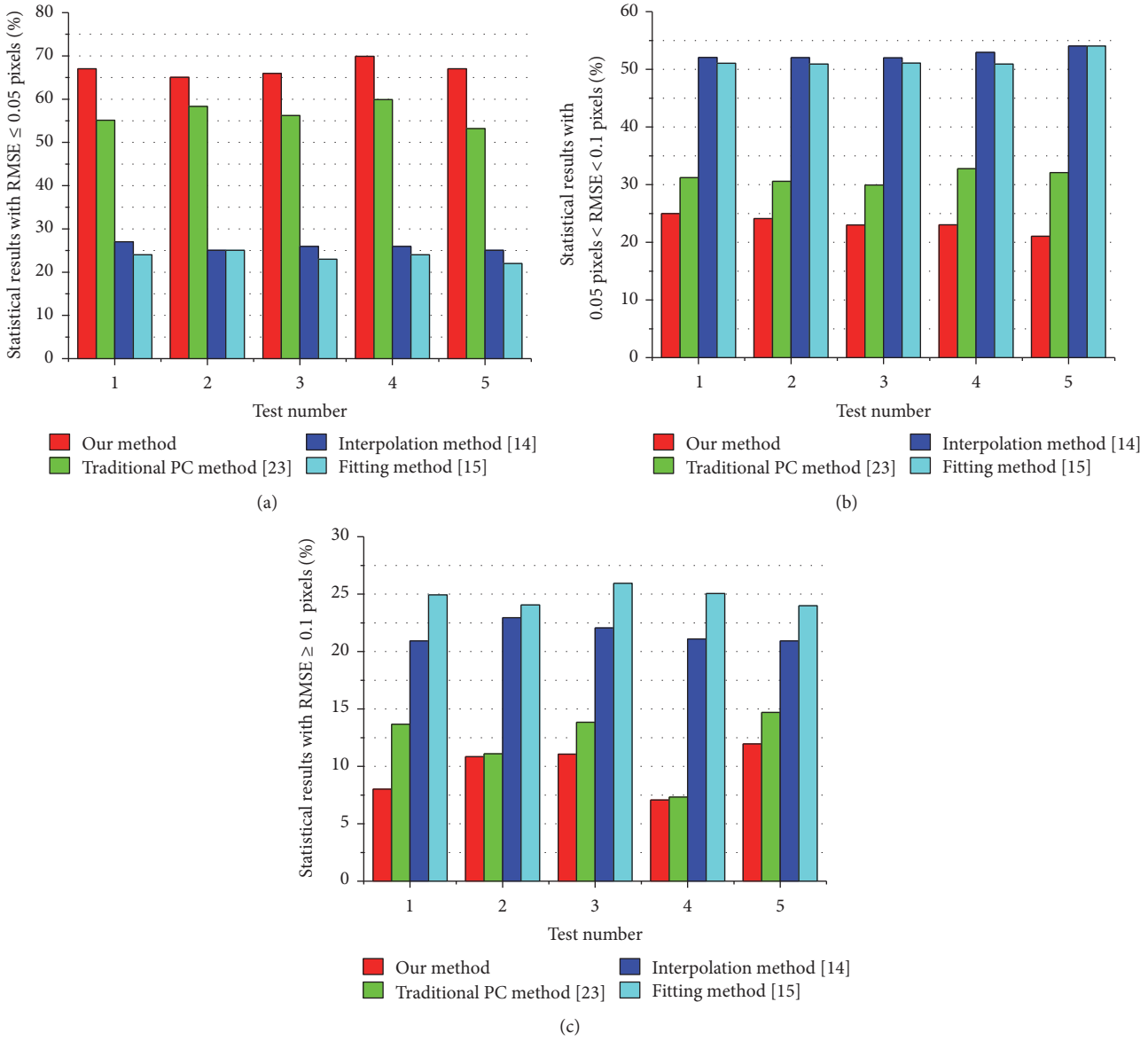

Figure 8: The statistical results of the quantitative evaluation. (a) Statistical results of RMSE less than or equal to 0.05 pixels; (b) statistical results of RMSE greater than 0.05 pixels and less than 0.1 pixels; and (c) statistical results of RMSE greater than or equal to 0.1 pixels.

error is the absolute difference between the true and the extracted elevation. The simulated narrow baseline remotely sensed image pair is matched 300 times by each subpixel image matching method. Figures 11 and 12 show the statistical results of four methods for targets and buildings, respectively. The results show that the RMSE and the mean elevation error obtained by our method are lower than the other three methods for most targets and buildings. Table 3 shows the average values of RMSE and mean elevation error. The true average elevation of 22 targets is 67.818 m, and the true average elevation of 40 buildings is 112.353 m. According to the statistical results in Table 3, the mean elevation error of targets estimated by our method is 0.303 m, and the mean elevation error of buildings estimated by our method is 0.406 m. Such precision can satisfy the requirements for stereovision of narrow baseline remotely sensed imagery; therefore, it is proved that the image matching method based on phase correlation proposed in this paper has practical application value.

5.3. Computational Complexity. Assume that there are N_1 points needed to be matched. In integer-pixel prematching step of our algorithm, the complexity of constructing the cross-based support window for each point is $O(1)$, and the total complexity for all points of this prematching step is $O(N_1 \cdot d)$, where d is the disparity range.

In the subpixel matching step, the core algorithm is based on the phase correlation; therefore, the complexity is unrelated to the disparity range but related to the size of subimage. Assume that there are N_2 pixels in the extracted subimage.

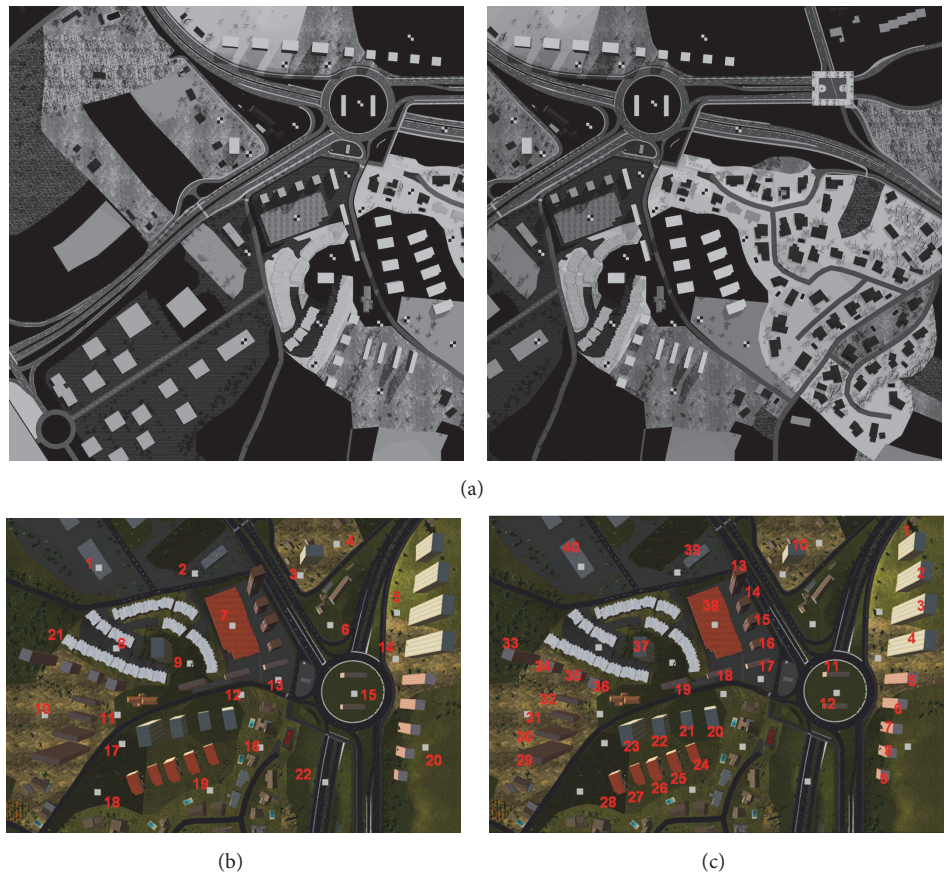

(a)

(b)

(c)

FIGURE 9: The simulated narrow baseline remotely sensed image pair and distribution of targets and buildings. (a) The image pair with a B/H ratio of 0.05. (b) The distribution of targets. (c) The distribution of buildings.

The complexity of fast DFT is $O(N_2 \cdot \log N_2)$, the complexity of Hanning window is $O(N_2)$, the complexity of normalized cross-power spectrum is $O(N_2)$, and the complexity of IDFT of normalized cross-power spectrum is $O(N_2 \cdot \log N_2)$. The peak evaluation is a least square fitting operation for S sets of uniformly spaced sampled-data essentially. The minimum value of S is 1; that is, the peak position is located at the most left or right of sampled-data. However, the maximum value of S is $((\sqrt{N_2} - 1)/2)$; this means the peak position is located at the center of sampled-data; thus $S \leq ((\sqrt{N_2} - 1)/2)$. The complexity of subpixel peak position evaluation utilizing the least square method is $O((\sqrt{N_2}-1)/2)^2$, which is equivalent to $O(N_2)$. The complexity of a single point matching in subpixel matching step is $O(N_2 \cdot \log N_2)$; thus the complexity of total points is $O(N_1 \cdot N_2 \cdot \log N_2)$. The complexity of complete image matching algorithm is $O(N_1 \cdot d) + O(N_1 \cdot N_2 \cdot \log N_2)$. Because the complexity of subpixel matching is higher than that of integer-pixel prematching, the complexity of our algorithm is $O(N_1 \cdot N_2 \cdot \log N_2)$.

In order to clearly illustrate the complexity of our algorithm, we compare with the classical normalized cross correlation (NCC) algorithm [2]. Assume that the support window of NCC is φ; in the practical image matching, $\varphi \approx N_2 \ll N_1$. When $\log N_2 \approx d$, the complexity of our method is similar to that of NCC. Generally, the size of subimage is 30×30~40×40 pixels; the number of pixels in subimage is 900~1600; thus the value range of $\log N_2$ is 9.814~10.644. The disparity range of narrow baseline stereo image pair is usually within 20 pixels. In our experiment, the disparity range is 17 pixels; $\log N_2 \approx d$ is established; therefore, the complexity of our method is similar to that of the classical NCC method.

6. Conclusion

Through the analysis of narrow baseline remotely sensed imagery stereovision, a subpixel image matching approach based on improved phase correlation is proposed. The cross-based local matching method is employed for prematching the image pair, and the obtained integer-pixel disparity reduces the search range of subpixel matching. A high precision subpixel matching step is implemented under the guidance of integer-pixel disparity. A peak evaluation method based on uniformly spaced sampling is designed to improve the precision of disparity estimation. The experimental results show that our method has superior performance on precision and efficiency, and it is beneficial to the stereovision of narrow baseline remotely sensed imagery.

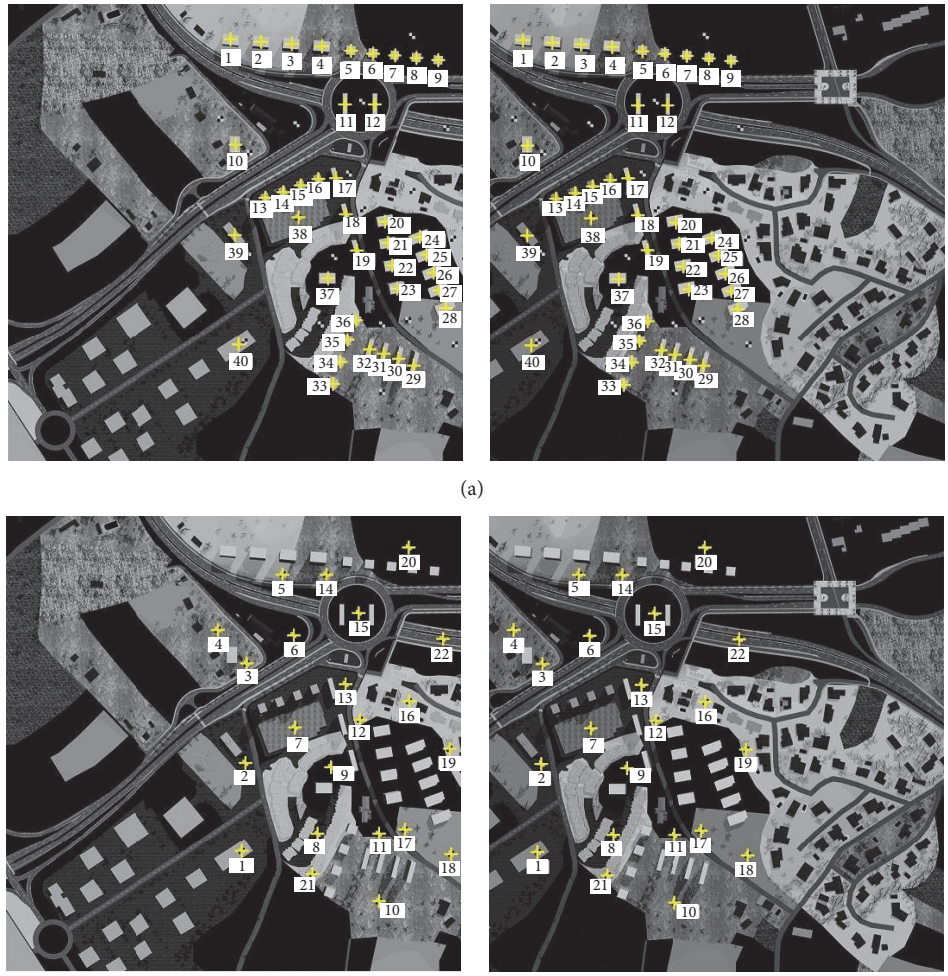

(a)

(b)

Figure 10: The matching results. (a) The distribution of matched points for the buildings. (b) The distribution of matched points for the targets.

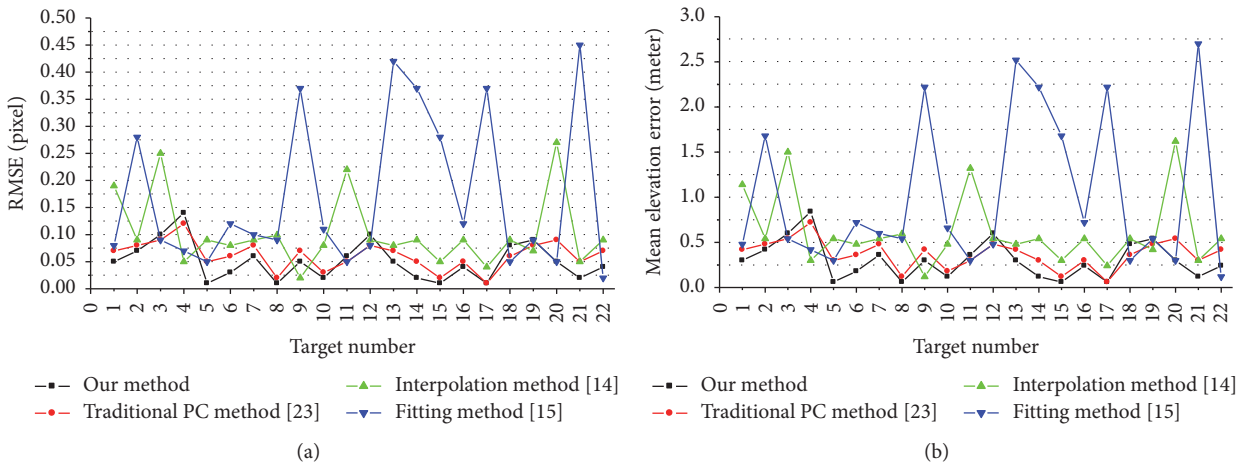

Figure 11: The statistical results of targets. (a) Comparison of RMSE. (b) Comparison of mean elevation error.

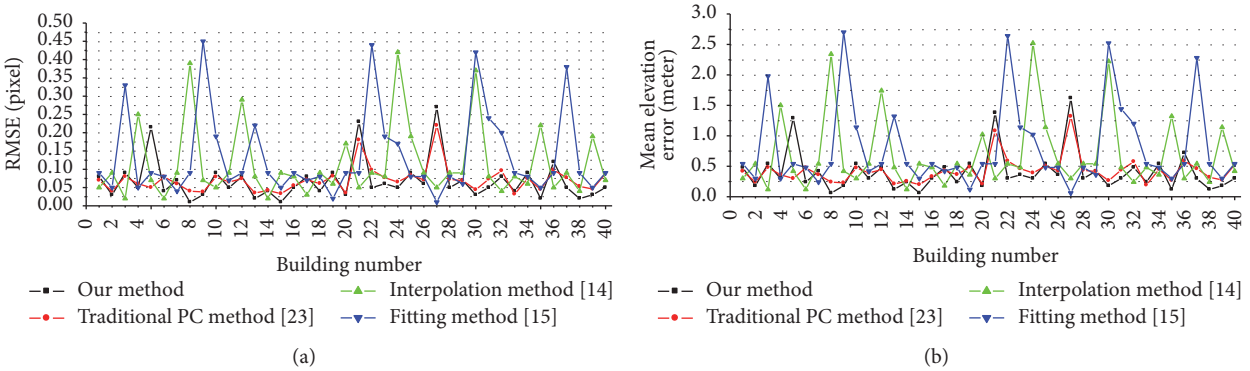

Figure 12: The statistical results of buildings. (a) Comparison of RMSE. (b) Comparison of mean elevation error.

Table 2: The general information of the test image pair.

Target number	Elevation (meter)	True disparity (pixel)	Building number	Elevation (meter)	True disparity	Building number	Elevation (meter)	True disparity (pixel)
1	73	12.167	1	111.42	18.570	21	97.3	16.217
2	65	10.833	2	131.54	21.923	22	131.33	21.888
3	63	10.500	3	147.13	24.522	23	165.92	27.653
4	65	10.833	4	153.77	25.628	24	134.85	22.475
5	67	11.167	5	123.43	20.572	25	85.14	14.190
6	61	10.167	6	104.77	17.462	26	92.28	15.380
7	67	11.167	7	98.22	16.370	27	71.51	11.918
8	82	13.667	8	88.81	14.802	28	83.5	13.917
9	74	12.333	9	75.07	12.512	29	169.2	28.200
10	72	12.000	10	98.46	16.410	30	131.22	21.870
11	75	12.500	11	79.79	13.298	31	98.42	16.403
12	65	10.833	12	72.94	12.157	32	98.42	16.403
13	60	10.000	13	155.81	25.968	33	154.57	25.762
14	64	10.667	14	111.81	18.635	34	115.5	19.250
15	63	10.500	15	133.81	22.302	35	105.21	17.535
16	61	10.167	16	100.81	16.802	36	133.07	22.178
17	76	12.667	17	92.21	15.368	37	157.59	26.265
18	64	10.667	18	120.38	20.063	38	66.3	11.050
19	62	10.333	19	162.39	27.065	39	72.5	12.083
20	66	11.000	20	145.29	24.215	40	72.44	12.073
21	92	15.333	—	—	—	—	—	—
22	55	9.167	—	—	—	—	—	—

Table 3: The RMSE and mean elevation error of four methods.

Algorithms	Targets		Buildings	
	RMSE (pixel)	Mean elevation error (meter)	RMSE (pixel)	Mean elevation error (meter)
Interpolation method [14]	0.103	0.619	0.114	0.681
Fitting method [15]	0.169	1.012	0.133	0.797
Traditional PC method [23]	0.061	0.368	0.071	0.422
Our method	**0.051**	**0.303**	**0.068**	**0.406**

Competing Interests

The authors declare no conflict of interests.

Authors' Contributions

Ning Ma proposed the idea of the method. Ning Ma and Yubo Men performed the validation experiment of the method. Ning Ma, Chaoguang Men, and Xiang Li wrote this paper. All the authors read and approved the final paper.

Acknowledgments

This work was supported by National Natural Science Foundation of China (Grant nos. 11547157 and 61100004), Natural Science Foundation of Heilongjiang Province of China (Grant no. F201320), and Harbin Municipal Science and Technology Bureau (Grant no. 2014RFQXJ073).

References

[1] T. Long, W. Jiao, G. He, and Z. Zhang, "A fast and reliable matching method for automated georeferencing of remotely-sensed imagery," *Remote Sensing*, vol. 8, no. 1, article 56, 2016.

[2] J. Delon and B. Rougé, "Small baseline stereovision," *Journal of Mathematical Imaging and Vision*, vol. 28, no. 3, pp. 209–223, 2007.

[3] C. C. Pham and J. W. Jeon, "Domain transformation-based efficient cost aggregation for local stereo matching," *IEEE Transactions on Circuits and Systems for Video Technology*, vol. 23, no. 7, pp. 1119–1130, 2013.

[4] D. Fan, E. Shen, L. Li et al., "Small baseline stereo matching method based on phase correlation," *Journal of Geomatics Science and Technology*, vol. 30, pp. 154–157, 2013.

[5] G. L. K. Morgan, J. G. Liu, and H. Yan, "Precise subpixel disparity measurement from very narrow baseline stereo," *IEEE Transactions on Geoscience and Remote Sensing*, vol. 48, no. 9, pp. 3424–3433, 2010.

[6] J.-L. Bian, C.-G. Men, and X. Li, "A fast stereo matching method based on small baseline," *Journal of Electronics and Information Technology*, vol. 34, no. 3, pp. 517–522, 2012.

[7] N. Sabater, J. M. Morel, and A. Almansa, "How accurate can block matches be in stereo vision?" *SIAM Journal on Imaging Sciences*, vol. 4, pp. 472–500, 2011.

[8] L. Igual, J. Preciozzi, L. Garrido et al., "Automatic low baseline stereo in urban areas," *Inverse Problems and Imaging*, vol. 1, pp. 318–348, 2007.

[9] E. Shen, D. Fan, and X. Sun, "Smallbaseline stereo matching method based on SGM and phase correlation," *Journal of China University of Mining and Technology*, vol. 44, no. 1, pp. 183–188, 2015.

[10] N. Sabater, G. Blanchet, L. Moisan, A. Almansa, and J.-M. Morel, "Review of low-baseline stereo algorithms and benchmarks," in *Image and Signal Processing for Remote Sensing XVI, 783005*, 12, Toulouse, France, October 2010.

[11] T. Arai and A. Iwasaki, "Fine image matching for narrow baseline stereovision," in *Proceedings of the 32nd IEEE International Geoscience and Remote Sensing Symposium (IGARSS '12)*, pp. 2336–2339, Munich, Germany, July 2012.

[12] J. Inglada, V. Muron, D. Pichard, and T. Feuvrier, "Analysis of artifacts in subpixel remote sensing image registration," *IEEE Transactions on Geoscience and Remote Sensing*, vol. 45, no. 1, pp. 254–264, 2007.

[13] V.-C. Miclea, C.-C. Vancea, and S. Nedevschi, "New sub-pixel interpolation functions for accurate real-time stereo-matching algorithms," in *Proceedings of the 11th IEEE International Conference on Intelligent Computer Communication and Processing (ICCP '15)*, pp. 173–178, IEEE, Cluj-Napoca, Romania, September 2015.

[14] I. Haller and S. Nedevschi, "Design of interpolation functions for subpixel-accuracy stereo-vision systems," *IEEE Transactions on Image Processing*, vol. 21, no. 2, pp. 889–898, 2012.

[15] C. Stentoumis, L. Grammatikopoulos, I. Kalisperakis, and G. Karras, "On accurate dense stereo-matching using a local adaptive multi-cost approach," *ISPRS Journal of Photogrammetry and Remote Sensing*, vol. 91, pp. 29–49, 2014.

[16] J. Žbontar and Y. Le Cun, "Computing the stereo matching cost with a convolutional neural network," in *Proceedings of the IEEE Conference on Computer Vision and Pattern Recognition (CVPR '15)*, pp. 1592–1599, Boston, Mass, USA, June 2015.

[17] C. Shi, G. Wang, X. Yin, X. Pei, B. He, and X. Lin, "High-accuracy stereo matching based on adaptive ground control points," *IEEE Transactions on Image Processing*, vol. 24, no. 4, pp. 1412–1423, 2015.

[18] N. Jiang, Y. Qu, and Y. Li, "Fast sub-pixel accuracy stereo image matching based on disparity plane," in *Proceedings of the International Conference on Optical Instruments and Technology: Optoelectronic Imaging and Processing Technology*, Beijing, China, May 2015.

[19] F. Besse, C. Rother, A. Fitzgibbon, and J. Kautz, "PMBP: PatchMatch Belief Propagation for correspondence field estimation," *International Journal of Computer Vision*, vol. 110, no. 1, pp. 2–13, 2014.

[20] S. Xu, F. Zhang, X. He, X. Shen, and X. Zhang, "PM-PM: PatchMatch with potts model for object segmentation and stereo matching," *IEEE Transactions on Image Processing*, vol. 24, no. 7, pp. 2182–2196, 2015.

[21] S. Nagashima, T. Aoki, T. Higuchi, and K. Kobayashi, "A subpixel image matching technique using phase-only correlation," in *Proceedings of the International Symposium on Intelligent Signal Processing and Communications (ISPACS '06)*, pp. 701–704, IEEE, Yonago, Japan, December 2006.

[22] H. S. Stone, M. T. Orchard, E.-C. Chang, and S. A. Martucci, "A fast direct Fourier-based algorithm for subpixel registration of images," *IEEE Transactions on Geoscience and Remote Sensing*, vol. 39, no. 10, pp. 2235–2243, 2001.

[23] H. Foroosh, J. B. Zerubia, and M. Berthod, "Extension of phase correlation to subpixel registration," *IEEE Transactions on Image Processing*, vol. 11, no. 3, pp. 188–199, 2002.

[24] X. Tong, Y. Xu, Z. Ye et al., "An improved phase correlation method based on 2-D plane fitting and the maximum kernel density estimator," *IEEE Geoscience and Remote Sensing Letters*, vol. 12, no. 9, pp. 1953–1957, 2015.

[25] J. Lu, K. Shi, D. Min, L. Lin, and M. N. Do, "Cross-based local multipoint filtering," in *Proceedings of the IEEE Conference on Computer Vision and Pattern Recognition (CVPR '12)*, pp. 430–437, IEEE, Providence, RI, USA, June 2012.

Hindawi
Mathematical Problems in Engineering
Volume 2017, Article ID 2819795, 16 pages
https://doi.org/10.1155/2017/2819795

Research Article

Implications of a Spatial Multicriteria Decision Analysis for Urban Development in Ulaanbaatar, Mongolia

Purevtseren Myagmartseren,[1] Myagmarsuren Buyandelger,[2] and S. Anders Brandt[3]

[1]*Department of Geography, School of Arts and Science, National University of Mongolia, 14201-46A Ulaanbaatar, Mongolia*
[2]*Land Administration Department of Capital City, 15160 Ulaanbaatar, Mongolia*
[3]*Department of Industrial Development, IT and Land Management, Faculty of Engineering and Sustainable Development, University of Gävle, 801 76 Gävle, Sweden*

Correspondence should be addressed to S. Anders Brandt; sab@hig.se

Received 28 October 2016; Accepted 26 December 2016; Published 15 February 2017

Academic Editor: Huade Guan

New technology has provided new tools for effective spatial planning. Through the example of locating suitable sites for urban development in Ulaanbaatar, this paper illustrates how multicriteria decision analysis and geographical information systems can be used for more effective urban planning. Several constraint and factor criteria were identified, transformed into map layers, and weighted together using the analytic hierarchy process. Besides localization results, this study shows the effect of using poor elevation data and how a sensitivity analysis can be applied to yield further information, spot weighting weaknesses, and assess the quality of the criteria.

1. Introduction

1.1. Background. Spatial planning for urban development is always associated with different types of decision-making problems and strategies, and the outcomes of planning will clearly differ depending on who the stakeholders and analysts are, together with which approaches and techniques are used. Until as recent as the last decade, most spatial planning activities worldwide have been done without the use of geographic information systems (GIS) and multicriteria decision analysis (MCDA) technologies, and even today they are rarely combined, despite the fact that most planning organizations have sufficient computer and software resources. For example, Bhatta [1, p. 57] stated "that compared to the swift adoption of GIS, urban analysts have been slower to embrace technical developments in spatial analysis." The reason for this lack of use of spatial-analytical tools that may be beneficial for planning can partly be linked to a shortage of domain-specific expertise among spatial planners, or as Berke et al. [2, p. 91] put it: "Without a planning staff skilled in computer applications, the new technology is of little use." Most critical is "the 'soft' side of the 'technology package': technique, organization, and knowledge" (Klosterman [3, p. 4]). Therefore, nowadays many university programs in planning try to incorporate GIS in their program curricula, but so far most programs do not show any explicit content of the combination of GIS and MCDA in their course syllabi. Although there is a slow increase of using these tools by university students and researchers, to a large extent planning practitioners are still unaware of the opportunities these tools provide, especially in developing countries.

1.2. Multicriteria Decision Analysis for Spatial Planning. One of the biggest challenges local governments and community groups face today is to find new areas for development in a sustainable way, without degrading land values. GIS and MCDA together provide tools for handling such natural resource management issues (National Research Council [4]; Malczewski [5]; Chen et al. [6]). In short, GIS-based MCDA takes data (input) and combines it into a weighted map (output). As GIS is capable of handling and combining different types of data (both nonspatial and spatial as well as multitemporal and multiscale) in a time-efficient and cost-effective

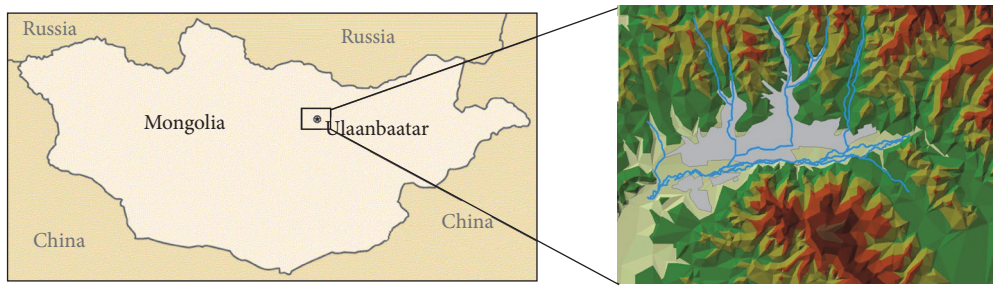

Figure 1: Map over the study area. (a) Location of Ulaanbaatar; (b) TIN model with rivers and urban areas (gray = built-up area; light green–brown = TIN).

way, there has been a steady increase in interest for using GIS together with MCDA techniques (Chen et al. [6]). Furthermore, the previous conventional map overlay approaches have been considerably advanced thanks to the integration of MCDA techniques with GIS (Malczewski [5]), and therefore local governments and community groups, among others, have started to implement the technology together with more sophisticated spatial analysis (National Research Council [4]). For successful implementation of spatial MCDA two things are of critical importance (Malczewski [5, p. 33]):

(i) "The GIS capabilities of data acquisition, storage, retrieval, manipulation, and analysis"

(ii) "The MCDM capabilities for combining the geographical data and the decision maker's preferences into unidimensional values of alternative decisions"

With the advent of powerful personal computers, practical MCDA tools, and user-friendly GIS, a number of studies have been carried out showing the usefulness of these techniques. With respect to land management, already in the 1960s the Land Inventory branch of the Canadian government and the Harvard Lab for Computer Graphics and Spatial Analysis created a GIS for developing land management plans (Malczewski [5]). Examples from the 80s and 90s include Lyle and Stutz [7], who looked at urban suitability modeling, and Miller et al. [8], who looked at potential sites for greenway development in a town, and more recent ones encompass Berke et al. [2], Carr and Zwick [9], Jain and Subbaiah [10], Liu et al. [11], Zucca et al. [12], Yang et al. [13], Önüt et al. [14], Park et al. [15], and Rikalovic et al. [16].

1.3. Aims. Mongolia is a post-communist country, and together with many others, like post-Soviet states, planning practitioners have been used to plan the cities without any involvement of citizens, making the planning process both very straightforward, fast, and without any interruptions in the initial project periods. Today, many of these countries have new legislation requiring public participation input and at the same time the technology and higher education may have fallen behind. As to our knowledge, no scientific studies have been reported on physical planning in Mongolia where spatial MCDA is used. Together with the fact that most spatial MCDA studies are carried out by specialists, not working in regular planning departments in the public sector, and for many developing countries they do not even exist, this justifies the need for examples illustrating the advantages and opportunities these tools provide. Then the planning process can benefit from technology (technical point of view), as well as from understanding of the underlying problem and democratic perspectives (social points of view).

Taking Ulaanbaatar as an example, the general scope of this paper is to bring practitioners, especially those in developing countries, knowledge of the opportunities of combining MCDA with GIS. This will be achieved through fulfilling the following objectives:

(i) Illustrate how MCDA and GIS can be used in the planning process for new urban areas, in order to raise the awareness among planners when strong domain knowledge is lacking, and present a strategy for locating new urban areas.

(ii) Identify relevant criteria for carrying out a spatial MCDA for new urban area development.

(iii) Compare different resolution of the digital elevation data to see how results are affected.

(iv) Illustrate how the sensitivity analysis can contribute to see if the relative weights of criteria are robust.

The structure of the paper is as follows: Section 2 contains the methods descriptions; Section 3 describes the results; Section 4 finishes with discussion and conclusions.

2. Methods

2.1. Study Area. To achieve the aims of the paper, Ulaanbaatar, the capital city of Mongolia, and its surroundings are used as an example. The city is located in northeastern Mongolia, in the narrow valley of Tuul River in the Khentii Mountain Range (Figure 1), at the boundary of taiga, mountain forest, and steppe.

With annual mean temperature of −1.3°C and minimum temperatures often below −30°C, Ulaanbaatar is one of the coldest cities of Mongolia as well as the coldest capital city in the world. Although summers are warm (July average 16.9°C), winters are cold (January average −22.3°C). Total annual precipitation is on average 281.7 mm, which mostly

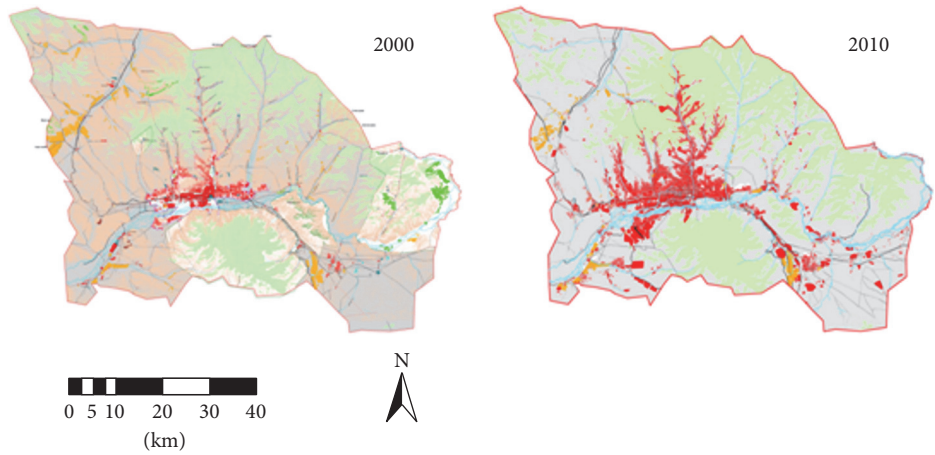

Figure 2: Urban areas (red) in the Ulaanbaatar city area, Mongolia, in 2000 and 2010. Light green color is forest, green is wetland, mandarin is arable land, and gray is pasture and others (adapted from source: cadastral map and time series land use planning data in National Land Information Database).

Table 1: Urban land use in Ulaanbaatar for 2001 and 2012 (data from Purevtseren et al. [19] and Myagmartseren et al. [20]).

Land use	% 2001	% 2012	Percentage points change
Residential (total)	33.2	58.7	25.5
Residential (sprawl)	28.2	51.8 whereof 32% ger districts and 19.8% in green belt	23.6
Infrastructure	5.2	9.4	4.2
Industry	10.0	8.3	−1.7
Service	13.7	6.3	−7.4
Special purpose and others (defense, public land, water buffer, mining, etc.)	6.9	15.1	8.2
Unused and reservation	28.8	10.0	−18.8

comes as summer rain (>82% in June–September) and as small amounts of snow in the cold season (Sato [17]).

With respect to land use, the city has undergone a dramatic urbanization trend during the last decade (the urban land use distribution of Ulaanbaatar city is presented in Table 1). Using high-resolution satellite image fusion interpretation, Amarsaikhan et al. [18] concluded that the central part of Ulaanbaatar city was urbanized very rapidly. In the socialist time, 1930–1990, 571 buildings were constructed, while during the first years of post-socialist time, 1990–2008, 792 buildings were raised, which demonstrates a significant land demand for urban development. Herders and farmers, many of them migrating from rural places, have played a big role in this urban expansion (sprawl). Just half a decade ago, in 1956, the city's population was 118,000, but today 1.3 million residents, out of Mongolia's 3 million in total, are living in the Ulaanbaatar region. One key factor for such rapid urbanization is probably due to the nomadic life style of Mongolian people; that is, it is not more difficult to put up a traditional ger tent in the outskirts of a city than it is to put it up anywhere else.

In the residential zone ger area, which covers about 32% percent of all territory of the city, urban expansion has accelerated so far so it adversely impacts green-belt areas, wetlands, water buffer zones, open space, and public land (see how the red area in Figure 2 is changing between 2001 and 2010 and also that it is mainly spreading in the narrow valleys out from the city center).

2.2. Workflow and Criteria Treated. This study consisted of two main stages: data processing and MCDA (Figure 3). In the first stage, relevant criteria were identified with respect to physical considerations and the minimum requirements found in Ulaanbaatar urban plan and vision documents, and in the second stage the actual analysis was performed.

For the locational and physical criteria, example tables for standard residential urban development are provided by, for example, McDonald et al. [21], Rowe et al. [22], Wells and King [23], USDA [24], FAO [25], and NSW Environment Protection Authority [26]. These sources were used as inspiration for this study (Table 2). Based on Table 2 and other criteria, the constraints shown in Table 3 were considered.

2.3. Analytic Hierarchy Process. Unless all criteria are of Boolean data type, that is, either true or false, some kind of weighting needs to be employed to be able to combine them. Malczewski [29] noted that in the last 20 years of scientific works related to the integration of MCDA with GIS there have been a number of multicriteria decision rules invented. However, some are used more frequent. Out of the total 259 surveyed papers treating multiattribute decision analysis, 143 were of the type Boolean overlay or weighted summation. A similar, but more developed method is the analytic hierarchy process (AHP) developed by Saaty [30], which uses additive

Table 2: Suitability criteria for urban development.

Land attribute	Suitability criteria of factor		
	Unsuitable	Moderate with limitations	Most suitable
Slope gradient (%)	>15	8–15	<8
Soil texture*	Sand, silt	Loamy sand, sandy clay loam, silt clay loam	Loam, clay loam, silt loam
Soil character	Moving sand, undeveloped soil, boggy, saline, rock	Water, wind eroded, content of stones, low humus, permafrost, and so forth	No evidence of erosion, low amounts of stone, sufficient humus content, and so forth
Distance from road** (m)	<100; >3000	1500–3000	100–1500
Aspect (degrees)	North 0–22.5; 337.5–360	West 22.5–112.5 East 247.5–337.5	South 112.5–247.5
Close to built-up area (m)	>3000	1500–3000	150–1500
Close to river (m)	<500; >3000	1500–3000	500–1500
Vegetation cover (NDVI index)	<0.2	0.2–0.3	0.3–0.8

*Department of Housing [27].
**City and village planning and construction norms and rules (no. 30-01-04) of Mongolia [28].

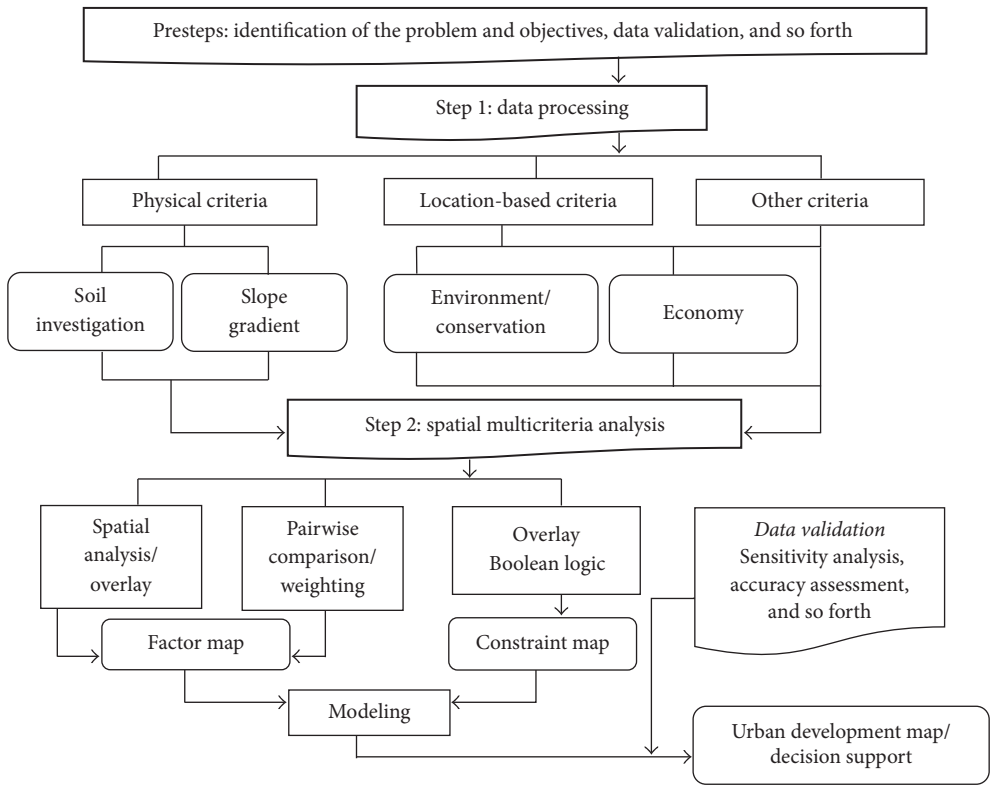

Figure 3: Overview of workflow for this study.

weighting and also can derive the weights associated with the map layers as well as being able to aggregate and include the level representing alternatives into the hierarchy structure (Malczewski [29]). Furthermore, AHP is capable of relating both tangible and intangible criteria.

To derive values for criteria weights, we treated all factor maps as if they belonged to the same hierarchy level (using the freeware software AHP 2.0 by Brandt [31]). In AHP, as some criteria may be relatively more important than other criteria, the criteria are compared pairwise against each other in order to get relative weights for each of them. Then the final suitability score of each pixel in the final map can be calculated from

$$S = \sum_{i=1}^{n} w_i x_i, \tag{1}$$

where S is the suitability with respect to the objective being considered, w_i is the relative weight of factor i, and x_i is

Table 3: Urban development location factor and constraints criteria.

Criteria: urban development site	Consideration
Must not be located in or near agricultural areas	Safety
Must avoid forest reserved areas	Environment/resources
Must be on a gentle slope (i.e., <15%)	Safety/environment
Must avoid wetlands	Safety/environment
Must be near to rivers, but not in buffer zone	Economic/environment
Must have a sufficient amount of green grasses (NDVI)	Economic
Must not be located in national parks	Environment/resources
Must have optimal amount of solar radiation (aspect)	Economic/environment
Must have an optimal soil for construction and garden	Environment/resources

the criteria score of factor i. Through this weighted linear combination of factors, the sum of all weights will be 1, and all weights can be directly associated with their corresponding percent of importance. The criteria score, which also contains similar elements of importance, is determined after a normalization procedure (cf. Section 2.4.2).

In this study, all pairwise comparison weights were arbitrarily decided by us. The slope factor was assigned the highest weight. Thereafter, distance to already existing urban areas, soil type, distance to roads, distance to rivers, vegetation cover type, and finally the terrain aspect were assigned progressively lower weights (Table 4).

2.4. GIS Processing

2.4.1. Preparation of GIS Layers. To be able to produce both the factor maps (listed in Table 4) and constraint maps, which indicate if the areas can be considered at all, a number of data sources and methods to create the information layers were used (Table 5). Most information was collected from a subset of a Landsat 7 satellite image of September 2010 (free download available from http://landsat.usgs.gov/landsat-data-access) and radar-based SRTM elevation data of 2001 from the CGIAR Consortium (free download available from http://srtm.csi.cgiar.org/) and optical stereo-based ASTER GDEM elevation data (free download available from http://asterweb.jpl.nasa.gov/gdem.asp), but also other sources were used for data and information input.

2.4.2. Production of Constraint and Factor Maps. In spatial MCDA studies usually two different types of maps, or information layers, are used: constraint and factor maps. Constraint maps are of the Boolean data type, meaning that they consist of cells with only two possible values, zeroes (0) or ones (1), or in other words, false or true. When such maps are multiplied with each other, for a particular cell to result with the value 1, all layers have to contain that number. If as much as one layer contains the value 0, also the resulting map will have the value 0 for that cell, meaning that it is not possible at all to utilize for the intended purpose (in this case impossible to use for urban development). In this study constraint maps were produced for barren lands, forests, rivers including surrounding buffer zone, wetlands, national parks, and slopes that are too steep.

Factor maps, on the other hand, show for each factor each cell's suitability with respect to the goal (in this case urban development). Initially the factor maps can contain values of any type or size. For example, distance to agricultural areas may be represented by cell values in meters and soil types by plain text. To be able to analyze such different types of data together, all data need to be converted to numerical format as well as being normalized; that is, the value of high suitability with respect to one factor (criterion) has to have the same value as one of another factor. Therefore, to represent the suitability, all factors were normalized, meaning in this case that the value ranges of all factor maps were stretched from 0 to 255. This means that 0 is considered to be of very low suitability and 255 of very high suitability, irrespectively of factor type (criteria). The factor maps produced were slope gradient, urban distance, soil, road distance, river distance, vegetation cover, and aspect. As they all contained the whole range of values between 0 and 255, the maps produced could serve as continuous representations of distances to objects, suitability, and so forth.

2.4.3. Executing the MCDA. To execute the MCDA, all constraint maps were multiplied with each other, producing one combined constraint map. The factor maps, on the other hand, first had to be multiplied with their corresponding weights from the AHP and, thereafter, summed together into one combined factor map. Finally, the combined constraint map and the combined factor map were multiplied together. The general equation is

$$S = \sum_{i=1}^{n} w_i F_i \prod_{j=1}^{m} C_j, \tag{2}$$

where S is the total suitability score, w_i is the weight corresponding to F_i, that is, factor map i, and C_j is constraint map j. Now every pixel in the final result map contains a suitability score for urban development.

2.5. Sensitivity Analysis.

As many scientists argue that real-world decisions are uncertain because we have insufficient information or fuzzy descriptions of the semantic meaning of the events, phenomena, statements themselves, and so forth, the results of MCDA are usually associated with uncertainties or direct errors or undesirable consequences (Aerts et al. [32]; Malczewski [29]; Tenerelli and Carver [33]). Among errors and variability in model choice, system understanding, weighting factors, data used, and human judgment, one of the greatest contributors to controversy and uncertainty is the criteria weights, which also may have a significant impact on the results (Feizizadeh and Blaschke [34]).

One way to account for such uncertainties is to perform a sensitivity analysis that aims to assess the response of a model to changes in input parameters (Crosetto et al. [35]; Gómez Delgado and Bosque Sendra [36]; Ligmann-Zielinska and Jankowski [37]; Chen et al. [6]). Saltelli et al.'s [38, p. 45]

Table 4: Ranking and weighting of factors (resulting consistency ratio is 0.021).

Rank	Criterion	Slope	Urban	Soil	Road	River	Veg.	Aspect	Relative weight
1	Slope gradient	1	1	2	3	4	4	10	0.307
2	Urban distance	1	1	1	2	3	4	4	0.221
3	Soil	1/2	1	1	1	2	4	4	0.173
4	Road distance	1/3	1/2	1	1	1	2	3	0.116
5	River distance	1/4	1/3	1/2	1	1	1	2	0.081
6	Vegetation cover	1/4	1/4	1/4	1/2	1	1	1	0.058
7	Aspect	1/10	1/4	1/4	1/3	1/2	1	1	0.044

Table 5: Data sources used to create the various information layers for the criteria maps.

Features considered	Source	Method of creation
Urban areas	Landsat 7 satellite image	Unsupervised classification
Forest areas	Landsat 7 satellite image	Supervised classification
Topography (slope, aspect)	CGIAR-CSI DEM of 90 m resolution/Aster GDEM of 30 m	Import via GIS (grid) and Erdas (raster)
Hydrology	ASTER GDEM	Geoprocessing tool/hydrology tool in GIS
Vegetation	Landsat 7 satellite image	Normalized difference vegetation index (NDVI)
National parks	National parks map	Digitizing/georeferencing

definition of sensitivity analysis is "the study of how the uncertainty in the output of a model (numerical or otherwise) can be apportioned to different sources of uncertainty in the model input." Then it will be possible to see "'which of the uncertain input factors is more important in determining the uncertainty in the output of interest?' or 'if we could eliminate the uncertainty in one of the input factors, which factor should we choose to reduce the most the variance of the output?'" (Saltelli et al. [38, p. ix]).

There are different types of sensitivity methods that can be used, for example, probabilistic Monte Carlo simulations (e.g., Aerts et al. [32]; Benke and Pelizaro [39]), the Variance-based Global Sensitivity Analysis (GSA) method (Homma and Saltelli [40]), or representing weights with different degrees of fuzziness (Kordi and Brandt [41]). However, among the most popular sensitivity analysis methods is the One-Factor-At-A-Time (OAT) (cf. Daniel [42, 43]). This method changes the value of only one factor at a time, while keeping all other factor values constant. Although the method suffers from some limitations, there are a number of advantages compared with other methods: (1) it is intuitive (i.e., the analyst can see if a change by some percentage of one factor will result in a corresponding output change), (2) the results from the sensitivity analysis can be instantaneously visualized and explored, (3) no prior knowledge about OAT is required, and (4) it is computationally effective and does not require huge amounts of model executions (Ligmann-Zielinska and Jankowski [44]). Usually one of the following is done to analyze the criteria sensitivity: changing criteria values, changing relative importance of criteria, or changing criteria weights (Chen et al. [6]).

To test the robustness of our MCDA model and to see how the analyzed urban development locations change when small deviations in the criteria values are applied, a sensitivity analysis was performed by changing each of the factor criteria weight values at a time (OAT), that is, changing the values by ±6, ±12, and ±18%, respectively, from the original value (Table 6). Correspondingly, all other criteria lost proportional shares according to the equation given by Chen et al. [6]:

$$w(c_i, pc) = (1 - w(c_m, pc)) \times \frac{w(c_i, 0)}{(1 - w(c_m, 0))}; \quad i \neq m;\ 1 \leq i \leq n, \tag{3}$$

where $w(c_i, pc)$ is the weight of the ith criterion c_i at a certain percent level, $w(c_m, pc)$ is the weight of the main changing criterion c_m at a certain percent level, $w(c_i, 0)$ is the weight of the ith criterion c_i for the base map run, and $w(c_m, 0)$ is the weight of the main changing criterion c_m, for the base map run.

3. Results

3.1. Result of MCDA. Combined constraint maps were produced (containing the product of barren lands, forests, rivers including surrounding buffer zones, wetlands, national parks, and slopes that are too steep) for two different cases of DEM resolution (Figure 4). If as much as one criterion's value is 0 for a particular pixel, that pixel's resulting value will also be 0 and considered not possible for urban development (black areas in Figure 4). Furthermore, the effect of resolution can also be seen; for example, small constraint areas may appear within the suitable areas for the 30 m DEM, while the same areas for the 90 m DEM show up as larger contiguous suitable sites.

Also combined factor maps were produced (containing the weighted sum of slope gradient, urban distance, soil, road distance, river distance, vegetation cover, and aspect) for the two different DEM resolutions (Figure 5). In these

Table 6: Criteria weights in sensitivity analysis when one factor's weight is changed from original weight (i.e., base map) by −18, −12, −6, 6, 12, or 18%.

Change input	Weight values						
	Slope	Urban	Soil	Road	River	Vegetation	Aspect
Base map	*0.3072*	*0.2215*	*0.1731*	*0.1157*	*0.0807*	*0.0582*	*0.0436*
Slope −18%	0.2519	0.2392	0.1869	0.1249	0.0871	0.0628	0.0471
Slope −12%	0.2703	0.2333	0.1823	0.1219	0.0850	0.0613	0.0459
Slope −6%	0.2888	0.2274	0.1777	0.1188	0.0828	0.0597	0.0448
Slope +6%	0.3256	0.2156	0.1685	0.1126	0.0786	0.0567	0.0424
Slope +12%	0.3441	0.2097	0.1639	0.1095	0.0764	0.0551	0.0413
Slope +18%	0.3625	0.2038	0.1593	0.1065	0.0743	0.0536	0.0401
Urban −18%	0.3229	0.1816	0.1820	0.1216	0.0848	0.0612	0.0458
Urban −12%	0.3177	0.1949	0.1790	0.1197	0.0835	0.0602	0.0451
Urban −6%	0.3124	0.2082	0.1761	0.1177	0.0821	0.0592	0.0443
Urban +6%	0.3020	0.2348	0.1701	0.1137	0.0793	0.0572	0.0429
Urban +12%	0.2967	0.2481	0.1672	0.1117	0.0779	0.0562	0.0421
Urban +18%	0.2915	0.2614	0.1642	0.1098	0.0766	0.0552	0.0414
Soil −18%	0.3188	0.2298	0.1419	0.1201	0.0837	0.0604	0.0452
Soil −12%	0.3149	0.2271	0.1523	0.1186	0.0827	0.0597	0.0447
Soil −6%	0.3111	0.2243	0.1627	0.1172	0.0817	0.0589	0.0441
Soil +6%	0.3033	0.2187	0.1835	0.1142	0.0797	0.0575	0.0431
Soil +12%	0.2995	0.2159	0.1939	0.1128	0.0787	0.0567	0.0425
Soil +18%	0.2956	0.2132	0.2043	0.1113	0.0777	0.0560	0.0420
Road −18%	0.3144	0.2267	0.1772	0.0949	0.0826	0.0596	0.0446
Road −12%	0.3120	0.2250	0.1758	0.1018	0.0820	0.0591	0.0443
Road −6%	0.3096	0.2232	0.1745	0.1088	0.0813	0.0587	0.0439
Road +6%	0.3048	0.2198	0.1717	0.1226	0.0801	0.0577	0.0433
Road +12%	0.3024	0.2180	0.1704	0.1296	0.0794	0.0573	0.0429
Road +18%	0.3000	0.2163	0.1690	0.1365	0.0788	0.0568	0.0426
River −18%	0.3121	0.2250	0.1758	0.1175	0.0662	0.0591	0.0443
River −18%	0.3104	0.2238	0.1749	0.1169	0.0710	0.0588	0.0441
River −6%	0.3088	0.2227	0.1740	0.1163	0.0759	0.0585	0.0438
River +6%	0.3056	0.2203	0.1722	0.1151	0.0855	0.0579	0.0434
River +12%	0.3040	0.2192	0.1713	0.1145	0.0904	0.0576	0.0431
River +18%	0.3023	0.2180	0.1704	0.1139	0.0952	0.0573	0.0429
Vegetation −18%	0.3106	0.2240	0.1750	0.1170	0.0816	0.0477	0.0441
Vegetation −12%	0.3095	0.2231	0.1744	0.1166	0.0813	0.0512	0.0439
Vegetation −6%	0.3083	0.2223	0.1737	0.1161	0.0810	0.0547	0.0438
Vegetation +6%	0.3061	0.2207	0.1725	0.1153	0.0804	0.0617	0.0434
Vegetation +12%	0.3049	0.2199	0.1718	0.1148	0.0801	0.0652	0.0433
Vegetation +18%	0.3038	0.2190	0.1712	0.1144	0.0798	0.0687	0.0431
Aspect −18%	0.3097	0.2233	0.1745	0.1166	0.0814	0.0587	0.0358
Aspect −12%	0.3089	0.2227	0.1740	0.1163	0.0811	0.0585	0.0384
Aspect −6%	0.3080	0.2221	0.1736	0.1160	0.0809	0.0584	0.0410
Aspect +6%	0.3064	0.2209	0.1726	0.1154	0.0805	0.0580	0.0462
Aspect +16%	0.3055	0.2203	0.1722	0.1151	0.0803	0.0579	0.0488
Aspect +18%	0.3047	0.2197	0.1717	0.1148	0.0800	0.0577	0.0514

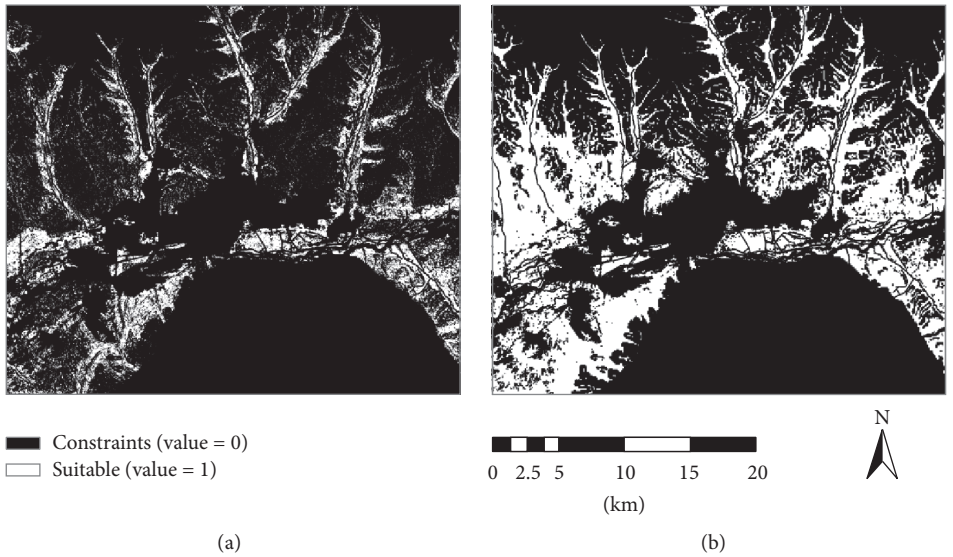

Figure 4: Final constraint maps where the slope criterion comes from (a) high-resolution DEM of 30 m and (b) low-resolution DEM of 90 m.

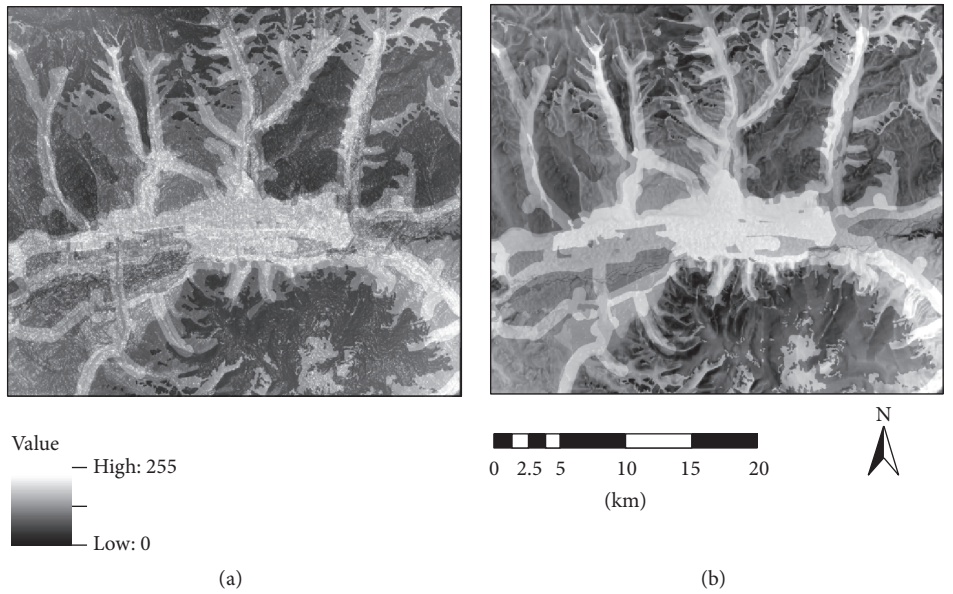

Figure 5: Final factor maps where the elevation related criteria come from (a) high-resolution DEM of 30 m and (b) low-resolution DEM of 90 m.

maps, all pixels have values that represent the total suitability, excluding the possibility of constraint occurrence. The main difference between them can be seen in the valleys where the low-resolution DEM leads to larger areas of high-ranked suitability.

Finally, for both sets of DEM resolution, the combined constraint map was multiplied with the combined factor map to produce final suitability maps for urban development (Figure 6).

3.2. Sensitivity Analysis. The results from the sensitivity analysis are presented in Table 7, which shows how many cells there are in each suitability class ($S1$ = low suitability, $S2$ = medium suitability, and $S3$ = high suitability), as well as how many and percentage of the cells that have shifted class compared with the base map.

To illustrate how the variation of criteria weights impacts the analysis, the sensitivity maps were compared with the original base map (Figure 7). The most suitable locations are shown in white and light gray and the unsuitable locations in dark gray to black. Considering the S3 class, most changes occurred for the two cases when slope gradient weight was decreased by 18% and urban distance weight was increased with 18%, that is, resulting in 47.7% and 23.7% areal change, respectively. Spatially most changes occurred in the north part of the Ulaanbaatar city vicinity. Particularly the valleys show pixels changing to or from the $S3$ class.

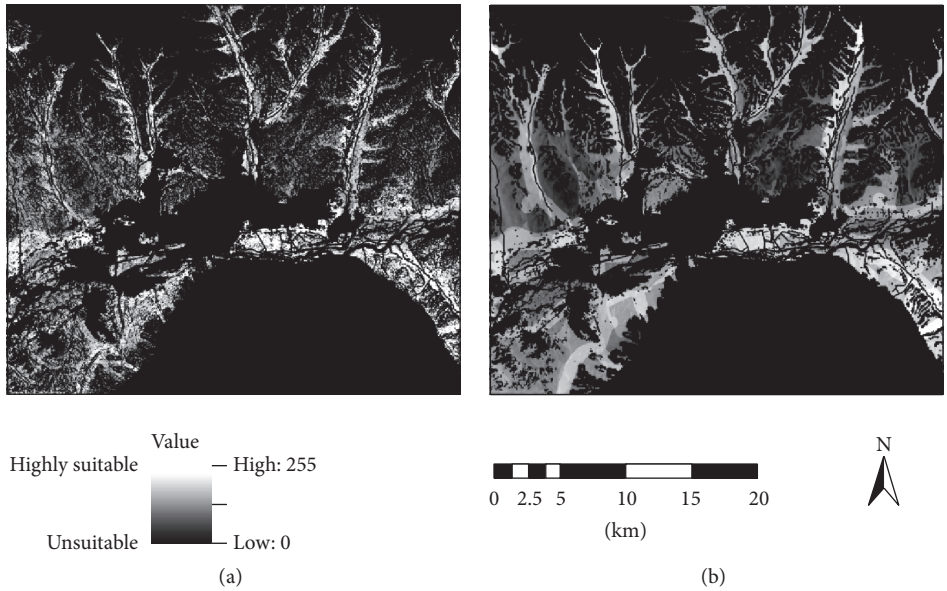

Figure 6: Final suitability maps where the elevation related criteria come from (a) high-resolution DEM of 30 m and (b) low-resolution DEM of 90 m.

In the sensitivity analysis, although many pixels changed class to and from class $S3$, out of the 14 pixels in the base map with very high suitability scores (where value ≥ 250) nine pixels still retained such high scores after a weight-change scenario of ±18% for all factors (Figure 8). This implies that the MCDA in fact is more robust than the statistics in Table 7 express.

3.3. Data Validation: Comparison with City Master Plan. Good reference or ground truth data are required for validation of the results of the MCDA. Provided that the earlier developed urban development zone map of Ulaanbaatar (i.e., the land management department of Ulaanbaatar's city master plan with legal binding urban development zones (Myagmartseren et al. [45])) was based on sound planning strategies and reliable data, an accuracy assessment could be carried out where the results of this MCDA were compared to that urban development zone map. The urban development zone map has three zones: (i) a zone for development of high density, (ii) a zone for development of low density, and (iii) a zone prohibited for development. The third zone consists of preurban agriculture, green-belt forests, or other natural conservation uses, as well as areas where soil, land, water, distance to other features, and so forth are very unsuitable for urban development and if utilized would require vast resources in terms of additional planning and special engineering measures. Therefore, it is both likely and desirable that these areas remain for conservation purposes only.

To keep comparisons simple, the suitability maps were reclassified into two classes: one suitable class ($S2 + S3$) with values 84–256 and one unsuitable class ($S1$) with values 0–84. For comparison, the suitable class was matched to the zone for development and the unsuitable class to nondevelopment zones according to the urban development zone map of Ulaanbaatar (Figure 9). Then a confusion/error matrix (Table 8) was calculated, including the commonly used overall accuracy, producer's accuracy, user's accuracy measurement, and Kappa analysis (Congalton [46]).

As the overall accuracy is 0.71, meaning that 71% of the pixels are identically classified in both maps, it appears that the final suitability map resembles previous land use planning represented by the urban development zone map. The Kappa coefficient, on the other hand, is relatively low. A value of 0.46 indicates that the classified map is about 46% better than a random assignment of these classes. However, it should be noted that the previous development zone map, besides pure suitability concerns, also is based on subjective thoughts and visions of planners, considerations of local people (e.g., that preurban local communities may have refused development activity), and others.

By extracting spatially contiguous pixels with the highest suitability values, especially areas located in the western parts of Ulaanbaatar were found particularly interesting for future development (Figure 10).

4. Discussion and Conclusions

In Mongolia, during the last decade, the use of remotely sensed data and simple overlaying techniques has been routinely practiced for urban land suitability evaluation and new settlement site selections. However, together with spatial MCDA techniques, environmental and land management activities may be more precise, quick, and cost effective. Furthermore, MCDA has also been shown to have a significant demonstrative effect for decision makers; hence the general scope of this paper is to bring practitioners knowledge of the opportunities of combining MCDA with GIS. As the results of this study clearly demonstrate the advantages of considering the opportunities using MCDA with GIS for

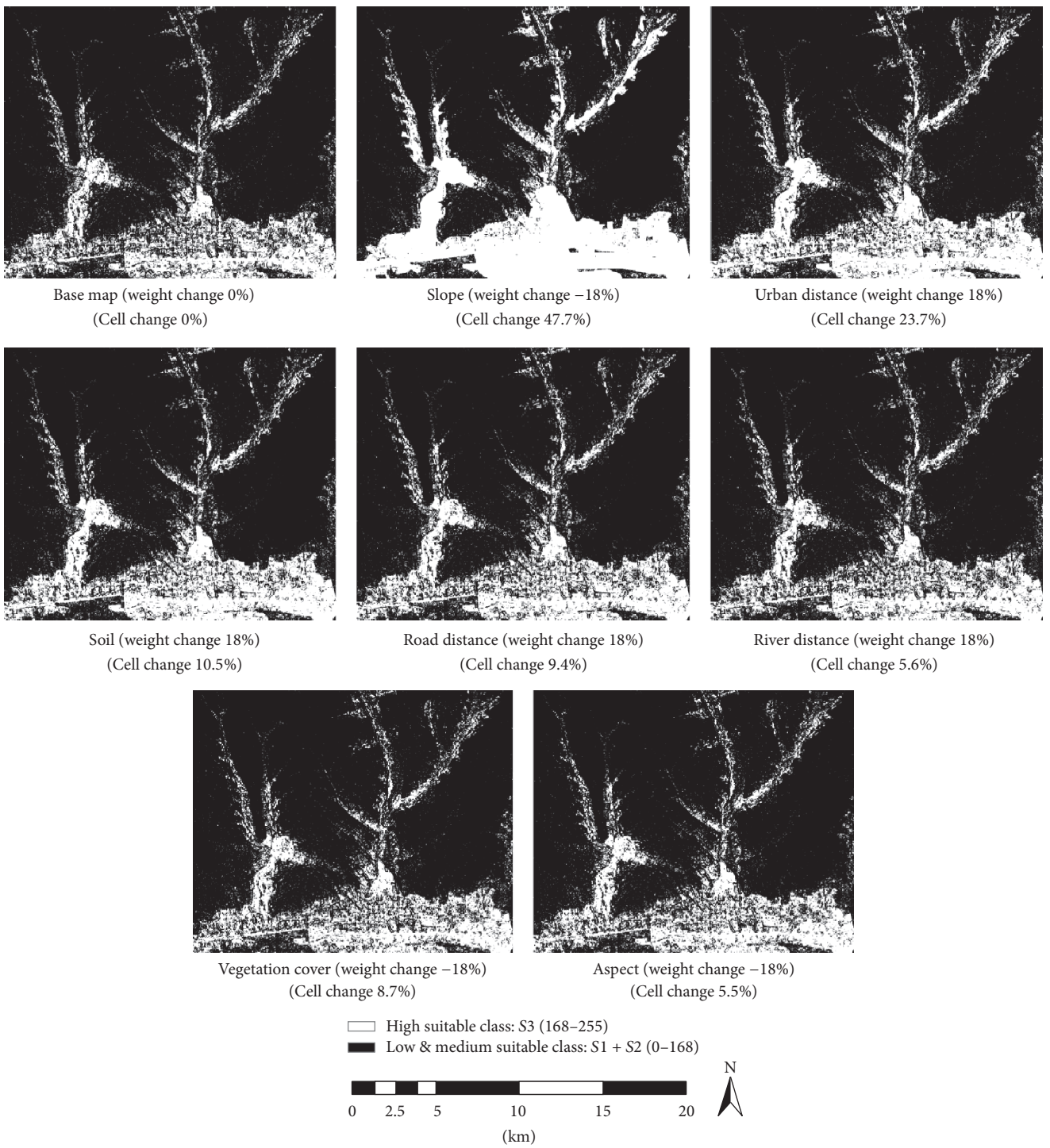

Figure 7: Result of sensitivity analysis over the northern part of the study area when one criterion is changed either +18 or −18%. White areas represent pixels that belonged to class *S*3 from the beginning and pixels that have changed to or from class *S*3. The cell change percentage value refers to the percent pixels that changed to or from *S*3 class.

urban development, these techniques should be considered mandatory in larger projects. For example, urban planners may be demanded to use detailed and classified suitability maps, such as those proposed by Hannam and Hicks [47], or to describe all constraints and factors in detail in the legends of maps (as van Gool et al. [48] did for land resources mapping). Building on the above, the following discussion will proceed from the specific objectives outlined in Section 1.3.

By following the general structure of this paper, a straightforward approach is presented on how to utilize MCDA and GIS in the planning process for locating new urban

Table 7: For different levels of change of one criterion (cf. Table 6), the number of cells in each suitability class, and the number and percentage of cells that have shifted class compared with the base map.

Change input	Sensitivity map			Difference between sensitivity map and base map					
	*S*1 (0–84) (# cells)	*S*2 (>84–168) (# cells)	*S*3 (>168–255) (# cells)	*S*1 (0–84) (# cells)	(%)	*S*2 (>84–168) (# cells)	(%)	*S*3 (>168–255) (# cells)	(%)
Base	*644239*	*1493369*	*214143*	*0*	*0*	*0*	*0*	*0*	*0*
Slope −18%	557807	1477549	316395	−86432	−13.4	−15820	−1.1	102252	47.7
Slope −12%	584823	1482800	284128	−59416	−9.2	−10569	−0.7	69985	32.7
Slope −6%	614137	1491049	246565	−30102	−4.7	−2320	−0.2	32422	15.1
Slope +6%	676054	1489162	186535	31815	4.9	−4207	−0.3	−27608	−12.9
Slope +12%	711534	1476143	164074	67295	10.4	−17226	−1.2	−50069	−23.4
Slope +18%	725447	1471445	154859	81208	12.6	−21924	−1.5	−59284	−27.7
Urban −18%	748595	1429919	173237	104356	16.2	−63450	−4.2	−40906	−19.1
Urban −12%	711589	1454280	185882	67350	10.5	−39089	−2.6	−28261	−13.2
Urban −6%	677243	1475205	199303	33004	5.1	−18164	−1.2	−14840	−6.9
Urban +6%	612625	1509268	229858	−31614	−4.9	15899	1.1	15715	7.3
Urban +12%	582593	1522757	246401	−61646	−9.6	29388	2.0	32258	15.1
Urban +18%	554993	1531849	264909	−89246	−13.9	38480	2.6	50766	23.7
Soil −18%	626473	1530169	195109	−17766	−2.8	36800	2.5	−19034	−8.9
Soil −12%	631098	1519343	201310	−13141	−2.0	25974	1.7	−12833	−6.0
Soil −6%	637251	1507001	207499	−6988	−1.1	13632	0.9	−6644	−3.1
Soil +6%	651642	1479202	220907	7403	1.1	−14167	−0.9	6764	3.2
Soil +12%	659334	1463997	228420	15095	2.3	−29372	−2.0	14277	6.7
Soil +18%	666484	1448725	236542	22245	3.5	−44644	−3.0	22399	10.5
Road −18%	614767	1540564	196420	−29472	−4.6	47195	3.2	−17723	−8.3
Road −12%	624185	1525776	201790	−20054	−3.1	32407	2.2	−12353	−5.8
Road −6%	634313	1509594	207844	−9926	−1.5	16225	1.1	−6299	−2.9
Road +6%	654300	1476911	220540	10061	1.6	−16458	−1.1	6397	3.0
Road +12%	664963	1459479	227309	20724	3.2	−33890	−2.3	13166	6.1
Road +18%	675633	1441832	234286	31394	4.9	−51537	−3.5	20143	9.4
River −18%	675076	1474173	202502	30837	4.8	−19196	−1.3	−11641	−5.4
River −12%	665153	1480465	206133	20914	3.2	−12904	−0.9	−8010	−3.7
River −6%	654294	1487117	210340	10055	1.6	−6252	−0.4	−3803	−1.8
River +6%	634151	1499720	217880	−10088	−1.6	6351	0.4	3737	1.7
River +12%	623218	1506307	222226	−21021	−3.3	12938	0.9	8083	3.8
River +18%	613213	1512423	226115	−31026	−4.8	19054	1.3	11972	5.6
Vegetation −18%	639094	1479907	232750	−5145	−0.8	−13462	−0.9	18607	8.7
Vegetation −12%	634103	1487175	230473	−10136	−1.6	−6194	−0.4	16330	7.6
Vegetation −6%	649638	1486011	216102	5399	0.8	−7358	−0.5	1959	0.9
Vegetation +6%	638737	1500874	212140	−5502	−0.9	7505	0.5	−2003	−0.9
Vegetation +12%	633322	1508804	209625	−10917	−1.7	15435	1.0	−4518	−2.1
Vegetation +18%	628014	1516474	207263	−16225	−2.5	23105	1.5	−6880	−3.2
Aspect −18%	634247	1491502	226002	−9992	−1.6	−1867	−0.1	11859	5.5
Aspect −12%	638020	1492129	221602	−6219	−1.0	−1240	−0.1	7459	3.5
Aspect −6%	640834	1492891	218026	−3405	−0.5	−478	0.0	3883	1.8
Aspect +6%	647603	1493941	210207	3364	0.5	572	0.0	−3936	−1.8
Aspect +12%	650659	1494456	206636	6420	1.0	1087	0.1	−7507	−3.5
Aspect +18%	654526	1494613	202612	10287	1.6	1244	0.1	−11531	−5.4

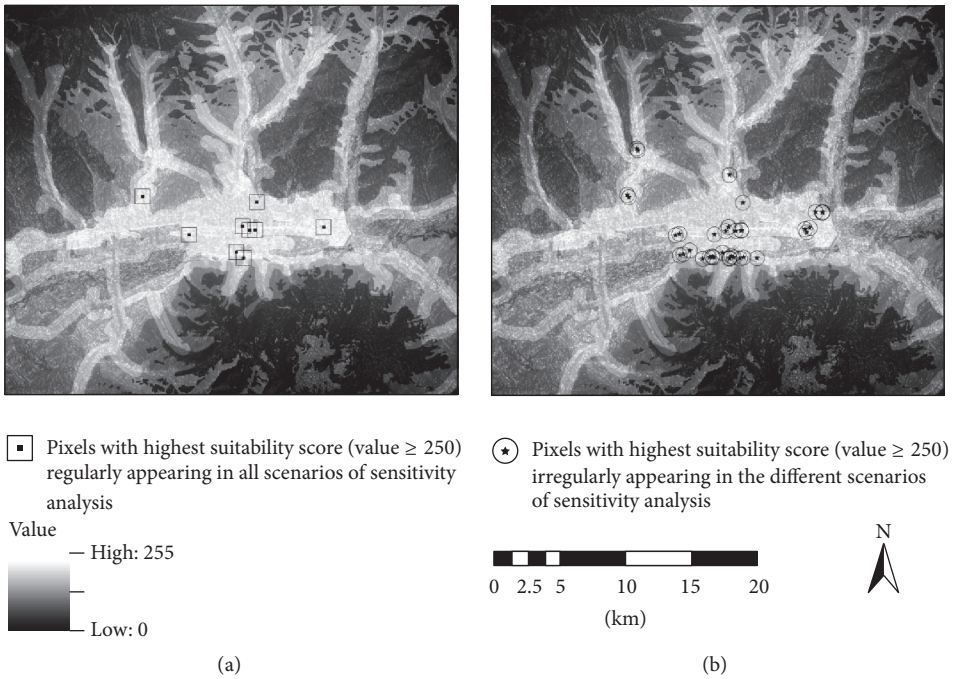

Figure 8: Location of pixels with the highest suitability scores (value ≥ 250) in sensitivity analysis. (a) The nine pixels that are present in all sensitivity scenarios. (b) Remaining high score pixels appearing at a variety of locations for the different sensitivity scenarios.

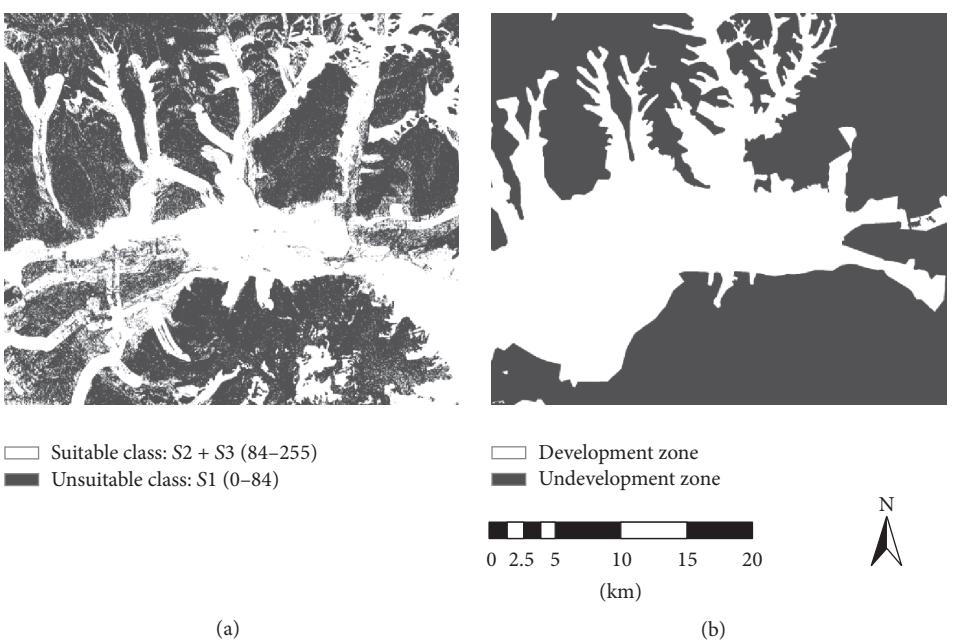

Figure 9: Comparison of the (a) final suitability map reclassified into two classes with the (b) urban development zone map of Ulaanbaatar, serving as reference in the accuracy assessment.

areas (Objective 1). The procedure generally starts with requests from politicians or official authority personnel to develop a city in one or another way. After the goals of development have been determined, it is the analyst's job to gather information on which criteria are needed for the analysis and get access to or prepare production of necessary data. The next step usually requires external input to be able to rank or weight the criteria against each other. Depending on the character of the criteria, this may be a straightforward and relatively easy task, or it may be a delicate one requiring well-thought analyses, maybe involving both experts and the general public, that may require special techniques to be able

Table 8: Error matrix for the accuracy assessment.

Suitability range values	Reference cells	Suitability compared cells	Matched cells	Producer's accuracy%	Users accuracy%
Suitable: *S*2 + *S*3 (84–255)	932193	1035752	879891	85	94
Unsuitable: *S*1 (0–84)	1413414	843566	791264	94	56
Total cells	2345607		1671155		

Overall accuracy: 0.71.
Kappa coefficient: 0.46.

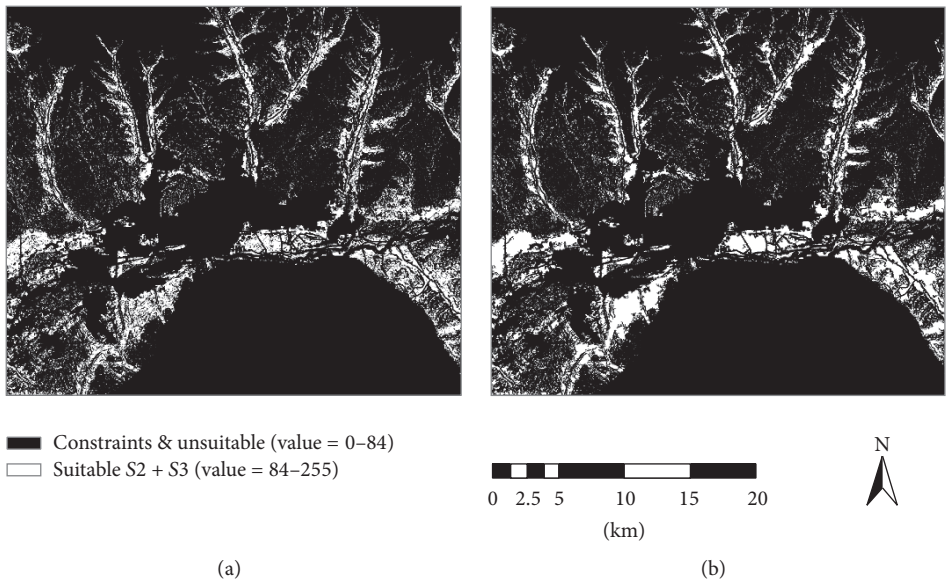

Figure 10: Identified suitable sites for urban development where (a) the suitability score is 84–255 and (b) where contiguous pixels of that score have an area larger than 0.05 km^2.

to combine diverse opinions (cf., e.g., Forman and Peniwati [49]; Matsatsinis and Samaras [50]; Jaganathan et al. [51]; Chakhar and Saad [52]; Shi et al. [53]). After the weights have been determined, the analyst produces the different map layers that represent the weighted criteria and performs the MCDA GIS analysis. Consecutively, an uncertainty analysis can be made if reference data are available to estimate inaccuracies, and through varying the weights within relevant ranges a sensitivity analysis can be carried out. Finally, the resulting suitability map has to be scrutinized for possible flaws and the most suitable locations have to be checked through field visits to see if the model successfully represents the reality or if there are other issues that may hinder further progress (e.g., cadastral or land-ownership issues).

Regarding identifying relevant criteria (Objective 2), the criteria listed in Section 2.2 seem to be generally accepted in previous research literature for this kind of study, as well as being feasible to carry out. However, it is also obvious that this study could have benefited from other or additional criteria. For example, geotechnical data were not used despite their importance regarding ground stability issues in the urban site selection process, nor were local people consulted for participation in the evaluation. Using local people's community knowledge about their land and their needs is a key issue in land use planning. In this respect, also planning agencies should be considered as they may be a conduit to resources external to a community. Including these kinds of criteria would most likely have resulted in changed weights in the AHP. Still, the reason for not including these criteria in this study was mainly due to shortage of data and the time factor, as the general purpose was not to produce the perfect urban development plan, but rather to provide an approach for using MCDA and GIS in planning. Furthermore, in general the use of remotely sensed data was shown to be very effective for production of many criteria layers, but also the methods used to create the GIS layers could have an effect on the criteria used in the analysis. For example, unsupervised classification, at least in this particular study, did provide better results for urban areas. But it did not clearly identify forest and open spaces, where, on the other hand, supervised classification performed better. It may also be wise to consider what will happen if the area is larger, necessitating even more criteria, if the area will provide countless alternatives for development, or if the best locations are even more suitable for other types of activities and should be kept for those.

To derive the slope and aspect GIS layers, two different elevation datasets of 30 m and 90 m spatial resolution were used, enabling a comparison to see how results were affected (Objective 3). These datasets are available for free and for

developing countries thus provide popular alternatives to more costly data collection methods, provided the resolution is adequate. As most criteria in this study were derived from 30 m Landsat ETM imagery, better resolution than 30 m seemed to be of no value. However, if the study area had been smaller and the analysis had required higher resolution, these elevation datasets, as well as satellite images, may have been too poor. When comparing the results of using the 90 m DEM with the sensitivity analysis, where only the 30 m DEM was used, it can be seen that the lower resolution DEM affected the final result in a greater way than did the change in relative criteria weights. Besides the general changes, a coarser DEM resolution led to larger contiguous areas of high-ranked suitability. This can be directly linked to the cell size's influence on the slope. Big cell sizes may smoothen local terrain variation, thereby resulting in lower slopes than small cell sizes would produce. However, in mountainous terrain, local pockets of flat terrain may produce higher scores for small cell sizes. Therefore, it is recommended to try to find DEMs with as high resolution as possible, while keeping in mind that the other criteria have to be of about the same resolution to take advantage of the DEM.

Through the sensitivity analysis, it could be determined if the model itself and the relative weights of the criteria were robust (Objective 4). In general, although sensitive to weight value changes, all criteria weights as well as the entire model can be considered to be robust. As expected, the largest number of pixels moving to or from the highest suitability class $S3$ occurred when the criterion of the largest relative weight, that is, slope, was tested. Roughly, the percent change of pixels belonging to S3 then was twice the size of the change in weight. With smaller relative weights, also the number of pixels changing suitability classes was smaller (e.g., vegetation cover and aspect). Geographically, it can be seen that most changes occurred in the northern part of the Ulaanbaatar city vicinity. This may be due to that two criteria—slope and urban distances—were largely constrained by the narrow valleys and localization of previous infrastructure, thereby abruptly changing the suitability of a pixel within short distance ranges. Therefore, it is of importance to first look at which criteria are capable of producing significantly changed results when exposed for weight changes in a sensitivity analysis. Secondly, it is important to try to minimize the uncertainties related to the weight determination of those criteria. However, as new areas of the highest suitability class may show up, the sensitivity maps could also function as additional tools for finding potential expansion areas for urban development.

When the result of the analysis was compared with the existing development plans, the general pattern of suitable locations coincides. However, the Kappa coefficient reveals that there is a disagreement between them. The main difference is that previous plans have dedicated a much larger area for future development. The reason could be due to different ways of thinking between a GIS expert and planners, with respect to territory development. The planners, for example, may have thought more on policies, local community responses, and visions rather than the actual conditions, which form the basis in the GIS analysis. If the difference is too large between these kinds of analyses and the vision of planners, there may be a risk of low implementation or even abandonment of using these kinds of analyses. Therefore, it is desirable to include both the planners and their visions into the MCDA analyses and the opposite—including MCDA in the planning process.

Competing Interests

The authors declare that there are no competing interests regarding the publication of this paper.

Acknowledgments

Thanks are due to all people that have helped the authors during this study, and special thanks go to the Land Administration Department of Capital City and Lanres Company who allowed them to use their digitized data. S. A. Brandt has also been financially supported by the EU through Tillväxtverket (Project GLOBES 2, no. 170430).

References

[1] B. Bhatta, *Analysis of Urban Growth and Sprawl from Remote Sensing Data*, Advances in Geographic Information Science, Springer, Heidelberg, Germany, 2010.

[2] P. R. Berke, D. R. Godschalk, E. J. Kaiser, and D. A. Rodriguez, *Urban Land Use Planning*, University of Illinois Press, Urbana, Ill, USA, 5th edition, 2006.

[3] R. Klosterman, "Planning support systems: a new perspective," in *Planning Support Systems: Integrating Geographic Information Systems, Models, and Visualization Tools*, R. Brail and R. Klosterman, Eds., pp. 263–284, ESRI Press, Redlands, Calif, USA, 2001.

[4] National Research Council, *GIS for Housing and Urban Development*, National Academies Press, Washington, DC, USA, 2003.

[5] J. Malczewski, "GIS-based land-use suitability analysis: a critical overview," *Progress in Planning*, vol. 62, no. 1, pp. 3–65, 2004.

[6] Y. Chen, J. Yu, and S. Khan, "Spatial sensitivity analysis of multi-criteria weights in GIS-based land suitability evaluation," *Environmental Modelling & Software*, vol. 25, no. 12, pp. 1582–1591, 2010.

[7] J. Lyle and F. P. Stutz, "Computerised land use suitability mapping," *Cartographic Journal*, vol. 20, no. 1, pp. 39–49, 1983.

[8] W. Miller, M. G. Collins, F. R. Steiner, and E. Cook, "An approach for greenway suitability analysis," *Landscape and Urban Planning*, vol. 42, no. 2–4, pp. 91–105, 1998.

[9] M. H. Carr and P. D. Zwick, *Smart Land-Use Analysis: The LUCIS Model: Land Use Conflict Identification Strategy*, ESRI Press, Redlands, Calif, USA, 2007.

[10] K. Jain and Y. V. Subbaiah, "Site suitability analysis for urban development using GIS," *Journal of Applied Sciences*, vol. 7, no. 18, pp. 2576–2583, 2007.

[11] Y. Liu, X. Lv, X. Qin et al., "An integrated GIS-based analysis system for land-use management of lake areas in urban fringe," *Landscape and Urban Planning*, vol. 82, no. 4, pp. 233–246, 2007.

[12] A. Zucca, A. M. Sharifi, and A. G. Fabbri, "Application of spatial multi-criteria analysis to site selection for a local park: a case study in the Bergamo Province, Italy," *Journal of Environmental Management*, vol. 88, no. 4, pp. 752–769, 2008.

[13] F. Yang, G. Zeng, C. Du, L. Tang, J. Zhou, and Z. Li, "Spatial analyzing system for urban land-use management based on GIS and multi-criteria assessment modeling," *Progress in Natural Science*, vol. 18, no. 10, pp. 1279–1284, 2008.

[14] S. Önüt, T. Efendigil, and S. S. Kara, "A combined fuzzy MCDM approach for selecting shopping center site: an example from Istanbul, Turkey," *Expert Systems with Applications*, vol. 37, no. 3, pp. 1973–1980, 2010.

[15] S. Park, S. Jeon, S. Kim, and C. Choi, "Prediction and comparison of urban growth by land suitability index mapping using GIS and RS in South Korea," *Landscape and Urban Planning*, vol. 99, no. 2, pp. 104–114, 2011.

[16] A. Rikalovic, I. Cosic, and D. Lazarevic, "GIS based multicriteria analysis for industrial site selection," *Procedia Engineering*, vol. 69, pp. 1054–1063, 2014.

[17] H. Sato, "Mongolia: the water situation in Ulaanbaatar," *Social System Review*, vol. 3, pp. 55–63, 2012.

[18] D. Amarsaikhan, V. Battsengel, E. Egshiglen, R. Gantuya, and D. Enkhjargal, "Applications of GIS and very high-resolution RS data for urban land use change studies in mongolia," *International Journal of Navigation and Observation*, vol. 2011, Article ID 314507, 8 pages, 2011.

[19] G. Purevtseren, P. Myagmartseren, and S. Jigjidsuren, *Master Land Use Plan of Ulaanbaatar City*, Governor Office of Capital City, Ulaanbaatar, Mongolia, 2001.

[20] P. Myagmartseren, I. Myagmarjav, and B. Erdenejargal, "Land use changes in urban areas of mongolia," in *Proceedings of the 9th International Conference Environment and Sustainable Development in Mongolian Plateau and Surrounding Regions*, A. K. Tulokhonov, E. Zh. Garmaev, and A. S. Mikheeva, Eds., vol. 2, pp. 18–21, Buryat State University, Ulan Ude, Russian Federation, August 2013.

[21] R. C. McDonald, R. F. Isbell, J. G. Speight, J. Walker, and M. S. Hopkins, *Australian Soil and Land Survey Field Handbook*, Inkata Press, Melbourne, Australia, 2nd edition, 1990.

[22] R. K. Rowe, D. F. Howe, and N. F. Alley, *Guidelines for Land Capability Assessment in Victoria*, Land Capability Assessment Section, Soil Conservation Authority, Victoria, 1981.

[23] M. R. Wells and P. D. King, "Land capability assessment methodology for rural-residential development and associated agricultural land uses," Land Resources Series no. 1, Western Australian Department of Agriculture, Perth, Australia, 1989.

[24] USDA, *National Soils Handbook. National Cooperative Soil Survey*, 430-VI-NSH, United States Department of Agriculture, Government Printer, Washington, DC, USA, 1983.

[25] FAO, *Guidelines: Land Evaluation for Rainfed Agriculture*, FAO Soils Bulletin No 52, FAO, Rome, Italy, 1983.

[26] NSW Environment Protection Authority, *Managing Urban Stormwater: Council Handbook. Draft*, Environment Protection Authority, Sydney South, 1997.

[27] Department of Housing, *Techniques for Soil & Water Management at Building Sites*, Department of Housing, Sydney, Australia, 1992.

[28] Ministry of Infrastructure of Mongolia, *City and Village Planning and Construction Norms and Rules (No 30-01-04) of Mongolia*, Ministry of Infrastructure of Mongolia, Ulaanbaatar, Mongolia, 2004.

[29] J. Malczewski, "GIS-based multicriteria decision analysis: a survey of the literature," *International Journal of Geographical Information Science*, vol. 20, no. 7, pp. 703–726, 2006.

[30] T. L. Saaty, "A scaling method for priorities in hierarchical structures," *Journal of Mathematical Psychology*, vol. 15, no. 3, pp. 234–281, 1977.

[31] S. A. Brandt, "AHP v. 2.0," Analytic hierarchy process software, 2006, http://sab.geovega.se/lattjo.html.

[32] J. C. J. H. Aerts, M. F. Goodchild, and G. B. M. Heuvelink, "Accounting for spatial uncertainty in optimization with spatial decision support systems," *Transactions in GIS*, vol. 7, no. 2, pp. 211–230, 2003.

[33] P. Tenerelli and S. Carver, "Multi-criteria, multi-objective and uncertainty analysis for agro-energy spatial modelling," *Applied Geography*, vol. 32, no. 2, pp. 724–736, 2012.

[34] B. Feizizadeh and T. Blaschke, "An uncertainty and sensitivity analysis approach for GIS-based multicriteria landslide susceptibility mapping," *International Journal of Geographical Information Science*, vol. 28, no. 3, pp. 610–638, 2014.

[35] M. Crosetto, S. Tarantola, and A. Saltelli, "Sensitivity and uncertainty analysis in spatial modelling based on GIS," *Agriculture, Ecosystems & Environment*, vol. 81, no. 1, pp. 71–79, 2000.

[36] M. Gómez Delgado and J. Bosque Sendra, "Sensitivity analysis in multicriteria spatial decision-making: a review," *Human and Ecological Risk Assessment*, vol. 10, no. 6, pp. 1173–1187, 2004.

[37] A. Ligmann-Zielinska and P. Jankowski, "A framework for sensitivity analysis in spatial multiple criteria evaluation," in *Geographic Information Science: 5th International Conference, GIScience 2008, Park City, UT, USA, September 23–26, 2008. Proceedings*, T. J. Cova, H. J. Miller, K. Beard, A. U. Frank, and M. F. Goodchild, Eds., vol. 5266 of *Lecture Notes in Computer Science*, pp. 217–233, Springer, Berlin, Germany, 2008.

[38] A. Saltelli, S. Tarantola, F. Campolongo, and M. Ratto, *Sensitivity Analysis in Practice*, John Wiley & Sons, Chichester, UK, 2004.

[39] K. K. Benke and C. Pelizaro, "A spatial-statistical approach to the visualisation of uncertainty in land suitability analysis," *Journal of Spatial Science*, vol. 55, no. 2, pp. 257–272, 2010.

[40] T. Homma and A. Saltelli, "Importance measures in global sensitivity analysis of nonlinear models," *Reliability Engineering and System Safety*, vol. 52, no. 1, pp. 1–17, 1996.

[41] M. Kordi and S. A. Brandt, "Effects of increasing fuzziness on analytic hierarchy process for spatial multicriteria decision analysis," *Computers, Environment and Urban Systems*, vol. 36, no. 1, pp. 43–53, 2012.

[42] C. Daniel, "On varying one factor at a time," *Biometrics*, vol. 14, no. 3, pp. 430–431, 1958.

[43] C. Daniel, "One-at-a-time plans," *Journal of the American Statistical Association*, vol. 68, no. 342, pp. 353–360, 1973.

[44] A. Ligmann-Zielinska and P. Jankowski, "Spatially-explicit integrated uncertainty and sensitivity analysis of criteria weights in multicriteria land suitability evaluation," *Environmental Modelling & Software*, vol. 57, pp. 235–247, 2014.

[45] P. Myagmartseren, I. Myagmarjav, and G. Gantulga, *Amendment of Master Land Use Plan of Ulaanbaatar City*, Land Administration Department of Capital City, Ulaanbaatar, Mongolia, 2012.

[46] R. G. Congalton, "Putting the map back in map accuracy assessment," in *Remote Sensing and GIS Accuracy Assessment*, R. S. Lunetta and J. G. Lyon, Eds., pp. 1–13, CRC Press, Boca Raton, Fla, USA, 2004.

[47] I. D. Hannam and R. W. Hicks, "Soil conservation and urban land use planning," *Journal, Soil Conservation Service of New South Wales*, vol. 36, no. 3, pp. 134–145, 1980.

[48] D. van Gool, P. Tille, and G. Moore, *Land Evaluation Standards for Land Resource Mapping*, Resource Management Technical Report 298, Department of Agriculture, Government of Western Australia, 3rd edition, 2005.

[49] E. Forman and K. Peniwati, "Aggregating individual judgments and priorities with the Analytic Hierarchy Process," *European Journal of Operational Research*, vol. 108, no. 1, pp. 165–169, 1998.

[50] N. F. Matsatsinis and A. P. Samaras, "MCDA and preference disaggregation in Group Decision Support Systems," *European Journal of Operational Research*, vol. 130, no. 2, pp. 414–429, 2001.

[51] S. Jaganathan, J. J. Erinjeri, and J.-I. Ker, "Fuzzy analytic hierarchy process based group decision support system to select and evaluate new manufacturing technologies," *The International Journal of Advanced Manufacturing Technology*, vol. 32, no. 11-12, pp. 1253–1262, 2007.

[52] S. Chakhar and I. Saad, "Incorporating stakeholders' knowledge in group decision-making," *Journal of Decision Systems*, vol. 23, no. 1, pp. 113–126, 2014.

[53] S. Shi, J. Cao, L. Feng, W. Liang, and L. Zhang, "Construction of a technique plan repository and evaluation system based on AHP group decision-making for emergency treatment and disposal in chemical pollution accidents," *Journal of Hazardous Materials*, vol. 276, pp. 200–206, 2014.

Hindawi
Mathematical Problems in Engineering
Volume 2017, Article ID 5032091, 10 pages
https://doi.org/10.1155/2017/5032091

Research Article

Detection of Decreasing Vegetation Cover Based on Empirical Orthogonal Function and Temporal Unmixing Analysis

Di Xu,[1] Ruishan Chen,[2] Xiaoshi Xing,[3] and Wenpeng Lin[4]

[1] *Urban Development Research Institution, Shanghai Normal University, Shanghai 200234, China*
[2] *School of Geographic Sciences, East China Normal University, Shanghai 200062, China*
[3] *Center for International Earth Science Information Network (CIESIN), Columbia University, 61 Route 9W, P.O. Box 1000, Palisades, NY 10964, USA*
[4] *Tourism College, Shanghai Normal University, Shanghai 200234, China*

Correspondence should be addressed to Ruishan Chen; Chenrsh04@gmail.com

Received 18 October 2016; Revised 16 December 2016; Accepted 11 January 2017; Published 13 February 2017

Academic Editor: Hasi Bagan

Vegetation plays an important role in the energy exchange of the land surface, biogeochemical cycles, and hydrological cycles. MODIS (MODerate-resolution Imaging Spectroradiometer) EVI (Enhanced Vegetation Index) is considered as a quantitative indicator for examining dynamic vegetation changes. This paper applied a new method of integrated empirical orthogonal function (EOF) and temporal unmixing analysis (TUA) to detect the vegetation decreasing cover in Jiangsu Province of China. The empirical orthogonal function (EOF) statistical results provide vegetation decreasing/increasing trend as prior information for temporal unmixing analysis. Temporal unmixing analysis (TUA) results could reveal the dominant spatial distribution of decreasing vegetation. The results showed that decreasing vegetation areas in Jiangsu are distributed in the suburbs and newly constructed areas. For validation, the vegetation's decreasing cover is revealed by linear spectral mixture from Landsat data in three selected cities. Vegetation decreasing areas pixels are also calculated from land use maps in 2000 and 2010. The accuracy of integrated empirical orthogonal function and temporal unmixing analysis method is about 83.14%. This method can be applied to detect vegetation change in large rapidly urbanizing areas.

1. Introduction

Information on vegetation change has practical significance for revealing surface spatial variation and evaluating the regional ecological quality [1–3]. Vegetation indices are effective quantitative indicators of vegetation health spatial distribution and key parameters to study in landscape ecology, climate change, and soil erosion in various researches of surface processes [4–6]. MODIS EVI dataset is utilized to examine regional vegetation changes due to its excellent presentation of vegetation information and anti-interference against the soil background and atmosphere [7].

In China, land use change is mainly characterized by urbanization [8, 9]. Land use and land cover changes are primarily identified based on the repeated acquisition of remote sensing datasets. Proposed approaches for multitemporal analysis include (1) images classification [10], (2) wavelet decomposition [11], (3) a multitemporal dataset which is transformed by principal component (PC) analysis (then the resulting component could reflect various changes [12]), (4) spatial statistical analysis which calculates the quantitative analysis of the changing scope, strength, and trend [13], (5) change vector analysis which can calculate the change type and intensity [14], and (6) temporal unmixing modeling [15]. These changing analytical methods have their own characteristics and emphases, but, for multitemporal images, the most important aspect is to remove noise and determine the dominant dimensions [16]. In this study, prior information on increasing/decreasing vegetation spatial coverages is calculated by empirical orthogonal function (EOF).

The empirical orthogonal function is usually employed to model the spatial-temporal patterns of the sea surface temperature [17], dynamical atmospheric [18], sea-level rise [19], and shoreline variability [20]. The empirical orthogonal

function has been applied on the night lights dataset and MODIS EVI for characterization and modeling of the changing extent, intensity, and distribution [21]. Temporal unmixing is used to model the spatial distribution of crop types [22, 23], forest [24], and sea ice imagery [25]. Compared with other approaches [23, 26], the empirical orthogonal function can describe vegetation change trend without ancillary information in this research. The integrated of empirical orthogonal function and temporal unmixing method is first provided to model the spatial-temporal patterns of crop types [16]. Spectral mixture analysis is used to monitor vegetation change eliminating the background influence, but it is not suitable for a large area [27]. Because of the fast urbanization in China, new construction results in widely decreasing vegetation. In this study, the empirical orthogonal function aims to take the decreasing vegetation curves as a prior for temporal unmixing models in Jiangsu Province. The combination method using empirical orthogonal function (EOF) and temporal unmixing analysis (TUA) is introduced to quickly detect decreasing vegetation areas in a large area.

This study aims to evaluate the integrated empirical orthogonal function and temporal unmixing to detect the changing vegetation area and apply the approach in Jiangsu Province, a rapidly urbanized province in southern China [28]. The theories of empirical orthogonal function and temporal unmixing and the application results in Jiangsu are presented first. Next, contrasting Landsat data are used to validate the accuracy and consistent spatial distribution of decreasing vegetation with MODIS EVI by empirical orthogonal function and temporal unmixing method. At last, this analysis also identifies strengths and uncertainties of the combined empirical orthogonal function and temporal unmixing method.

2. Materials and Methods

2.1. Study Area and Datasets. Jiangsu Province is located at 116°18′–121°57′E, 30°45′–35°20′N, with a 10.26-million hectare area that accounts for 1.1% of the total terrestrial area in China. The plains area is 7.06 million hectares and the water area is 1.73 million hectares. The elevation of more than 90% of areas in Jiangsu Province is lower than 50 meters. Jiangsu belongs to warm temperate to north subtropical transitional climate (Figure 1).

Jiangsu Province's comprehensive economic strength of Jiangsu has been at the forefront in China. After the open-door policy was issued in 1978 in China, the urban area and the growth rate increased significantly in Jiangsu. In 1990, Jiangsu had an urban population of 14.59 million and a rural population of 53.08 million. As a contrast, there was an urban population of 49.90 million and a rural population of 29.30 million in 2012. In 2012, GDP per capita in Jiangsu reached \$11,113.3 compared to the national average of \$6251.87 [29]. The urbanization rate of Jiangsu was 63% in 2012, and more than 80% of the urban growth area occurred outwards from the pregrowth urban fringes at the expense of rural lands [28]. Due to urbanization, the arable land area per farmer decreased to less than 335 m^2 [8]. Urban sprawl has environmental impacts, such as enhancing urban heat island and increasing carbon emissions, affecting the quality of life in urban areas [30]. Therefore, during the growing process, the timely and effective supervision of vegetation is of importance.

2.2. Datasets. The 16-day MODIS EVI (MOD 13Q1) composites with a 250 m spatial resolution were downloaded from the USGS website (http://glovis.usgs.gov/). EVI temporal profiles span from February 2000 to December 2012 (296 images). EVI is less susceptible to cloud and haze contamination than NDVI [31]. The EVI time series are mosaicked, reprojected, and resampled to 1000 m for displaying dominant vegetation change trend.

One validation dataset is Landsat TM images in 2000, 2002, 2006, and 2009 by linear spectral unmixing method. The three net spectral endmembers (substrate, vegetation, and dark) are provided and validated from this research results [32]. We use spectral unmixing model of ENVI software.

Another dataset to validate the temporal unmixing analysis method accuracy is land use maps in 2000 and 2010. The land use map production is from Institute of Geographic Sciences and Natural Resources Research, Chinese Academy of Sciences. We also use ArcGIS software to generate 60 random points and compare the land surface type (Agriculture, Grass, Forest, Water, and impervious surface) of google earth and the land use map in 2000 and 2010. The accuracy of the land use map is about 91%.

2.3. Empirical Orthogonal Function. The empirical orthogonal function method decomposes the original data into the product of temporal function and spatial function [18, 33]. The curves of empirical orthogonal function represent temporal patterns, which are the eigenvectors of the covariance matrix from the principal transform of the original data. PCs represent the spatial weight of the corresponding curves from empirical orthogonal function. In this research, the curves of empirical orthogonal function are the vegetation increasing/decreasing change curves. PCs display the spatial distribution of corresponding curves of empirical orthogonal function. There is principal components function in the ENVI software. The eigenvectors from the statistic file are EOFs.

In the empirical orthogonal function method, the original data (X) is divided into the product of a temporal function (EOFs-V) and spatial function (PCs-Z) [34, 35]:

$$X = VZ. \tag{1}$$

Suppose that x_j has large projection on the first K vectors in the j spatial field:

$$x_j = \sum_{1}^{K} v_k Z_{kj} - \varepsilon_j (K), \tag{2}$$

where ε is the residual error when X is expressed by K vectors.

$$\varepsilon_j (K) = x_j - \sum_{k=1}^{K} v_k z_{kj}, \tag{3}$$

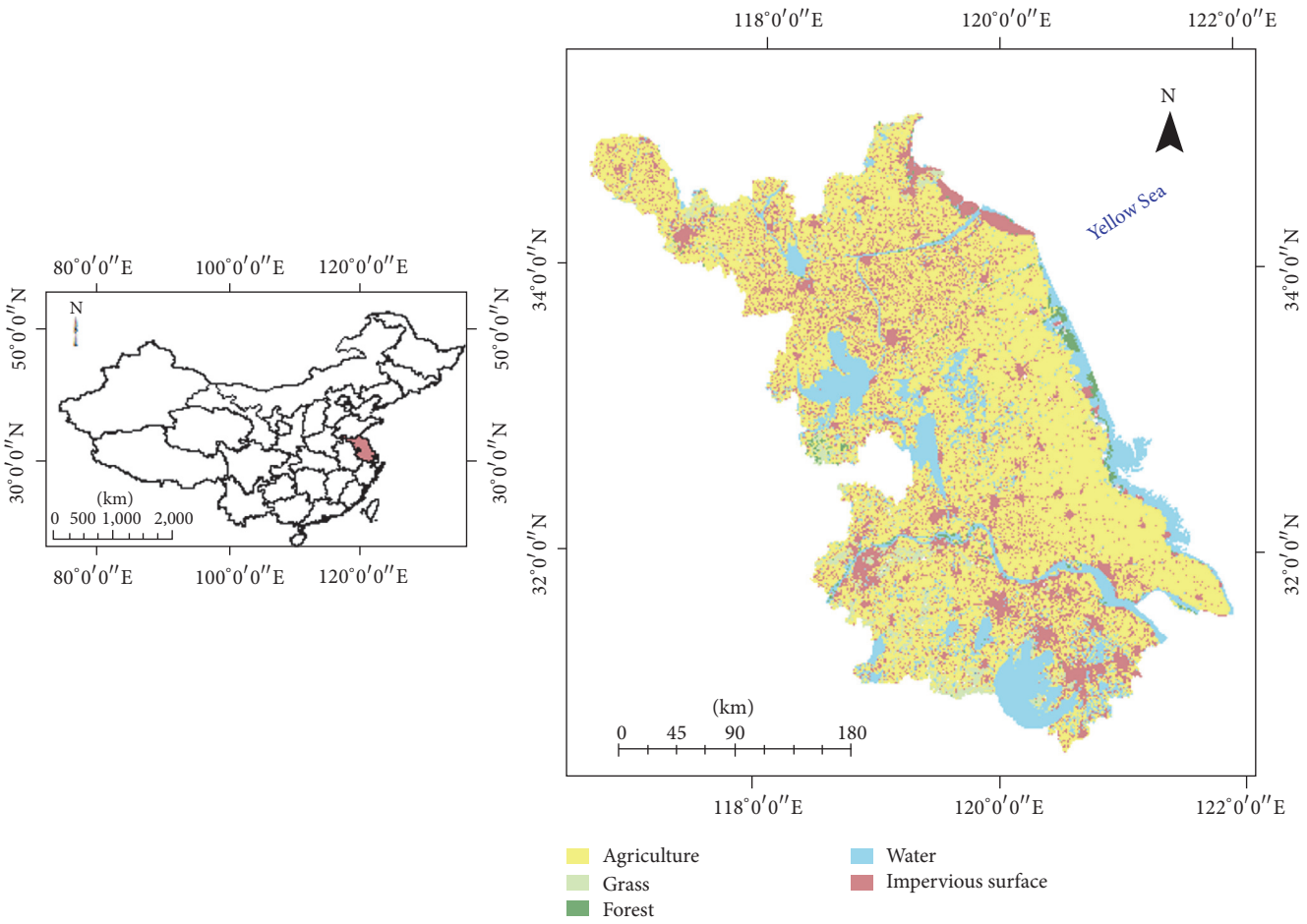

Figure 1: Location of Jiangsu Province and land use classification in 2010 (the land use production is from Institute of Geographic Sciences and Natural Resources Research, Chinese Academy of Sciences).

where $\varepsilon_j(K)$ represents error. K is the spatial dimension number, and j is the different time.

$E(K)$ is the variance for the total error. It is the sum of variance of each pixel error:

$$E(K) = \frac{1}{n}\sum_{j=1}^{n} E_j(K) = \frac{1}{n}\sum_{j=1}^{n}\left(x_j - \sum_{k=1}^{K} v_k z_{kj}\right)^T \left(x_j - \sum_{k=1}^{K} v_k Z_{kj}\right), \tag{4}$$

where $E(K)$ is the exception of error equation.

The constraint condition is

$$V^T V = VV^T = I$$

$$E(1) = \frac{1}{n}\sum_{j=1}^{n} {x_j}^T x_j - {v_1}^T \frac{1}{n} XX^T v_1$$

$$\Sigma = \frac{1}{n}XX^T = \frac{1}{n}\sum_{j}^{n}\left(x_j {x_j}^T\right) \tag{5}$$

$$F(v_1) = \frac{1}{n}\sum_{j=1}^{n} {x_j}^T x_j - {v_1}^T \sum v_1 + \lambda\left({v_1}^T v_1 - 1\right),$$

where λ is Lagrangian constant.

$$\frac{\partial F}{\partial v_1} = -2\sum v_1 + 2\lambda v_1 = 0$$

$$(\Sigma - \lambda)\, v_1 = 0. \tag{6}$$

If the v_1 has nonzero solution, it must be $|\Sigma - \lambda I| = 0$. v_1 is the eigenvector of $\Sigma = (1/n)XX^T$ and v_1 is the EOF1. λ is the corresponding eigenvalue. $Z = V^{-1}X$ is special function and Z is PC.

Moreover, the empirical orthogonal function method aims to reduce the dimensionality with a minimum loss of information while maintaining the majority of the variation affected by independent processes and capturing the essential features [36, 37].

In this analysis, the curves from empirical orthogonal function with decreasing trends are temporal patterns and represent the vegetation cover reduction. In conventional empirical orthogonal function, the PCs and empirical orthogonal function are separately interpreted in terms of spatiotemporal processes, and the empirical orthogonal function only represents statistically unrelated modes of variance. In the context of this study, much more attention

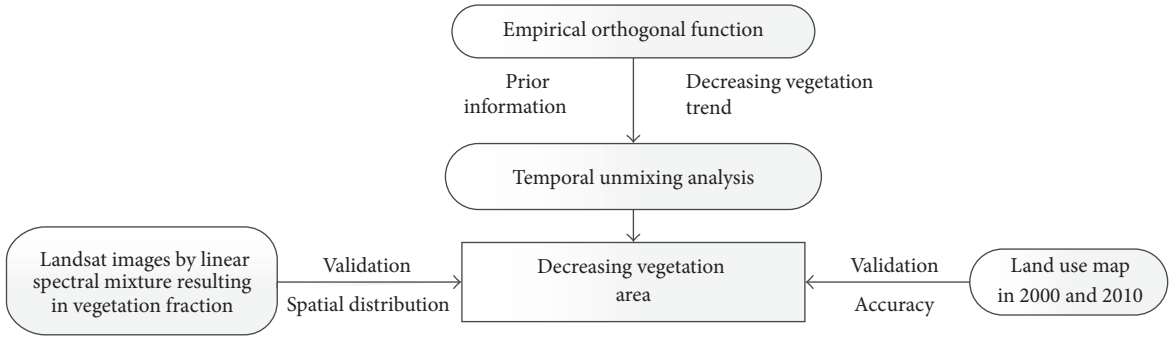

Figure 2: Technical flow chart.

is paid to the decreasing curves of empirical orthogonal function related to vegetation reduction, which provides prior information for temporal unmixing model. The curves of empirical orthogonal function and PCs can be obtained by ENVI software.

2.4. Temporal Unmixing Analysis. Temporal unmixing analysis is an extension of the linear spectral unmixing. The concept of the temporal unmixing model is that each pixel is the linear combination of temporal endmembers and corresponding fractions [22]. Fractions of endmember should be equal or greater than zero and the sum of fractions in one pixel should equal to one.

Accurate endmembers and temporal dimensions are the keys to the temporal unmixing model. Endmembers are in the extreme position of the feature space and represent different fundamental processes. The selection of endmembers is crucial for the temporal unmixing model; here, endmembers are selected by the geometric vertex method [38, 39]. The curves of empirical orthogonal function provide vegetation increasing/decreasing trend as prior information. From the EOF curves with decreasing trend, the pixels with decreasing trend can be found in the corresponding PC. Temporal vegetation decreasing endmembers can be extracted from the corresponding PC scatter plot.

The temporal unmixing used here has two differences with the traditional temporal unmixing [40]. First, the approach only selects one decreasing vegetation endmember to model the temporal unmixing analysis. Second, here the curves of empirical orthogonal function provide vegetation decreasing prior information for temporal unmixing [16]. In this research, the integration of empirical orthogonal function and temporal unmixing is useful for identifying the processes of decreasing and increasing vegetation cover. The temporal unmixing analysis is completed in ENVI software.

The technical flow chart for the research to detect decreasing vegetation trend and validate the accuracy is as follows (Figure 2).

3. Results

The first curve of empirical orthogonal function has primary eigenvalues, which contributes to approximately 89.25% of the variance (Figure 3(a)). Other curves' variances

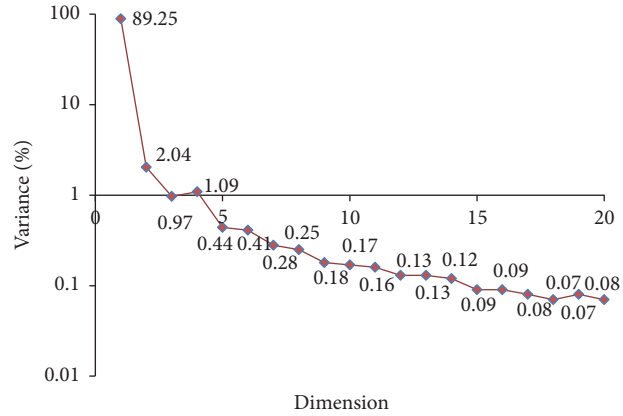

Figure 3: Eigenvectors variance of empirical orthogonal function.

continuously decrease. The variance of the second to the seventh eigenvector of empirical orthogonal function account for 2.04%, 1.09%, 0.97%, 0.44%, 0.41%, and 0.28%, respectively. It is important to acquire the vegetation decreasing/increasing trends as prior information from the eigenvectors which account for large variance.

The amplitudes of the first ten curves of empirical orthogonal function could be quantified in the time domain (Figure 4). The first ten curves of empirical orthogonal function are temporal eigenvectors of the EVI variance structure. The first curve has relatively low amplitude because it is the mean value of EVI with no variance. The second and third curves have annual and biannual peaks. Distinctly, the fourth curve shows an increasing trend. The fifth curve also displays periodic cycles with biannual peaks. The sixth and seventh curves have decreasing trends before 2006 and gradually increase afterward.

The temporal curves of empirical orthogonal function provide prior information for the temporal unmixing model. The fourth, sixth, and seventh curves are related to vegetation change trend, but the fourth curve accounts for more variance than the sixth and seventh curves. The fourth curve could reveal increasing vegetation cover changes, so the opposite pixels of the fourth curve are related to vegetation decreasing.

In this analysis, the third PC and the fourth PC are defined as X and Y apexes to obtain endmembers that can describe the details for vegetation trend change (Figure 5(a)). The

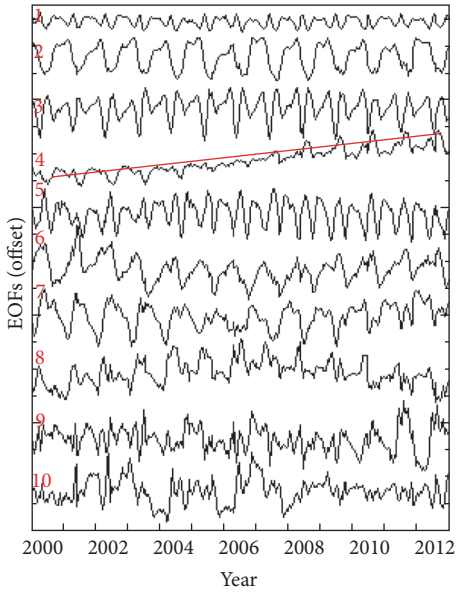

Figure 4: Curves amplitude of the first ten of empirical orthogonal function could be quantified in the time domain. Importantly, the fourth curve has increasing trend which is opposite to decreasing vegetation trend.

EOF provides prior information for temporal unmixing. The fourth EOF has the increasing trend, so there are pixels with increasing trend in the fourth PC; further, the vegetation decreasing pixels are in the opposite direction of vegetation increasing endmembers in the fourth PC. In the scatter plot, the pixels in the top position are related to vegetation increasing as the fourth EOF curve provides prior information. Oppositely, the vegetation decreasing endmembers can be found in the bottom vertex pixels.

Scatter plots of PC3 and PC4 were used to select endmembers (Figure 5(a)) representing decreasing vegetation cover between 2000 and 2012 (Figure 5(b)). The decreasing vegetation endmember reveals the vegetation reduction processes from 2000 to 2012. It is taken as the average vegetation decreasing representation in Jiangsu for temporal unmixing model, because the third and fourth PCs are used to select the decreasing vegetation endmembers.

Spatial distribution of decreasing vegetation endmember by temporal unmixing model is shown in Figure 5(c). It can be observed that the decreasing vegetation endmember is mainly located in the suburbs. In Suqian City, the decreasing vegetation cover is displayed in the suburbs. In Nanjing City, the decreasing vegetation is shown in the suburbs and in the south new area. In Taizhou City, the decreasing vegetation is in the suburbs and in the southern part. In the middle part of Jiangsu Province, the decreasing vegetation endmember is along the Yangtze River. In the southern part of Jiangsu, Suzhou City, the decreasing vegetation endmember not only is in the urban edge but also has scattered distribution, because there is a high speed economic development in Suzhou. In the development of Jiangsu Province during 13 years, the vegetation decreasing speed in the south is much faster than that in the north.

4. Validation

4.1. Validation Based on Landsat Dataset by Linear Spectra Unmixing. The vegetation fractions in 2000, 2006/2002, and 2009 in Suqian, Nanjing, and Suzhou correspond to the blue, green, and red channels in Figure 6. The dark areas mean no vegetation from 2000 to 2009. The blue areas mean vegetation cover in 2000 but with no vegetation in 2006/2002 and 2009, which clearly exhibits vegetation change processes.

The typical urbanization processes around the old city center, leading to vegetation decreasing in suburbs of Suqian City (Figure 6(a)). Suqian is in the north of Jiangsu Province. Comparing Figure 6(a) with Figure 5(c), the linear spectral unmixing and temporal unmixing methods both display same vegetation decreasing area in the suburbs of Suqian City.

The decreasing vegetation cover area in the middle of Nanjing is located in the suburbs due to urban expansion (Figure 6(b)). At the same time, the vegetation reduction in the southern part is due to new construction. Contrasting Figure 6(b) with Figure 5(c), the empirical orthogonal function and temporal unmixing methods detect the same decreasing vegetation area with linear spectral unmixing method.

Vegetation reduction in Suzhou presents a star-scattered pattern. Suzhou City is in the southern region of Jiangsu Province. Urbanization and economic development are the main reason for vegetation decreasing. The spatial changes of the vegetation fractions (Figure 6(c)) are consistent with the decreasing vegetation distribution of the empirical orthogonal function and temporal unmixing method (Figure 5(c)). Both display decreasing vegetation of star-scattered patterns and similar spatial distribution in the suburbs of Suzhou City.

4.2. Validation Based on Land Use Map. Decreasing vegetation areas are calculated from land use map from 2000 to 2010 (Figure 7). The blue part is vegetation decreasing area from empirical orthogonal function and temporal unmixing method. The red part is vegetation decreasing area from the land use map in 2000 and 2010. Vegetation decreasing area is larger in the south due to faster economic development than that in the north of Jiangsu.

According to decreasing vegetation pixels coincidence from the land use map and temporal unmixing analysis, the accuracy of empirical orthogonal function and temporal unmixing analysis is 83.14% (Table 1). Vegetation decreasing area from empirical orthogonal function and temporal unmixing analysis is 6956 km^2. Vegetation decreasing area from the land use map during 2000 and 2010 is 7111 km^2. As a result, the spatial coincidence is 5912 km^2.

5. Discussion

5.1. Strengths and Uncertainties. The combination method of empirical orthogonal function and temporal unmixing was first mentioned [16] for identifying and representing phenology spatiotemporal patterns. The approach used the number of phenology dimensions based on empirical orthogonal function and modeled the vegetation phenology distribution by temporal unmixing analysis. Here, we pay attention

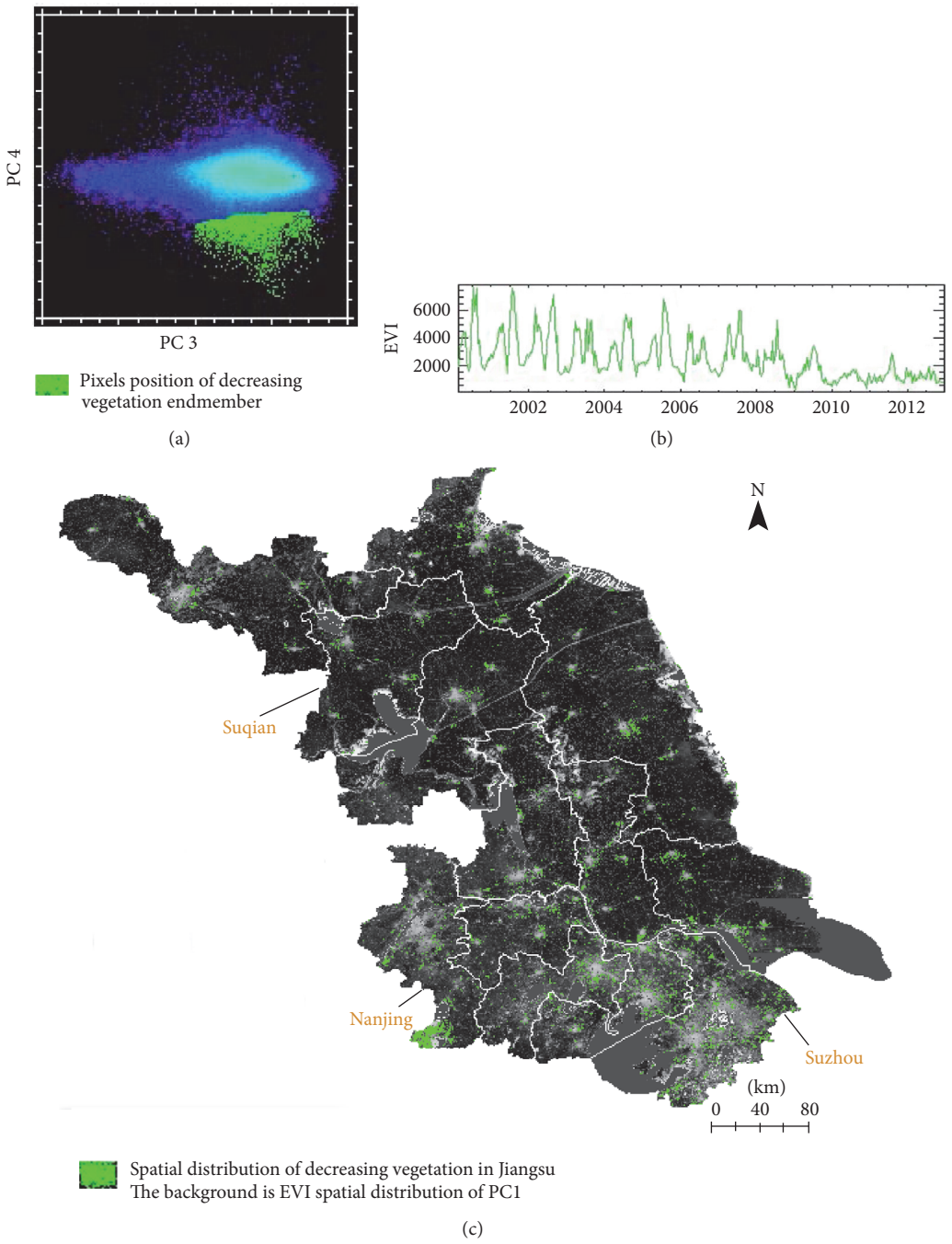

Figure 5: Feature space representation of the third and fourth PCs for temporal unmixing analysis. The decreasing vegetation endmembers are found in the south part of PC space (a). Decreasing vegetation endmember (b). Spatial distribution of decreasing vegetation area estimated by temporal unmixing analysis in Jiangsu (c).

Table 1: EOF and TUA method accuracy analysis.

Vegetation decreasing area from EOF & TUA (Km^2)	Vegetation decreasing area from land use map in 2000 and 2010 (Km^2)	Spatial coincidence area (Km^2)	EOF & TUA method accuracy
6956	7111	5912	83.14%

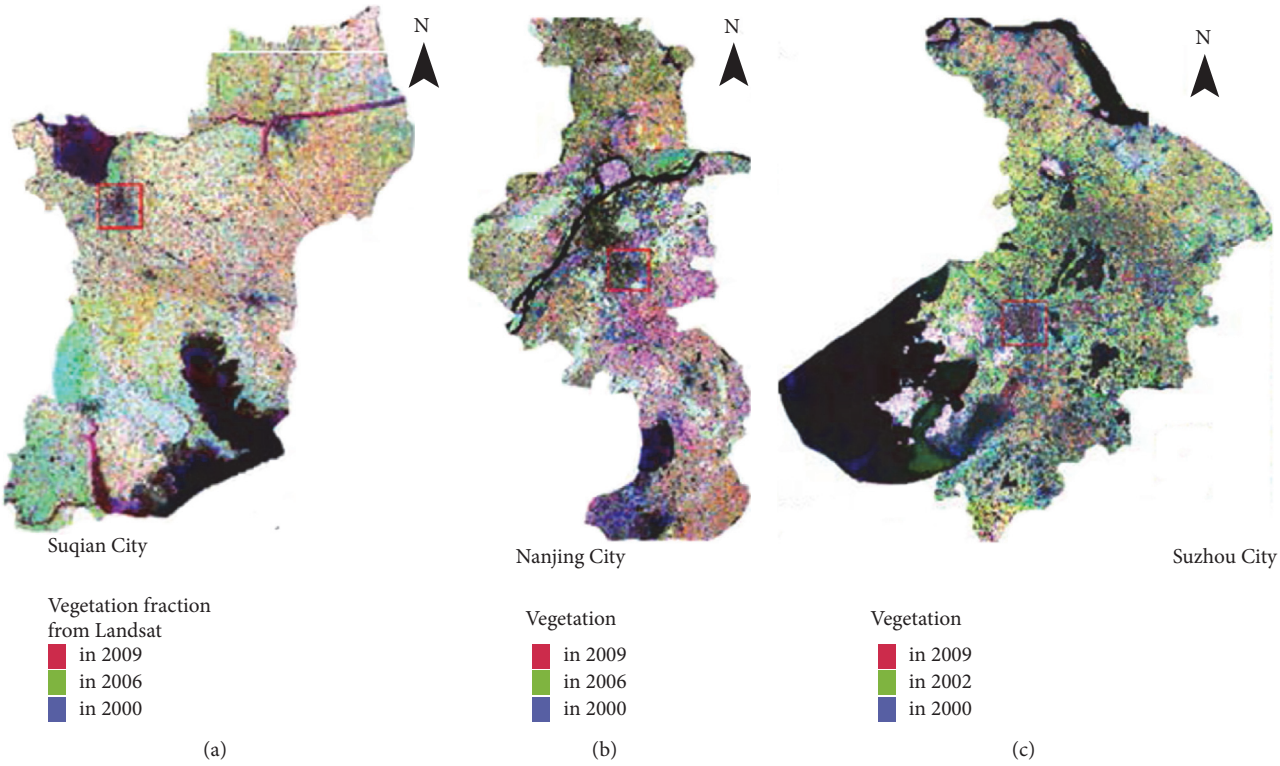

Figure 6: Vegetation fraction map in Suqian City (a), Nanjing City (b), and Suzhou City (c) in Jiangsu Province. Vegetation endmember fractions in 2000, 2006/2002, and 2009 are shown as blue, green, and red channels. The dark areas mean no vegetation from 2000 to 2009. The blue areas mean vegetation cover in 2000, but with no vegetation in 2006/2002 and 2009, which clearly exhibits vegetation change processes. The whole area is the city and the red rectangles refer to central urban.

to vegetation decreasing and increasing eigenvectors from empirical orthogonal function and select the vegetation decreasing endmembers based on temporal feature space. The two approaches both take statistical empirical orthogonal function results as prior information but emphasize different vegetation changes. The approaches described in [16] aim to describe the temporal phenology endmembers and spatial distribution, whereas the approach here aims to display the spatial distribution of decreasing vegetation. The advantage of this combined method is using the EOF as prior information for temporal unmixing analysis and using the vegetation decreasing endmembers to unmix the spatial distribution of vegetation decreasing area.

In another research [41], the approach enables the detection of different types of changes occurring in time series, including the dates of changes occurring within seasonal and trend components. This research here only pays attention to the decreasing and increasing vegetation trend and does not emphasize the accurate phenology dates of vegetation changes.

In this analysis, the unmixing processes corresponding to the spatial distribution are selected manually. Manual selection could allow for the consideration of stable endmembers. Compared with other methods, this method highlights the important benefit to quickly detect decreasing vegetation over large areas without classification and auxiliary [21].

5.2. Further Application. Further research is necessary to apply the empirical orthogonal function and temporal unmixing method to different study areas to detect boundary sensitivity of the endmembers when the decreasing vegetation endmembers are selected. In a research [16], pixels with a strong trend of vegetation increase and decrease are identified due to the annual cycle of rising and falling of water. In this study, we have focused on the spatial distribution of decreasing vegetation. Future work may improve the accuracy of decreasing vegetation endmembers. Here, Landsat data at a 30 m spatial resolution can serve to illustrate the spatial mapping accuracy.

Decision makers could use MODIS EVI by empirical orthogonal function and temporal unmixing to quickly detect the spatial extent of decreasing vegetation and it could help in land use planning. Vegetation plays an important part in the land surface characterization, climate change modeling, and biogeochemical cycles. During the processes of urbanization in China, urban expansion is the significant driver for changes toward decreasing vegetation [42]. However, monitoring vegetation over large areas at regular intervals is expensive. The combination approach of empirical orthogonal function and temporal unmixing analysis to detect decreasing vegetation could be seen as a preliminary tool. Furthermore, the vegetation fraction by linear spectral unmixing could be utilized to focus on the plots. The new

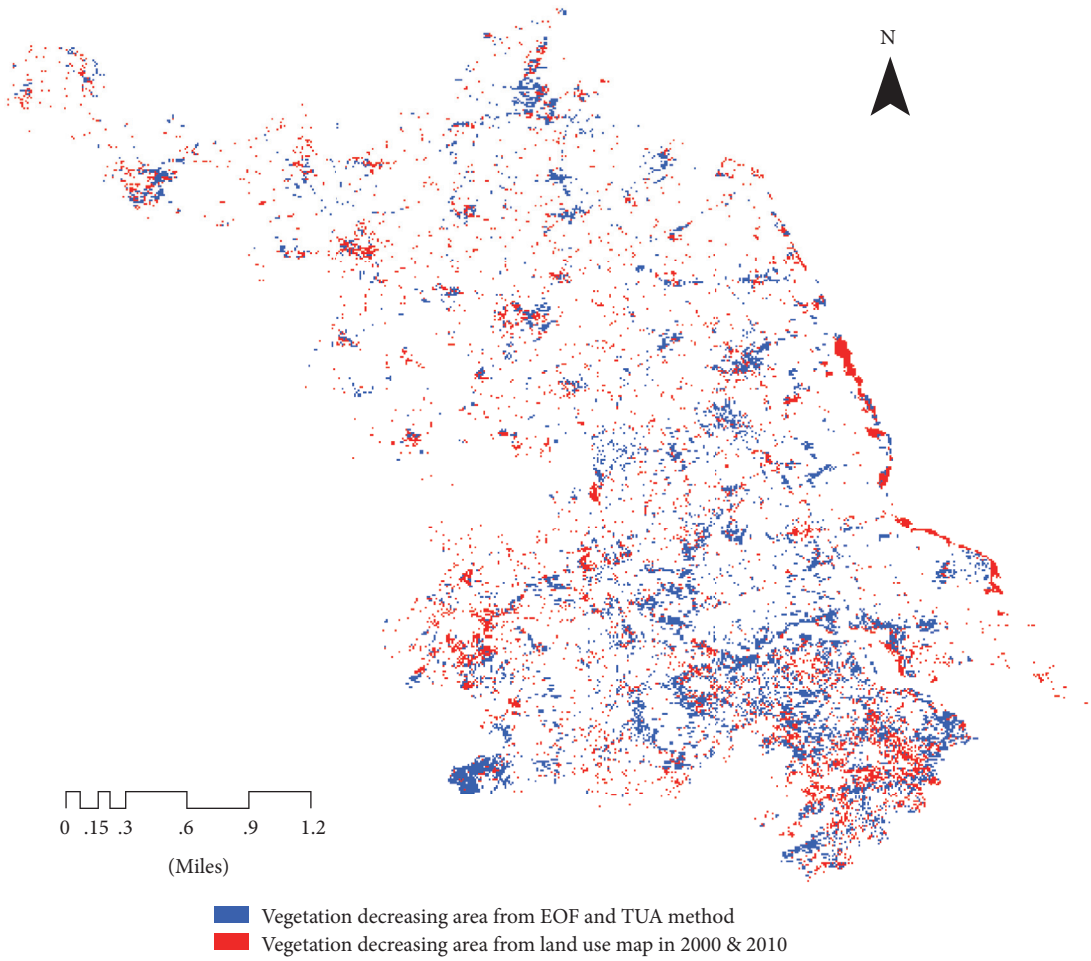

Figure 7: The blue part is vegetation decreasing area from empirical orthogonal function and temporal unmixing analysis. The red part is vegetation decreasing area from land use map in 2000 and 2010. Vegetation areas are mainly distributed in the suburbs.

combination method of empirical orthogonal function and temporal unmixing analysis contributes to vegetation cover mapping and monitoring.

6. Conclusions

Empirical orthogonal function analysis uses principal temporal and spatial patterns to present the original dataset. In this study, much more attention is paid to the increasing and decreasing vegetation eigenvectors which provide prior information for the temporal unmixing analysis.

Here temporal unmixing analysis identifies the spatial distribution of decreasing vegetation endmembers. This approach extracts decreasing vegetation endmembers from temporal principal components to model the spatial distribution. In Jiangsu Province, the decreasing vegetation mainly is distributed in the suburbs due to urbanization.

The Landsat dataset by linear spectral mixture is used for analysis in consistency of decreasing vegetation distribution with the integrated empirical orthogonal function and temporal unmixing analysis. The three components linear spectral unmixing provide estimates of vegetation fraction and the vegetation decreasing patterns. The decreasing vegetation in Suzhou displayed star-scattered pattern around the old city. The decreasing vegetation in Suqian is located in the suburbs. The decreasing vegetation in Nanjing is in the suburbs and new constructed area in the south. The empirical orthogonal function and temporal unmixing method display the same spatial extent of decreasing vegetation with linear spectral unmixing based on the Landsat dataset. Compared with vegetation changes from land use map in 2000 and 2010, the accuracy of the integrated empirical orthogonal function and temporal unmixing method is about 83.14%.

Abbreviations

MODIS: MODerate-resolution Imaging Spectroradiometer
EVI: Enhanced Vegetation Index
PC: Principal component
EOF: Empirical orthogonal function
TUA: Temporal unmixing analysis.

Competing Interests

The authors declare no conflict of interests.

Authors' Contributions

Di Xu and Ruishan Chen designed the experiments and analyzed the data; Xiaoshi Xing and Wenpeng Lin contributed analysis tools; all authors read and approved final manuscript.

Acknowledgments

The research was supported by the National Natural Science Foundation of China (NSFC) Project (no. 41401094 and no. 41571047).

References

[1] D. A. Wardle, M. Jonsson, S. Bansal, R. D. Bardgett, M. J. Gundale, and D. B. Metcalfe, "Linking vegetation change, carbon sequestration and biodiversity: insights from island ecosystems in a long-term natural experiment," *Journal of Ecology*, vol. 100, no. 1, pp. 16–30, 2012.

[2] G. J. Nowacki and M. D. Abrams, "Is climate an important driver of post-European vegetation change in the Eastern United States?" *Global Change Biology*, vol. 21, no. 1, pp. 314–334, 2015.

[3] X. Li, W. Zhou, and Z. Ouyang, "Relationship between land surface temperature and spatial pattern of greenspace: what are the effects of spatial resolution?" *Landscape and Urban Planning*, vol. 114, pp. 1–8, 2013.

[4] X. Ma, A. Huete, Q. Yu et al., "Parameterization of an ecosystem light-use-efficiency model for predicting savanna GPP using MODIS EVI," *Remote Sensing of Environment*, vol. 154, no. 1, pp. 253–271, 2014.

[5] L. K. Gray, T. Gylander, M. S. Mbogga, P.-Y. Chen, and A. Hamann, "Assisted migration to address climate change: recommendations for aspen reforestation in western Canada," *Ecological Applications*, vol. 21, no. 5, pp. 1591–1603, 2011.

[6] J. Li, W. Zhao, and X. Zhang, "The application of remote sensing data to assess soil erosion," in *Proceedings of the International Conference on Multimedia Technology (ICMT '10)*, pp. 1–4, IEEE, Ningbo, China, October 2010.

[7] N. T. Son, C. F. Chen, C. R. Chen, V. Q. Minh, and N. H. Trung, "A comparative analysis of multitemporal MODIS EVI and NDVI data for large-scale rice yield estimation," *Agricultural and Forest Meteorology*, vol. 197, pp. 52–64, 2014.

[8] Y. S. Liu, J. Y. Wang, and H. L. Long, "Analysis of arable land loss and its impact on rural sustainability in Southern Jiangsu Province of China," *Journal of Environmental Management*, vol. 91, no. 3, pp. 646–653, 2010.

[9] B. Wilson and A. Chakraborty, "The environmental impacts of sprawl: emergent themes from the past decade of planning research," *Sustainability*, vol. 5, no. 8, pp. 3302–3327, 2013.

[10] A. B. Miller, E. S. Bryant, and R. W. Birnie, "An analysis of land cover changes in the Northern Forest of New England using multitemporal Landsat MSS data," *International Journal of Remote Sensing*, vol. 19, no. 2, pp. 245–265, 1998.

[11] L. Zhao, P. Tang, and L. Huo, "A 2-D wavelet decomposition-based bag-of-visual-words model for land-use scene classification," *International Journal of Remote Sensing*, vol. 35, no. 6, pp. 2296–2310, 2014.

[12] P. Sinha and L. Kumar, "Binary images in seasonal land-cover change identification: a comparative study in parts of New South Wales, Australia," *International Journal of Remote Sensing*, vol. 34, no. 6, pp. 2162–2186, 2013.

[13] S. Du, Q. Wang, and L. Guo, "Spatially varying relationships between land-cover change and driving factors at multiple sampling scales," *Journal of Environmental Management*, vol. 137, pp. 101–110, 2014.

[14] S. Xiaolu and C. Bo, "Change detection using change vector analysis from Landsat TM images in Wuhan," *Procedia Environmental Sciences*, vol. 11, pp. 238–244, 2011.

[15] M. Jain, P. Mondal, R. S. DeFries, C. Small, and G. L. Galford, "Mapping cropping intensity of smallholder farms: a comparison of methods using multiple sensors," *Remote Sensing of Environment*, vol. 134, pp. 210–223, 2013.

[16] C. Small, "Spatiotemporal dimensionality and time-space characterization of multitemporal imagery," *Remote Sensing of Environment*, vol. 124, pp. 793–809, 2012.

[17] L. E. Keiner and X.-H. Yan, "Empirical orthogonal function analysis of sea surface temperature patterns in Delaware Bay," *IEEE Transactions on Geoscience and Remote Sensing*, vol. 35, no. 5, pp. 1299–1306, 1997.

[18] A. Hannachi, I. T. Jolliffe, and D. B. Stephenson, "Empirical orthogonal functions and related techniques in atmospheric science: a review," *International Journal of Climatology*, vol. 27, no. 9, pp. 1119–1152, 2007.

[19] B. D. Hamlington, M. W. Strassburg, R. R. Leben, W. Han, R. S. Nerem, and K.-Y. Kim, "Uncovering an anthropogenic sea-level rise signal in the Pacific Ocean," *Nature Climate Change*, vol. 4, no. 9, pp. 782–785, 2014.

[20] J. K. Miller and R. G. Dean, "Shoreline variability via empirical orthogonal function analysis: Part I temporal and spatial characteristics," *Coastal Engineering*, vol. 54, no. 2, pp. 111–131, 2007.

[21] C. Small and C. D. Elvidge, "Night on earth: mapping decadal changes of anthropogenic night light in asia," *International Journal of Applied Earth Observation and Geoinformation*, vol. 22, no. 1, pp. 40–52, 2013.

[22] M. Ozdogan, "The spatial distribution of crop types from MODIS data: temporal unmixing using Independent Component Analysis," *Remote Sensing of Environment*, vol. 114, no. 6, pp. 1190–1204, 2010.

[23] D. B. Lobell and G. P. Asner, "Cropland distributions from temporal unmixing of MODIS data," *Remote Sensing of Environment*, vol. 93, no. 3, pp. 412–422, 2004.

[24] M. C. Torres-Madronero, M. Velez-Reyes, S. J. Van Bloem, and J. D. Chinea, "Multi-temporal unmixing analysis of Hyperion images over the Guanica Dry Forest," in *Proceedings of the 3rd Workshop on Hyperspectral Image and Signal Processing: Evolution in Remote Sensing (WHISPERS '11)*, pp. 1–4, IEEE, 2011.

[25] J. M. Piwowar, D. R. Peddle, and E. F. Ledrew, "Temporal mixture analysis of Arctic sea ice imagery: a new approach for monitoring environmental change," *Remote Sensing of Environment*, vol. 63, no. 3, pp. 195–207, 1998.

[26] D. Xu and M. Fu, "Detection and modeling of vegetation phenology spatiotemporal characteristics in the middle part of the huai river region in China," *Sustainability (Switzerland)*, vol. 7, no. 3, pp. 2841–2857, 2015.

[27] P. Hostert, A. Röder, and J. Hill, "Coupling spectral unmixing and trend analysis for monitoring of long-term vegetation dynamics in Mediterranean rangelands," *Remote Sensing of Environment*, vol. 87, no. 2, pp. 183–197, 2003.

[28] C. Xu, M. Liu, C. Zhang, S. An, W. Yu, and J. M. Chen, "The spatiotemporal dynamics of rapid urban growth in the Nanjing metropolitan region of China," *Landscape Ecology*, vol. 22, no. 6, pp. 925–937, 2007.

[29] National Bureau of Statistics, *Statictical Yearbook of Jiangsu Province*, China's Statistics Publishing House, 2013.

[30] M. P. Johnson, "Environmental impacts of urban sprawl: a survey of the literature and proposed research agenda," *Environment and Planning A*, vol. 33, no. 4, pp. 717–735, 2001.

[31] Y. Pan, L. Li, J. Zhang, S. Liang, X. Zhu, and D. Sulla-Menashe, "Winter wheat area estimation from MODIS-EVI time series data using the Crop Proportion Phenology Index," *Remote Sensing of Environment*, vol. 119, pp. 232–242, 2012.

[32] C. Small and C. Milesi, "Multi-scale standardized spectral mixture models," *Remote Sensing of Environment*, vol. 136, pp. 442–454, 2013.

[33] K.-Y. Kim and Q. Wu, "A comparison study of EOF techniques: analysis of nonstationary data with periodic statistics," *Journal of Climate*, vol. 12, no. 1, pp. 185–199, 1999.

[34] W.-Y. Xu and Y. Kamide, "Decomposition of daily geomagnetic variations by using method of natural orthogonal component," *Journal of Geophysical Research: Space Physics*, vol. 109, no. 5, Article ID A05218, 2004.

[35] N. I. Dvinskikh, "Expansion of ionospheric characteristics fields in empirical orthogonal functions," *Advances in Space Research*, vol. 8, no. 4, pp. 179–187, 1988.

[36] B. Munoz, V. M. Lesser, and F. L. Ramsey, "Design-based empirical orthogonal function model for environmental monitoring data analysis," *Environmetrics*, vol. 19, no. 8, pp. 805–817, 2008.

[37] H.-L. Yu and H.-J. Chu, "Understanding space-time patterns of groundwater system by empirical orthogonal functions: a case study in the Choshui River alluvial fan, Taiwan," *Journal of Hydrology*, vol. 381, no. 3-4, pp. 239–247, 2010.

[38] X. Luís Deán-Ben, N. C. Deliolanis, V. Ntziachristos, and D. Razansky, "Fast unmixing of multispectral optoacoustic data with vertex component analysis," *Optics and Lasers in Engineering*, vol. 58, pp. 119–125, 2014.

[39] M. O. Smith, P. E. Johnson, and J. B. Adams, "Quantitative determination of mineral types and abundances from reflectance spectra using principal components analysis," *Journal of Geophysical Research: Solid Earth*, no. S2, pp. C797–C804, 1985.

[40] F. Yang, B. Matsushita, T. Fukushima, and W. Yang, "Temporal mixture analysis for estimating impervious surface area from multi-temporal MODIS NDVI data in Japan," *ISPRS Journal of Photogrammetry and Remote Sensing*, vol. 72, pp. 90–98, 2012.

[41] J. Verbesselt, R. Hyndman, G. Newnham, and D. Culvenor, "Detecting trend and seasonal changes in satellite image time series," *Remote Sensing of Environment*, vol. 114, no. 1, pp. 106–115, 2010.

[42] M. Alberti and J. M. Marzluff, "Ecological resilience in urban ecosystems: linking urban patterns to human and ecological functions," *Urban Ecosystems*, vol. 7, no. 3, pp. 241–265, 2004.

Hindawi
Mathematical Problems in Engineering
Volume 2017, Article ID 8098029, 8 pages
https://doi.org/10.1155/2017/8098029

Research Article

Feasibility of Oil Slick Detection Using BeiDou-R Coastal Simulation

Yun Zhang, Shanshan Chen, Zhonghua Hong, Yanling Han, Binbin Li, Shuhu Yang, and Jing Wang

College of Information Technology, Shanghai Ocean University, 999 Hu-Chenghuan Road, Shanghai 201306, China

Correspondence should be addressed to Zhonghua Hong; zhhong@shou.edu.cn

Received 28 October 2016; Accepted 5 January 2017; Published 1 February 2017

Academic Editor: Hajime Seya

Oil spills, which can cause severe immediate and long-term harm to marine ecological environments for decades after the initial accident, require rapid and accurate monitoring. Currently, optical and radar satellite images are used to monitor oil spills; however, remote sensing generally needs a long revisit period. Global Navigation Satellite System reflected signals (GNSS-R) can provide all-weather and all-day ocean monitoring and is therefore more suitable for oil spill monitoring. To assess the feasibility of the BeiDou Navigation Satellite System reflected signals (BeiDou-R) in detecting oil slicks, a BeiDou-R coastal simulated experiment is performed in this study on the oil slick distribution of an oil pipeline explosion accident. We set up an observation point and selected observation satellites, and a delay-Doppler map (DDM) of an oil-slicked sea surface under coastal scenarios was created by combining the mean-square slope (MSS) model for oil-slicked/clean surfaces and the Zavorotny–Voronovich (Z–V) scattering model. DDM simulation of the coastal scenarios effectively represents the scattering coefficient distribution of the presence of an oil slick. Theoretical analysis revealed that oil slicks can be detected within a radius of less than 5 km around the specular reflection point (SP) for BeiDou-R coastal simulation.

1. Introduction

Pollution by oil slicks in open ocean areas and coastal waters, whether accidental or deliberate, is a serious threat to marine environments, the economy, and human life. An oil spill occurs somewhere in the world almost every day of the year. The Deepwater Horizon oil spill accident in the Gulf of Mexico, which began on April 20, 2010, directly affected 176,000 km^2 of the Gulf's surface [1]. In addition, an oil pipeline explosion occurring in the Yellow Sea on November 22, 2013, heavily contaminated more than 3000 m^2 of the sea surface; the direct economic loss of this accident has been calculated as 750 million Yuan [2]. To reduce the impact of oil spill disasters on the environment and human health, accurate monitoring of oil spills at sea is of particularly importance. Operational oil spill monitoring is currently accomplished using a combination of optical and radar satellite images [3, 4]. However, because optical satellites are easily affected by weather, they cannot detect oil slicks under adverse conditions. Radar is used for monitoring under all-weather conditions and all day; however, the observation model is often in side-scan mode, which significantly affects the accuracy of oil spill detection owing to speckle noise in Synthetic Aperture Radar (SAR) images. In contrast, Global Navigation Satellite System reflected signals (GNSS-R) provide reflectivity information of the L-band, which is capable of penetrating cloud cover. In addition, the most important difference between GNSS and traditional remote sensing applications is that GNSS remote sensing is a bistatic technique. The transmitter and the receiver are not collocated, resulting in the transmitted GNSS signal reflecting or scattering in a forward direction; traditional remote sensing applications use more conventional back-scattered signals [5]. Moreover, GNSS-R payloads installed on different platforms can receive signals from the navigation satellites in large parts of the ocean and can provide long-term monitoring of oil slicks in all-weather conditions and all day.

The powerful GNSS-R was originally put forward in 1993 by Martin-Neira [6] as a new technique for ocean altimetry. Since then, reflections of GNSS signals from different types of surfaces have been widely studied. Several remote sensing applications presently using GNSS-R technology include

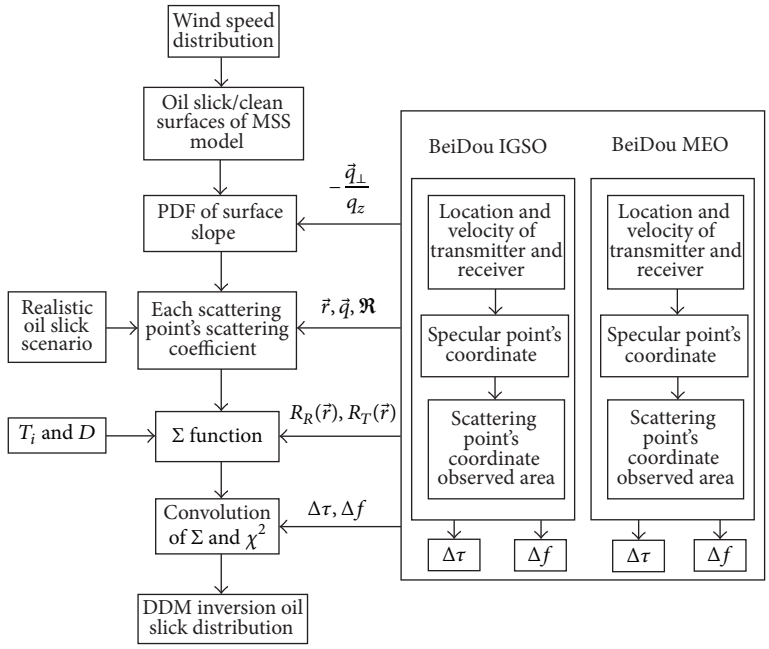

Figure 1: Flowchart of delay-Doppler map (DDM) simulation.

ocean altimetry [7–10], ocean wind [11–13], ocean wave sensing [14–16], and sea ice detection [17–19]. In addition, the possibility of detecting an oil-slicked sea surface using GNSS-R technology simulation has been investigated by Valencia et al. [20, 21]. This technique is based mainly on scattering coefficient retrieval using a delay-Doppler map (DDM). Li and Huang (2013) applied the methodology of a spatial integration approach (SIA) to sea surface oil slick detection simulation using DDM obtained under a simplified scenario with elevation angle of 90° [22]. This method has also been extended to general scenarios [23]; details of the DDM process simulation have been previously reported [24].

In addition to Global Positioning System (GPS), Global Navigation Satellite System (GNSS), and Galileo, other GNSS instruments currently in development include China's BeiDou constellation [25]. The development of the BeiDou system provides a new signal source to monitor ocean. Previous research focuses mainly on oil spill simulation detection using GPS reflected signals (GPS-R) technology. However, GPS uses only Medium Earth Orbit (MEO) satellites. Compared with existing GNSS constellations, the Chinese BeiDou satellite navigation system consists of MEO satellites in addition to Inclined Geosynchronous Orbit (IGSO) and Geostationary Earth Orbit (GEO) satellites. Until March 2015, five GEO, five IGSO, and six MEO BeiDou navigation satellites were in orbit. Moreover, the mixed constellation structure of BeiDou allows persistent monitoring of a given ocean area from multiple angles simultaneously. Currently, very few studies are available on ocean oil slick detection simulation using BeiDou-R. To test the performance of oil slick detection by using the BeiDou-R, the present study uses coastal simulation to detect oil-slicked ocean surfaces by using BeiDou IGSO and MEO satellites. Because BeiDou GEO satellites are almost stationary relative to Earth, they cannot use relative motion to produce Doppler frequency shift of DDM and are not considered in simulation experiments. The coastal simulation in this study is based on an actual oil spill accident that caused marine oil pollution. Based on the polluted area, we set up an observation point and select the corresponding observation satellites to monitor the oil spill conditions. Simulation DDM of the oil-slicked surface is then calculated by using the mean-square slope (MSS) model for oil-slicked/clean surfaces and the Z–V scattering model.

2. Simulation Approach

2.1. Framework. In this paper, a realistic scenario is simulated to improve the reliability of BeiDou-R for detection oil spill, which is derived from QuickBird multispectral images. Furthermore, this paper gives comparative analysis on the performance difference between BeiDou IGSO and MEO satellites for oil slick detection.

Figure 1 shows the specific DDM simulation process for an oil slick scenario. In the proposed framework, coastal simulation experiments using two BeiDou IGSO and MEO satellites are conducted on the basis of a realistic oil slick scenario. First, according to the geographic location information of the oil spill area, we set up the coastal observation point and selected the corresponding observation satellites. The location of the specular reflection point (SP) and the scattering point needs to be implemented according to the design of the coastal scenario. Under the conditions of observing the scattering coefficient distribution of a realistic oil slick, DDM simulation of the oil-slicked surface was then calculated by combining the MSS model for oil-slicked/clean surfaces and the Z–V scattering model. Finally, DDM simulation had been used to retrieve the scattering coefficient distribution of the presence of an oil slick based on the signal delay and

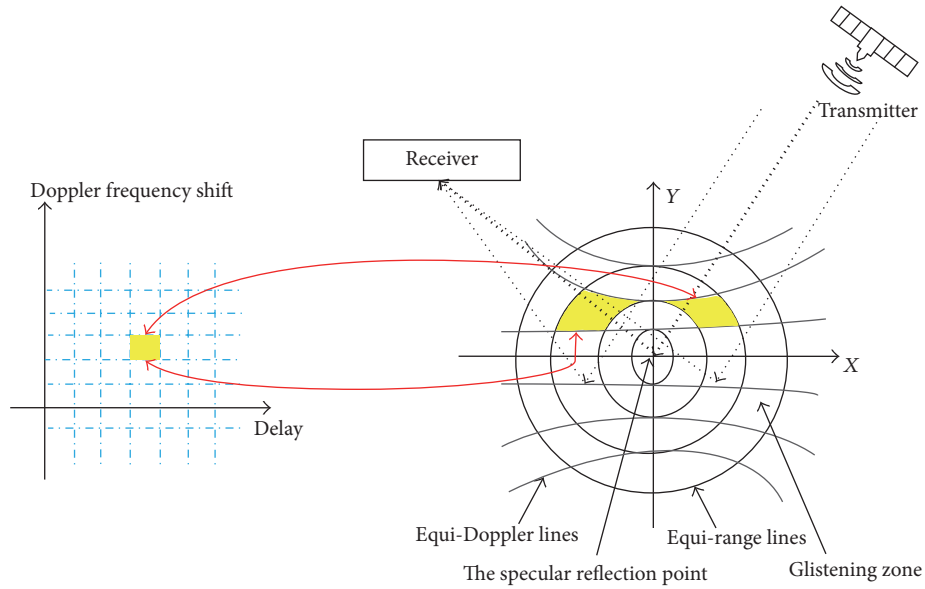

FIGURE 2: Corresponding relationship between the scattering units and the delay-Doppler units.

Doppler frequency shift. Oil slicks were detected within a radius coverage area around the SP based on the DDM. These methods are discussed in detail in the following sections.

2.2. DDM Theory. In an actual GNSS-R operational system, GNSS signals need to be received and processed using a bistatic configuration. GNSS-R receiver measurement of the sea-scattered signal is based on scattering from the different scattering units of the sea surface. The differences in delay and Doppler frequency shift correspond to the different scattering units of the sea surface, as shown in Figure 2.

GNSS signals scattered from the ocean are affected by the reflecting surface when it presents oil slicks. In such cases, the changes induced by the oil slick surface can be described by the correlation power waveform of the scattered signal in different delay and Doppler frequency shift values.

The DDM accounts for the correlation power distribution of the sea surface signals scattered as a function of delay and Doppler frequency shift with respect to the SP by using the GNSS-R scattering model proposed by Zavorotny and Voronovich expressed as [26, 27]

$$\left\langle \left| Y\left(\Delta\tau, \Delta f_D\right)\right|^2 \right\rangle = \Sigma\left(\Delta\tau, \Delta f_D\right) * \chi^2\left(\Delta\tau, \Delta f_D\right), \quad (1)$$

where $*$ indicates two-dimensional convolution and χ is the ambiguity function described as

$$\chi^2\left(\Delta\tau, \Delta f_D\right) = \Lambda^2\left(\Delta\tau\right) \cdot \left|S\left(\Delta f_D\right)\right|^2, \quad (2)$$

where the triangle of the $\Lambda(\Delta\tau)$ function is described as $\Lambda(\Delta\tau) = 1 - |\Delta\tau|/\tau_c$ if $|\Delta\tau| < \tau_c$ and $\Lambda(\Delta\tau) = 0$ otherwise, τ_c is the length of a chip of the C/A code (BeiDou $\tau_c = 1$ ms/2046, GPS $\tau_c = 1$ ms/1023), and $S(\Delta f_D) = \sin(\pi\Delta f_D T_i)/(\pi\Delta f_D T_i) \times \exp(-\pi i \Delta f_D T_i)$.

In the application of the GNSS-R signals, the delay and the Doppler at the SP are used as the reference point. $\Delta\tau$ is the delay of the scattering point with respect to the SP expressed as

$$\Delta\tau = \tau\left(\vec{r}\right) - \tau\left(0\right) = \frac{\left(R_T\left(\vec{r}\right) + R_R\left(\vec{r}\right)\right) f}{c} - \tau\left(0\right), \quad (3)$$

where f is the frequency of C/A code (BeiDou $f = 2.046 \times 10^6$ Hz, GPS $f = 1.023 \times 10^6$ Hz), $R_T(\vec{r})$ is the distance from the transmitter to the scattering point, $R_R(\vec{r})$ is the distance from the receiver to the scattering point, and c is the speed of light. Δf is the Doppler frequency shift of the scattering points with respect to the SP expressed as [28]

$$\Delta f = f_D\left(\vec{r}\right) - f_D\left(0\right) = \frac{\left(\vec{V}_T \cdot \widehat{m} - \vec{V}_R \cdot \widehat{n}\right)}{\lambda} - f_D\left(0\right), \quad (4)$$

where $\vec{V}_T$ and $\vec{V}_R$ are the velocities of transmitter and receiver, respectively; $\widehat{m}$ is the unit vector of the incident wave; and $\widehat{n}$ is the unit vector of the scattered wave. The Doppler frequency shift of the signal at different scattering points across the surface can be accurately determined by using (4) with respect to the known positions and velocities of the transmitter, receiver, and SP. Before calculating the received power, Σ of each scattering point is determined as

$$\Sigma\left(\Delta\tau, \Delta f_D\right) = \frac{T_i^2 D^2\left(\vec{r}\right)\sigma^0\left(\vec{r}\right)}{4\pi R_R^2\left(\vec{r}\right) R_T^2\left(\vec{r}\right)} ds, \quad (5)$$

where T_i is the coherent integration time, D is the antenna radiation pattern, and $\vec{r}$ is the displacement vector of a scattering point from the SP. The SP can be calculated by using the known locations of the receiver and transmitter; details of the calculation are shown elsewhere [5]. The expression of each scattering point of the scattering coefficients over the sea surface is [26]

$$\sigma^0\left(\vec{r}\right) = \pi\left|\Re\right|^2 \left(\frac{\left|\vec{q}\right|}{q_z}\right)^4 P_{\text{pdf}}\left(-\frac{\vec{q}_\perp}{q_z}\right), \quad (6)$$

where $|\Re|^2$ is the Fresnel reflection coefficient; $\vec{q}$ is the scattering vector, which is defined as $\vec{q} = \kappa(\hat{n} - \hat{m}) = \vec{q}_\perp + q_z\hat{z}$; and κ is the carrier wave number. $P_{\text{pdf}}(-\vec{q}_\perp/q_z)$ represents the probability density function (PDF) of the given sea surface slope. Soulat presented the PDF of surface slopes for arbitrary wind direction [29]. Here, we assume that the wind direction is along the x-axis of the Earth-centered X-Z incidence (ECXI) system. The slope PDF can be written as [26]

$$P_{\text{pdf}}\left(-\frac{\vec{q}_\perp}{q_z}\right) = \frac{1}{2\pi\sqrt{\sigma_\mu^2\sigma_c^2}} \cdot \exp\left[-\frac{1}{2}\left(\frac{\left(-q_{\perp,c}/q_z\right)^2}{\sigma_c^2} + \frac{\left(-q_{\perp,\mu}/q_z\right)^2}{\sigma_\mu^2}\right)\right], \tag{7}$$

where $-q_{\perp,c}/q_z$ and $-q_{\perp,\mu}/q_z$ represents the upwind and crosswind ocean slope, respectively; σ_c^2 is a crosswind MSS component; and σ_μ^2 is an upwind MSS component. According to the Cox and Munk MSS model, the presence of oil slicks on the sea surface translates into changes in the surface MSS [30]. Accordingly, the relationship among the ocean surface's MSS and the wind speed (WS) can be formulated as

$$\begin{aligned}\sigma_{c,c}^2 &= 0.003 + 1.92 * 10^{-3}U_{10},\\ \sigma_{\mu,c}^2 &= 3.16 * 10^{-3}U_{10}.\end{aligned} \tag{8}$$

To model the effect of the oil slick presence, the oil slick surface's MSS is computed by using the appropriate relationship with the WS as

$$\begin{aligned}\sigma_{c,s}^2 &= 0.003 + 0.84 * 10^{-3}U_{10},\\ \sigma_{\mu,s}^2 &= 0.005 + 0.78 * 10^{-3}U_{10},\end{aligned} \tag{9}$$

where the second subscripts of MSS, that is, c and s, represent clean and oil-slicked surfaces, respectively and U_{10} is the WS at the height of 10 m from the sea surface. This MSS model was originally proposed for optical wavelengths signals. To apply the model to L-band GNSS-R signals, an empirical modification was proposed by Katzberg et al. [31] in 2006. In this paper, we adopted this empirical MSS model for the clean and slicked regions in the simulation.

Oil slicks on the sea surface cause changes in the scattering coefficient distribution over the observed surface and thus change the corresponding entire DDM. By using this oil slick model, the impacts of the oil slick on the DDM can be distinguished.

3. Simulation Scenarios

The coastal simulation experiment is based on the oil slick distribution from an oil pipeline explosion that occurred in the district of Qingdao, China. The oil spill distribution data were used as input for the DDM simulation by using QuickBird multispectral images. According to the location of oil spill on the sea surface, we assumed two observation points, R1 and R2 receivers, for monitoring the oil spill. At the R1 observation point, we used the BeiDou IGSO C06 satellite to conduct simulation experiments; this simulation is hereafter referred to as experiment I. Figure 3 shows the Skyplot point of IGSO C06 at experiment I at 08:10 LT on November 27, 2013. At the R2 observation point, we used the BeiDou MEO C11 satellite to conduct simulation experiments; this simulation is hereafter referred to as experiment II. Figure 4 shows the Skyplot point of MEO C11 for experiment II at 23:50 LT on November 27, 2013.

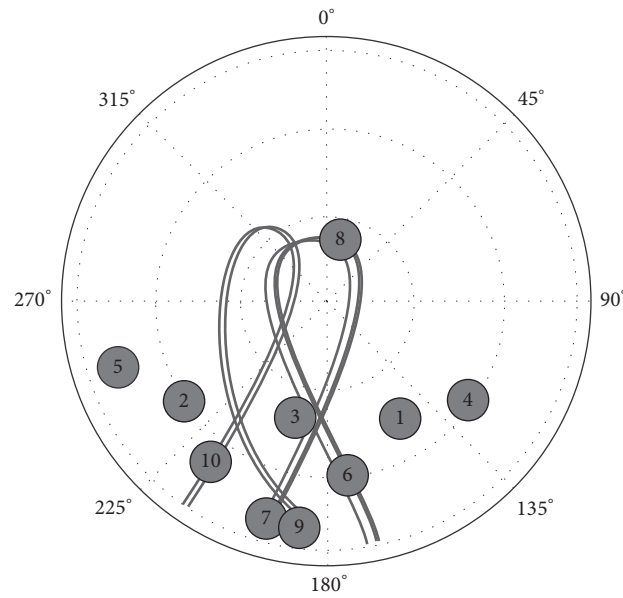

Figure 3: Skyplot point of Inclined Geosynchronous Orbit (IGSO) C06 for experiment I (08:10 LT, November 27, 2013).

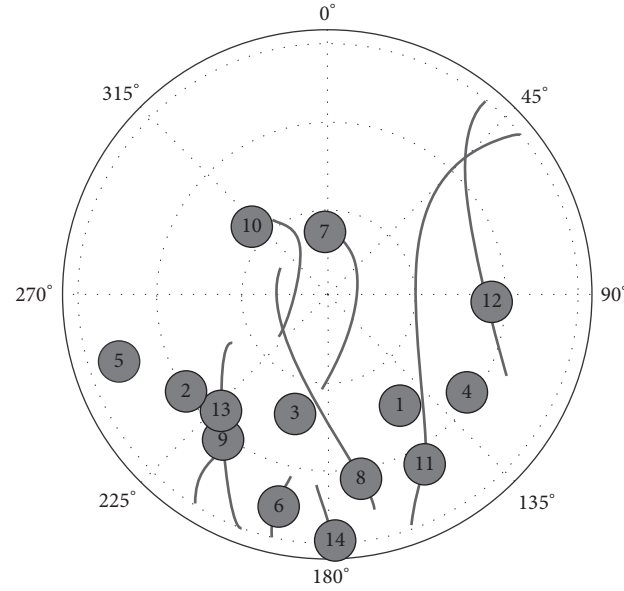

Figure 4: Skyplot point of Medium Earth Orbit (MEO) C11 for experiment II (23:50 LT, November 27, 2013).

Table 1: Simulation experiment parameters.

Scenario parameters	Experiment I	Experiment II
Transmitter satellite	BeiDou IGSO C06	BeiDou MEO C11
Time	08:00–08:10 LT Nov.27, 2013	23:40–23:50 LT Nov.27, 2013
Transmitter position (T_{nx}, T_{ny}, T_{nz})	$(-1.54, 0, 3.93)\ 10^7$ m	$(-1.45, 0, 2.38)\ 10^7$ m
Transmitter velocity (V_{Tx}, V_{Ty}, V_{Tz})	$(-1.65, -0.53, -2.03)$ km/s	$(-2.21, 1.38, -1.58)$ km/s
Receiver position (R_{nx}, R_{ny}, R_{nz})	$(0.0067, 0, 6.37)\ 10^6$ m	$(0.01, 0, 6.37)\ 10^6$ m
Receiver velocity (V_{Rx}, V_{Ry}, V_{Rz})	(0, 0, 0) km/s	(0, 0, 0) km/s
Elevation angle at SP	31°	24°
Oil slick image	QuickBird multispectral images	
Constellations	BeiDou ephemeris	
Coherent integration times	10 ms	
Wind velocity and direction	6.6 m/s, along the x-axis (ECXI system)	
Observation surface, y-direction	[−10–10] km	
Observation surface, x-direction	[0–10] km	
Reflect antenna toward	180°	
Receiver height	15 m	

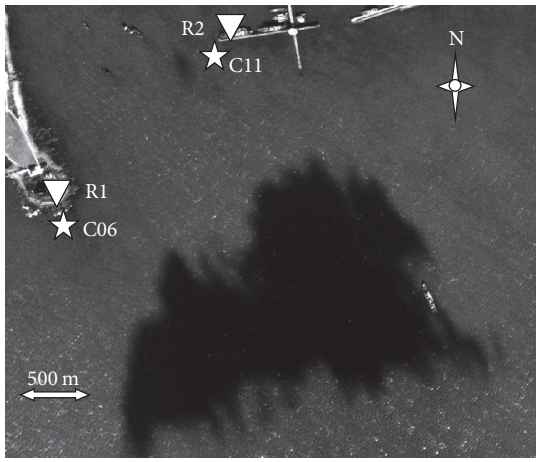

Figure 5: QuickBird multispectral images of oil slick at Qingdao on November 27, 2013, and the specular reflection points (SPs) of C06 and C11.

Figure 5 shows the analog scene monitoring of oil slicks observed on the sea surface, and the black color in the figure represents the shape of the oil slick; the inverted triangles represent the locations of the receiver as R1 and R2; and star points represent the final SPs of C06 (IGSO) and C11 (MEO) in the two experiments. According to the theory of DDM oil slick detection mentioned in Section 2.2, the relative motions of the transmitter and the receiver can produce a Doppler shift to develop DDM for the present of oil slick distinguish in our simulation. The GEO satellite is almost stationary and is therefore not suitable for coastal DDM technology. Thus, the GEO satellite was not considered in our coastal simulation.

In this work, we did not consider the simulation system noise. The influence of the Earth's curvature on the simulation experiment was also not considered because the height of the antenna is only 15 m. On the basis of nearby weather station data from the same period, we determined that the WS observed surface was 6.6 m/s and that the distribution was homogeneous over the entire observation surface. Specific descriptions of the simulation scenarios are shown in Table 1. Here, the ECXI system was used [24].

4. Simulation Results and Discussion

On the basis of the experiment I simulation parameters, we obtained the averaged scattering coefficients of both oil-slicked and clean ocean surfaces over the observation surface by using (6), (8), and (9). Figure 6(a) shows the averaged scattering coefficients of both oil-slicked and clean ocean surfaces in the IGSO scenario. It should be noted that the scattering coefficient of the oil slick decreased more rapidly than that of the clean ocean surface. The figure clearly shows that the scattering coefficients of the two types of surfaces became identical at scattering points 6 km from the SP, which suggests that the oil slick can be easily detected within a range of about 6 km from the scattering points in our simulation conditions.

On the basis of experiment II simulation parameters, we obtained the averaged scattering coefficients of both oil-slicked and clean ocean surfaces over the observation surface by using (6), (8), and (9). Figure 6(b) shows the averaged scattering coefficients of both oil-slicked and clean ocean surfaces in the MEO scenario. It appears that the averaged scattering coefficients of the two types of surfaces became the same as the scattering points 8 km from the SP, which suggests that oil slicks can be detected in this range.

As shown in Figure 6, the horizontal axis represents the location of each scattering point relative to the SP over the observation surface, and the vertical axis represents the averaged scattering coefficients of both oil-slicked areas and clean areas. The SP is located at the center of the coordinate system ($x = 0$, $y = 0$).

A contamination mask was derived from the QuickBird multispectral images (Figure 3) for our simulation, which was

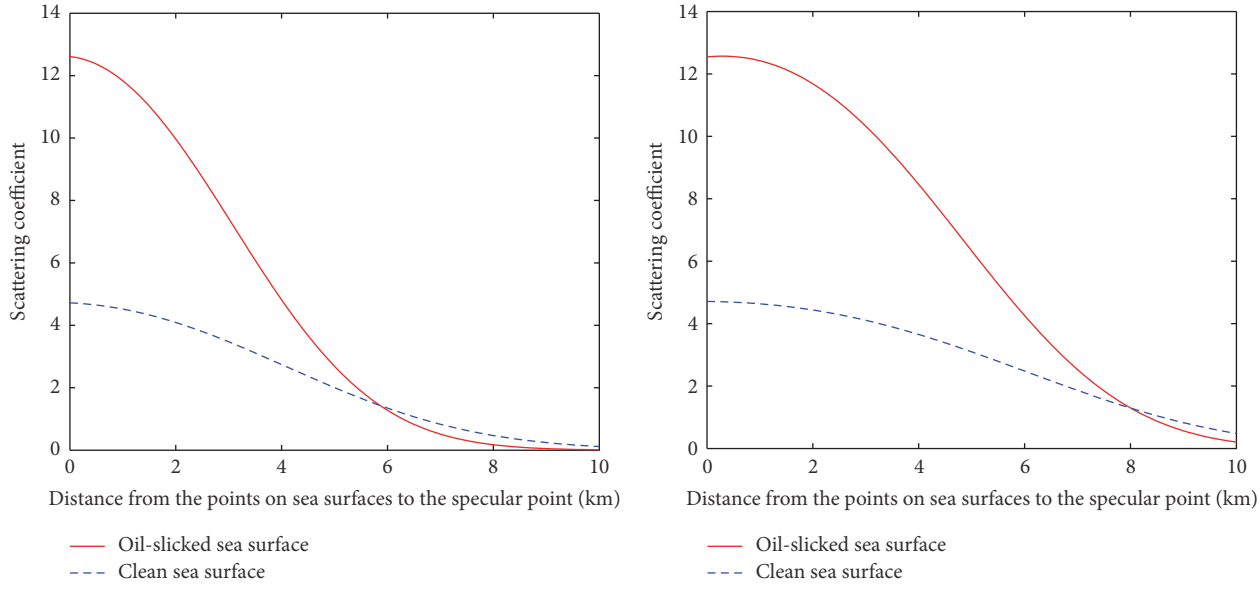

(a) Results of the scattering coefficients from the BeiDou Inclined Geosynchronous Orbit (IGSO) simulation experiment

(b) Results of the scattering coefficients from the BeiDou Medium Earth Orbit (MEO) simulation experiment

Figure 6: Scattering coefficients of both oil-slicked areas and clean areas versus distance to the specular reflection point (SP) based on the two different simulation experiments.

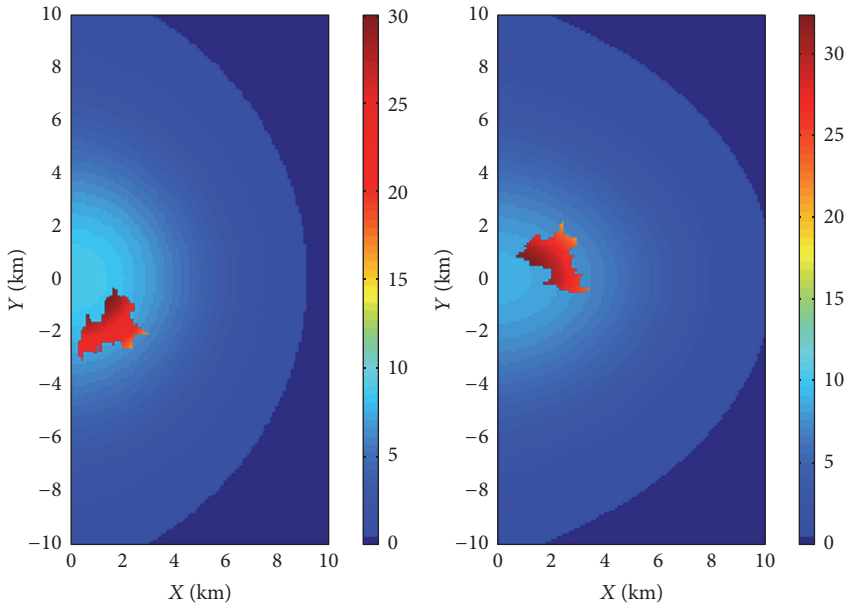

(a) Scattering coefficient distribution based on Inclined Geosynchronous Orbit (IGSO) scenario

(b) Scattering coefficient distribution based on Medium Earth Orbit (MEO) scenario

Figure 7: Simulation results of scattering coefficient distribution from both scenarios.

used as input for the DDM simulation. By combining the design in Figure 6 of the two simulations of oil slick detection scenarios and observed actual oil spill distribution, we obtained the scattering coefficient distributions of each scattering point observation surface including the ocean and the oil slick surface by using (6), (8), and (9). Figures 7(a) and 7(b) show the corresponding scattering coefficient distributions of the two experiments, IGSO and MEO scenarios, respectively. The oil slick area can be clearly distinguished in Figure 7, because it presents a higher scattering coefficient than that of the clean surface. This is attributed to oil damping of the surface waves, which causes more power to be reflected in the

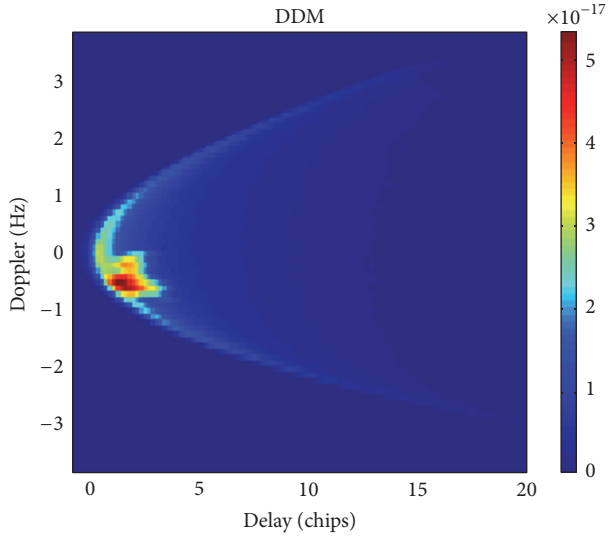

Figure 8: Simulated DDM results for simulation experiment I for Inclined Geosynchronous Orbit (IGSO) scenario.

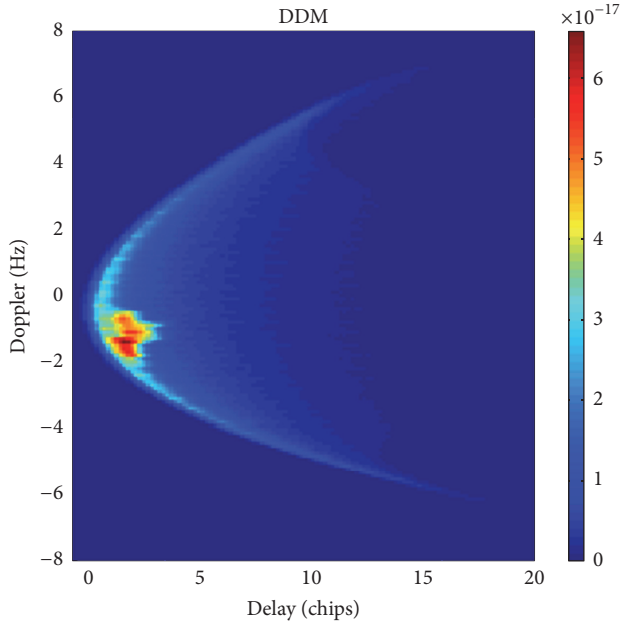

Figure 9: Simulated DDM results for simulation experiment II for Medium Earth Orbit (MEO) scenario.

forward direction from this observation surface, although the WS over the entire observation surface is considered uniform.

In Figure 7, the horizontal (vertical) axis indicates the location of each scattering point relative to the SP over the observation surface x-direction (y-direction). In the figure, the red (blue) color indicates the scattering coefficient distribution of the oil slick (ocean) surface over the observation surface. The SP is ($x = 0$, $y = 0$).

Both simulation experiments I and II were employed in the DDM based on Figure 7. Figure 8 shows the simulated DDM results for simulation experiment I, which represents the scattering coefficient distribution in the presence of the oil slick shown in Figure 7(a). Figure 9 shows that for experiment II, which represents the scattering coefficient distribution in the presence of the oil slick shown in Figure 7(b). As shown in Figures 8 and 9, the area of the oil spill can be clearly distinguished from the simulated DDMs of the two scenarios, and their ranges are within the theoretical ranges of Figures 6 and 7. Hence, the results of the two simulation experiments indicate that it is feasible to use the BeiDou-R coastal setup to detect oil slicks over the observed surface. In Figures 8 and 9, the horizontal axis indicates the delay in chips and the vertical axis indicates Doppler. The different colors represent the scattered power values of the corresponding signals.

In the coastal setup, the receiver's location is fixed; thus, the satellite's height and velocity are major factors in the DDM map. A comparison of Figures 8 and 9 revealed that the Doppler shift and the output power from MEO were wider and stronger, respectively, than those from IGSO. This occurred because the velocity of MEO was faster than that of IGSO in the observed period, and the height of MEO was lower than that of IGSO. According to the DDM theory introduced in Section 2.2, if the observed surface points from MEO are more than IGSO, oil slicks can be distinguished more easily from MEO in our observation period.

5. Conclusion

This study used BeiDou-R simulation to prove the capability of oil slick detection under a coastal scenario based on a DDM obtained by combining the MSS model for oil-slicked/clean surfaces and the Z–V scattering model. The simulated retrieval process was based on an oil pipeline explosion accident that occurred in 2013 in the district of Qingdao, China. We conducted two simulation experiments of oil slicks by using the BeiDou IGSO C06 and MEO C11 satellites under the same wind conditions. The simulation results showed that the oil-slicked area could be clearly distinguished by using DDM map technology from BeiDou MEO and IGSO satellites with the coastal setup.

By analysis and comparison, the oil slick was detected more easily by MEO, and oil slicks were clearly distinguishable within a coverage area radius of less than 5 km around the SP in the observation period. Because the receiver's location is fixed in the coastal setup, the satellite's height and velocity affect the DDM results and the oil slick inversion effect. Therefore, a lower satellite height and faster satellite velocity result in stronger output power and better inversion.

Competing Interests

The authors declare that there is no conflict of interests regarding the publication of this paper.

Acknowledgments

The work described in this paper was substantially supported by National Natural Science Foundation of China (Grant nos. 41376178, 41401489, and 41506213).

References

[1] https://en.wikipedia.org/wiki/Deepwater_Horizon_oil_spill#cite_note-area_of_spill-4.

[2] Y. Zhu, X.-M. Qian, Z.-Y. Liu, P. Huang, and M.-Q. Yuan, "Analysis and assessment of the Qingdao crude oil vapor explosion accident: lessons learnt," *Journal of Loss Prevention in the Process Industries*, vol. 33, pp. 289–303, 2015.

[3] C. S. L. Grimaldi, D. Casciello, I. Coviello, T. Lacava, N. Pergola, and V. Tramutoli, "Satellite oil spill detection and monitoring in the optical range," in *Proceedings of the 30th IEEE International Geoscience and Remote Sensing Symposium (IGARSS '10)*, July 2010.

[4] A. H. S. Solberg, C. Brekke, and P. O. Husøy, "Oil spill detection in Radarsat and Envisat SAR images," *IEEE Transactions on Geoscience and Remote Sensing*, vol. 45, no. 3, pp. 746–754, 2007.

[5] S. Gleason, S. Lowe, and V. Zavorotny, "Remote sensing using bistatic GNSS reflections," in *GNSS Applications and Methods*, S. Gleason and D. Gebre-Egziabher, Eds., Artech House, Norwood, Mass, USA, 2009.

[6] M. Martin-Neira, "A passive reflectometry and interferometry system (PARIS): application to ocean altimetry," *ESA Journal*, vol. 17, no. 4, pp. 331–355, 1993.

[7] A. Rius, E. Cardellach, and M. Martín-Neira, "Altimetric analysis of the sea-surface GPS-reflected signals," *IEEE Transactions on Geoscience and Remote Sensing*, vol. 48, no. 4, pp. 2119–2127, 2010.

[8] H. Park, E. Valencia, A. Camps, A. Rius, S. Ribó, and M. Martín-Neira, "Delay tracking in spaceborne GNSS-R ocean altimetry," *IEEE Geoscience and Remote Sensing Letters*, vol. 10, no. 1, pp. 57–61, 2013.

[9] Y. Zhang, L. Tian, W. Meng, Q. Gu, Y. Han, and Z. Hong, "Feasibility of code-level altimetry using coastal BeiDou reflection (BeiDou-R) setups," *IEEE Journal of Selected Topics in Applied Earth Observations and Remote Sensing*, vol. 8, no. 8, pp. 4130–4140, 2015.

[10] A. Ghavidel, D. Schiavulli, and A. Camps, "Numerical computation of the electromagnetic bias in GNSS-R altimetry," *IEEE Transactions on Geoscience and Remote Sensing*, vol. 54, no. 1, pp. 489–498, 2016.

[11] J. L. Garrison, A. Komjathy, V. U. Zavorotny, and S. J. Katzberg, "Wind speed measurement using forward scattered GPS signals," *IEEE Transactions on Geoscience and Remote Sensing*, vol. 40, no. 1, pp. 50–65, 2002.

[12] N. Rodriguez-Alvarez, D. M. Akos, V. U. Zavorotny, J. A. Smith, A. Camps, and C. W. Fairall, "Airborne GNSS-R wind retrievals using delay-doppler maps," *IEEE Transactions on Geoscience and Remote Sensing*, vol. 51, no. 1, pp. 626–641, 2013.

[13] W. Li, F. Fabra, D. Yang et al., "Initial results of typhoon wind speed observation using coastal GNSS-R of BeiDou GEO satellite," *IEEE Journal of Selected Topics in Applied Earth Observations and Remote Sensing*, vol. 9, no. 10, pp. 1–10, 2016.

[14] F. Soulat, M. Caparrini, O. Germain, P. Lopez-Dekker, M. Taani, and G. Ruffini, "Sea state monitoring using coastal GNSS-R," *Geophysical Research Letters*, vol. 31, no. 21, 2004.

[15] M. Caparrini, A. Egido, F. Soulat et al., "Oceanpal®: monitoring sea state with a GNSS-R coastal instrument," in *Proceedings of the IEEE International Geoscience and Remote Sensing Symposium (IGARSS '07)*, pp. 5080–5083, Barcelona, Spain, June 2007.

[16] K. M. Larson, R. D. Ray, F. G. Nievinski, and J. T. Freymueller, "The accidental tide gauge: a GPS reflection case study from Kachemak Bay, Alaska," *IEEE Geoscience and Remote Sensing Letters*, vol. 10, no. 5, pp. 1200–1204, 2013.

[17] M. B. Rivas, J. A. Maslanik, and P. Axelrad, "Bistatic scattering of GPS signals off arctic sea ice," *IEEE Transactions on Geoscience and Remote Sensing*, vol. 48, no. 3, pp. 1548–1553, 2010.

[18] F. Fabra, E. Cardellach, A. Rius et al., "Phase altimetry with dual polarization GNSS-R over sea ice," *IEEE Transactions on Geoscience and Remote Sensing*, vol. 50, no. 6, pp. 2112–2121, 2012.

[19] Z. Yun, M. Wanting, G. Qiming et al., "Detection of bohai bay sea ice using GPS-reflected signals," *IEEE Journal of Selected Topics in Applied Earth Observations and Remote Sensing*, vol. 8, no. 1, pp. 39–46, 2015.

[20] E. Valencia, A. Camps, H. Park et al., "Oil slicks detection using GNSS-R," in *Proceedings of the IEEE International on Geoscience and Remote Sensing Symposium (IGARSS '11)*, vol. 142, pp. 4383–4386, July 2011.

[21] E. Valencia, A. Camps, N. Rodriguez-Alvarez, H. Park, and I. Ramos-Perez, "Using GNSS-R imaging of the ocean surface for oil slick detection," *IEEE Journal of Selected Topics in Applied Earth Observations and Remote Sensing*, vol. 6, no. 1, pp. 217–223, 2013.

[22] C. Li and W. Huang, "Sea surface oil slick detection from GNSS-R delay-Doppler maps using the spatial integration approach," in *Proceedings of the IEEE Radar Conference (RadarCon '13)*, pp. 1–6, Ottawa, Canada, May 2013.

[23] C. Li, W. Huang, and S. Gleason, "Dual antenna space-based GNSS-R ocean surface mapping: oil slick and tropical cyclone sensing," *IEEE Journal of Selected Topics in Applied Earth Observations and Remote Sensing*, vol. 8, no. 1, pp. 425–435, 2015.

[24] C. Li and W. Huang, "Simulating GNSS-R delay-doppler map of oil slicked sea surfaces under general scenarios," *Progress in Electromagnetics Research B*, vol. 48, pp. 61–76, 2013.

[25] M. Z. Bhuiyan, S. Söderholm, S. Thombre, L. Ruotsalainen, and H. Kuusniemi, "Overcoming the challenges of beidou receiver implementation," *Sensors*, vol. 14, no. 11, pp. 22082–22098, 2014.

[26] V. U. Zavorotny and A. G. Voronovich, "Scattering of GPS signals from the ocean with wind remote sensing application," *IEEE Transactions on Geoscience and Remote Sensing*, vol. 38, no. 2, pp. 951–964, 2000.

[27] J. F. Marchan-Hernandez, A. Camps, N. Rodriguez-Alvarez, E. Valencia, X. Bosch-Lluis, and I. Ramos-Perez, "An efficient algorithm to the simulation of delay-doppler maps of reflected global navigation satellite system signals," *IEEE Transactions on Geoscience and Remote Sensing*, vol. 47, no. 8, pp. 2733–2740, 2009.

[28] S. Gleason, "Towards sea ice remote sensing with space detected GPS signals: demonstration of technical feasibility and initial consistency check using low resolution sea ice information," *Remote Sensing*, vol. 2, no. 8, pp. 2017–2039, 2010.

[29] F. Soulat, *Sea surface remote sensing with GNSS and sunlight reflections [Ph.D. thesis]*, Universitat Politècnica de Catalunya, Catalunya, Spain, 2003.

[30] C. Cox and W. Munk, "Measurement of the roughness of the sea surface from photographs of the Sun's glitter," *Journal of the Optical Society of America*, vol. 44, no. 11, pp. 838–850, 1954.

[31] S. J. Katzberg, O. Torres, and G. Ganoe, "Calibration of reflected GPS for tropical storm wind speed retrievals," *Geophysical Research Letters*, vol. 33, no. 18, Article ID L18602, 2006.

Hindawi
Mathematical Problems in Engineering
Volume 2017, Article ID 1316505, 13 pages
https://doi.org/10.1155/2017/1316505

Research Article

A Detailed and High-Resolution Land Use and Land Cover Change Analysis over the Past 16 Years in the Horqin Sandy Land, Inner Mongolia

Xiulian Bai,[1] Ram C. Sharma,[2,3] Ryutaro Tateishi,[2] Akihiko Kondoh,[2] Bayaer Wuliangha,[4] and Gegen Tana[2]

[1]*Graduate School of Science, Chiba University, 1-33 Yayoi-cho, Inage-ku, Chiba 263-8522, Japan*
[2]*Center for Environmental Remote Sensing (CEReS), Chiba University, 1-33 Yayoi-cho, Inage-ku, Chiba 263-8522, Japan*
[3]*Department of Informatics, Tokyo University of Information Sciences, 4-1 Onaridai, Wakaba-ku, Chiba 265-8501, Japan*
[4]*College of Geographical Science, Inner Mongolia Normal University, Hohhot 010022, China*

Correspondence should be addressed to Xiulian Bai; baixiulian@163.com

Received 13 October 2016; Revised 9 December 2016; Accepted 26 December 2016; Published 31 January 2017

Academic Editor: Hasi Bagan

Land use and land cover (LULC) change plays a key role in the process of land degradation and desertification in the Horqin Sandy Land, Inner Mongolia. This research presents a detailed and high-resolution (30 m) LULC change analysis over the past 16 years in Ongniud Banner, western part of the Horqin Sandy Land. The LULC classification was performed by combining multiple features calculated from the Landsat Archive products using the Support Vector Machine (SVM) based supervised classification approach. LULC maps with 17 secondary classes were produced for the year of 2000, 2009, and 2015 in the study area. The results showed that the multifeatures combination approach is crucial for improving the accuracy of the secondary-level LULC classification. The LULC change analyses over three different periods, 2000–2009, 2009–2015, and 2000–2015, identified significant changes as well as different trends of the secondary-level LULC in study area. Over the past 16 years, irrigated farming lands and salinized areas were expanded, whereas the waterbodies and sandy lands decreased. This implies increasing demand of water and indicates that the conservation of water resources is crucial for protecting the sensitive ecological zones in the Horqin Sandy Land.

1. Introduction

Desertification is one of the crucial environmental issues that restrict the social, economic, and political development in arid and semiarid area [1, 2]. Desertification has been defined in several ways; however, the most widely accepted one has defined the desertification as the land degradation in arid, semiarid, and dry subhumid areas resulting from various factors, including climate variations and human activities [3–6]. In recent years, many socioenvironmental problems such as land shortage, environmental deterioration, reduction of biological and economic productivity, water scarcity, poverty, and migrations have emerged due to rapid spread of the desertification. These problems have threatened the human survival and sustainable economic development [7–9]. It is argued that sustainability will be a great challenge of the human society in coming decades particularly in the transitional and marginal agricultural zones [10–12].

China is a developing country with large population and scarce arable land, which is plagued by a long-term and large-scale desertification [13]. In China, desertified areas are mostly distributed in the western part of the northeast China, the north part of the northern China, and most parts of the northwest China [14, 15]. The desert areas in China are still expanding by 2460–10,400 km^2 per year. As much as 3.317 million km^2 (34.6% of the total land area) land area in China is affected by the desertification; and up to 400 million people are struggling with unproductive

agricultural land and water shortages [14]. The government of China and social media have focused on the desertification problems [15]. The government has implemented a series of ecological engineering programs to combat the desertification, including the Three-North Shelter Forest Program from 1978, Beijing and Tianjin Sandstorm Source Treatment Program from 2001 to 2010, Grain to Green Program from 2003, and Returning Grazing Land to Grassland Program from 2003 [13]. However, monitoring and assessment of these programs have identified very limited success in a few local regions [16–20], while desertification is increasing further in some desertification areas.

The Horqin Sandy Land, one of the four largest sandy land in the northern China, has a long history of desertification and land degradation. Rapid increase in population and inappropriate human activities such as agricultural reclamation, overgrazing, excessive collection of fuel wood and herbs, unmanaged tourism, overconsumption of water resource, and mining and road cutting have induced the desertification continuously in the Horqin Sandy Land [18, 21, 22]. Moreover, climate change in the recent decades has severely intensified the desertification [23]. During Liao Dynasty (907–1125 AD), the Horqin Sandy Land was full of tall forests and dense grasslands which used to sustain nomadic herders [13]. Since the nineteenth century, rapid increase of agriculturalist migrants into this region started to convert the ancient grassland and woodland into agricultural areas which reduced the available grazing land and put the marginal lands under cultivation. This situation continued to twentieth century and reached the peak of development in the 1950s–1960s, with rapid expansion of the human settlements and urban areas [24]. In the beginning of the Great Leap Forward (1958–1960) and during the following two decades, expanding cultivation led to forcing the local nomadic herders to moving into the border area, and most of the area was occupied by agriculturalists [25, 26]. By the early 1980s, the rural reform program under the "household responsibility" system played a key role in the overgrazing of grassland; and now the implementation of "double responsibility" system by the local government may do little to reduce the overgrazing [24]. With the development in the agricultural and industrial sectors, these essentially uncontrolled activities have resulted in the destruction of woodland and grassland, degradation of surface soil, and increased water consumption [24].

Accurate land use and land cover (LULC) maps derived from the remote sensing data are highly important for the monitoring and quantification of the global environment as well as spatiotemporal changes [27]. The LULC change analysis assists decision-makers to understand the dynamics of changing environment and can ensure the sustainable development [28]. Multitemporal and multiscale remote sensing can provide substantial information about the land surface and facilitate the monitoring of environmental problems such as land degradation [29]. The combination of spectral, textural, and topographic features has been suggested for improving the accuracy of LULC mapping while producing the recent nationwide 30 m resolution LULC map of Japan [30]. Since the previous studies in the Horqin Sandy Land have focused on mapping of the LULC and spatial-temporal change analysis mainly based on the spectral information from the satellite data [31], accuracy of the resulting change information is a major concern that is immensely important for the decision-makers.

The availability of the high spatial resolution and multitemporal satellite imagery from the archived Landsat datasets provides a unique opportunity for the monitoring of land degradation and desertification. This study deploys the archived Landsat datasets of years 2000, 2009, and 2015 for deriving the high-resolution LULC change information to present detailed LULC change pattern. Since 2000, the state and local government implements a series of ecological restoration projects to mitigate the further desertification and restoration of desertified grassland in the fragile environment of the Horqin Sandy Land [13]. The main objective of this study is to analyze the spatiotemporal pattern of the LULC changes in the Horqin Sandy Land. This study presents the improvement of the LULC classification accuracy by combining the multiple features (spectral features, spectral indices, spectral transformations, and textural and topographic features) derived from the satellite data using the Support Vector Machine (SVM) based supervised classification approach. While the previous studies in the Horqin Sandy Land have analyzed the LULC changes using major land cover types only [11], this study has achieved the more detailed LULC change information by adding the secondary classes. The analysis on the spatiotemporal change pattern is expected to reveal the mechanisms responsible for the desertification processes.

2. Materials and Methods

2.1. Study Area. This study was carried out in Ongniud Banner, in the western part of the Horqin Sandy Land in Inner Mongolia, China. The Ongniud Banner belongs to the transitional zone of the agricultural and animal husbandry region, which is vulnerable ecological region to natural changes and anthropogenic activities [32]. This region is severely suffering from soil erosion and overconsumption and overexploiting of land resources [32, 33]. The location map of the study area is shown in Figure 1. The study area covers an area of 11,882 km^2, which stretches 250 km from east to west and 84 km from north to south.

The three typical geomorphological characteristics throughout the study area are from west to east in the order of high elevation alluvial flats, low mountains and hills, and low Aeolian dunes, and the altitude decreases from 2025 m in the west to 286 m in the east [33]. The climate of this region is characterized by temperate semiarid with windy and dry winters/springs, warm and relatively rainy summers, and cool autumns. The mean annual temperature is 7°C; annual mean precipitation is 300 mm, of which 70% precipitation falls between July and September. The mean annual wind velocity is 4.2 m s^{-1} [34]; the windy season lasts from early March to late May. As the study area is comprised of the mosaic of farmland, grassland, and steppe desert with different soil types and land cover forms, this study area offers an opportunity to assess the performance

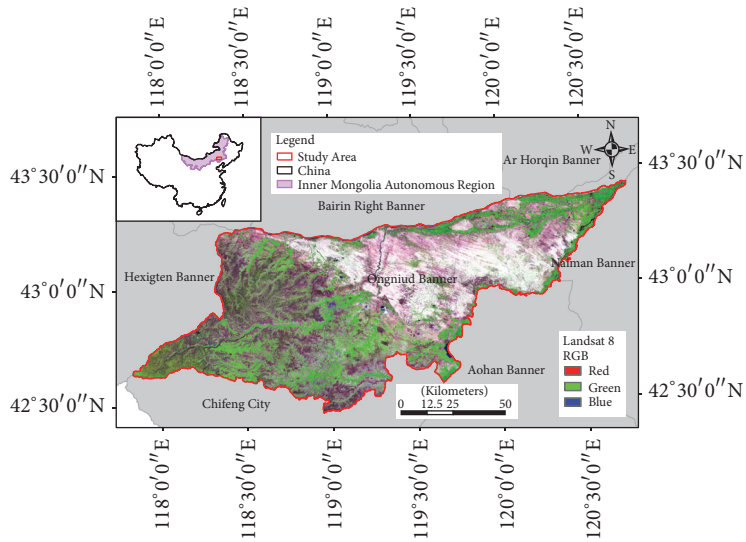

Figure 1: Location map of the study area (red polygon) displayed over the Landsat 8 data based false color composite (FCC) image.

of remote sensing data for change analysis of the detailed, secondary-level classes.

2.2. Datasets and Preprocessing. In this research, the Landsat 5 Thematic Mapper (TM) datasets of years 2000 and 2009 and Landsat 8 Operational Land Imager/Thermal Infrared Sensor (OLI/TIRS) datasets of year 2015 available from the United States Geological Survey (USGS) were used. The details on the Landsat datasets used in the research are shown in Table 1. All the 30 m resolution Landsat scenes used in the research were carefully selected from the highest vegetation activity period between July and September; and they were without cloud cover. In addition to the Landsat 5 and Landsat 8 datasets, 30 m resolution Shuttle Radar Topography Mission (SRTM) based Digital Elevation Model (DEM) data available from the United States Geological Survey (USGS) was used.

The land use dataset of Inner Mongolia at 1 : 10,0000 of years 1995 and 2000, desert distribution dataset of China at 1 : 10,0000, vegetation map of China at 1 : 400,0000, and China soil database available from the Chinese Academy of Sciences were used as the reference datasets [12]. Due to different created time and lower resolution of data, it was just used to grasp broader view of the LULC types in the study area. In addition, very high-resolution (2.5 m) SPOT-5 mosaic image of year 2009, Google Earth based images, and local knowledge were mainly used for reference data to training data collection and validation of secondary-level LULC classes. The preprocessing of the Landsat data involves calculation of the top of atmosphere reflectance (TOA), ground control points (GCPs) based coregistration of the multitemporal images, mosaicking, and final subsetting of the data over the study area.

2.3. Classification Scheme and Training Data. Collection of the highly representative training data is a crucial task for the supervised classification of the LULC. In the research, following with the land cover classification system defined by the Chinese Academy of Sciences through field survey, training data belonging to 17 secondary classes were collected for each of these years (2000, 2009, and 2015). Existing land use and vegetation maps, false color composite images prepared from Landsat 5 and Landsat 8 data, Google Earth images, and Spot-5 images were used as the reference datasets while collecting the training and validation data. The classification scheme used in the research and the number of training data (polygons/pixels) collected are listed in Table 2.

To enhance the comparability of land cover classification results during three periods, we used the same training sites as much as possible when no change occurred. The pixel-base region of interest polygons was not a constant grid size but varied with the size and shape of the feature of interest. This variation was in order to take into account the areal distribution of various land cove features and to avoid oversampling one land cove type. The reliability of the training data over the entire study area was further ensured by using Jeffries-Matusita (J-M) distance [35]. The J-M distance algorithm used to calculate the separability of two land cover classes according to the following algorithm:

$$\mathrm{JM}_{(i,j)} = 2\left[1 - e^{(-a_{(i,j)})}\right], \tag{1}$$

where $\mathrm{JM}_{(i,j)}$ indicate Jeffries-Matusita distance between classes i and j and $a_{(i,j)}$ is shown as follows:

$$a_{(i,j)} = 0.125\left[M_{(i)} - M_{(j)}\right]\ln V\left[A_{(i,j)}\right]\left[M_{(i)} - M_{(j)}\right] + 0.5\ln\left\{\frac{\left(\det\left(A_{(i,j)}\right)\right)}{\left(\det\left(S_{(i)} \times \det\left(S_{(j)}\right)\right)\right)}\right\}^{1/2}, \tag{2}$$

where M indicate mean vector and S indicate covariance matrix.

J-M distance value ranges from 0 to 2; if J-M distance value close to 2 indicates training data of two land types with

Table 1: Description of the Landsat scenes used in the research.

Datasets	Path/row	Date acquired	Spatial resolution	Data source
Landsat 5 TM	121/30	30 August 2000	Bands 1–5 and 7 with 30 m; Bands 6 with 120 m	United States Geological Survey (USGS) (http://glovis.usgs.gov/)
	122/30	6 September 2000		
	121/30	23 August 2009		
	122/30	15 September 2009		
Landsat 8 OLI/TIRS	121/30	7 July 2015	Bands 1–7 with 30 m; Bands 10 and 11 with 100 m	http://glovis.usgs.gov/
	122/30	15 August 2015		
	123/30	15 September 2015		

Table 2: LULC classification system and the number of training data (polygons/pixels) used in the research.

First level classes	Second level classes	Training data: number of polygons (pixels)		
		2000	2009	2015
Cropland	Paddy	18 (3641)	21 (2969)	17 (3684)
	Dry land	43 (7489)	57 (9793)	64 (10792)
	Irrigation land	35 (3919)	51 (4643)	57 (7686)
Woodland	Forest	50 (4113)	39 (4347)	52 (7150)
	Shrub	29 (2852)	30 (8171)	27 (6396)
	Other forests	26 (4194)	27 (3969)	31 (5370)
Grassland	Dense grass	34 (5085)	31 (3573)	29 (5936)
	Moderate grass	32 (3005)	32 (3005)	26 (5933)
	Sparse grass	33 (2369)	34 (2671)	35 (8244)
Water body	Rivers and lakes	24 (5379)	18 (4682)	21 (6118)
	Tidal	20 (1181)	19 (1340)	25 (1835)
Built-up land	Urban built-up	15 (1877)	10 (3312)	10 (4385)
	Rural settlements	40 (3846)	37 (3527)	40 (4548)
Unused land	Sandy land	31 (7993)	31 (9423)	46 (16651)
	Salina	22 (3121)	22 (3121)	19 (2913)
	Swampland	11 (1588)	9 (560)	5 (742)
	Bare	43 (1837)	50 (3283)	37 (3909)

a high degree of separability, then those values close to 0 indicate a low degree of separability.

2.4. Multifeatures Combination and Supervised Classification. The study area is mix of the diverse types of LULC. Considering the spectral complexity of the study area, combination of the multiple features (spectral features, spectral indices, spectral transformations, textures, and topographic features) calculated from the satellite data was used to improve the accuracy of the LULC classification. The list of spectral features used in the research is shown in Table 3. Altogether, 25 feature images were used as an input dataset in the research. These features were calculated separately for each of these years (2000, 2009, and 2015) using the satellite data of the corresponding year.

The six spectral bands of the Landsat data were used for the principal component analysis, and the first principal component which included more than 90% spectral information was used to calculate textural features. Eight textural measures (mean, variance, homogeneity, contrast, dissimilarity, entropy, second moment, and correlation) were calculated using the Gray Level Cooccurrence Matrix (GLCM) with the moving window size of 3 by 3 pixels.

LULC classification and mapping were conducted for each of these years (2000, 2009, and 2015) using the above-mentioned 25 feature images and the training data collected. The supervised classification was conducted using the Support Vector Machine (SVM) [36] algorithm. SVM is a nonparametric classification method which can also work with the small amount of training data and produce higher classification accuracy [37, 38].

The success of the SVM method depends on how well the process is trained. Principally, SVM is a binary classifier that set an optimal separating hyperplane during classes to correctly separate the data point into two classes [39]. If the training data with k number of samples are represented as $(x_1, y_1), \ldots, (x_k, y_k)$ where $x \in R^n$ is an n-dimensional space and $y \in \{+1, -1\}$ is class label, then these training data will be separated by the two hyperplanes parallel to the optimal

Table 3: List of feature images used in the research.

Features	Descriptions	Total
Spectral	Blue, green, red, near infrared, shortwave infrared, and thermal infrared	6
Spectral indices	Normalized difference vegetation index (NDVI), normalized difference built-up index (NDBI), normalized difference bareness index (NDBaI), normalized difference salinity index (NDSI), normalized difference water index (NDWI)	5
Spectral transformations	Tasseled cap-wetness, tasseled cap-greenness, tasseled cap-brightness	3
Textural	Mean, variance, homogeneity, contrast, dissimilarity, entropy, second moment, correlation	8
Topographic	Slope, altitude, aspect	3
Total		25

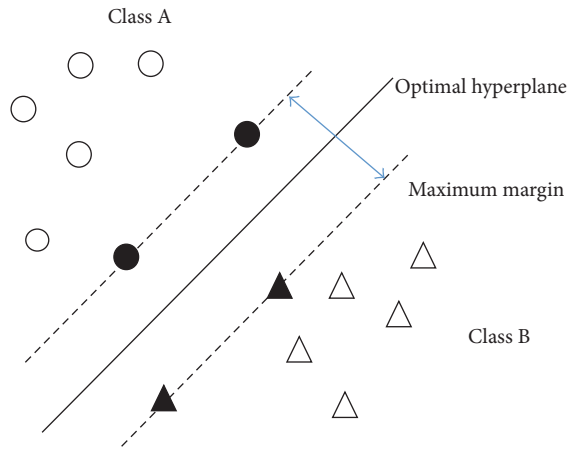

Figure 2: Original idea of SVM.

hyperplane with maximum margin into the respective classes shown in

$$W \cdot x_i + b \geq +1 \quad \text{for } y_i = +1,\ i = 1, 2, \ldots, k, \tag{3a}$$

$$W \cdot x_i + b \leq -1 \quad \text{for } y_i = -1. \tag{3b}$$

The original idea of SVM is presented in Figure 2.

SVM can classify the data linearly and nonlinearly, and kernel function is used for nonlinear classification. The SVM provide four types of kernels: linear, polynomial, and radial basis function (RBF), and sigmoid. According to the previous studies, radial basis function kernel works better for remote sensing image classification [40]. The equation of radial basis function kernel is presented as follows:

$$K\left(x_i, x_j\right) = \exp\left(-g \left\| x_i - x_j \right\|^2\right), \quad g > 0, \tag{4}$$

where g indicate the gamma term in the radial basis kernel function. This study utilized the default parameter provided by ENVI software to perform supervised classification on Landsat images.

2.5. Change Analysis and Accuracy Assessment. Accuracy of the LULC classification was assessed by collecting the different sets of validation data. The collection procedure was similar to the training data, but the training data used for training the SVM model were not used for assessing the classification accuracy. Altogether, 50 pixels for each secondary class were randomly chosen from the classified image, and the corresponding geolocation points were confirmed by visual interpretation of the reference datasets. The overall accuracy and kappa coefficient were used as the metrics for assessing the classification accuracy. After the production of LULC maps of each of these years (2000, 2009, and 2015) in the study area and their validation, the postclassification comparison (PCC) technique was used for the derivation of LULC change information. The spatiotemporal change analysis of 17 secondary classes is presented in the research.

3. Results and Discussion

3.1. LULC Classification Results. The LULC classification maps of years 2000, 2009, and 2015 produced in the research are displayed in Figures 3, 4, and 5, respectively. Each of these maps includes 17 secondary classes in the study area.

The areal coverage and proportion of 17 LULC secondary classes for each year (2000, 2009, and 2015) are presented in Figure 6 and Table 4.

The main LULC classes of the study area in the year 2015 were found to be grassland (dense grass, moderate gras,s and sparse grass), woodland (forest, shrub, and other forests), and cropland (dry farmland, irrigated farmland, and paddy) with the coverage of 39.3%, 20.5%, and 19.7% of the study area, respectively.

3.2. Spatiotemporal Changes. The annual rates of change (%) of the 17 LULC secondary classes during 2000–2009, 2009–2015, and 2000–2015 are presented in Table 5.

As shown in Table 5, significant changes in the LULC secondary classes over the past 16 years (2000–2015) have been detected in the study area. Over this period (2000–2015), dry land, irrigation land, paddy, urban built-up, and rural settlement were expanded with an annual rate of 1.11%, 4.07%, 1.57%, and 2.00%, respectively, in which irrigation

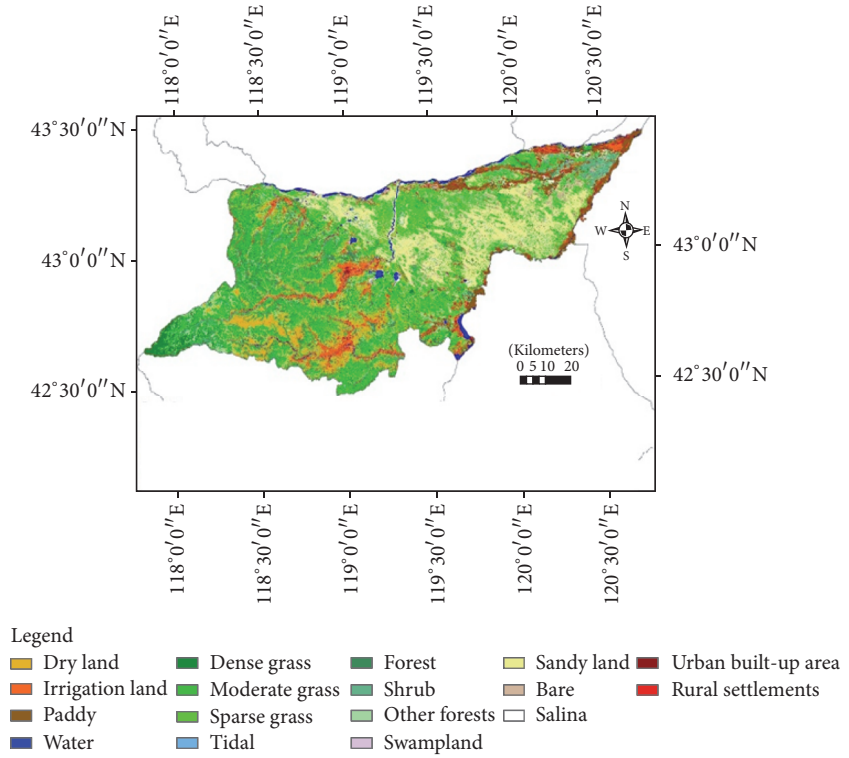

Figure 3: LULC classification map of year 2000 in the study area.

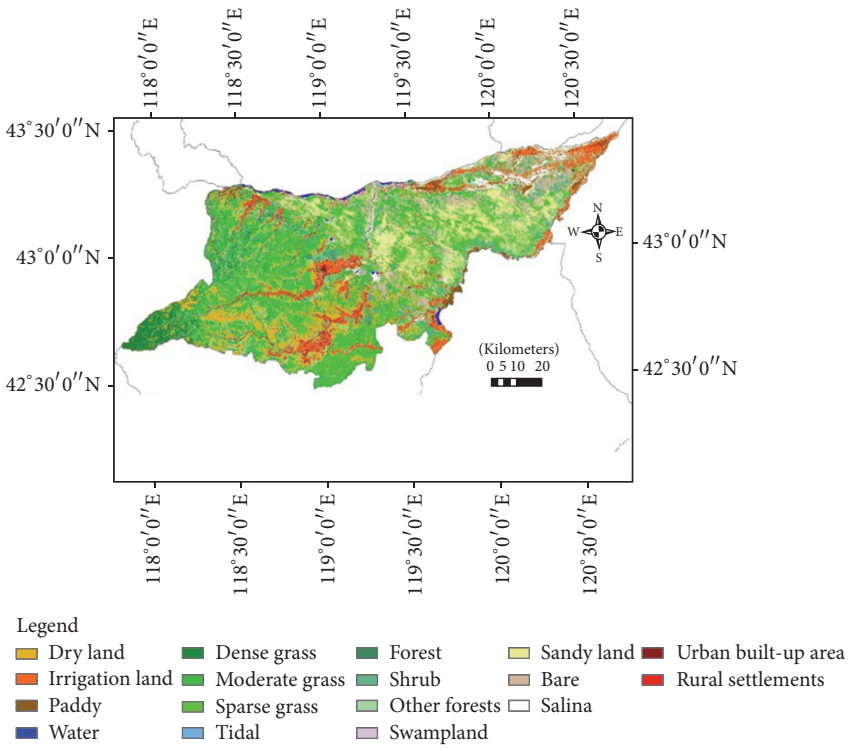

Figure 4: LULC classification map of year 2009 in the study area.

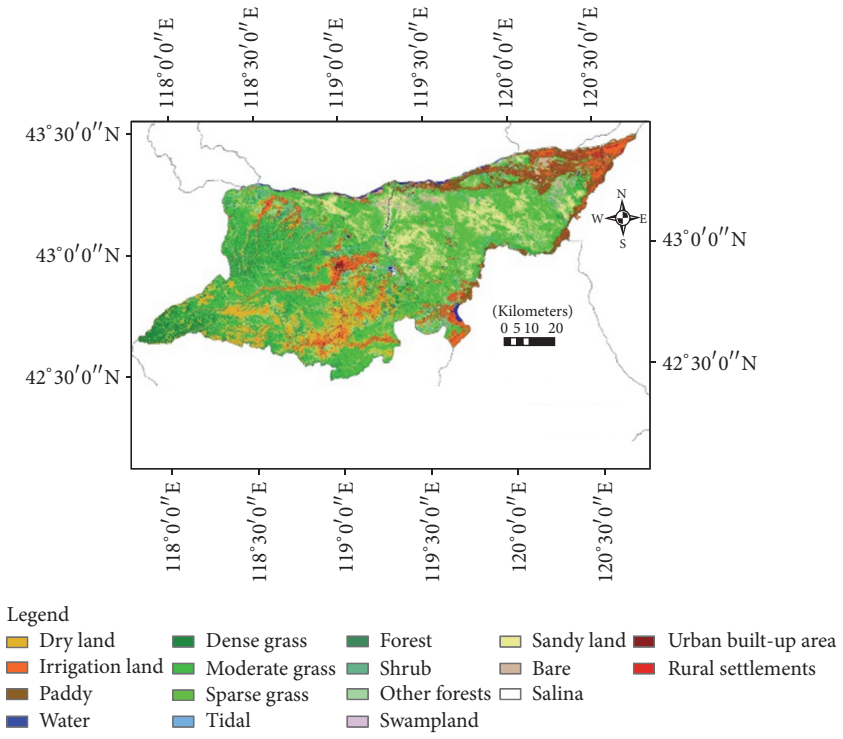

Figure 5: LULC classification map of year 2015 in the study area.

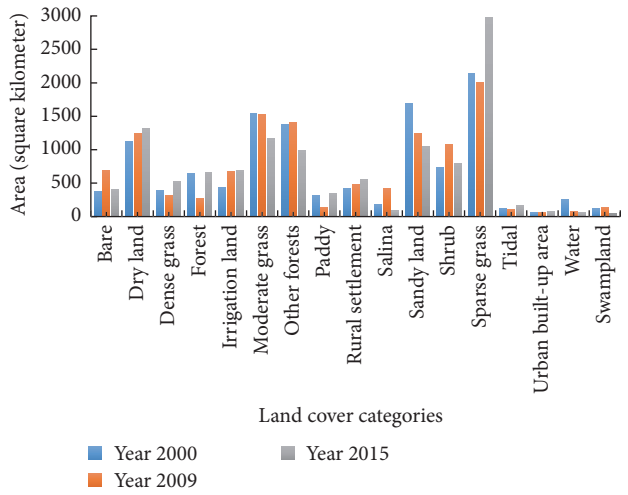

Figure 6: Areal coverage of the 17 LULC secondary classes of years 2000, 2009, and 2015 in the study area.

land is expanding most fast. However, at the same period (2000–2015), water, swampland, sandy land, and moderate grass were reduced at an annual rate of 4.87%, 3.74%, 2.51%, and 1.59%, respectively.

The fluctuation trend of the LULC classes was also detected in the study area. During the period 2000–2009, bare, salina, and shrub expanded significantly (positive annual changes) with an annual rate of 9.65%, 15.51%, and 5.33%; however, they decreased (negative annual changes) in the next 6 years (2009–2015). On the other hand, dense grass, forest, paddy, sparse grass, and tidal decreased between 2000 and 2009; however, these classes expanded during 2009–2015.

The most evident spatial-temporal changes of the water bodies, irrigation lands, sandy lands, and salina (salinized lands) found over the period of 2000–2015 in the research are demonstrated in Figures 7–10, respectively.

The Ongniud Banner region located in the western part of the Horqin Sandy Land is a typical transition zone of agricultural and animal husbandry. Over the past five decades, this region has been affected by land degradation

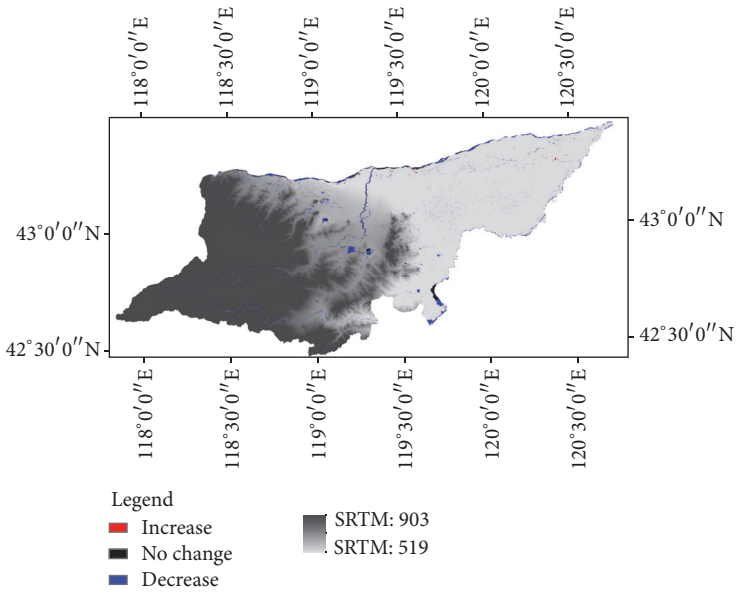

Figure 7: Changes in water bodies between 2000 and 2015 in the study area.

Table 4: The areal coverage and proportion of the 17 LULC secondary classes of years 2000, 2009, and 2015 in the study area.

LULC types	Area (square kilometers)			Proportion (%)		
	2000	2009	2015	2000	2009	2015
Bare	370.32	691.94	398.99	3.12	5.82	3.36
Dry land	1123.82	1241.67	1310.58	9.46	10.45	11.03
Dense grass	390.56	321.36	526.04	3.29	2.70	4.43
Forest	650.07	277.11	654.82	5.47	2.33	5.51
Irrigation land	430.31	674.35	693.33	3.62	5.67	5.83
Moderate grass	1537.22	1520.58	1169.51	12.93	12.79	9.84
Other forest	1370.81	1407.63	989.34	11.53	11.84	8.32
Paddy	313.58	138.46	341.18	2.64	1.16	2.87
Rural settlement	421.63	477.35	548.19	3.55	4.02	4.61
Salina	175.09	419.46	85.02	1.47	3.53	0.72
Sandy land	1684.27	1245.83	1051.09	14.17	10.48	8.84
Shrub	728.48	1078.00	790.45	6.13	9.07	6.65
Sparse grass	2135.63	2001.15	2971.38	17.97	16.84	25.00
Tidal	124.93	108.95	162.29	1.05	0.92	1.37
Urban built-up area	60.22	67.63	74.36	0.51	0.57	0.63
Water	250.60	76.84	67.47	2.11	0.65	0.57
Swampland	118.35	137.56	51.87	1.00	1.16	0.44
Total	11882	11882	11882	100	100	100

and desertification due to climate change and irrational human activities [41].

In the arid and semiarid regions, temperature and precipitation are important climatic factors. The analysis of the mean annual temperature and mean annual precipitation in the study area (Figure 11) shows that, between 1998 and 2007, the temperature slightly increased whereas the precipitation decreased significantly, which lead to the dry and hot climate in study area.

Figure 10 exhibited that the minimum annual precipitation occurred in 2001 and 2009 and the study area suffers from severe drought event in year 2009 [47]. According to the detailed analysis result of land cover change from 2000 to 2009, the increase of the salinized area and bare area between 1998 and 2009 mainly resulted from the dry and hot climate occurred from 1998 to 2007. In particular, less precipitation from 1998 to 2009 plays the key role in the decrease of dense grasses, shrinking swamp land and water body between 2000

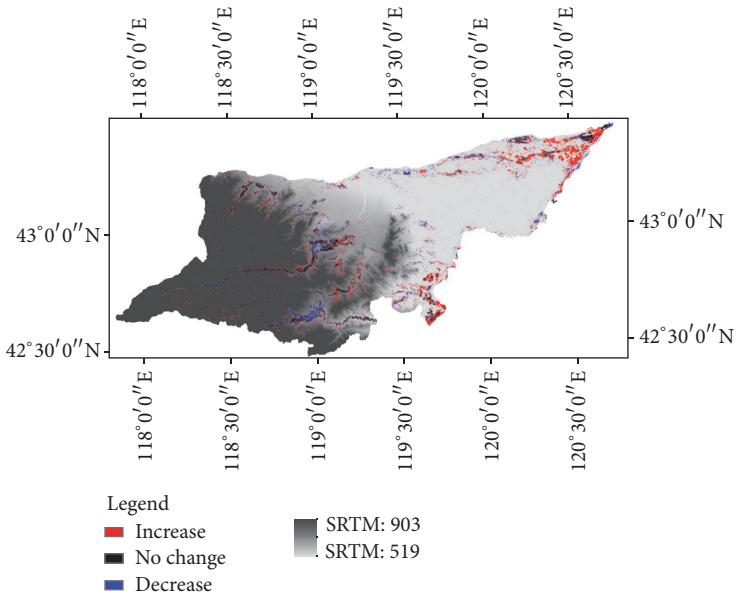

Figure 8: Changes in irrigated lands between 2000 and 2015 in the study area.

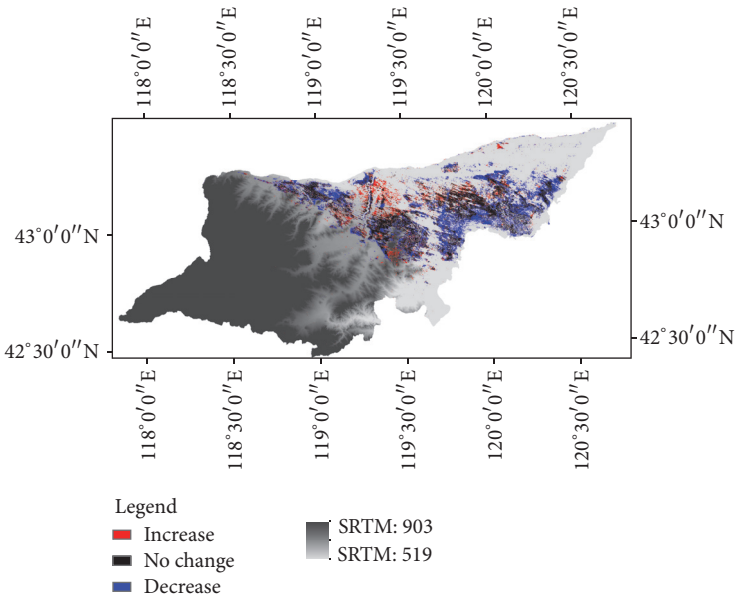

Figure 9: Changes in sandy lands between 2000 and 2015 in the study area.

and 2009. On the other hand, the climate variations between 2009 and 2012 exhibited the overall trend with the decrease of annual mean temperature and the increase of annual mean precipitation resulted in increased sparse grasses between 2009 and 2015. The decrease of the precipitation and soil moisture in warm and dry climate restricts the growth of vegetation resulting in exposed soil, shrinkage of water body, and the increase of barren and tidal areas. In contrast, the increase of the precipitation is favorable to the growth of vegetation and biodiversity with high soil moisture and less soil erosion.

The increase of the population and the increase of livestock numbers in the study are two major proxies of anthropogenic causes of the LULC changes in Ongniud Banner region of the Horqin Sandy Land. According to the Inner Mongolia statistical yearbook record, the total population of the Ongniud Banner increased from 463,293 in 2000 to 482,114 in 2014 [42]; and the population density increased from 35.6 persons per km^2 in 1986 to 41 persons per km^2 in 2014. Similarly, the livestock numbers also increased significantly from 460,000 in 1999 to 1409,300 in 2012. The significant increase of the population and livestock numbers accelerated the demands for water, food, and grazing lands which transformed the natural grasslands and woodlands into cultivated, residential, and degraded areas. As many programs on the protection and restoration of the ecological

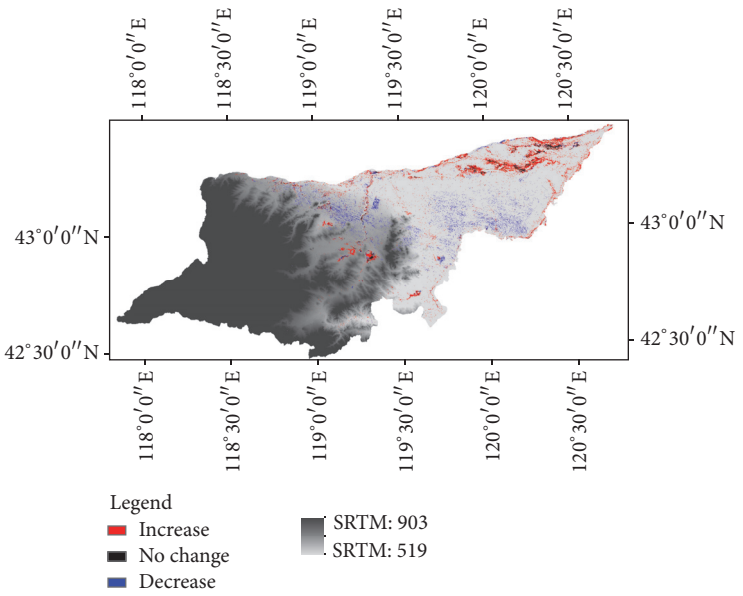

Figure 10: Changes in salina between 2000 and 2015 in the study area.

Table 5: The annual change rate (%) of the 17 LULC secondary classes during 2000–2009, 2009–2015, and 2000–2015 in the study area. Positive (negative) value indicates increasing (decreasing) trend over the time period.

LULC classes	Annual rate of change (%)		
	2000–2009	2009–2015	2000–2015
Bare	9.65	−7.06	0.52
Dry land	1.17	0.92	1.11
Dense grass	−1.97	10.62	2.31
Forest	−6.37	22.72	0.05
Irrigation land	6.30	0.47	4.07
Moderate grass	−0.12	−3.85	−1.59
Other forest	0.30	−4.95	−1.86
Paddy	−6.20	24.40	0.59
Rural settlement	1.47	2.47	2.00
Salina	15.51	−13.29	−3.43
Sandy land	−2.89	−2.61	−2.51
Shrub	5.33	−4.45	0.57
Sparse grass	−0.70	8.08	2.61
Tidal	−1.42	8.16	1.99
Urban built-up area	1.37	1.66	1.57
Water	−7.70	−2.03	−4.87
Swampland	1.80	−10.38	−3.74

zones have been launched by the government, encroachment of the desertification areas should have been controlled. However, expanding agriculture and depletion of groundwater table as reported by previous studies [45] may limit the sustainable development of the region.

3.3. Validation Results. The LULC classification was carried out for each year by accounting for the contribution of each of the additional feature (spectral indices, spectral transformations, textural and topographic features) to the basic Landsat based spectral feature (Landsat 6 bands). The one by one performance of these additional features is shown in Table 6. Based on this analysis, only highly performed features were chosen for the production of the LULC maps. The exclusion of the less contributed features could reduce the data volume for further processing.

Table 6: Contribution of the additional features for the LULC classification in the study area.

Additional features	Contribution
DEM	Improving discrimination among irrigation land, swampland, and paddy
Slope	Improving discrimination of grassland and forest and bare area and tidal
Aspect	Less contribution
NDVI	Improving discrimination between grassland and forest
NDWI	Improving discrimination between irrigated land and swampland
NDSI	Improving discrimination between salina land and sandy land
NDBI	Enhancing discrimination of built-up and rural settlement area
NDBaI	Improving discrimination between bare area and salinized area
Greenness	Less contribution
Brightness	Less contribution
Wetness	Less contribution
Mean	Improving discrimination between rural settlements and urban built-up area
Variance	Less contribution
Homogeneity	Improving discrimination between rural settlements and urban built-up area
Contrast	Less contribution
Dissimilarity	Improving discrimination between cropland and built-up area
Entropy	Improving discrimination between artificial grassland and cropland
Second moment	Enhancing discrimination of the tidal and rural settlement
Correlation	Less contribution

Table 7: Confusion matrix of the LULC classification for each year in the study area.

Classes	Year 2000		Year 2009		Year 2015	
	User's accuracy	Producer's accuracy	User's accuracy	Producer's accuracy	User's accuracy	Producer's accuracy
Bare	0.88	0.61	0.86	0.77	0.88	0.56
Dry land	0.74	0.8	0.88	0.75	0.86	0.57
Dense grass	0.96	0.76	0.88	0.92	0.8	0.83
Forest	0.94	0.86	0.88	0.86	0.8	0.85
Irrigation land	0.94	0.82	0.92	0.81	0.96	0.65
Moderate grass	0.92	0.88	0.92	0.87	0.84	0.84
Other forests	0.74	0.93	0.92	0.92	0.68	0.92
Paddy	0.88	1	0.94	0.96	0.64	1
Rural settlements	0.8	0.89	0.82	0.8	0.76	0.79
Salina	0.84	0.98	0.88	0.96	0.74	0.97
Sandy land	0.82	0.91	0.98	0.88	0.96	0.91
Shrub	0.86	0.88	0.92	0.92	0.86	0.84
Sparse grass	0.92	0.7	0.9	0.87	0.84	0.76
Tidal	0.86	0.93	0.82	0.89	0.82	0.91
Urban built-up area	0.62	1	0.78	1	0.76	1
Water	1	1	0.96	1	1	1
Swampland	0.84	0.93	0.86	0.98	0.78	0.98
Overall accuracy	0.86		0.89		0.82	
Kappa coefficient	0.85		0.88		0.81	

The performance of the resulting LULC maps assessed through the confusion matrix based analysis using the validation data is shown in Table 7.

The overall accuracy (kappa coefficient) obtained for 17 secondary classes in the study area were 0.86 (0.85), 0.89 (0.88), and 0.82 (0.81) for years 2000, 2009, and 2015, respectively. The classification results of 17 land cover types for 2000, 2009, and 2015 were generally reliable. In comparison, the detailed LULC classification map of year 2009 was with a higher overall classification accuracy than both maps of 2000 and 2015. The land cover types, bare, dry land and urban built-up area, are confused with each other with the producer's accuracy for bare being less than 0.7 except in 2009. The producer's accuracy for dry land is less than 0.7 in 2015.

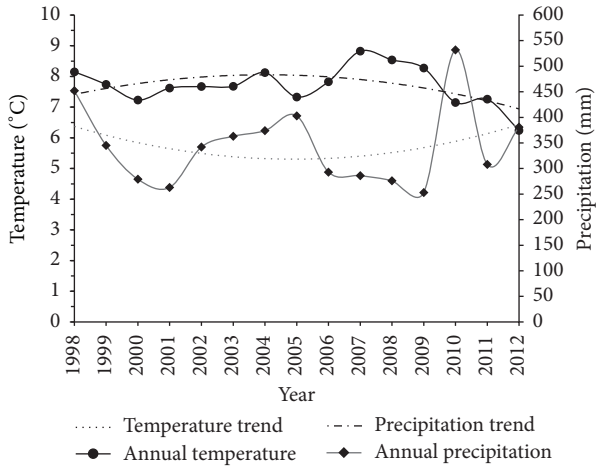

Figure 11: Changes in the annual temperature and annual precipitation in the study area.

The irrigation land is confused with swampland and paddy, with the producer's accuracy being less than 0.7 in Landsat OLI image of 2015. Other classes are considered to be well classified even in Landsat TM and Landsat OLI imagery.

4. Conclusion

Previous studies in the Horqin Sandy Land utilized only the spectral feature from the satellite data for the change analysis of major LULC classes. The analysis of the contribution of each features in the research showed that only the spectral features from the Landsat data are not enough for improving the classification accuracy as the misclassification between the secondary classes such as irrigated land and swampland, swampland and paddy, bare area and tidal, cropland and bare area, bare area and urban, grassland and forest were significant. The additional features (spectral indices, spectral transformations, and textural and topographic features) could improve the classification accuracy significantly.

The secondary class level LULC change analysis performed in the research provides very detailed change information of the LULC over the past 16 years. The high resolution (30 m) LULC change analysis over the past 16 years in the research showed a significant LULC change in Ongniud Banner, western part of the Horqin Sandy Land in Inner Mongolia. Different trends of the LULC changes over three periods, 2000–2009, 2009–2015, and 2000–2015, were also detected. Interaction of the human activities and the climatic factors (precipitation and temperature) could be linked to the trend of LULC changes.

The satellite remote sensing based detailed LULC change analysis as performed in the study is important for assessing the performance of the ecological protection and restoration programs. The spatiotemporal change analyses of the detailed secondary classes in the research are expected to contribute to the policy makers for the protection and sustainable management of the environmentally sensitive ecological resources in the Horqin Sandy Land. This research has confirmed the expansion of irrigated farming lands and salinized areas over the past 16 years, whereas the waterbodies and sandy lands decreased. This trend implies the increasing demand of water resource. Therefore, a continuous and long-term monitoring of the LULC changes related to water resource and salinization problem is suggested to promote sustainable development and ecological security of the northeast China. Based on these research results, rational use of limited water resource and planting water saving vegetation community such as shrub is recommended to the local people. On the other hand, to protect minority land cove types such as swampland, it is challenging to reduce landscape fragmentation and preserve the biodiversity.

Competing Interests

The authors declare that there are no competing interests regarding the publication of this paper.

References

[1] A. Warren and C. Agnew, "An assessment of desertification and land degradation in arid and semi-arid areas," International Institute for Environment and Development, Dryland Programme, Dryland Paper 02, Ecology and Conservation Unit, University College, London, UK, 1988.

[2] Y. Chen and H. Tang, "Desertification in north China: background, anthropogenic impacts and failures in combating it," *Land Degradation and Development*, vol. 16, no. 4, pp. 367–376, 2005.

[3] World Health Organization (WHO), "United Nations Environment Programme (UNEP)," in *Urban Air Pollution in Megacities of the World*, Blackwell, Cambridge, Mass, USA, 1992.

[4] M. Sciortino, "Desertification in the mediterranean," in *Proceedings of the Contributed Paper of the 22th International School on Disarmament and Research on Conflicts (ISODARCO '01)*, Candriai, Italy, June 2001.

[5] M. B. K. Darkoh, "The nature, causes and consequences of desertification in the drylands of Africa," *Land Degradation & Development*, vol. 9, no. 1, pp. 1–20, 1998.

[6] UNCOD and Secretariat, "Desertification: its causes and consequences," in *Secretariat of United Nations Conference on Desertification*, Pergamon Press, Oxford, UK, 1977.

[7] S.-J. Wang, Q.-M. Liu, and D.-F. Zhang, "Karst rocky desertification in southwestern China: geomorphology, landuse, impact and rehabilitation," *Land Degradation & Development*, vol. 15, no. 2, pp. 115–121, 2004.

[8] M. O. H. EI-Karouri, "The impact of desertification on land productivity in Sudan," in *Physics of Desertification*, pp. 52–58, Springer Netherlands, 1986.

[9] P. Bullock and H. Le Houérou, "Land degradation and desertification," in *Climate Change 1995: Impacts, Adaptations and Mitigation of Climate Change: Scientific-Technical Analyses. Contribution of Working Group II to the Second Assessment Report of the Intergovernmental Panel on Climate Change*, pp. 171–190, Cambridge University Press, 1996.

[10] R. M. Pink, *Water Rights in Southeast Asia and India*, Palgrave Macmillan, New York, NY, USA, 2016.

[11] J. Li, B. Xu, X. Yang et al., "Characterizing changes in grassland desertification based on Landsat images of the Ongniud and Naiman Banners, Inner Mongolia," *International Journal of Remote Sensing*, vol. 36, no. 19-20, pp. 5137–5149, 2015.

[12] H. Bagan, W. Takeuchi, T. Kinoshita, Y. Bao, and Y. Yamagata, "Land cover classification and change analysis in the Horqin Sandy Land from 1975 to 2007," *IEEE Journal of Selected Topics in Applied Earth Observations and Remote Sensing*, vol. 3, no. 2, pp. 168–177, 2010.

[13] F. Wang, X. Pan, D. Wang, C. Shen, and Q. Lu, "Combating desertification in China: past, present and future," *Land Use Policy*, vol. 31, pp. 311–313, 2013.

[14] F. Plit, J. Plit, and W. Żakowski, "Drylands development and combating desertification: bibliographic study of experiences in countries of the CIS," Environment and Energy Paper 14, Food & Agriculture Organization, 1995.

[15] Jun, "Chinese newspaper report for the issue of desertification of Inner Mongolia," *Bulletin of the Graduate School, Toyo University*, vol. 49, pp. 25–39, 2012 (Japanese).

[16] F. Huang, P. Wang, and X. Liu, "Monitoring vegetation dynamic in Horqin Sandy Land from SPOT Vegetation Time series imagery," in *Proceedings of the International Archives of the Photogrammetry, Remote Sensing and Spatial Information Sciences*, pp. 915–920, Beijing, China, 2008.

[17] Z. Han, T. Wang, C. Yan et al., "Change trends for desertified lands in the Horqin Sandy Land at the beginning of the twenty-first century," *Environmental Earth Sciences*, vol. 59, no. 8, pp. 1749–1757, 2010.

[18] H.-C. Duan, T. Wang, X. Xue, S.-L. Liu, and J. Guo, "Dynamics of aeolian desertification and its driving forces in the Horqin Sandy Land, Northern China," *Environmental Monitoring and Assessment*, vol. 186, no. 10, pp. 6083–6096, 2014.

[19] F. Shengyue and Z. Lihua, "Desertification control in China: possible solutions," *Ambio: a journal of the Human Environment*, vol. 30, no. 6, pp. 384–385, 2001.

[20] T. Wang, W. Wu, X. Xue, Z. Han, W. Zhang, and Q. Sun, "Spatial-temporal changes of Sandy desertified land during last 5 decades in Northern China," *Acta Geographica Sinica*, vol. 59, no. 2, pp. 203–212, 2004.

[21] X.-Y. Zhao, C.-M. Zhang, X.-A. Zuo et al., "Challenge to the desertification reversion in Horqin Sandy Land," *Chinese Journal of Applied Ecology*, vol. 20, no. 7, pp. 1559–1564, 2009.

[22] H.-L. Zhao, X.-Y. Zhao, R.-L. Zhou, T.-H. Zhang, and S. Drake, "Desertification processes due to heavy grazing in sandy rangeland, Inner Mongolia," *Journal of Arid Environments*, vol. 62, no. 2, pp. 309–319, 2005.

[23] X. Wang, F. Chen, and Z. Dong, "The relative role of climatic and human factors in desertification in semiarid China," *Global Environmental Change*, vol. 16, no. 1, pp. 48–57, 2006.

[24] J. Ellis, *Grasslands and Grassland Sciences in Northern China*, National Academies Press, Washington, DC, USA, 1992.

[25] W. Yan, *New Paradigm of International Environmental Cooperation—Practice of Comprehensive Policy Studies in Desertification Countermeasure in China*, Keio University Press, 2008 (Japanese).

[26] Wulantuya, "Land reclamation and land-use changes during last 50 years in Ke'erqin deserts, Inner Mongolia," *Progress in Geography*, vol. 19, no. 3, pp. 273–278, 2000 (Chinese).

[27] J. Paneque-Gálvez, J.-F. Mas, G. Moré et al., "Enhanced land use/cover classification of heterogeneous tropical landscapes using support vector machines and textural homogeneity," *International Journal of Applied Earth Observation and Geoinformation*, vol. 23, no. 1, pp. 372–383, 2013.

[28] M. F. Iqbal and I. A. Khan, "Spatiotemporal Land Use Land Cover change analysis and erosion risk mapping of Azad Jammu and Kashmir, Pakistan," *Egyptian Journal of Remote Sensing and Space Science*, vol. 17, no. 2, pp. 209–229, 2014.

[29] L. C. Alatorre and S. Beguería, "Identification of eroded areas using remote sensing in a badlands landscape on marls in the central Spanish Pyrenees," *Catena*, vol. 76, no. 3, pp. 182–190, 2009.

[30] R. C. Sharma, R. Tateishi, K. Hara, and K. Iizuka, "Production of the Japan 30-m land cover map of 2013—2015 using a random forests-based feature optimization approach," *Remote Sensing*, vol. 8, no. 5, article no. 429, 2016.

[31] S. Brogaard and S. Prieler, "Land cover in the Horqin grasslands, North China. Detecting changes between 1975 and 1990 by means of remote sensing," IIASA Interim Report, International Institute for Applied System Analysis, Laxenburg, Austria, 1998, http://citeseerx.ist.psu.edu/viewdoc/download?doi=10.1.1.41.6920&rep=rep1&type=pdf.

[32] S.-H. Ran and J.-J. Jin, "Evolvement and control of vulnerable ecological region—a case study in Ongniud Banner and Aohan Banner, Inner Mongolia," *Chinese Geographical Science*, vol. 14, no. 2, pp. 135–141, 2004.

[33] Q. L. Yan, J. J. Zhu, Z. B. Hu, and O. J. Sun, "Environmental impacts of the shelter forests in Horqin Sandy Land, Northeast China," *Journal of Environmental Quality*, vol. 40, no. 3, pp. 815–824, 2011.

[34] S. Yan and Z. Liu, "Effects of dune stabilization on the plant diversity of interdune wetlands in northeastern Inner Mongolia, China," *Land Degradation & Development*, vol. 21, no. 1, pp. 40–47, 2010.

[35] J. A. Richards and X. Jia, *Remote sensing digital image analysis*, Springer, Berlin, Germany, 1999.

[36] T. Kavzoglu and P. M. Mather, "The use of backpropagating artificial neural networks in land cover classification," *International Journal of Remote Sensing*, vol. 24, no. 23, pp. 4907–4938, 2003.

[37] G. Mountrakis, J. Im, and C. Ogole, "Support vector machines in remote sensing: a review," *ISPRS Journal of Photogrammetry and Remote Sensing*, vol. 66, no. 3, pp. 247–259, 2011.

[38] P. Mantero, G. Moser, and S. B. Serpico, "Partially supervised classification of remote sensing images through SVM-based probability density estimation," *IEEE Transactions on Geoscience and Remote Sensing*, vol. 43, no. 3, pp. 559–570, 2005.

[39] C. Huang, L. S. Davis, and J. R. G. Townshend, "An assessment of support vector machines for land cover classification," *International Journal of Remote Sensing*, vol. 23, no. 4, pp. 725–749, 2002.

[40] T. Kavzoglu and I. Colkesen, "A kernel functions analysis for support vector machines for land cover classification," *International Journal of Applied Earth Observation and Geoinformation*, vol. 11, no. 5, pp. 352–359, 2009.

[41] Z. Kou, "Amelioration of desertification and construction of sustainable landuse system in Wulan-Aodu area," *Towards Solving the Global Desertification Problem*, vol. 4, pp. 45–47, 1994.

[42] Inner Mongolia Statistics Bureau, *Inner Mongolia Statistical Yearbook*, China Statistics Press, Beijing, China, 2015 (Chinese).

Hindawi
Mathematical Problems in Engineering
Volume 2017, Article ID 5209173, 11 pages
https://doi.org/10.1155/2017/5209173

Research Article

Analysis of Drought Characteristics in Xilingol Grassland of Northern China Based on SPEI and Its Impact on Vegetation

Siqin Tong,[1,2,3] Yuhai Bao,[2,3] Rigele Te,[2,3] Qiyun Ma,[1] Si Ha,[1] and A. Lusi[1]

[1]*School of Environment, Northeast Normal University, Changchun 130117, China*
[2]*College of Geographical Science, Inner Mongolia Normal University, Hohhot 010022, China*
[3]*Inner Mongolia Key Laboratory of Remote Sensing and Geographic Information System, Hohhot 010022, China*

Correspondence should be addressed to Yuhai Bao; baoyuhai@imnu.edu.cn

Received 20 September 2016; Revised 11 November 2016; Accepted 7 December 2016; Published 18 January 2017

Academic Editor: Hasi Bagan

This research is based on the standardized precipitation evapotranspiration index (SPEI) and normalized difference vegetation index (NDVI) which represent the drought and vegetation condition on land. Take the linear regression method and Pearson correlation analysis to study the spatial and temporal evolution of SPEI and NDVI and the drought effect on vegetation. The results show that (1) during 1961–2015, SPEI values at different time scales showed a downward trend; SPEI-12 has a mutation in 1997 and the SPEI value significantly decreased after this year. (2) During 2000–2015, the annual growing season SPEI has an obvious upward trend in time and the apparent wetting spatially. (3) In the recent 16 years, the growing season NDVI showed an upward trend and more than 80% of the total area's vegetation increased in Xilingol. (4) Vegetation coverage in Xilingol grew better in humid years and opposite in arid years. SPEI and NDVI had a significant positive correlation; 98% of the region showed positive correlation, indicating that meteorological drought affects vegetation growth more in arid and semiarid region. (5) The effect of drought on vegetation has lag effect, and the responses of different grassland types to different scales of drought were different.

1. Introduction

Grassland is one of the widely distributed ecosystems on the earth; it plays an important role in global carbon cycle and climate system [1] and also has vital function on animal husbandry production and socioeconomic development [2]. However, grassland is one of the most vulnerable ecosystems as well, which is seriously affected by climate changes [1]. Global climate change, whether it is warming or cooling, and greenhouse gas concentration change will lead to changes on spatial-temporal distribution pattern of climate factors, such as sunlight, temperature, and precipitation, which are the indispensable factor in the process of vegetation growth [3]; moreover these changes will be exacerbated the formation of disastrous elements [4] and then will have a profound impact on changes of vegetation growth, productivity, and accompanying socioeconomic progress [5, 6].

Drought is one of the most serious natural disasters in the world. It has the characteristics of high frequency, wide range, and long duration [7]. It also has great influence on agriculture, water resources, natural ecosystem, and society, and then it brings huge economic losses, famine, epidemic, land degradation, and other negative effects [8]. Because of the global climate warming, drought occurs frequently and there is a clear upward trend. It has a direct impact on the development of agriculture and animal husbandry in Mongolia steppe [9] and accelerates the desertification and causes severe sand storm [10]. Therefore, drought assessment and monitoring are essential to reducing the losses and ensuring the safety of human being and property. Although the drought phenomenon is very complex, it can still be characterized by drought index, such as the Standardized Precipitation Index (SPI), Palmer Drought Severity Index (PDSI), Surface Water Supply Index (SWSI), and Effective Drought Index (EDI) [11]. The drought index can be used to quantify the intensity and duration of drought, as well as the occurrence of spatial extent [12]. In this study, the standardized precipitation evapotranspiration index (SPEI)

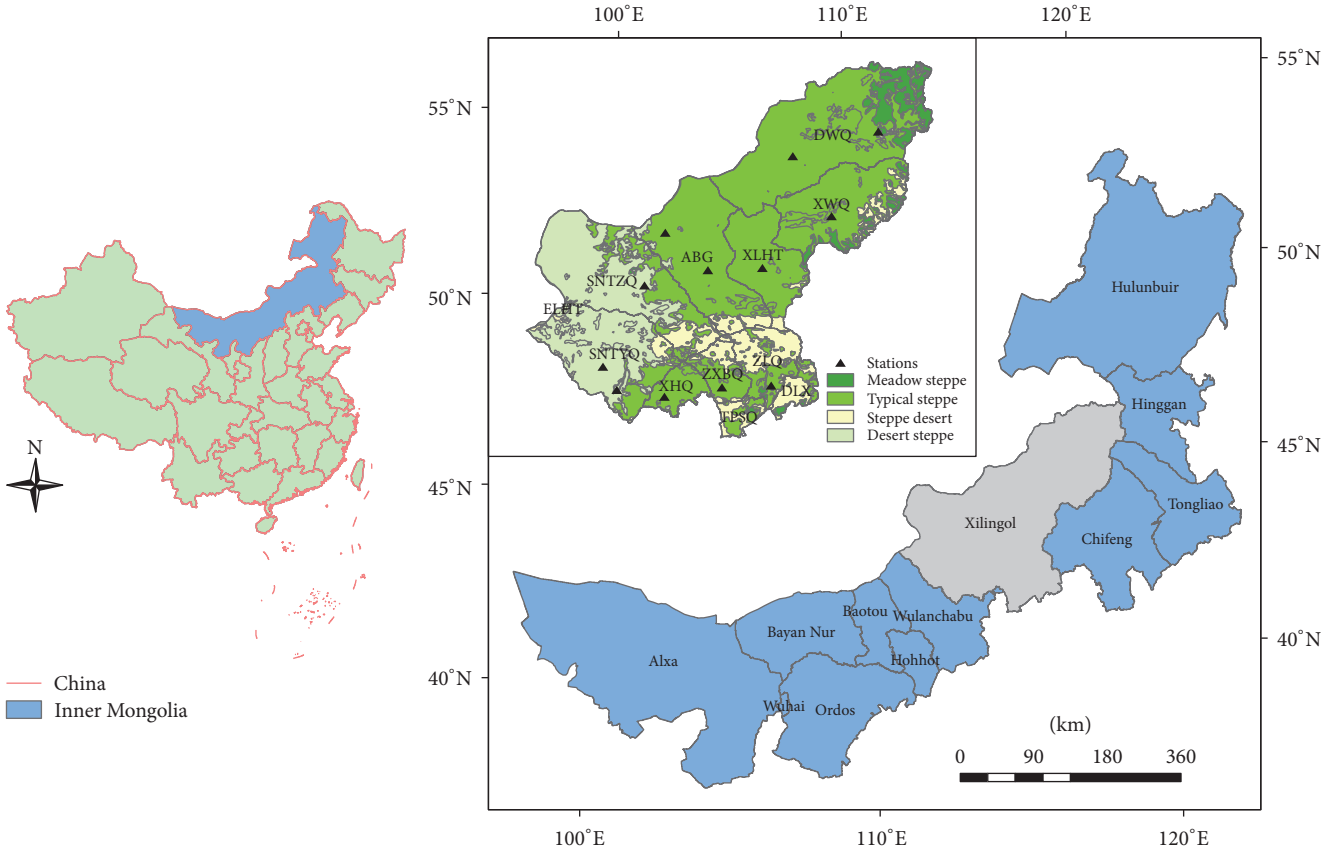

Figure 1: Location of study area, spatial distribution of meteorological stations, and grassland types of Xilingol.

was selected to analyze the dynamics of drought. It is widely used to analyze drought in various fields, because it not only considers the role of precipitation and evapotranspiration in drought causes, but also retained the sensitivity of SPI and PDSI index to temperature and precipitation, and it also has advantage of multiscale and multispace [13]. The frequent occurrence of drought and long duration hinder the normal green up and growth of grassland, cause the decrease of productivity in grassland, and pose a great threat to the sustainable development of the economy of animal husbandry. Therefore, it is of great significance to monitor and reveal the impact of drought to vegetation and to study the relationship between climate change and terrestrial ecosystem. In recent years, a great number of researchers have studied the relationship between vegetation and drought; however, the current study mainly concentrated on the relation between vegetation and single climate factor [14–17]. And this is not able to reflect the effect of climate change on vegetation [7]. On the other hand, most studies focused on a watershed analysis and have less attention on the correlation analysis of vegetation and drought, especially the drought impact on vegetation in Xilingol grassland which has not been reported yet.

Xilingol grassland locates in the north of China, and it is one of the three major natural grasslands of China and the typical temperate grassland of Eurasia, as well as the most complete preservation of word's temperate grassland in the Central Plains plants. However, due to the typical continental climate and fragile ecological system, Xilingol grassland is vulnerable to global climate change and human activities. Studies have shown that the degradation of grassland in Xilingol reached to 64% of total area because of the global climate change and expansion of usage and intensity in grassland types [18]. The environmental problems such as sand storm, drought, and desertification became progressively worse [19], bringing adverse effect on local animal husbandry production and ecological environment [20]. Therefore, we make use of the MODIS NDVI and meteorological data to monitor the dynamic of vegetation and drought in Xilingol grassland and discuss the drought impact on vegetation at different time scales. This will have an important theoretical and practical significance to the spatial-temporal change pattern of vegetation in grassland, rational use of limited grassland resources, effective management and forecast the impact of climate change on grassland ecosystem, and risk assessment and early warning on the natural disasters in grassland pasturing area [21].

2. Data and Method

2.1. Study Area. Xilingol grassland (41°35′ ~46°46′N, 111°09′ ~119°58′E) is located in northern China, central Inner Mongolia (Figure 1); it is the largest natural pasture and animal husbandry base in China and belongs to the arid and semiarid

continental climate. The annual average temperature ranges from 0 to 3°C and it is gradually increasing from east to west, While the precipitation gradually decreases from east to west and ranges from 300 to 380 mm. There is distributed meadow steppe, typical steppe, steppe desert and desert steppe, and continuous steppe in the spatial grassland from the northeast to the southeast. The south of Xilingol has a Hunshandake sandy land and farming-pastoral zone (DLX and TPSQ).

2.2. Data Sources and Preprocessing. The usage of NDVI dataset is MODIS NDVI, which can be downloaded from the NASA Goddard Space Flight Center (https://ladsweb.nascom.nasa.gov/) for free. The original MOD13A2 data has a spatial resolution of 1000 meters with 16-day composite. The monthly NDVI is generated with the Maximum Value Composite (MVC) method. MVC chooses the highest value of each pixel from the multitemporal data to represent the current NDVI value [22]. The annual growing season NDVI is defined as the average of NDVI values from April to October of each calendar year, because most vegetation in Xilingol almost stops growing or is covered with snow in winter.

The climate data used in this study was acquired from the China Meteorological Data Sharing Service System (http://data.cma.cn/), including monthly mean air temperature and monthly precipitation for the period 1961–2015, with the 15 meteorological stations that cover the whole area of Xilingol. And these two datasets are used to calculate the SPEI drought index.

The grassland type's data were extracted from the 1 : 1000000 vector vegetation map of Inner Mongolia. Xilingol has four different grassland types and its distribution is shown in Figure 1 [23].

2.3. Standardized Precipitation Evapotranspiration Index (SPEI). It is a kind of multitime scale index for drought, and it uses the difference between precipitation and evapotranspiration to characterize the intensity of drought in a certain region. The main steps for calculating SPEI are shown as follows [13]:

(1) Potential Evapotranspiration (PET) is estimated by the Thornthwaite method [24].

$$\mathrm{PET} = 16K\left(\frac{10T_i}{I}\right)^m, \tag{1}$$

where T_i (°C) is the monthly mean temperature; I is the yearly heat index, $I = \sum_{i=1}^{12} I_i = \sum_{i=1}^{12} (T_i/5)^{1.514}$; i is the month; m is a constant value, $m = 6.75E^{-7}I^3 - 7.71E^{-5}I^2 + 1.79E^{-2}I + 0.492$; E is exponential function; K is correction factor.

(2) Calculate water balance, which is the difference between precipitation (P) and PET, as follows:

$$D_i = P_i - \mathrm{PET}_i, \tag{2}$$

where D is water balance; P (mm) is precipitation; PET (mm) is potential evapotranspiration.

(3) Water balance at different time scales is aggregated.

$$D_n^k = \sum_{i=0}^{k-1} \left(P_{n-1} - \mathrm{PET}_{n-i}\right), \quad n \geq k, \tag{3}$$

where k (month) is the scale of interest; n is the calculation month; D_n^k is the accumulated water balance.

(4) The water balance is normalized into a log-logistic probability distribution to calculate the SPEI index series.

$$f(x) = \frac{\beta}{\alpha}\left(\frac{x-\gamma}{\alpha}\right)^{\beta-1}\left[1 + \left(\frac{x-\gamma}{a}\right)\right]^{-2}, \tag{4}$$

where α, β, and γ are the scale, shape, and origin parameters, respectively. The probability distribution function of the D series is given by

$$F(x) = \left[1 + \left(\frac{x-\gamma}{\alpha}\right)^{\beta}\right]^{-1}. \tag{5}$$

(5) With $F(x)$ the SPEI can easily be obtained as the standardized value of $F(x)$.

$$\mathrm{SPEI} = W - \frac{C_0 + C_1 W + C_2 W^2}{1 + d_0 W + d_2 W^2 + d_3 W^3}, \tag{6}$$

where $W = \sqrt{-2\ln(P)}$; if $P \leq 0.5$, $P = 1 - F(x)$; if $P > 0.5$, $P = 1 - P$. The constants are $C_0 = 2.515517$, $C_1 = 0.802853$, $C_2 = 0.010328$, $d_1 = 1.432788$, $d_2 = 0.189269$, and $d_3 = 0.001308$. And linear regression method and Pearson correlation analysis were used to study the spatiotemporal change of SPEI and its relationship with NDVI.

3. Results and Discussion

3.1. Interannual Variations of Drought at Different Time Scales in Xilingol. The sensitivity of the SPEI value at different time scales was obviously different as the time changes. The smaller the time scale, the more significant the change of wetness and dryness, and the value of SPEI would change greatly and even fluctuates between positive and negative. On the contrary, the larger the time scale, the more smooth the wet-dry rotation; there is only a number of continuous precipitation or no rain, high temperature, and so forth and it will make the change, which is reasonable to monitor long-term drought condition. According to Figure 2, SPEI shows a slight decrease trend at different time scales from 1961 to 2015. SPEI-1 fluctuates violently along the zero value, which fully reflects the frequent alternation of monthly drought and flood in Xilingol. The period of fluctuation of SPEI-3 and SPEI-6 is relatively long, reflecting the changing regularity of the wet-dry season. SPEI-12 was relatively stable and could reflect the interannual variation characteristics of drought.

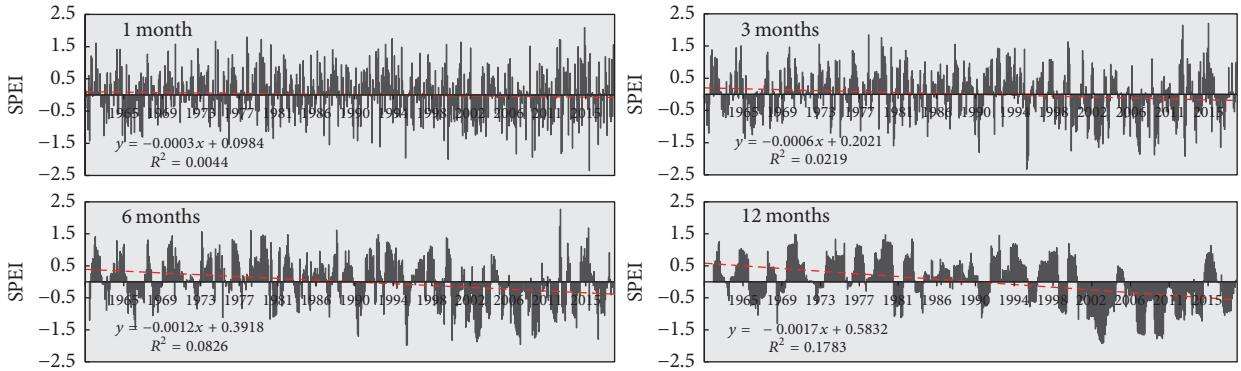

Figure 2: Time series of SPEI at 1-, 3-, 6-, and 12-month scales for period 1961–2015 of Xilingol.

Table 1: The standardized precipitation index (SPEI) categories based on the initial classification of SPEI values.

Categories	SPEI values
Extreme drought	Less than −2.00
Severe drought	−1.99 to −1.50
Moderate drought	−1.49 to −1.00
Light drought	−0.99 to −0.50
Near normal	−0.49 to 0.50
Humid	More than 0.50

The situation of drought shown by SPEI-12 was similar to that of Xilingol in arid years in history, such as 1962, 1963, 1972, 1980, 1989, 1994, 2000–2002, and 2005–2008, and the serious drought affected large area, reduction in grain yield, and the number of livestock; thus it caused great difficulties to farmers and herdsmen's life. Comparing with the drought severity classification table (Table 1), the drought frequency of SPEI decreased and the duration increased with the increase of time scale. In the period from 1961 to 1999, the frequency of drought in Xilingol was low, and duration was short and the drought was less harmful. After 2000, the Xilingol region entered into the drought-frequent stage, and it lasted for a long time.

In order to further reveal the temporal variation of drought in Xilingol region, the Mann-Kendall, which is a nonparametric test method for testing the trend of time series allowing missing value and no need to prove the distribution of time series [25], was used to test 1961–2015 SPEI-12 sequence. The results are shown in Figure 3; the UF curve is the time series statistical curve and UB curve is the reverse time series statistical curve. When the significant level was 0.05, the UF and UB curves intersect in year 1997, and then the UF curve drops significantly and passes the significance level. The results showed that the drought in Xilingol region had obvious mutation change characteristics in interannual variation, and SPEI-12 decreased from 1997 showing trend of aridity.

3.2. Spatiotemporal Dynamics of SPEI and NDVI in Growing Season. Most of the vegetation in the Xilingol region stopped growing or was covered by snow in winter. In this paper the annual growing season from April to October was selected as the research period. In addition, due to the limited time series of MODIS data, 2000–2015 was chosen.

It can be seen from Figure 4(a) that the SPEI value of Xilingol region in the recent 16 years is probably in the range of −2 (2001)~1 (2012), and the rising rate is 0.0058/yr. 2003 and 2012 are the humid period of Xilingol; 2001 and 2007 are the severe drought period. Figure 5 records the spatial distribution of drought in Xilingol from 2000 to 2015 of the growing season. The annual drought distribution in Xilingol region is shown clearly. Due to the uneven distribution of water and heat in the region, the degree of drought is not the same each year, so a larger area of drought appeared in 2000, 2001, 2005, and 2007. The spatial variation of SPEI showed an increasing tendency in the whole growing season in Xilingol area, 40% of which increased significantly, mainly in the eastern meadow steppe of the study area (Figure 6(a)).

In the recent 16 years, the average NDVI in Xilingol steppe showed an upward trend with an increasing rate of 0.0021/yr (Figure 4(b)), which was in accordance with the general improvement of Xilingol grassland vegetation in recent years [26]. For example, NDVI in 2003 and 2012 correspond to the peak of SPEI, while the NDVI trough in 2001 and 2007 corresponds to the SPEI trough of same year. And the NDVI in 81.53% of the region increased specially (Figure 6(b)), which was consistent with the increase of SPEI, indicating that drought was the main factor affecting the growth of Xilingol grassland vegetation.

3.3. Drought Impact on Vegetation NDVI in Xilingol. According to the above analysis, between 2000 and 2015, the SPEI and NDVI in Xilingol region are highly consistent with the change of time series, and the vegetation growth is relatively good in humid years. Through the Pearson correlation analysis, we can see that in the annual growing season SPEI and NDVI are significantly positively correlated ($r = 0.905$, $P < 0.01$). Figure 6(c) shows the results of pixel-by-pixel correlation analysis of SPEI and NDVI. The results showed that the area of positive correlation between SPEI and NDVI in the growing season was much larger than that of negative correlation area, and the positive correlation area was 98.42%

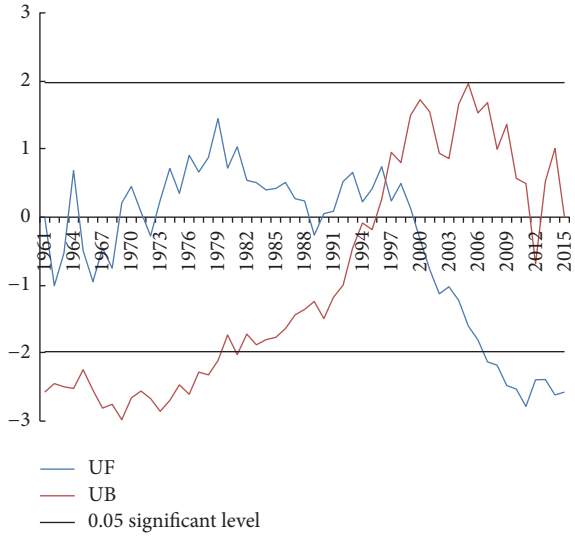

Figure 3: Mann-Kendall test for annual SPEI-12 series in Xilingol from 1961 to 2015.

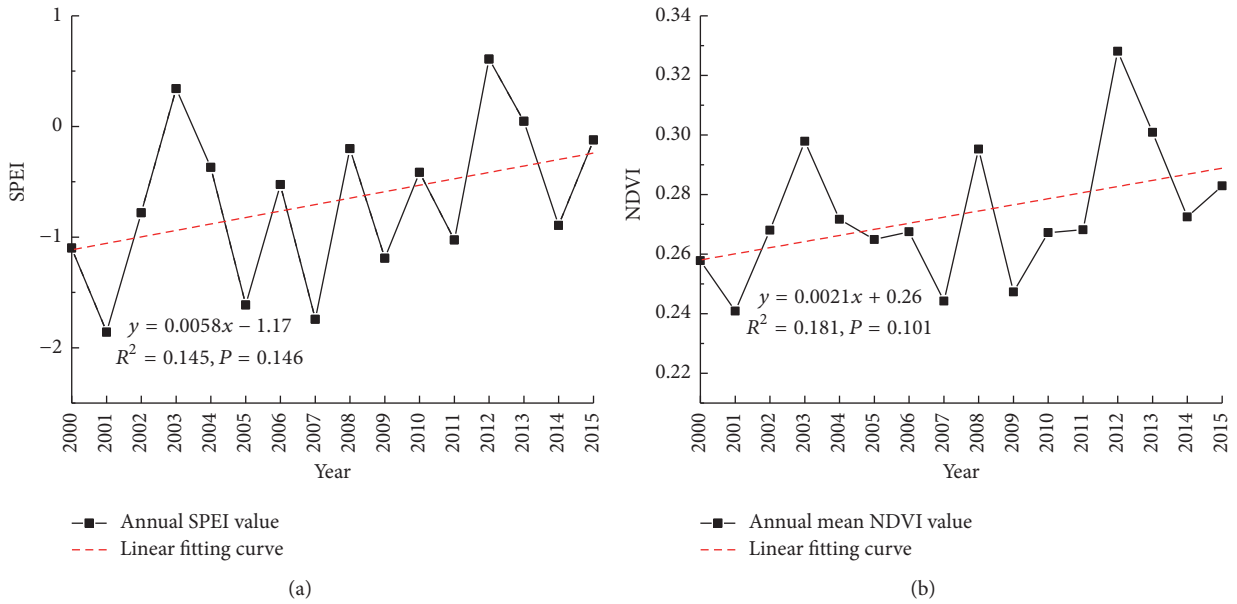

Figure 4: Interannual variations of SPEI (a) and NDVI (b) in Xilingol during 2000–2015.

of the total area of the study area. Among them, 24.32% has no significant positive correlation, mainly in the Dongwuqi and eastern and southern grassland desert in Xiwuqi and northern Sunitezuoqi. It can be seen from Table 2 that whole of Xilingol and its four grassland types have a significant positive response to drought at different time scales. The correlation coefficient was the largest for desert steppe at the 3-month time scale, while for other types the correlation coefficients were the highest at the 6-month time scale. And except for the steppe desert, the correlation coefficients were the lowest at the 12-month time scale, indicating that Xilingol grassland has a strong response to the short-term (SPEI-1), seasonal (SPEI-3), and medium-term (SPEI-6) drought and a lower response to long-term (SPEI-12) drought.

Table 2: Pearson correlation coefficients between SPEI and NDVI at different time scales.

	SPEI-1	SPEI-3	SPEI-6	SPEI-12
Xilingol	0.72	0.76	0.83	0.64
Meadow steppe	0.48	0.53	0.64	0.53
Typical steppe	0.69	0.73	0.79	0.61
Steppe desert	0.62	0.65	0.79	0.71
Desert steppe	0.66	0.69	0.65	0.44

The above analysis shows that drought has vital impact on the annual NDVI. However, the effect of drought on monthly NDVI was variable [27]. In order to examine the drought

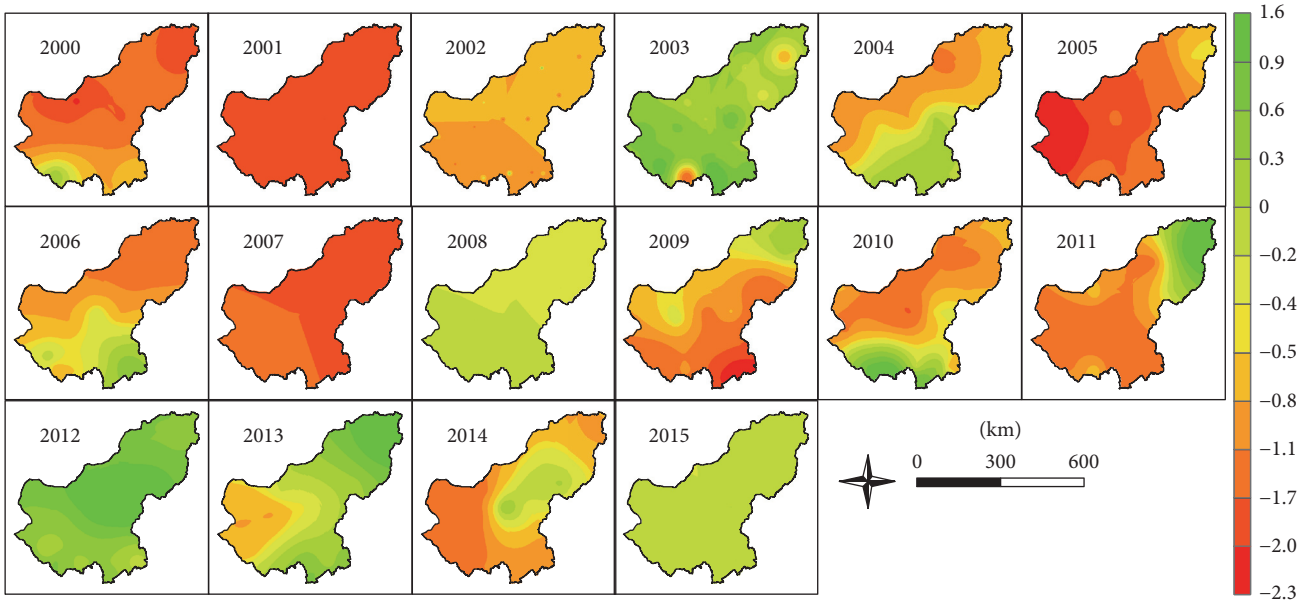

Figure 5: Spatial distribution of drought in Xilingol during 2000–2015.

Table 3: Pearson correlation coefficient of NDVI and SPEI in Xilingol at different time scales.

NDVI	SPEI			
	0 month	1 month	2 months	3 months
April	−0.411	0.184	0.051	−0.362
May	0.204	0.408	0.044	0.288
June	0.576*	0.182	0.102	0.224
July	0.708**	0.730**	0.001	−0.102
August	0.078	0.808**	0.481	−0.4
September	0.34	0.457	0.681**	0.626**
October	0.004	0.488	0.303	0.717**

Significant at $^{*}a = 0.05$ and $^{**}a = 0.01$ levels.

impact on the monthly NDVI, we choose the humid years 2003 and 2012 and dry years 2001 and 2007 to investigate the dynamics of SPEI and NDVI of each month in growing season. It can be seen from Figure 7 that the vegetation in Xilingol was the best in the July and August, while the drought is severe in July and August. The possible reason for this phenomenon is that the precipitation in Xilingol region is abundant in July and August, and the temperature is the highest. The summer vegetation in this area is mainly controlled by precipitation, and the high temperature will accelerate the evaporation and lead to the drought intensification [28]. In the wet years 2003 and 2012, the NDVI and SPEI curves of the growing season were above the mean NDVI and the multiyear average SPEI curves. In 2003, NDVI reached the highest value in July; SPEI was higher in May and June; in 2012, NDVI reached the highest value in August; SPEI value was higher in June and July. In the dry years 2001 and 2007, the NDVI and SPEI curves were below the multiyear averaged NDVI and SPEI curves. In 2001, NDVI reached the highest value in July, and SPEI was higher in July and August, indicating that the effect of drought on vegetation is lagging. And there was moderate drought in April 2007, but it did not have a negative impact on the vegetation in April, indicating that drought had little effect on green up.

In order to study the lag effect of drought on vegetation, we selected 0 month, 1 month, 2 months, and 3 months scale to analyze the correlation between SPEI and NDVI by Pearson correlation analysis. The results are shown in Table 3; we found in April and May that NDVI and SPEI showed a weak positive correlation; 4-5 months is Xilingol grassland's returning green period, indicating that the drought in the Xilingol grassland turning green has little effect. There was a significant positive correlation between NDVI and 0 month SPEI in June and NDVI in July and SPEI in 0 month and 1 month in July and a significant positive correlation between NDVI and 0 month SPEI in June and 1 month in August, indicating that the drought in the month and the previous month grassland growth play an extremely

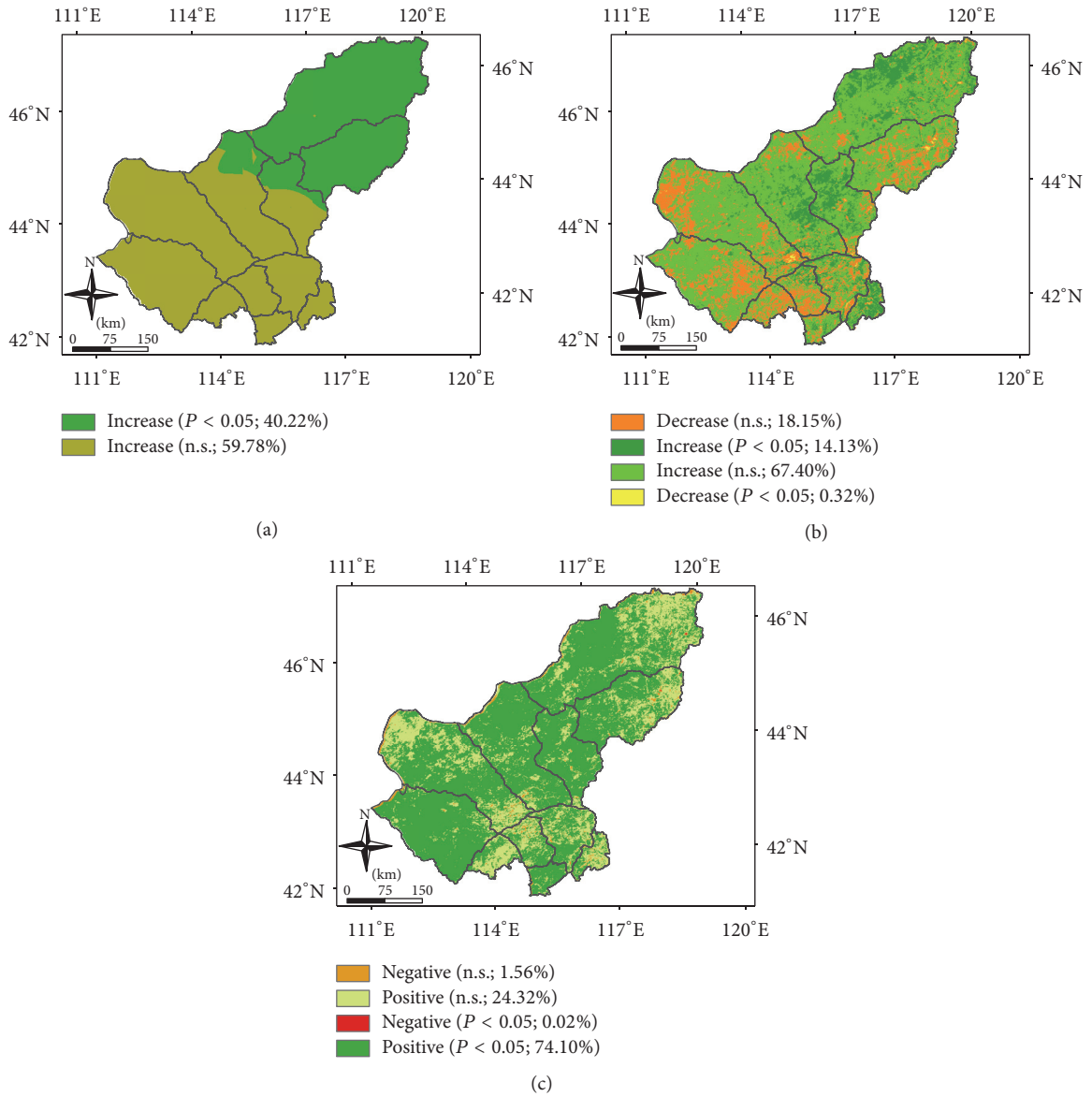

Figure 6: Spatial pattern of SPEI (a), NDVI (b) trend, and their correlation (c) during 2000–2015.

important role. During September to October, NDVI had a significant positive response to SPEI of 2 months and 3 months and a strong response to short-term drought.

3.4. Changes of Vegetation in Different Grassland Types and Their Response to Drought. Different grassland types in Xilingol region have different responses to drought due to their own physiological and ecological characteristics and geographical differences. Figure 8 shows the change trend of SPEI and NDVI of different grassland types during 2000 to 2015, with different degrees of rising trend. And the SPEI values stayed the same, decreasing in the order of meadow steppe > steppe desert > typical steppe > desert steppe, with the mean values of −0.510, −0.635, −0.672, and −0.814, respectively. In addition to natural conditions, the steppe desertification is mainly affected by human activities. That is to say, grassland types are gradually transformed by artificial transformation such as planting trees and grasses. The diversity of shrub communities is relatively abundant, and the coverage was also relatively high [29]. This may be the reason why the steppe desert NDVI is slightly higher than typical steppe in the study area, but the gap is not obvious.

Figure 9 shows the response characteristics of different grassland types to different scales of drought. The correlation coefficients of NDVI and SPEI index of meadow steppe are shown in Figure 9(a). It showed that there is no significant correlation between the NDVI and SPEI index of meadow steppe in April, and the correlation between NDVI and drought index in May was significantly higher than that in April. The reason is that most of the meadow steppe turned green in May and small part of them became green in late April, so the meadow steppe in April had no obvious response

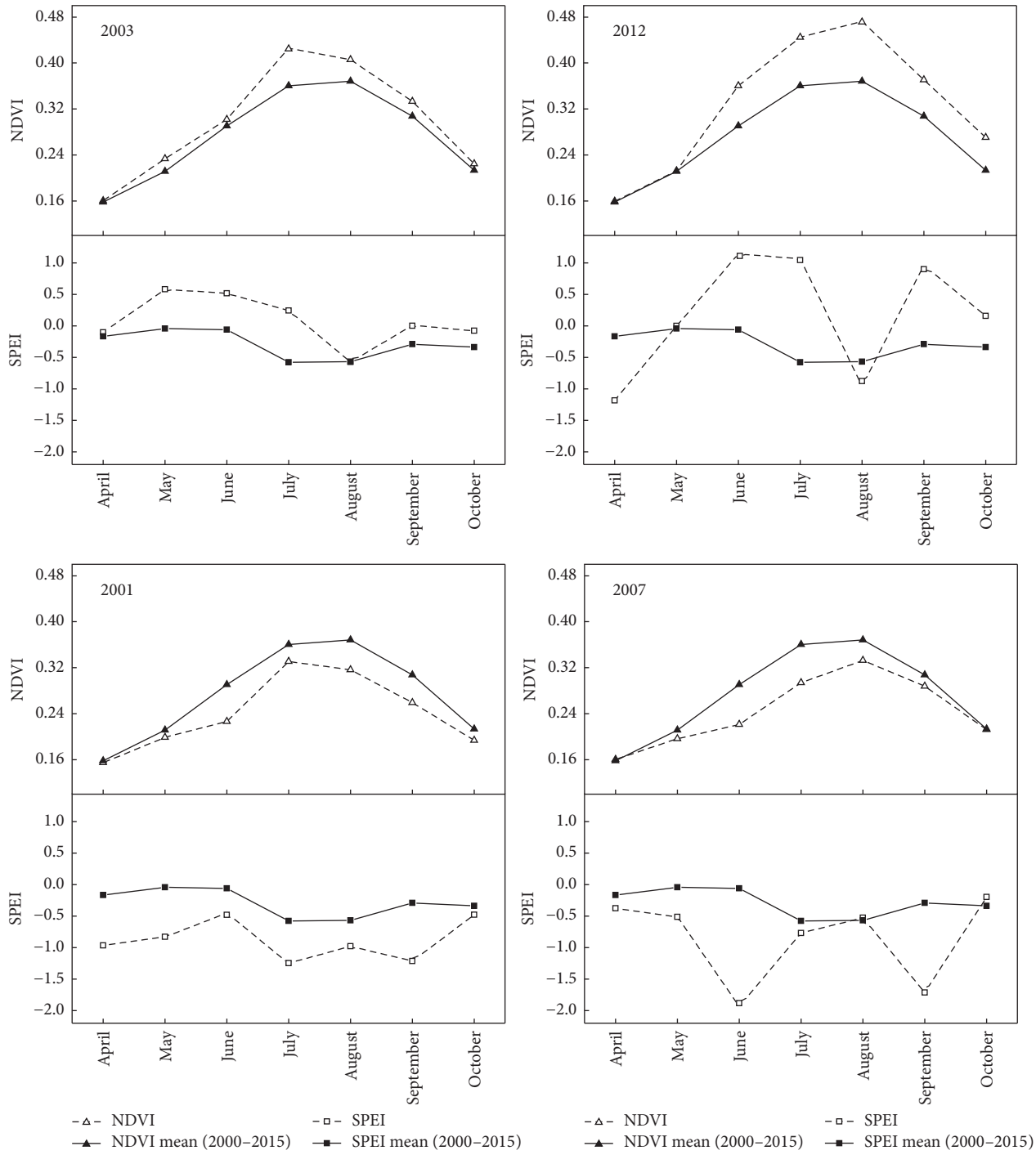

Figure 7: Monthly variations in mean NDVI and SPEI in growing season (April to October) of 2001, 2003, 2007, and 2012 and the 2000–2015 average in Xilingol. The dashed and solid lines denote the 16 years' mean and monthly NDVI or SPEI, respectively.

to the climate drought. And, in May, the steppe began to develop and the steppe turned into the growing season, the drought response gradually increased. In June, the NDVI of meadow steppe showed strong correlation with SPEI of 0 month, and NDVI of steppe was more sensitive to drought. NDVI in July and 1 month, NDVI in August and 2 months, and NDVI in September and 3 months showed a significant positive correlation indicating that these three months of vegetation had a positive response to drought in the earlier period and the effect of drought on vegetation had lagged. In October, the correlation between NDVI and SPEI in meadow steppe was weak, which indicated that the response to climate drought was not obvious. When entering October, the steppe vegetation entered the period of yellowing and the

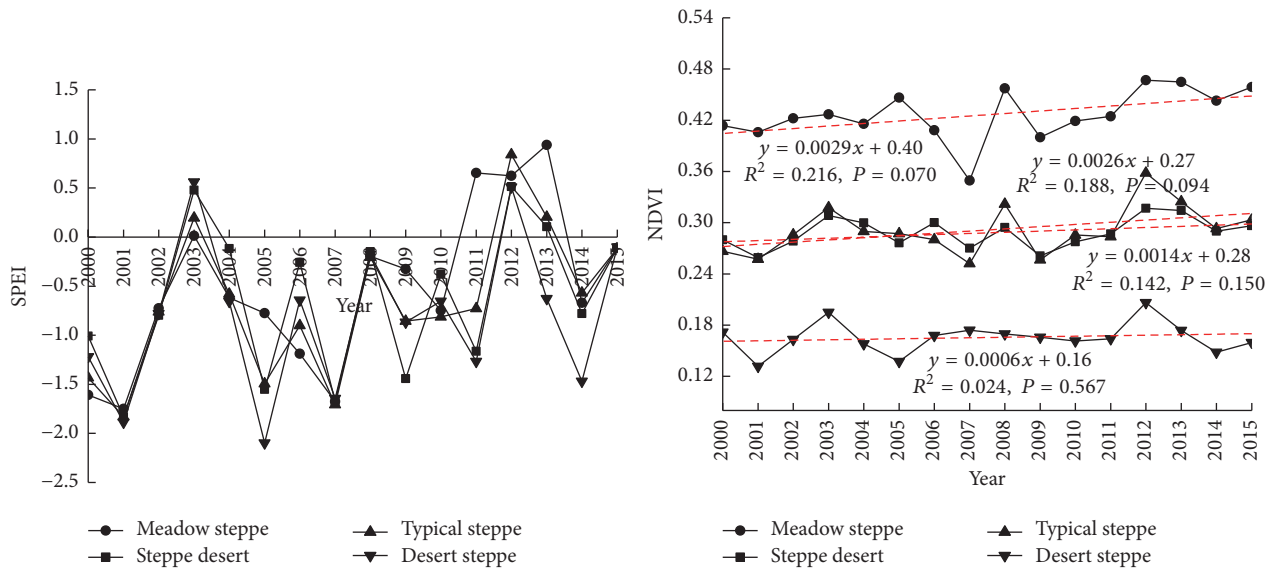

Figure 8: Interannual variations of NDVI and SPEI in four grassland types of Xilingol during 2000–2015.

temperature decreased, which led to the decrease of grassland green rate.

According to the correlation analysis between time series of NDVI and SPEI of typical steppe, the results are shown in Figure 9(b). Compared with meadow steppe, the NDVI of typical steppe was highly correlated with SPEI at different time scales, indicating that the response of typical steppe to drought was more obvious than that of meadow steppe. The correlation between grassland NDVI and SPEI was not significant at the early stage of typical grassland growth, which indicated that grassland turning green period had less response to drought at these different time scales. During June to August, the grassland NDVI had a significant positive response to the drought in the same month and in the early period. After entering September, the grassland began to wither short-term drought on the typical steppe to a certain extent.

The correlation of time series between NDVI and SPEI of steppe desert is shown in Figure 9(c). It can be seen that the correlation coefficient of steppe desert NDVI and SPEI change temporally, which indicates that the response of steppe desert to drought climate at different time scales is very different. The correlation between NDVI and SPEI at different time scales in April was greater, indicating that drought had a greater impact on the greening of steppe desert. The response of NDVI to drought was similar to that of desert steppe (Figure 9(d)) in other months. The correlation between NDVI and SPEI at different time scales was not as obvious as in other types of steppe. In general, the response of SPEI in different grassland types in Xilingol grassland was not significant in the early of the growing season, and June-August NDVI respond to 0 month and 1 month SPEI strongly, In October, grassland withering period, NDVI was sensitive to 3-month SPEI.

4. Conclusions

In this study, we explore the spatial and temporal dynamics of SPEI and NDVI over the Xilingol grassland and investigate the impact of drought on the NDVI in Xilingol grassland during the growing season (April–October). The main conclusions include the following:

(1) There is an increasing trend of annual drought in Xilingol during 1961–2015, and it has a mutation in 1997 and the drought becomes more intense after this year.

(2) In the recent 16 years, the annual growing season SPEI has an obvious upward trend in time and the apparent wetting spatially. Correspondingly, the growing season NDVI showed upward trend.

(3) Vegetation coverage in Xilingol grew better in humid years and opposite in arid years. SPEI and NDVI had a significant positive correlation ($r = 0.905$, $P < 0.01$); 98% of the region showed positive correlation, indicating that meteorological drought affects vegetation growth more in arid and semiarid region.

(4) Xilingol grassland has a strong response to the short-term, seasonal, and medium-term drought and a lower response to long-term drought. And the effect of drought on vegetation has lag effect, and the responses of different grassland types to different scales of drought were different.

Competing Interests

The authors declare that there is no conflict of interests regarding the publication of this paper.

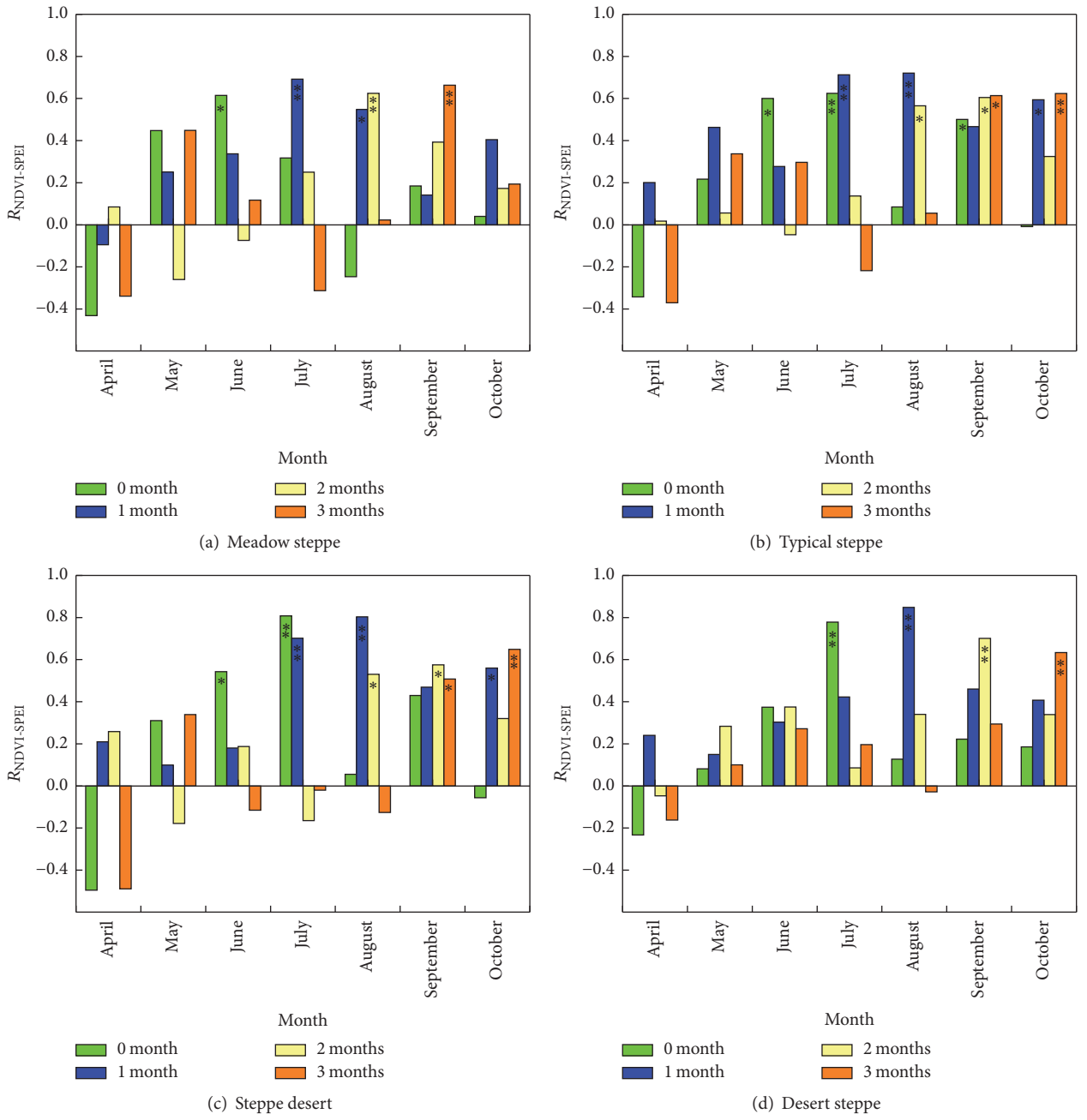

Figure 9: Pearson correlation coefficient of NDVI and SPEI in four grasslands at different timescales (the horizontal axis was the months, and the vertical axis was the correlation coefficient between SPEI and NDVI). $*$ is 0.1 significance level and $**$ is 0.05 significance level.

Acknowledgments

This study was supported by the national "12th-five" Science and Technology Support Projects of China (Grants nos. 2013BAK05B01 and 2013BAK05B02).

References

[1] D. S. Ojima, B. O. M. Dirks, E. P. Glenn, C. E. Owensby, and J. O. Scurlock, "Assessment of C budget for grasslands and drylands of the world," *Water, Air, and Soil Pollution*, vol. 70, no. 1, pp. 95–109, 1993.

[2] G. X. Liu, "Current situation of monitoring, assessment, problems and countermeasures of grassland eco-environmental quality," *Chinese Journal of Grassland*, vol. 31, no. 3, pp. 8–12, 2009.

[3] Y. L. Wang, W. L. Yun, W. Wang, and Q. Hou, "Effect of climate warming on spatial pattern and temporal change of precipitation in typical steppe," *Journal of Arid Land Resources and Environment*, vol. 23, no. 1, pp. 82–85, 2009.

[4] H. Xiang-Zhong, H. Yan-Bin, W. Yan-Fen, Z. Xiao- Qi, H. Xi, and H. Jun-Jie, "Impact of extreme drought on net ecosystem exchange from lemus chinensis steppe in xilin river basin, china," *Chinese Journal of Plant Ecology*, vol. 30, no. 6, pp. 894–900, 2006.

[5] S. Piao, A. Mohammat, J. Fang, Q. Cai, and J. Feng, "NDVI-based increase in growth of temperate grasslands and its responses to climate changes in China," *Global Environmental Change*, vol. 16, no. 4, pp. 340–348, 2006.

[6] S. L. Piao, J. Y. Fang, J. S. He, and X. Xiao, "Spatial distribution of grassland biomass in China," *Acta Phytocecologica Sinica*, vol. 28, no. 4, pp. 491–498, 2004.

[7] S. L. Liu, Y. Y. Tian, Y. J. Yin, N. N. An, and S. K. Dong, "Temporal dynamics of vegetation NDVI and its response to drought conditions in Yunnan Province," *Acta Ecologica Sinica*, vol. 36, no. 15, pp. 4699–4707, 2016.

[8] S. Beguería, S. M. Vicente-Serrano, and M. Angulo-Martínez, "A multiscalar global drought dataset: The SPEI base: a new gridded product for the analysis of drought variability and impacts," *Bulletin of the American Meteorological Society*, vol. 91, no. 10, pp. 1351–1356, 2010.

[9] A. S. Goudie and N. J. Middleton, "The changing frequency of dust storms through time," *Climatic Change*, vol. 20, no. 3, pp. 197–225, 1992.

[10] S. D. Schubert, M. J. Suarez, P. J. Pegion, R. D. Koster, and J. T. Bacmeister, "On the cause of the 1930s dust bowl," *Science*, vol. 303, no. 5665, pp. 1855–1859, 2004.

[11] H. Wang, X.-B. Li, X. Li, and D.-D. Wang, "Grassland response to drought in northern China," *Shengtai Xuebao/ Acta Ecologica Sinica*, vol. 28, no. 1, pp. 172–182, 2008.

[12] A. K. Mishra and V. P. Singh, "A review of drought concepts," *Journal of Hydrology*, vol. 391, no. 1-2, pp. 202–216, 2010.

[13] S. M. Vicente-Serrano, S. Beguería, and J. I. López-Moreno, "A multiscalar drought index sensitive to global warming: the standardized precipitation evapotranspiration index," *Journal of Climate*, vol. 23, no. 7, pp. 1696–1718, 2010.

[14] L. G. Cao, P. X. Liu, K. X. Zhang, and H. Y. Wang, "Analysis on response of grasslands to climate change and its spatial difference in Xilingol League," *Arid Zone Research*, vol. 28, no. 5, pp. 789–794, 2011.

[15] C. Chen, J. Wang, X. B. Pan, Z. H. Pan, and Y. R. Wei, "Simulation study regarding the impact of climate change on grass productivity in Inner Mongolia," *Acta Agrestia Sinica*, vol. 21, no. 5, pp. 850–860, 2013.

[16] Z. H. Gu, J. Chen, P. J. Shi, and M. Xu, "Correlation analysis of NDVI difference series and climate variables in Xilingole steppe from 1983 to 1999," *Acta Phytoecologica Sinica*, vol. 29, no. 5, pp. 753–765, 2005.

[17] H. Bagan, Q. Wang, Y. Yang, Y. Yasuoka, and Y. Bao, "Land cover classification using moderate resolution imaging spectrometer-enhanced vegetation index time-series data and self-organizing map neural network in Inner Mongolia, China," *Journal of Applied Remote Sensing*, vol. 1, no. 1, pp. 157–167, 2007.

[18] Z. H. Li, Y. J. Bao, H. M. Wang, T. Xu, Y. Cheng, and J. X. Gao, "The analysis on degeneration status and the driving force of Xilinguole steppe," *Ecology and Environment*, vol. 17, no. 6, pp. 2312–2318, 2008.

[19] Y. L. Gong, H. F. Zhang, and X. Xiao, "3S Based disaster relief of drought disaster in Xilingol League," *Journal of Catastrophology*, vol. 24, no. 2, pp. 123–127, 2009.

[20] J. W. Wu, J. R. Li, T. Sun, F. Li, and X. S. Zhou, "Risk assessment on climatic factors resulting in sandstorm disasters in Xilingol region," *Arid Zone Research*, vol. 28, no. 6, pp. 936–943, 2011.

[21] R. Zhang, H. Zou, M. Hong, A. Zhou, and G. Zeng, "Risk analysis of water resources crisis in the Lancang-Mekong river drainage basin under the background of climate change," *Journal of Risk Analysis and Crisis Response*, vol. 2, no. 3, pp. 209–213, 2012.

[22] B. N. Holben, "Characteristics of maximum-value composite images from temporal AVHRR data," *International Journal of Remote Sensing*, vol. 7, no. 11, pp. 1417–1434, 1986.

[23] Y. L. Hang, G. Bao, Y. H. Bao, Burenjirigala, and D. Altantuya, "Spatiotemporal changes of vegetation coverage in Xilin Gol grassland and its responses to climate change during 2000–2010," *Acta Agrestia Sinica*, vol. 22, no. 6, pp. 1194–1204, 2014.

[24] C. W. Thornthwaite, "An approach toward a rational classification of climate," *Geographical Review*, vol. 38, no. 1, pp. 55–94, 1948.

[25] Z. Ma and C. Fu, "Some evidence of drying trend over northern China from 1951 to 2004," *Chinese Science Bulletin*, vol. 51, no. 23, pp. 2913–2925, 2006.

[26] Y. Yan, A. Tengtuya, Y. Hu, Y. Liu, and G. Yu, "The tendency and its spatial pattern of grassland changes in the east xilin gol from 1975 to 2009," *Geo-information Science*, vol. 13, no. 4, pp. 549–555, 2011.

[27] R. Trigo, C. M. Gouveia, S. Begueria, and S. Vicente-Serrano, "Drought impacts on vegetation dynamics in the Mediterranean based on remote sensing and multi-scale drought indices," Keio-IES Discussion Paper Series 17, 2014.

[28] L. Zhou, C. J. Tucker, R. K. Kaufmann, D. Slayback, N. V. Shabanov, and R. B. Myneni, "Variations in northern vegetation activity inferred from satellite data of vegetation index during 1981 to 1999," *Journal of Geophysical Research Atmospheres*, vol. 106, no. 17, pp. 20069–20083, 2001.

[29] X. Li and X. Zhang, "Biodiversity of shrub community in desert steppe and steppe desert on Erdos plateau," *Chinese Journal of Applied Ecology*, vol. 10, no. 6, pp. 665–669, 1999.

Hindawi
Mathematical Problems in Engineering
Volume 2017, Article ID 2048098, 10 pages
https://doi.org/10.1155/2017/2048098

Research Article

Multisensor Fusion of Landsat Images for High-Resolution Thermal Infrared Images Using Sparse Representations

Hong Sung Jin[1] and Dongyeob Han[2]

[1]*Department of Mathematics, Chonnam National University, 77 Yongbongro, Bukgu, Gwangju 61186, Republic of Korea*
[2]*Department of Marine and Civil Engineering, Chonnam National University, 50 Daehakro, Yeosu, Jellanamdo 59626, Republic of Korea*

Correspondence should be addressed to Dongyeob Han; hozilla@chonnam.ac.kr

Received 31 October 2016; Accepted 5 December 2016; Published 12 January 2017

Academic Editor: Hajime Seya

Land surface temperature (LST) is an important parameter in the analysis of climate and human-environment interactions. Landsat Earth observation satellite data including a thermal band have been used for environmental research and applications; however, the spatial resolution of this thermal band is relatively low. This study investigates an efficient method of fusing Landsat panchromatic and thermal infrared images using a sparse representation (SR) technique. The application of SR is used for the estimation of missing details of the available thermal infrared (TIR) image to enhance its spatial features. First, we propose a method of building a proper dictionary considering the spatial resolution of the original thermal image. Second, a sparse representation relation between low- and high-resolution images is constructed in terms of the Landsat spectral response. We then compare the fused images created with different sampling factors and patch sizes. The results of both qualitative and quantitative evaluation show that the proposed method improves spatial resolution and preserves the thermal properties of basic LST data for use with environmental problems.

1. Introduction

Land surface temperature (LST) is defined as the temperature emitted by the surfaces of land objects. LST is a key variable in agricultural, climatological, hydrological, and environmental and ecological studies [1, 2]. Furthermore, it is a combination of the results of surface-atmosphere interactions and energy fluxes between the atmosphere and the ground [3]. For urban climate research, satellite-based LST has the ability to depict comprehensively a complex temperature distribution spatially in highly heterogeneous urban environments [2].

LST can be obtained for a particular set of sample points from ground weather stations or, with the modern development of satellites and high-resolution sensors, LST can be estimated over large regions through the use of thermal infrared band data supplied by satellites [4]. Many satellite sensors can sense thermal infrared radiation (TIR) with different spectral and spatial resolutions [5]. Medium-resolution thermal infrared imagery/data, LANDSAT TM/ETM+, and ASTER have been used extensively for analysis on a regional scale to study surface temperature variations and to relate them to land cover characteristics [6].

Unfortunately, such TIR images from satellite sensors have low spatial resolutions and high noise levels. In contrast, the panchromatic band has a relatively higher resolution. The motivation for fusing TIR and panchromatic data is to produce data with an improved spatial resolution.

Panchromatic images observe radiation reflected from Earth's surface over a visible and near-infrared (NIR) wavelength range of 0.4 to 0.9 μm, whereas TIR images observe radiation emitted from Earth's surface over a TIR wavelength range of 8 to 15 μm [7]. The physical processes in the panchromatic and TIR images from different bands result in difficulty in fusing the two types of images.

Many researchers in the field of image processing have developed efficient image fusion algorithms such as the expectation maximization (EM), discrete wavelet transform (DWT), and Laplacian pyramid [8, 9] methods. Much literature focuses on presenting techniques of integrating IR and visible image information for enhanced visual quality.

In addition to these general multiresolution fusion methods, many techniques have been developed specifically for the fusion of multispectral satellite images [9]. However, those methods have the requirement overlapping spectral responses, for example, between RGB visible bands and the panchromatic band. Additionally, fusion methods for satellite TIR and visible band images have been proposed using a physical property-based postcorrection solution using a two-step process [9] or using an optimal scaling factor in order to control the trade-off between spatial detail and the thermal information [10]. However, using existing approaches, it is still necessary to preserve thermal properties in a one-step process.

Image fusion methods based on compressive sensing (CS) have gained attention in recent years; in these approaches, the high-frequency details of reconstructed high-resolution (HR) images can be learned from HR training images [11]. Yang and Li [12] first introduced the use of sparse representation (SR) in image fusion. The sliding window technique (overlapping patches) is adopted in their method to make the fusion process more robust against noise and misregistration. Yang et al. [13] presented an SR method in the CS framework, which needs to train two dictionaries to ensure that the low-resolution (LR) and HR image patches have the same coefficients. However, the performance of this method relies heavily on the number of atoms in the dictionaries. Jiang et al. [14] proposed a practical fusion method using dictionaries constructed from a set of available PAN and MS images. Liu et al. [15] presented a general image fusion framework combining multiscale transforms (MST) and SR to overcome simultaneously the inherent defects of both the MST- and SR-based fusion methods. Low-pass bands are merged using an SR-based fusion approach that uses the max-L1 rule to obtain a fused sparse vector.

Inspired by these ideas, we propose a fusion method based on SR for Landsat TIR and panchromatic images. The proper TIR dictionary is shaped considering the spatial resolution of the original thermal images, and a SR relation between low- and high-resolution images is constructed in terms of the satellite sensor's spectral response. To verify the effectiveness of the proposed framework, four fusion methods, including the cross bilateral filter (CBF) [16], multiwavelet (MW) [9], discrete wavelet transform (DWT) [17], and optimal-scaling-factor-based fusion (OSF) [10] methods, are tested in our experiments.

The rest of this paper is organized as follows. We first introduce the basic theory of CS and describe the detailed fusion framework in Section 2. In Section 3, experimental results are shown and compared with the results of other approaches. Finally, Section 4 summarizes the main conclusions of this paper.

2. Proposed Fusion Framework

To better illustrate the proposed framework based on SR method, we present the details of our framework in this section.

2.1. Compressive Sensing. Consider obtaining the value of $\boldsymbol{\alpha}$ in the following problem for $\mathbf{y} \in R^M$ and $\boldsymbol{\alpha} \in R^N$

$$\mathbf{y} = \mathbf{D}\boldsymbol{\alpha}; \tag{1}$$

when $M > N$, it is incomplete, and when $M < N$, it is overcomplete.

Only in the case of $M = N$ do we expect that the inverse of D exists. For the incomplete case no solution exists. For the overcomplete case, there exists more than one solution. This means that we obtain the desired solution only for certain conditions, which leads to optimization problems in the signal representation. Under the sparsity condition of a signal, we can choose the best signal recovery approach in the overcomplete case. If we assume that $\mathbf{y}$ is a measurement and D is some transform matrix or dictionary, we must decide what constitutes the true signal $\boldsymbol{\alpha}$. When the signal $\boldsymbol{\alpha}$ is k-sparse,

$$\|\boldsymbol{\alpha}\|_0 := \left|\operatorname{supp} \boldsymbol{\alpha}\right| \leq k, \tag{2}$$

then we can use the methods of optimizing problems:

$$\widehat{\boldsymbol{\alpha}} = \arg\min \quad \|\boldsymbol{\alpha}\|_0 \quad \text{such that } \mathbf{y} = \mathbf{D}\alpha \tag{3}$$

which is an l_0-minimization problem. It is an NP-hard problem, and it has several methods for approximation such as basis pursuit (BP) and orthogonal matching pursuit (OMP) [18].

Another optimization approach is the l_1-minimization, which involves the following:

$$\begin{aligned} &\min_{\boldsymbol{\alpha} \in C^N} \quad \|\boldsymbol{\alpha}\|_1 \\ &\text{subject to} \quad \mathbf{y} = \mathbf{D}\alpha. \end{aligned} \tag{4}$$

Optimization based on l_1-minimization can exactly recover k-sparse signals and closely approximate compressible signals with high probability using only $M \geq ck \log(N/k)$ i.i.d. Gaussian measurements [19].

2.2. Signal Recovery Algorithm. A stable solution of (3) can be found by using relaxation techniques such as basis-matching pursuit or greedy algorithms such as orthogonal matching pursuit (OMP). We used the OMP method [20] to approximate the true signal $\boldsymbol{\alpha}$ for the given dictionary D, measured data $\mathbf{y}$, and the sparsity of the true signal $\boldsymbol{\alpha}$. The OMP method chooses k columns out of the dictionary by using projection methods for k-sparse signal recovery. Initially, the signal $\mathbf{y}$ is projected to all the columns of D. The column having maximal inner product is selected and an index set representing the position of the column is made. This is later used as an index for signal support. Then, the residual is saved as a new signal and the same procedure above is repeated until we obtain the index set of elements equal to the degree of sparsity. Finally, the residuals and the index set also successively update and the signal is approximated.

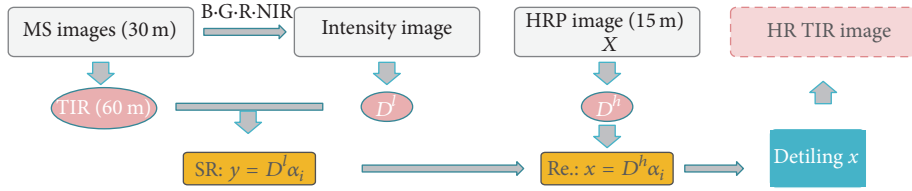

Figure 1: Schematic of the proposed SRT technique (we call our proposed method the SRT).

2.3. Problem Statement. Let MS $= \{\text{MS}_k\}$, $k = 1, \ldots, B$, be the available MS image composed of B bands, with P as the HR PAN image. In our research, the objective of the fusion process is the estimation of the TIR image at the resolution of the PAN image, which is denoted as HR TIR (see Figure 1). $\mathbf{X}$ is tiled in M overlapping patches of size NR × NR, where R is the resolution ratio between the MS and PAN images, and N is a scalar coefficient tuned by the user.

Let $\mathbf{x} = [x_1] \in R^{R^2N^2}$ denote a vector containing the pixels, arranged by columns, belonging to a generic patch of X. In the SR-based framework, x is approximated as a linear combination of the elements of a dictionary $\mathbf{D^h}$, where the superscript $\mathbf{h}$ indicates that the dictionary is composed of high-spatial-resolution pixels

$$\mathbf{x} = \mathbf{D^h}\boldsymbol{\alpha}. \tag{5}$$

The aim of our SRT is to find an optimal combination of $\mathbf{x}$ using the elements of the dictionary subject to a sparsity constraint on the coefficients α, which results in minimum reconstruction error. The sparsity constraint enforces that the coefficient vector α has few nonzero entries (i.e., a small "pseudonorm" $\|\boldsymbol{\alpha}\|_0$). A good choice of dictionary enables signal description using a (very) sparse representation.

Consequently, the suitability of the approach for the problem at hand derives itself from the consideration that patterns tend to repeat several times within an image, and the number of recurrences is smaller for high-variance zones. In other words, there are fewer recurrences for zones characterized by a greater amount of spatial detail [21].

As in [14], we construct the dictionary as

$$\mathbf{D^h} = \text{diag}\left(\boldsymbol{\Delta}_\mathbf{1}^\mathbf{h}\right) = \text{diag}\left(\left[\delta_{1,1}^h, \ldots, \delta_{1,M}^h\right]\right). \tag{6}$$

Dictionary $\boldsymbol{\Delta}_\mathbf{1}^\mathbf{h}$ is composed of M patches of the PAN image P.

The estimation of the coefficient α is performed at a simulated low-resolution PAN image scale from the original MS image by solving (5). This process is based on the scale-invariance hypothesis that is justified by the direct correspondence of patches in the fused and original image [14]. In more detail, we consider the underdetermined system $\mathbf{y} = \mathbf{D^l}\alpha$ under the sparsity constraint over α; namely, we solve

$$\widehat{\boldsymbol{\alpha}} = \arg\min \quad \|\boldsymbol{\alpha}\|_0 \quad \text{such that } \mathbf{y} = \mathbf{D^l}\alpha. \tag{7}$$

In (7), $\mathbf{y} = [y_1]^T \in R^{N^2}$ denotes a patch of the TIR image arranged by columns, which is a band of the original MS images (see Figure 1). The dictionary $\mathbf{D^l} = \text{diag}(\boldsymbol{\Delta}_\mathbf{1}^\mathbf{l})$ is the reduced-scale counterpart of $\mathbf{D^h}$ and consists of $\boldsymbol{\Delta}_\mathbf{1}^\mathbf{l} = [\delta_{1,1}^l, \ldots, \delta_{1,M}^l]$, each of which is composed of M patches of the low-resolution (LR) PAN image. The relative spectral response functions of the Landsat satellite sensors are shown in Figure 2. According to Figure 2, the LR PAN image patch M can be expressed as a nearly linear combination of all the bands of the corresponding original MS image patch [22].

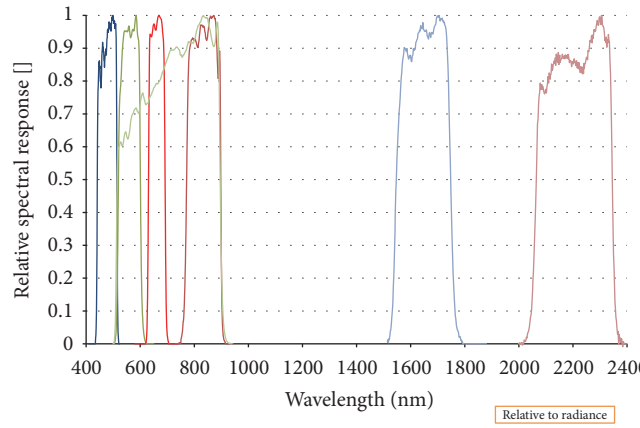

Figure 2: Landsat 7 ETM+ in-band band-average relative spectral response (http://landsat.usgs.gov/documents/L7_RSR.xlsx).

We apply the OMP procedure to the TIR band. In other words, we find the vector $\alpha = [\alpha_{\text{TIR}}]$. This allows an appreciable computational ease with respect to the overall optimization problem defined by (7) without introducing significant performance degradation [23]. Each single corresponding patch of the image X is reconstructed by using formula (5). The whole image HR TIR is finally obtained by averaging the patches in the overlapping zones.

3. Experimental Results

3.1. Source Images. We tested the proposed fusion approach using Landsat 7 multispectral images. Landsat 7 satellite data were downloaded from the US Geological Survey Global Visualization Viewer (GloVis) website (http://glovis.usgs.gov/, accessed August 2016). The test data were acquired on 25 October 2015 from 115/036 (path/row) in World Reference System-2 (WRS-2). The ETM+ sensor scans a spectrum of eight bands with high resolution to provide images of Earth's surface with resolutions of 30 m for

Table 1: Bands available with the Landsat 7 ETM+ sensor.

Band	Wavelength (μm)	Resolution (m)
Blue	0.45–0.52	30
Green	0.52–0.60	30
Red	0.63–0.69	30
Near IR	0.76–0.90	30
SWIR	1.55–1.75	30
Thermal IR	10.40–12.50	60
SWIR	2.08–2.35	30
Panchromatic	0.5–0.9	15

a multispectral TM image and 15 m for a panchromatic image (LPSO). The ETM+ Band 6 is acquired at 60 m resolution, but products are resampled to 30 m resolution. Table 1 presents the sensor characteristics for LANDSAT 7 ETM+. The blue, green, red, near IR, thermal IR, and panchromatic bands were used to test the fusion algorithm.

The test data cover Jellanamdo in South Korea, including mountains, agricultural fields, coastlines, and city areas. Consequently, we tested the performance of the fusion approach in both urban and rural areas. Figures 3(a) and 5(b) present Landsat 7 PAN images of size 512×512 and TIR image of size 256×256, respectively.

Spatial details including paddy fields, foreshores, roads, and mountains are apparent from the PAN image in Figure 3(a), but we can recognize only the overall pattern of features from the TIR image in Figure 3(b). As seen in the PAN image (Figure 3(a)), most mountains, rivers, and foreshores have relatively lower reflectance values, and most paddy fields are brighter than mountains. There are two targets that are brightest: a greenhouse and a vacant lot covered with cement. As for the TIR image, paddy fields are much brighter than mountains and rivers (Figure 3(b)). The brightest spot in the center of the studied area is Suncheon's water treatment plant (Figure 4). It should be noted that some features show different greyscales in PAN and TIR images. For example, roads covered with different cement and asphalt materials are represented differently in greyscale in the PAN and TIR images because the TIR image is related to surface emittance, namely, surface temperature (Figure 4). Thus, fusion must be carefully performed in order to maintain the emission properties of the ground surface and to allow interpretation of the spatial variation of surface features.

3.2. Objective Evaluation Metrics. The quantitative evaluation of different fusion images is not easy, because the reference temperature image, as a ground truth, does not exist in practice. Although various quality indices have been proposed to evaluate the image fusion performance, none of them is more plausible than the others [9, 24]. Thus, a few metrics are assessed for the fused image quality by evaluating the source images and the fused image. In this work, ten typical metrics are briefly introduced and employed to compare quantitatively the performances of the fusion methods.

(1) The pixel intensity mean (PIM) ($\overline{F}$) measures an index of overall pixel values and is given by $\overline{F} = \sum_{i=1}^{m}\sum_{j=1}^{n} f(i,j)/mn$, where $f(i,j)$ is the pixel value at (i,j) and the image size is $m \times n$. Because we process a thermal image, it is important to keep PIM as close as possible to the original thermal image.

(2) The average gradient (AG) measures the degree of clarity and sharpness using a high pass filter and is given by $\mathrm{AG} = \sum_i \sum_j ((f(i,j) - f(i+1,j))^2 + (f(i,j) - f(i,j+1))^2)^{0.5} f(i,j)/mn$.

(3) Entropy (E) estimates the amount of information present in the image and is given by $E = -\sum_{k=0}^{L-1} p_k \log_2(p_k)$, where p_k is the probability of the intensity value k in an L gray level image. An image with high information content will have high entropy, resulting in better fusion quality.

(4) Mutual information (MI) quantifies the overall mutual information transferred to the fused image from the source images. MI can be defined as $\mathrm{MI} = \mathrm{MI}_{AF} + \mathrm{MI}_{BF}$, where $\mathrm{MI}_{AF} = \sum_k \sum_l p_{A,F}(k,l)\log_2(p_{A,F}(k,l)/p_A(k)p_F(l))$ is the mutual information between the source image A and the fused image F, and $\mathrm{MI}_{BF} = \sum_k \sum_l p_{B,F}(k,l)\log_2(p_{B,F}(k,l)/p_B(k)p_F(l))$ is the mutual information between the source image B and the fused image F.

(5) The correlation coefficient (CC) indicates the degree of correlation between the fused image and the source images and is given by $\mathrm{CC} = (r_{AF} + r_{BF})/2$, where

$$r_{AF} = \frac{\sum_i \sum_j \left(a(i,j) - \overline{A}\right)\left(f(i,j) - \overline{F}\right)}{\sqrt{\left(\sum_i \sum_j \left(a(i,j) - \overline{A}\right)^2\right)\left(\sum_i \sum_j \left(f(i,j) - \overline{F}\right)^2\right)}},$$
$$r_{BF} = \frac{\sum_i \sum_j \left(b(i,j) - \overline{B}\right)\left(f(i,j) - \overline{F}\right)}{\sqrt{\left(\sum_i \sum_j \left(b(i,j) - \overline{B}\right)^2\right)\left(\sum_i \sum_j \left(f(i,j) - \overline{F}\right)^2\right)}}. \quad (8)$$

(6) The spatial frequency (SF) measures the overall information (activity) level on the blocks of an image and is computed as $\mathrm{SF} = \sqrt{\mathrm{RF}^2 + \mathrm{CF}^2}$, where row frequency $\mathrm{RF} = \sqrt{\sum_i \sum_j (f(i,j) - f(i,j-1))^2/mn}$ and column frequency $\mathrm{CF} = \sqrt{\sum_i \sum_j (f(i,j) - f(i-1,j))^2/mn}$. Larger spatial frequency represents better fusion quality.

(7) The total fusion performance $Q^{AB/F}$, fusion loss $L^{AB/F}$, and fusion artifacts $N^{AB/F}$ assess fusion by gradient information transfer, indicating that their sum should be equal to unity [25]. $Q^{AB/F} = 1$ indicates "ideal fusion" with no loss

$$Q^{AB/F} + L^{AB/F} + N^{AB/F} = 1. \quad (9)$$

(8) The sum of the correlations of differences (SCD) is a quality metric that makes use of the sum of correlation values as a quality measure of the fused images [24]. The difference images (D_1 and D_2) are the difference between the fused

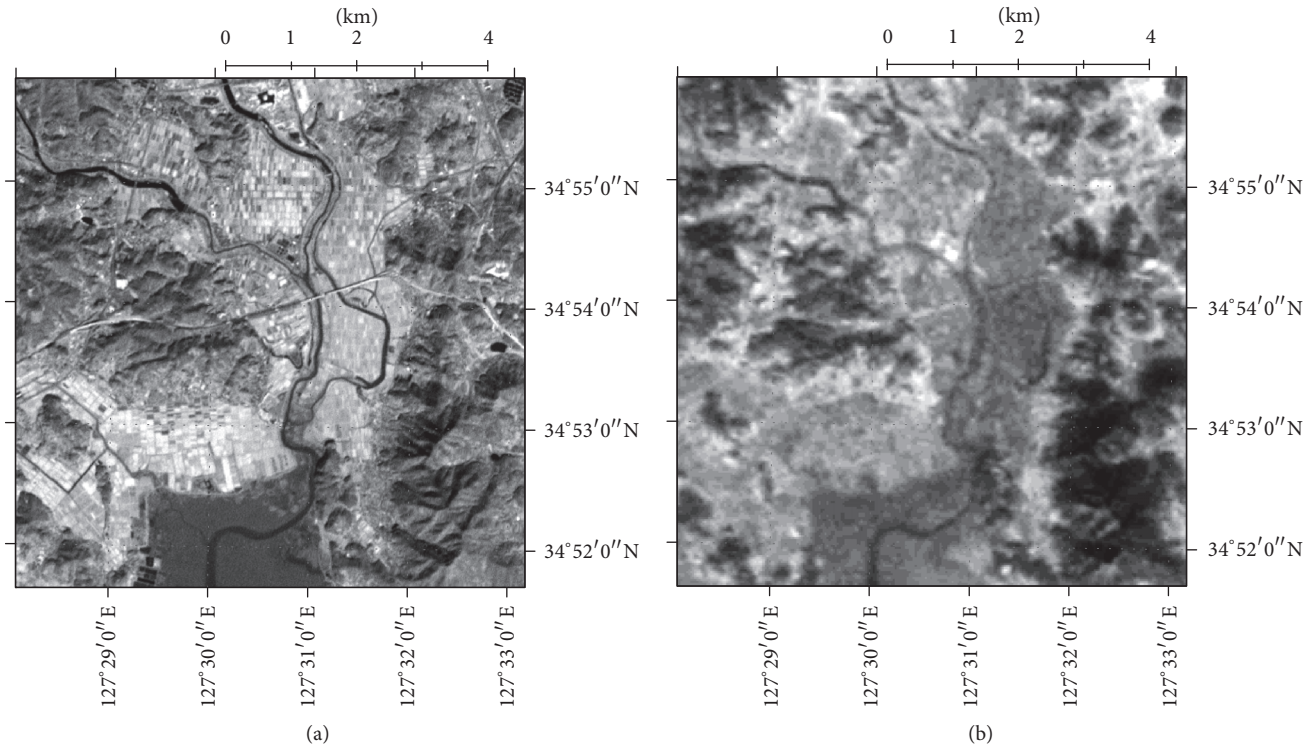

Figure 3: (a) PAN and (b) TIR images from Landsat 7 in the studied area.

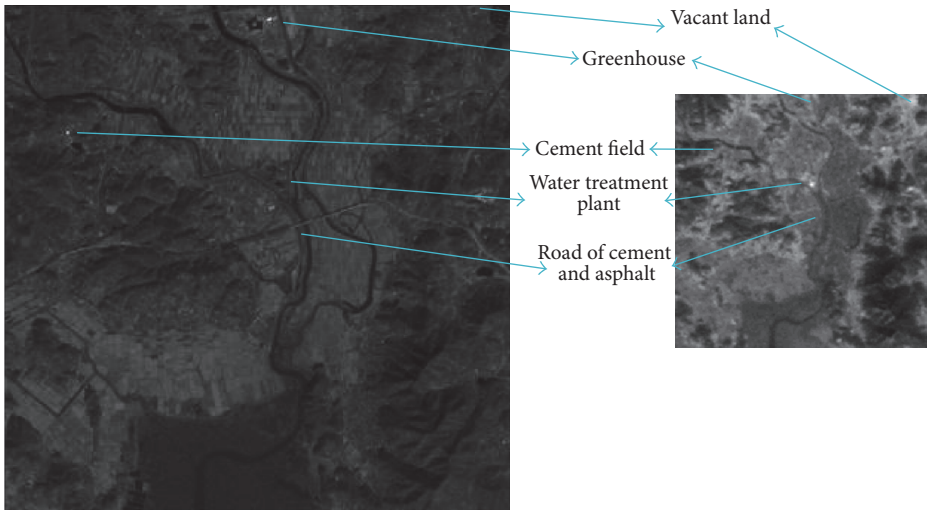

Figure 4: Region of interest for visual assessment.

image and the input images (A and B). It is formulated as follows:

$$\mathrm{SCD} = r\left(D_1, A\right) + r\left(D_2, B\right), \tag{10}$$

where $r(\cdot)$ is a function that calculates the correlations between A and D_1 and B and D_2.

(9) The average thermal energy deviation (AVGD) is used because the fusion method is based on thermal radiation. This parameter evaluates the deviation of thermal energy between the synthesized image and the original IR image [9].

(10) The universal image quality index (QI) was initially proposed as a universal measure of image quality achieved by modeling the structural distortion [26], but here we use it as an index of image similarity. The closer the QI to 1, the more similar the two images being compared.

For each of the ten metrics, a larger value generally indicates a better fused result except for $L^{AB/F}$, $N^{AB/F}$, and

Table 2: Visual assessment of the CBF, MW, DWT, OSF, and SRT methods.

Metric	Vacant land	Greenhouse	Cement field	Water treatment plant	Cement and asphalt road
CBF	X	X	X	X	X
MW	O	X	X	O	X
DWT	O	X	X	O	X
OSF	O	O	O	O	X
SRT-10-40	O	O	O	O	O

Table 3: Objective assessment of the CBF, MW, DWT, OSF, and SRT methods.

Metric	PIM	AG	E	MI	CC	SF	$Q^{AB/F}$	$L^{AB/F}$	$N^{AB/F}$	SCD	AVGD	UIQI
CBF	0.406	**4.142**	5.263	**3.019**	0.748	**4.933**	**0.986**	**0.010**	0.003	0.775	298.120	0.0753
MW	**1.000**	2.948	3.951	1.378	0.710	3.531	0.266	0.731	0.003	−0.025	4.035	0.3524
DWT	**1.000**	2.002	4.036	1.469	0.761	2.411	0.595	0.405	**0.000**	0.230	5.789	0.3370
OSF	0.387	3.916	**5.369**	1.786	**0.781**	4.641	0.880	0.104	0.017	**1.181**	307.297	0.1726
SRT-10-40	**1.000**	0.678	3.692	2.476	0.756	0.793	0.057	0.943	**0.000**	−0.287	**2.002**	**0.8077**

AVGD. To guarantee the objectivity of evaluation results, all the parameters in the above metrics are set to the default values reported in the related publications.

3.3. Investigation of Sampling and Patch Sizes. In this subsection, the effect of the sampling level and the dictionary patch size is studied for the optimal SRT fusion method. The low- and high-resolution dictionaries used in the sparse model are constructed and randomly sampled from the Landsat test image. The dictionary size is set to sampling levels 1/5, 1/10, 1/15, 1/20, 1/25, and 1/30. The local image patch sizes are selected to 20×20, 30×30, 40×40, 50×50, and 60×60 considering the computation time.

For convenience, a fusion method under the proposed framework, using a certain SRT, is denoted as SR-L-W. For example, SR-5-30 represents the fusion method using SRT with a 1/5 sampling level and 30×30 image patch dictionary. The error tolerance for the termination of the OMP algorithm is set to $1e-4$ and the OMP iteration number is fixed at 150. The step length of the sliding window in the patch tiling process is set to one.

We can see that the objective assessment results of the SRT methods according to various parameters suffer patch size effects when the sampling ratio is larger than 1/30 while the computation time increases with the size of the sampling data and patches (Figure 5). Therefore, we use SR-10-40 fusion for comparison with other popular fusion methods because it is desirable to use a patch size greater than 40 in this experiment.

3.4. Fused Results. In this subsection, four fusion algorithms, CBF, MW, OSF, and DWT [17], are used to illustrate the advantages of the proposed fusion framework. The principle of image fusion using DWT is to merge the wavelet decompositions of the two original images using fusion methods applied to approximation coefficients and detail coefficients. TIR images were used for approximation and their average images were used for detail. MW is a multiwavelet image fusion algorithm for extracting fine textural features from PAN images and superimposing them onto the TIR image.

First, for each specific method, the effectiveness of the proposed method is verified using the above objective fusion metrics, and the impact of the sampling level of the dictionary is studied. We then make an overall comparison in terms of both objective assessment and subjective visual quality. All the fusion methods in this work were implemented in MATLAB on a computer with a 3.4 GHz CPU and 32 GB of RAM.

Table 2 lists the visual assessments of the fusion methods for different regions in Figure 4. The proposed SRT method shows pixel values similar to those in the TIR images in all regions (Figure 6). The OSF method shows similar pixel values except for cement and asphalt roads. In particular, we cannot see regions of similar pixel values with CBF fusion. This is mainly because the maintenance of TIR properties in the previous method is neglected. The SRT method involves a similar range to that of the original TIR image, but other methods do not.

Quantitative analysis of five image fusion methods is shown in Table 3. The values in each column labeled in bold indicate the best performance among all the methods. The PIM of the CBF and OSF fused images were considerably smaller than those of the original TIR image, suggesting that the fusion process did not maintain physical properties from TIR sources. The PIM and range in the SRT method were preserved. The CBF had the best value in terms of AG, MI, SF, $Q^{AB/F}$, and $L^{AB/F}$. The OSF result has the best values in terms of E, CC, and SCD. Otherwise, the SRT method achieved the best values in terms of $N^{AB/F}$, UIQI, and AVGD. AG and SF reflect the local intensity variation. PAN has a high AG and SF value, and TIR has a low AG and SF value. Although the SRT method has a low AG and SF value, it may be considered

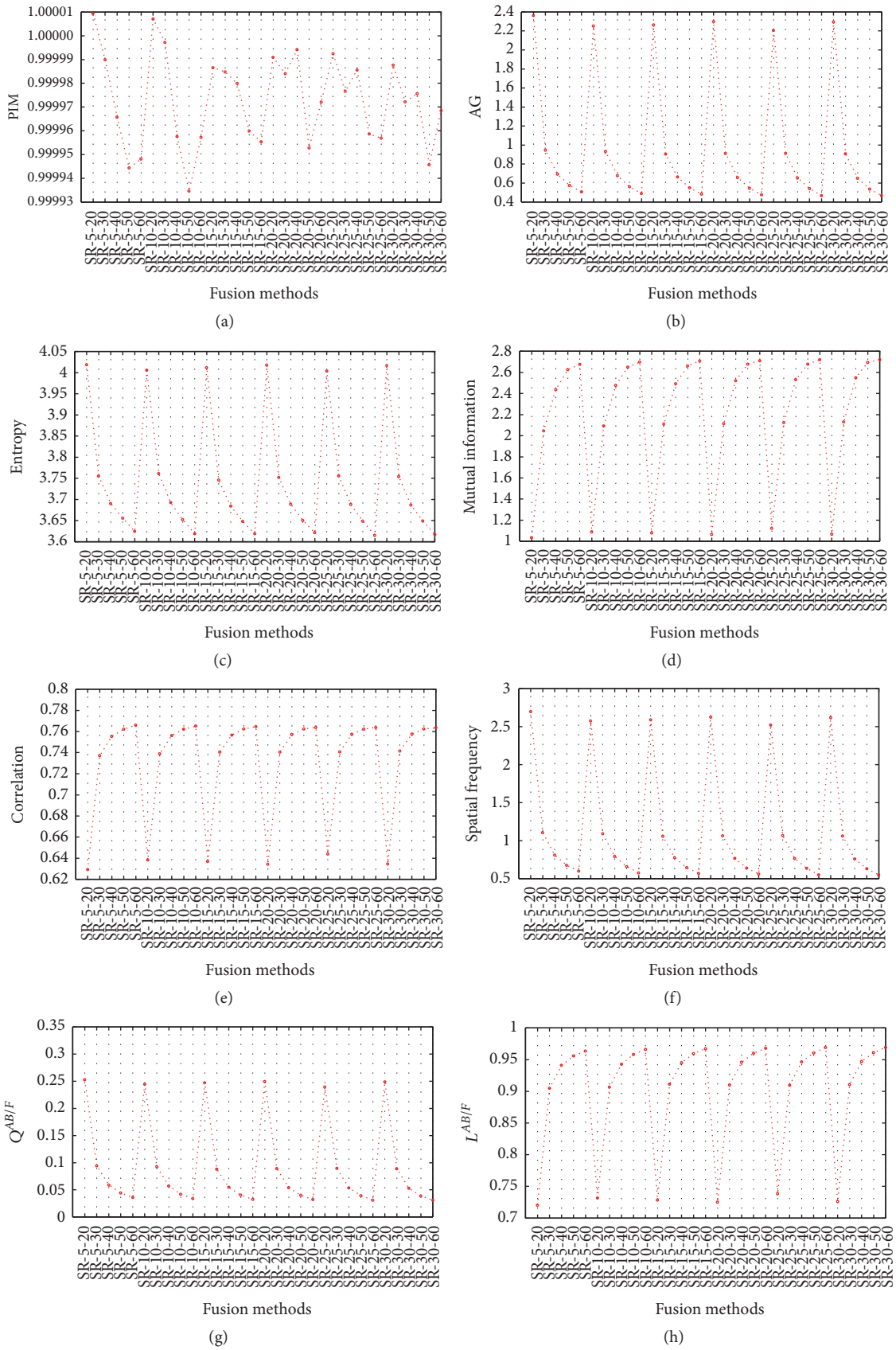

Figure 5: Continued.

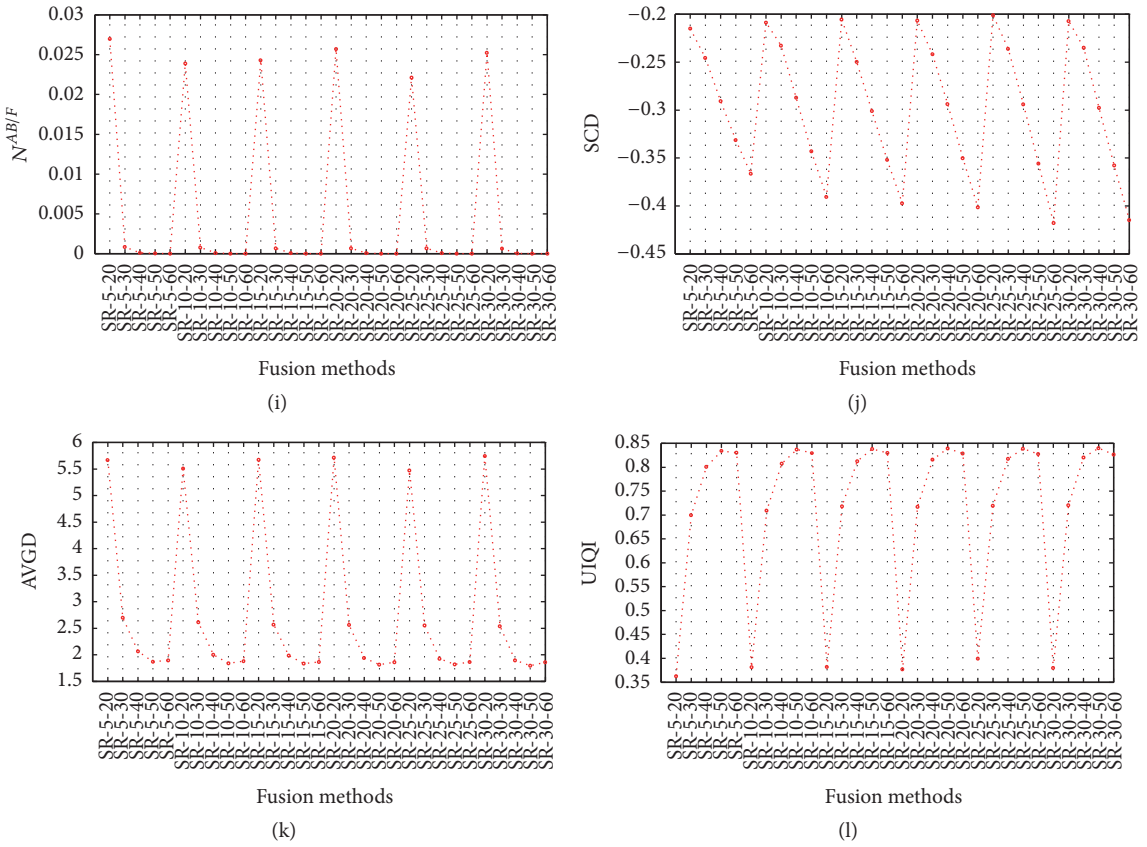

Figure 5: Objective assessment of SRT methods depending on sampling level and patch size. Red circles represent the proposed SRT metric values depending on the various parameter values.

to be relatively less affected by PAN image. The advantage of the SRT method over other methods is very clear in terms of minimal artifacts and less deviation from the original TIR images and, in terms of visual and some quantitative aspects. Our method obtains more meaningful information from TIR images, without physical correction of the fused images, while abandoning less relevant information from PAN images.

4. Conclusion

In this paper, we present an SR-based image fusion framework for Landsat thermal images. Many previously proposed image fusion methods are capable of synthesizing multiple sensor images and producing good visual effects, but they do not retain the thermal properties of IR images. Our method is designed to preserve surface-temperature-related information as well as spatial resolution. We applied a sparse-representation-based fusion method for estimating high-resolution thermal images. We tested the impact of sampling level and patch size for SRT parameter adjustment. Finally, our fusion results were compared with four other fusion methods' results and analyzed using visual and objective assessments. The experimental results demonstrated that the proposed method improves spatial properties of TIR images and preserves their spectral consistency. Therefore, the proposed method can contribute to the estimation of high-resolution land surface temperature for environmental analysis.

Although this work shows a new approach toward thermal image fusion, the proposed method has some defects. First, because it is difficult to distinguish each feature in the mountainous and agricultural field of the study site, various sites have to be tested through additional experiments. Second, the optimal parameter for the SRT fusion has not been determined. Finally, it is necessary to evaluate a fused image with a high-resolution thermal reference using a thermal drone for more accurate evaluation. For this, further research will be carried out.

Competing Interests

The authors declare that there is no conflict of interests regarding the publication of this paper.

Acknowledgments

This study was financially supported by an NRF grant (2016R1D1A3B01007236).

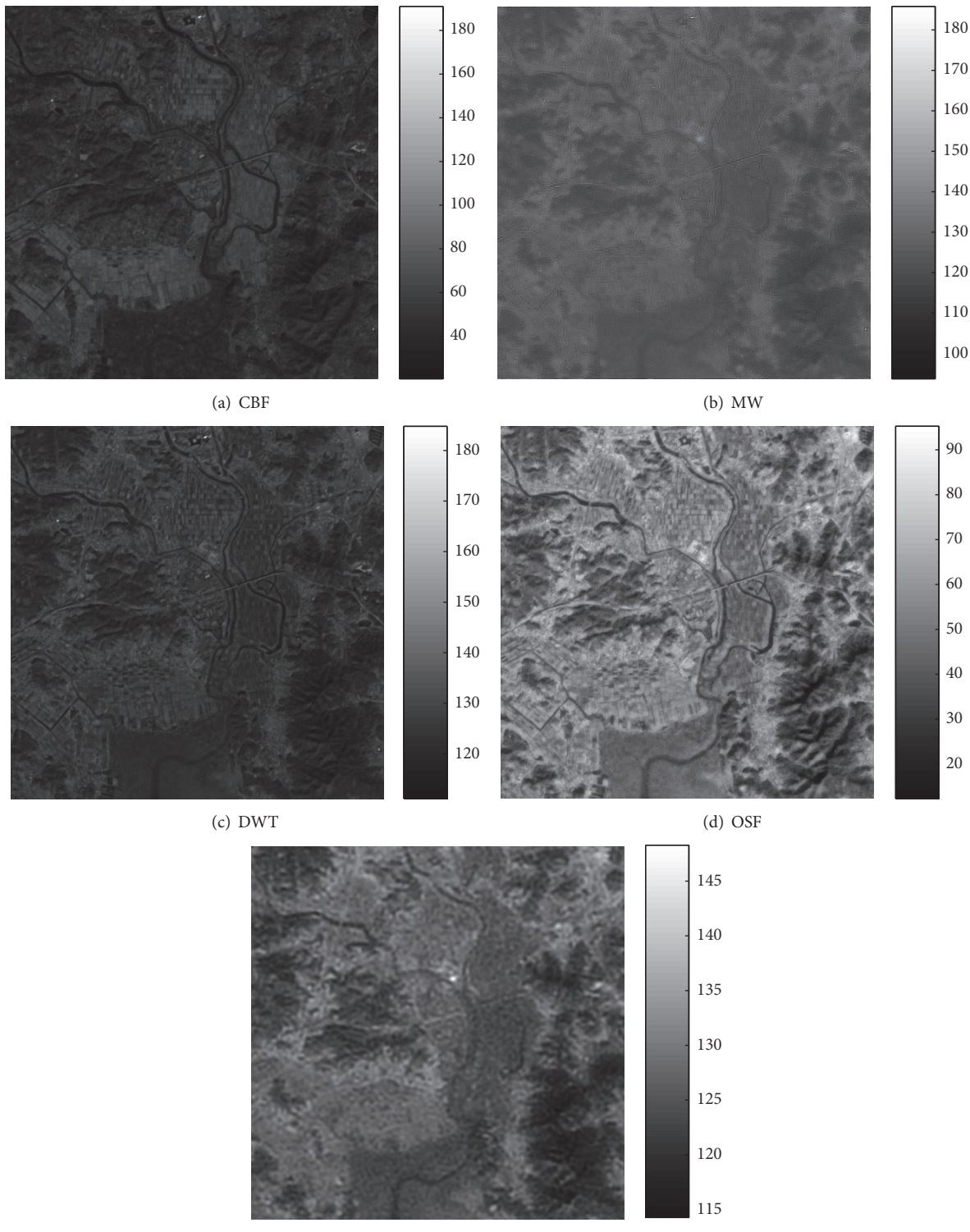

(a) CBF (b) MW

(c) DWT (d) OSF

(e) SRT-10-40

Figure 6: Landsat 7 thermal image fusion.

References

[1] S. Didari, H. Norouzi, S. Zand-Parsa, and R. Khanbilvardi, "Estimation of daily minimum land surface air temperature using MODIS data in southern Iran," *Theoretical and Applied Climatology*, pp. 1–13, 2016.

[2] L. Hu, A. J. Monaghan, J. A. Voogt, and M. J. Barlage, "A first satellite-based observational assessment of urban thermal anisotropy," *Remote Sensing of Environment*, vol. 181, pp. 111–121, 2016.

[3] M. Akhoondzadeh and M. R. Saradjian, "Comparison of land surface temperature mapping using MODIS and ASTER images in semi-arid area," in *Proceedings of the International Archives of the Photogrammetry, Remote Sensing and Spatial Information Sciences*, vol. 37, pp. 873–876, Beijing, China, 2008.

[4] A. Rajeshwari and N. D. Mani, "Estimation of land surface temperature of Dindigul district using Landsat 8 data," *International Journal of Research in Engineering and Technology*, vol. 3, no. 5, pp. 122–126, 2014.

[5] T. M. Lillesand, R. W. Kiefer, and J. W. Chipman, *Remote Sensing and Image Interpretation*, John Wiley & Sons, New York, NY, USA, 7th edition, 2015.

[6] Q. Weng and D. A. Quattrochi, "Thermal remote sensing of urban areas: an introduction to the special issue," *Remote Sensing of Environment*, vol. 104, no. 2, pp. 119–122, 2006.

[7] J. R. Jensen, *Remote Sensing of the Environment: An Earth Resource Perspective*, Prentice Hall, Upper Saddle River, NJ, USA, 2nd edition, 2006.

[8] X. Huang, R. Netravali, H. Man, and V. Lawrence, "Multi-sensor fusion of infrared and electro-optic signals for high resolution night images," *Sensors*, vol. 12, no. 8, pp. 10326–10338, 2012.

[9] L. Han, L. Shi, Y. Yang, and D. Song, "Thermal physical property-based fusion of geostationary meteorological satellite visible and infrared channel images," *Sensors*, vol. 14, no. 6, pp. 10187–10202, 2014.

[10] H.-S. Jung and S.-W. Park, "Multi-sensor fusion of landsat 8 thermal infrared (TIR) and panchromatic (PAN) images," *Sensors*, vol. 14, no. 12, pp. 24425–24440, 2014.

[11] W. Huang, L. Xiao, H. Liu, and Z. Wei, "Hyperspectral imagery super-resolution by compressive sensing inspired dictionary learning and spatial-spectral regularization," *Sensors*, vol. 15, no. 1, pp. 2041–2058, 2015.

[12] B. Yang and S. Li, "Multifocus image fusion and restoration with sparse representation," *IEEE Transactions on Instrumentation and Measurement*, vol. 59, no. 4, pp. 884–892, 2010.

[13] J. Yang, J. Wright, T. S. Huang, and Y. Ma, "Image super-resolution via sparse representation," *IEEE Transactions on Image Processing*, vol. 19, no. 11, pp. 2861–2873, 2010.

[14] C. Jiang, H. Zhang, H. Shen, and L. Zhang, "A practical compressed sensing-based pan-sharpening method," *IEEE Geoscience and Remote Sensing Letters*, vol. 9, no. 4, pp. 629–633, 2012.

[15] Y. Liu, S. Liu, and Z. Wang, "A general framework for image fusion based on multi-scale transform and sparse representation," *Information Fusion*, vol. 24, pp. 147–164, 2015.

[16] B. K. Shreyamsha Kumar, "Image fusion based on pixel significance using cross bilateral filter," *Signal, Image and Video Processing*, vol. 9, no. 5, pp. 1193–1204, 2015.

[17] M. Misiti, Y. Misiti, G. Oppenheim, and J. M. Poggi, *Wavelet Toolbox User's Guide*, The MathWorks, Natick, Mass, USA, 2016.

[18] R. G. Baraniuk, V. Cevher, M. F. Duarte, and C. Hegde, "Model-based compressive sensing," *IEEE Transactions on Information Theory*, vol. 56, no. 4, pp. 1982–2001, 2010.

[19] M. B. Wakin, J. N. Laska, M. F. Duarte et al., "Compressive imaging for video representation and coding," in *Proceedings of the 25th PCS: Picture Coding Symposium (PCS '06)*, 1306, 1289 pages, Beijing, China, April 2006.

[20] J. A. Tropp and A. C. Gilbert, "Signal recovery from random measurements via orthogonal matching pursuit," *IEEE Transactions on Information Theory*, vol. 53, no. 12, pp. 4655–4666, 2007.

[21] D. Glasner, S. Bagon, and M. Irani, "Super-resolution from a single image," in *Proceedings of the IEEE 12th International Conference on Computer Vision (ICCV '09)*, pp. 349–356, IEEE, Kyoto, Japan, October 2009.

[22] W. Wang, L. Jiao, and S. Yang, "Fusion of multispectral and panchromatic images via sparse representation and local autoregressive model," *Information Fusion*, vol. 20, no. 1, pp. 73–87, 2014.

[23] M. R. Vicinanza, R. Restaino, G. Vivone, M. Dalla Mura, and J. Chanussot, "A pansharpening method based on the sparse representation of injected details," *IEEE Geoscience and Remote Sensing Letters*, vol. 12, no. 1, pp. 180–184, 2015.

[24] B. K. Shreyamsha Kumar, "Multifocus and multispectral image fusion based on pixel significance using discrete cosine harmonic wavelet transform," *Signal, Image and Video Processing*, vol. 7, no. 6, pp. 1125–1143, 2013.

[25] V. Aslantas and E. Bendes, "A new image quality metric for image fusion: the sum of the correlations of differences," *AEU—International Journal of Electronics and Communications*, vol. 69, no. 12, pp. 1890–1896, 2015.

[26] Z. Wang and A. C. Bovik, "A universal image quality index," *IEEE Signal Processing Letters*, vol. 9, no. 3, pp. 81–84, 2002.

Hindawi Publishing Corporation
Mathematical Problems in Engineering
Volume 2016, Article ID 9850890, 8 pages
http://dx.doi.org/10.1155/2016/9850890

Research Article

Evaluating Urbanization and Spatial-Temporal Pattern Using the DMSP/OLS Nighttime Light Data: A Case Study in Zhejiang Province

Pengfei Xu,[1] Pingbin Jin,[1] Yangfan Yang,[1] and Quan Wang[2]

[1]*Institute of Urban and Regional Development, Zhejiang University, Hangzhou 310027, China*
[2]*Faculty of Agriculture, Shizuoka University, Shizuoka, Japan*

Correspondence should be addressed to Pingbin Jin; chshs@zju.edu.cn

Received 4 September 2016; Accepted 24 October 2016

Academic Editor: Hasi Bagan

The application of DMSP/OLS nighttime light data provides an effective measure for characterizing urbanization and its spatial-temporal changes. Combined with the social economic statistics and calibrated nighttime data, the nighttime light imagery of Zhejiang province was fully intercalibrated during the period 1992–2013. The backgrounds were explained and the model of region light index (RLI) was built to make further research. The methods of mutation detection, regression analysis, and spatial analysis were adopted in this study. The results show that the urbanization progress of Zhejiang experienced a transformation from rapid development to steady improvement and was accompanied by a changing direction of urban expansion from coastal to inland areas from 2000. Further research indicated that Zhejiang province possessed a relative high level of urbanization, where a spatial pattern of urbanization with one center and four axes was initially formed. It is a novel attempt to investigate the urbanization of Zhejiang province on the basis of the DMSP/OLS night-lighting data, which may provide a significant guideline for the urban planning and development.

1. Introduction

Urbanization is a phenomenon that involves changes in land cover, the economy, and demographics; it is a shift from traditional agricultural society to a modern society which focuses on manufacturing industries and services. There was sluggish development in China before the policy of reform and openness due to various factors at home and abroad. However, the progress of urbanization in China accelerated from 1978; the urbanization rate in mainland China has risen from 26% in 1990 to 52.6% by the end of 2012 according to the National Bureau of Statistics of China. Urban areas concentrate people, economic activities, and the built environment; urbanization will also have a profound effect on the geography pattern [1–3].

Methods of qualitative and quantitative analyses were adopted by many researches when it came to urbanization. Nevertheless, there were many shortages on timeliness and reliability for the reason of uncertainty and lag of statistical data [4, 5]. Meanwhile, only a few researches have been made from the perspective of spatial and temporal patterns due to the lack of spatial information. Adopting remote sensing data can effectively avoid the above problems. Some scholars used remote sensing images of different resolutions to conduct urbanization-related researches and achieved a certain degree of success. High spatial resolution remote sensing data such as IKONOS, SPOT HRV, and Quick Bird images can reflect the details of the study regions but they come with high cost and complicated data processing procedure; due to the complexity of the ground objects that cause spectral differences, together with the limited resolution of the data, it is difficult to use lower resolution satellites like NOAA/AVHRR, EOS/MODIS, and Landsat TM/ETM+ images to identify the features of ground objects accurately, which renders the

identification process more complicated [6–9]. This study highlights the utility of the Defense Meteorological Satellite Program/Operational Linescan System (DMSP/OLS) nighttime light data to analyze the urbanization in the selected regions.

The US Air Force Defense Meteorological Satellite Program's Operational Linescan System was designed to collect global clouds illuminated by moonlight. Different from other remote sensing satellites, the DMSP/OLS instrument can detect nocturnal artificial lighting in clear night conditions without moonlight owing to its low-light imaging capability. OLS has a wide view over the earth surface with a 3000 km swatch width and a spatial resolution of 2.7 km. The DMSP/OLS can distinguish other dark areas by capturing artificial lighting present on the earth's surface, such as that generated by human settlements, fishing boats, fires, and gas flares. This makes it convenient to analyze human activity and urban change from the perspective of space.

Since the 1980s, DMSP/OLS nighttime light data have gained widespread attention with related researches focusing on fields including technical methods exploration, population density estimation, energy consumption, land extraction, and urban sprawl monitoring [10–15]. Croft extracted the urban areas with the data of DMSP/OLS nighttime light for the first time in 1978 [16]. After this, more and more researches were made on a global and regional scale, but these researches were restricted by the influence of clouds and unstable light. Henderson et al. [17] extracted cities with different economic levels like Beijing, San Francisco, and so on by the method of threshold value and after comparing with that extracted from Landsat TM images, they drew the conclusion that DMSP/OLS nighttime light can be an effective data source to detect urbanization and urban areas. Chunyang et al. [18] found that DMSP/OLS nighttime light can reflect urbanization progress in China by rebuilding urbanization of mainland in China with nighttime data and related statistic data. Similar conclusion was also drawn by Liu et al. [19]. Yi et al. analyzed the land use pattern in northeast China by establishing the unit circle urbanization evaluation model and finally found that the Urban Light Index had a strong correlation with urban built-up areas and regional GDP [20]. The result indicating a stepwise transition of nighttime light brightness during urban expansion was found by Ma et al. through the brightness gradient and neighborhood analysis method [21]. By combining DMSP/OLS nighttime light data and remote sensing data, and using appropriate data calibration process model, the existing studies, to some extent, have overcome the impact of saturation and overflow and meanwhile shown certain practical significance by their successful application in various fields of society, production, economy, security, and so forth.

This paper detects the urbanization of Zhejiang province in 1992–2013 from a geographic perspective using the methods of mutation detection and spatial analysis and builds the region light index (RLI) to explore the relationship between light and urbanization, as well as the spatial-temporal changes of different land use patterns.

2. Data Preparing

2.1. Data Source. Three types of data were used in the study of urbanization in Zhejiang province. The first type is nighttime stable light data from 1992 to 2013 in the Version 4 global DMSP/OLS nighttime lights series dataset. The data were obtained from the National Geophysical Data Center (NGDC) Website (http://www.ngdc.noaa.gov/dmsp/downloadV4composites.html) and include datasets from five different satellites: F10 (1992-1993), F12 (1994–1996), F14 (1997–2003), F16 (2004–2009), and F18 (2010–2013). Background noises were identified and replaced with the value of zero, and the DN values for lit pixels ranged from 1 to 63. To reduce the differences between sensors and improve comparability of nighttime lights data from different satellites, the individual composites had to be calibrated via an empirical procedure.

The second type of data is socioeconomic census data, including the nonagricultural population, proportion of secondary industry and tertiary industry, and Gross Domestic Product (GDP). These data were obtained from the Zhejiang Statistical Yearbook (1992–2014). The third type is the auxiliary data related to boundaries, especially the administrative boundaries of the province and cities within Zhejiang province, as well as the boundary of China.

2.2. Intercalibration. The nighttime light data of Zhejiang province during 1992–2013 is composed of images covering 22 years and related to 5 different satellites. There is no onbroad calibration on the OLS; the data we chose is lacking in continuity and comparability, so they cannot be used to extract urban areas directly in this study unless calibrated. In the literatures related to this topic, the NTL data was often calibrated with the method proposed by Christopher Elvidge by applying regression models [22]. Wu et al. also put forward an approach called invariant regions-method to calibrate NTL images; the global NTL imageries were calibrated using this method [23]. This research adopts the approach proposed by Wu to realize the intercalibration of NTL images of Zhejiang province.

We captured the NTL images from the global NTL graphics downloaded from the NGDC website based on the method named Region of Interest (RIO). Many studies treated urban areas with stable nighttime lights as reference regions, because the DMSP images in these areas have signal saturation. In this article, we chose the reference region with the process of False Color Compositing by overlaying images from different years. The false color composited image covering 1992, 2003, and 2013 is shown in Figure 1 and areas in white are definitely the urban area which has signal saturation. Satellite F14 in 1999 was used as the reference and the data from other satellites were adjusted to match the F14 1999 data range by using second-order polynomial regression:

$$\mathrm{DN}_{\mathrm{cal}} = a + b \times \mathrm{DN} + c \times \mathrm{DN}^2, \quad (1)$$

where $\mathrm{DN}_{\mathrm{cal}}$ is the adjusted DN and a, b, and c are coefficients.

The individual images were calibrated with (1) together with parameters in Table 1, and the influence of discontinuous

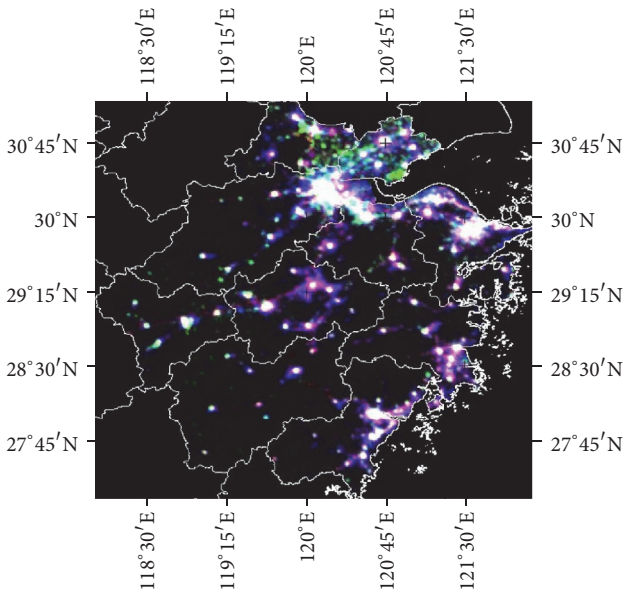

Figure 1: False color synthesis (1992: red; 2003: green; 2013: blue).

is eliminated in this way. The normalized conduction is also processed with

$$\mathrm{DN}_I = \frac{\left|X - \mathrm{DN}_{\min}\right|}{\mathrm{DN}_{\max} - \mathrm{DN}_{\min}}, \quad (2)$$

where DN_I is the value of pixels after normalization processing with the range between 0 and 1. $\mathrm{DN}_{\max}$ and $\mathrm{DN}_{\min}$ are the maximum and minimum values of normalized pixels. X is the DN value of each pixel.

3. Methods

The NTL data in this study were projected and resampled to a pixel size of 1 km, which means each pixel in the NTL image represents a region with an area of $1 * 1\,\mathrm{km}^2$. Each pixel is different in spatial attribution and has a DN value that equals the average brightness in the region. Meanwhile, the DN value in urban areas, especially the Central Business District (CBD), is higher than other regions, and the value decreases steadily when it comes to the edge of the city. Based on the above analysis, methods of Mutation Detection and Slop Calculation are adopted to extract urban and rural areas.

3.1. Mutation Detection. A few methods are available to extract urban information from NTL images, including an empirical thresholding technique, the thresholding technique based on Mutation Detection, and the statistics method with ancillary data. Of all these methods, the Mutation Detection is widely used because of its simplicity and reliability. Therefore, we used the Mutation Detection method to extract urban information in Zhejiang province.

Mutation Detection which was first proposed by Imhoff et al. is widely used to extract threshold of urban areas. In his theory, the changes in polygon perimeter along with the increase in threshold were compared. As the threshold rose, the polygons representing urban or lit areas shrank in size, while, at a certain point in the thresholding process, the urban polygons did not necessarily get smaller around their perimeter but began to break up internally. This point is the threshold of the urban area [24, 25].

The process of Mutation Detection is shown in Figure 2. The first image in Figure 1 is the original NTL image of the selected area. When increasing the threshold the extracted urban areas change from image 2 to image 8. As the threshold rose to 0.81, the urban polygons began to break up; this means the value of 0.81 is definitely the threshold of the urban area in the study region.

3.2. Slop Calculation. As mentioned above, the DN values decrease when the distance from core city increases, but the variation tendency differs in different land use patterns. DN values in urban and rural areas change less due to the relative homogeneity in these regions, while the transition area between rural and urban has a quite drastic DN change and the spectral distribution curve is quite different (Figure 3).

Figure 3(a) is the X and Y profile segmentation of the study area and Figure 3(b) shows the spectral distribution curve of the profile. The transition region was confirmed by the drastic changes of DN values between red lines in Figure 3(b); then we analyzed the slop of the transition region and found out that the critical point is between rural and transition region. Figure 4 was the result of the regional segmentation.

Table 1: Distribution table of regression coefficient.

Satellites	Year	a	b	c	R^2
F10	1992	0.5614	0.2072	−0.002	0.792
	1993	−0.0325	0.2507	−0.0026	0.931
F12	1994	−0.1848	0.1497	−0.0008	0.967
	1995	0.3613	0.0848	0.0001	0.961
	1996	−0.7925	0.164	−0.0008	0.953
F14	1997	0.1617	0.1719	−0.0013	0.938
	1998	0.217	0.1289	−0.0005	0.965
	1999	0	1	0	1
	2000	−0.1921	0.098	0.0001	0.935
	2001	1.1786	−0.0072	0.0015	0.92
	2002	3.9886	−0.1798	0.0034	0.799
	2003	1.8356	−0.0923	0.0013	0.777
F16	2004	2.0823	−0.1012	0.0014	0.778
	2005	1.9593	−0.0984	0.0014	0.82
	2006	3.4457	−0.1801	0.0024	0.748
	2007	5.2046	−0.2214	0.0024	0.875
	2008	5.035	−0.2227	0.0025	0.82
	2009	−3.5291	0.1392	−0.001	0.652
F18	2010	4.8877	−0.1703	0.0015	0.671
	2011	−1.764	0.042	−0.0002	0.72
	2012	4.9955	−0.2903	0.0037	0.881
	2013	1.5588	−0.0654	0.0006	0.877

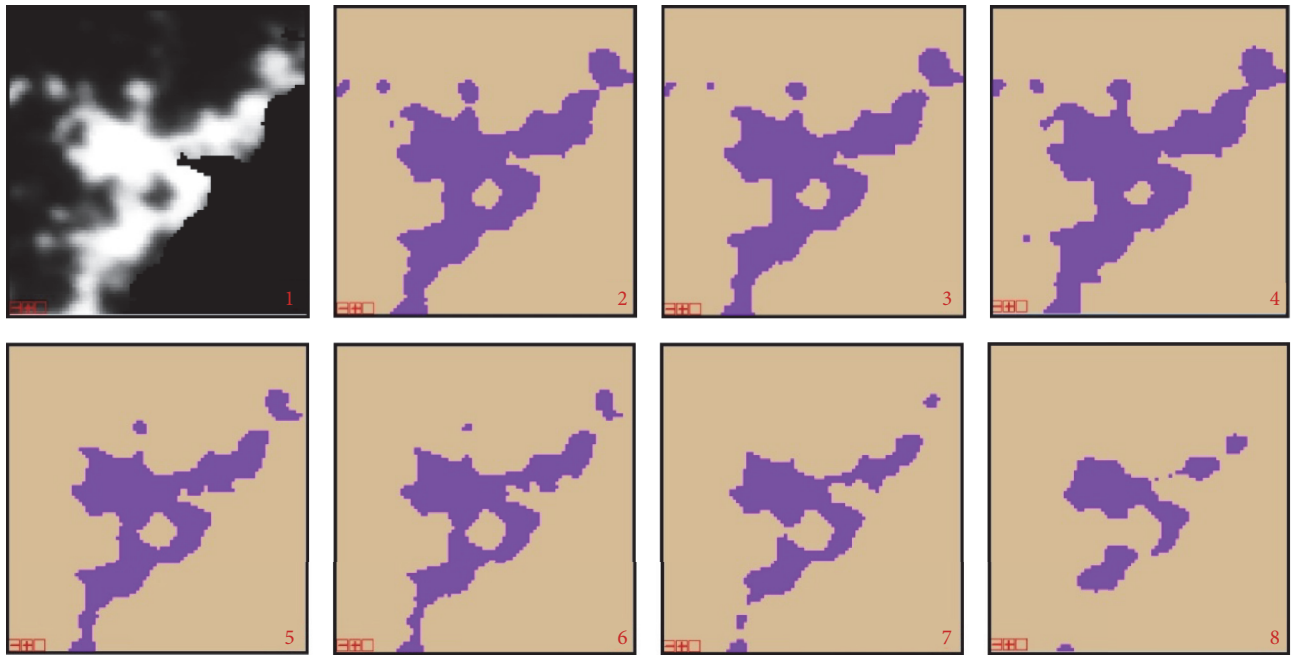

Figure 2: Images of mutation detection.

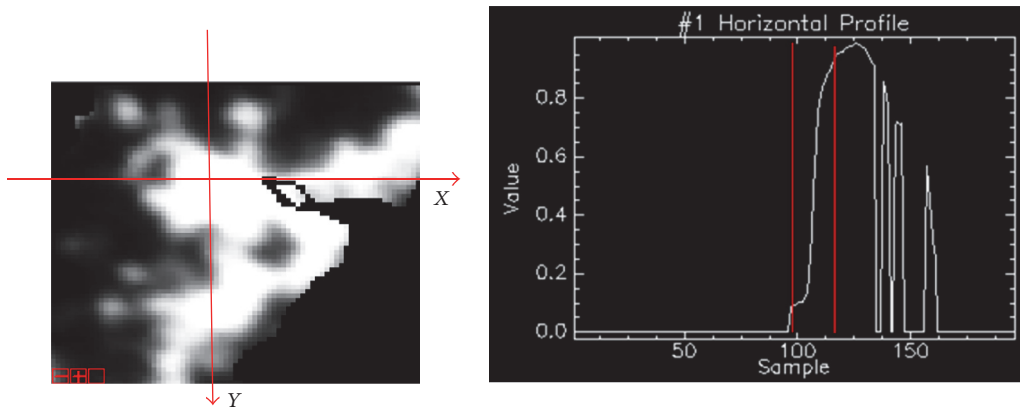

(a) (b)

Figure 3: (a) Images of profile segmentation and (b) spectral distribution curve.

3.3. The Region Light Index Model. The regions of rural, urban, and transition areas were extracted using methods of Mutation Detection and Slop Calculation. The study area composites pixels with different DN values; most pixels have quite low DN values which refer to farmland and forest [26]. In order to increase the accuracy and reliability of the study, pixels with DN values below 0.1 were abandoned for this research.

There are quite a lot of models to evaluate nighttime light features of cities, such as Urban Light Index (ULI) and Total Light Index (TLI), while few of these models focus on the effect of regional characteristics and land use patterns. The region light index (RLI) model provides an effective method to assess NTL intensity together with DN values and regional characteristics by

$$\mathrm{RLI} = \frac{S_u \times N_u \times a}{S} + \frac{S_r \times N_r \times b}{S} + \frac{S_t \times N_t \times c}{S}, \quad (3)$$

where S_u, S_r, and S_t are the areas of urban, rural, and transition areas; N_u, N_r, and N_t are pixels numbers of different land use patterns; a, b, and c refer to the average DN values of each region; S means the total area of the study region.

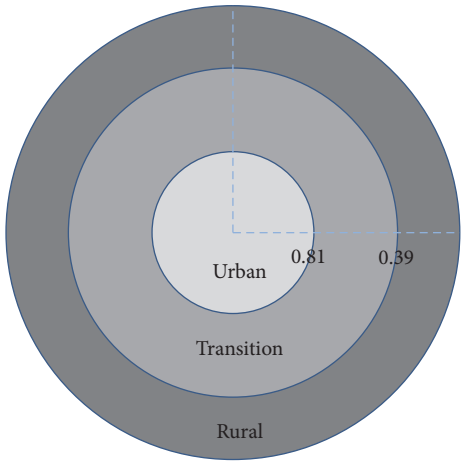

Figure 4: Result of region segmentation.

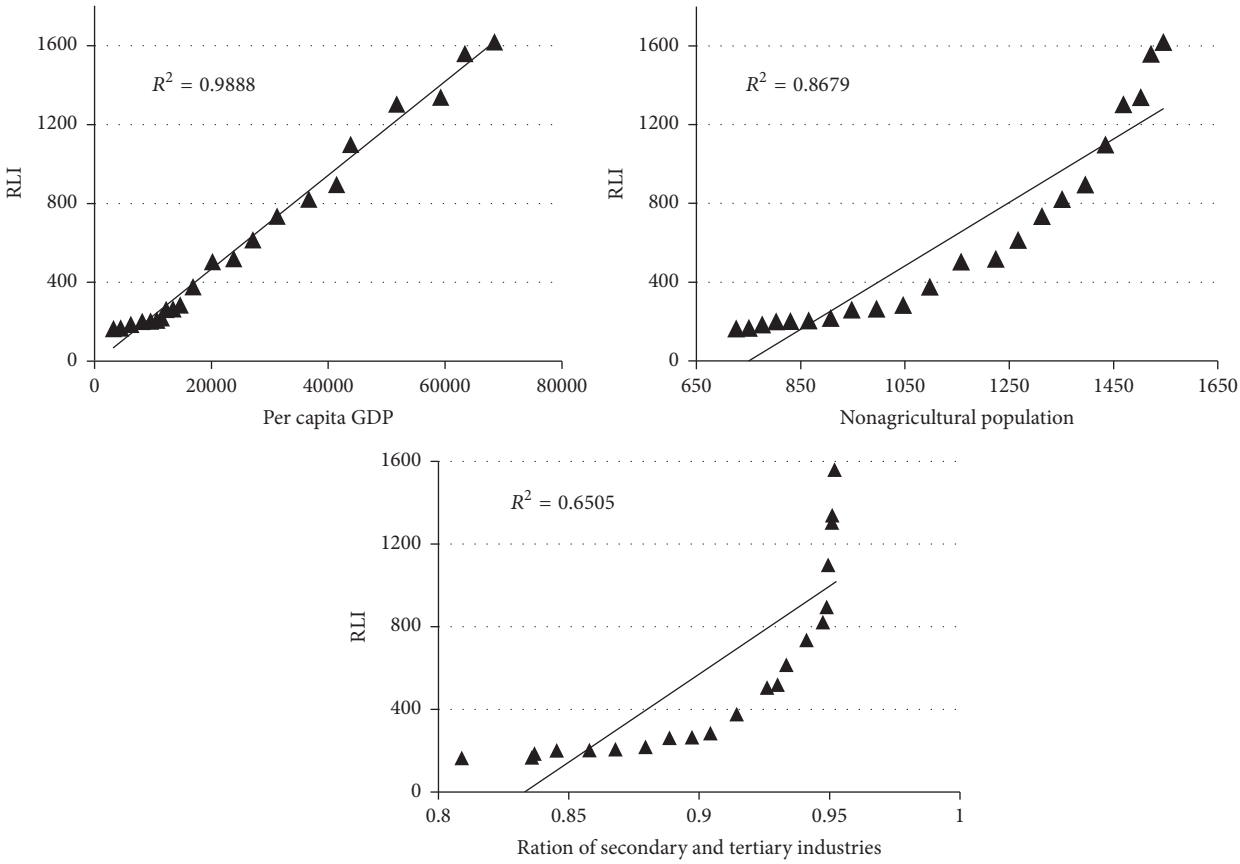

Figure 5: Correlations between RLI and urbanization indicators.

4. Result

4.1. The RLI and Urbanization. Urbanization is a complicated phenomenon related to demographic, economic, and land use changes. The distinguishable index of urbanization is concluded by two methods: one is the method of single or main index and the other is the compound indicator method.

The method of compound index is adopted to measure the relationship between RLI and urbanization in this study: indexes of per capita GDP, ration of secondary and tertiary industries, and nonagricultural population have also been selected in order to make further research [27].

The relationship between region light index (RLI) and urbanization level is measured based on the DMSP/OLS nighttime light data and ancillary economic statistical data with the method of regression analysis; the results are as in Figure 5.

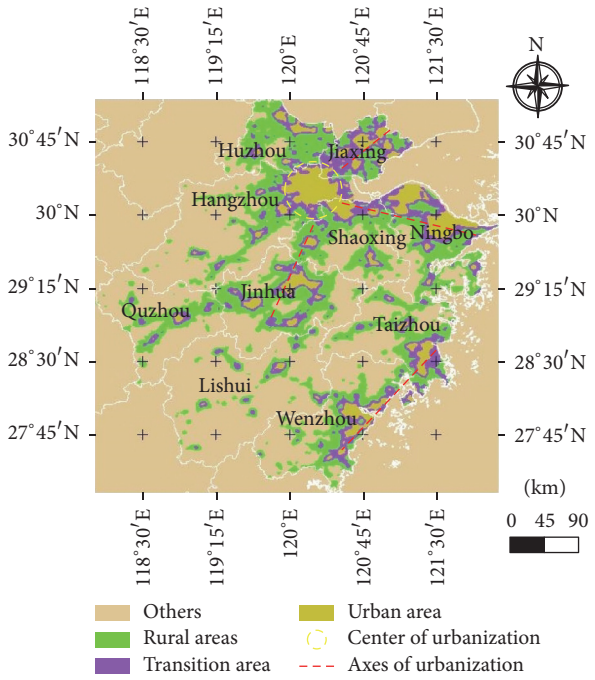

Figure 6: Spatial pattern of urbanization in Zhejiang province.

The regression analysis shows a strong positive relationship between RLI and indicators of urbanization level with high coefficients. Based on the analysis above, the model of region light index (RLI) can reflect urbanization level in regional scale precisely and can be used to measure the urbanization process in Zhejiang province.

4.2. Urbanization Pattern in Zhejiang Province. Figure 6 shows the spatial pattern of urbanization based on the latest DMSP/OLS NTL data of Zhejiang province. The urbanization pattern of "center-axes" in Zhejiang consists of the center of Hangzhou, axes of Hangzhou to Ningbo, Hangzhou to Jinhua (Lishui), Hangzhou to Jiaxing, and Wenzhou to Taizhou. With difference in economical level and regional geography, the brightness of NTL and urbanization levels vary from area to area. Based on the analysis of NTL images and new pattern of urbanization, it was found that areas around the Hangzhou Bay and near the coastal regions possess successional and brighter nighttime light, which means that the urbanization level in these areas is higher than other regions. Furthermore, the region brightness of NTL in Ningbo, Huzhou, Jiaxing, Hangzhou, and Jinhua in Figure 6 is much higher than other cities, as well as the urbanization level, which indicates that the urbanization process has expanded to inland from the coastal areas with changes of new patterns in geography.

4.3. Spatial and Temporal Variation of Urbanization in Zhejiang Province. The urban pattern in Zhejiang changed a lot in the process of urbanization, with agglomeration in urban cores and diffusion towards rural areas, as well as new spatial form in NTL images. Figure 7 shows the spatial and temporal change of urbanization pattern in Zhejiang province from 1992 to 2013 in selected years.

Table 2: Area statistic of RLI.

Year	Urban area	Transition area	Rural area	RLI
1992–1995	509.1549	2733.337	11057.4543	219.896
1996–1999	586.4639	2671.7617	11067.5625	213.8478
2000–2004	1397.9291	4529.9791	13241.7653	384.8646
2005–2008	2534.1677	8015.0679	16034.6284	743.3341
2009–2013	6143.4982	11962.9187	16772.6573	1384.89

Units: km^2.

There are 2 stages in the process of urbanization in Zhejiang province, the periods from 1992 to 2000 and 2000 to 2013. The urbanization area concentrated in the region of Hangzhou Bay which is located in the north of Zhejiang during the first stage, while, in the second stage, the urbanization level on the east coast and inland Zhejiang increased rapidly with the development of the economy and more and more metropolises appeared.

The direction of urban expansion also varies in different stage of urbanization. In the early urbanization period, the urban sprawls mainly focused on the horizontal direction, with more nonconstruction land converted into construction land. Nevertheless, the direction of urban sprawl transformed to vertical and more skyscrapers appeared when the urban area developed to a certain size, with the urban-land intensive utilization.

Table 2 is the data statistics of different areas based on the NTL data. As can be seen in the table, the areas of urban, transition area, and rural area increased from 1992 to 2013, especially the rural and transition areas. During the period of 2000–2008, the urban areas increased rapidly but the growth slowed down after that; this can be explained by the conversion of urban spatial expansion after the year 2000.

RLI can be used to reflect urbanization because of the strong relationship between RLI and indicators of urbanization. The RLI increases from 219.896 in the first stage (1992–1995) to 743.3341 in the fourth stage (2005–2008). However, the speed slowed down with an average value of 1384.89 in the fifth stage (2009–2013). On the strength of Table 2 and analysis above, the urbanization progress of Zhejiang has experienced a transformation from rapid development to steady improvement.

As can be seen in Table 2, the data statistics of rural area also increased a lot. This could have been caused by two different factors. Firstly, the pattern of rural area did not change in the process of urbanization, although there was migration movement from rural to urban areas. Secondly, rural development still exists along with urbanization.

5. Conclusion

DMSP/OLS data provide an accurate and comprehensive method to mirror urban growth, economic development, energy consumption, and so on. It also reduces the disadvantages of traditional qualitative and quantitative research

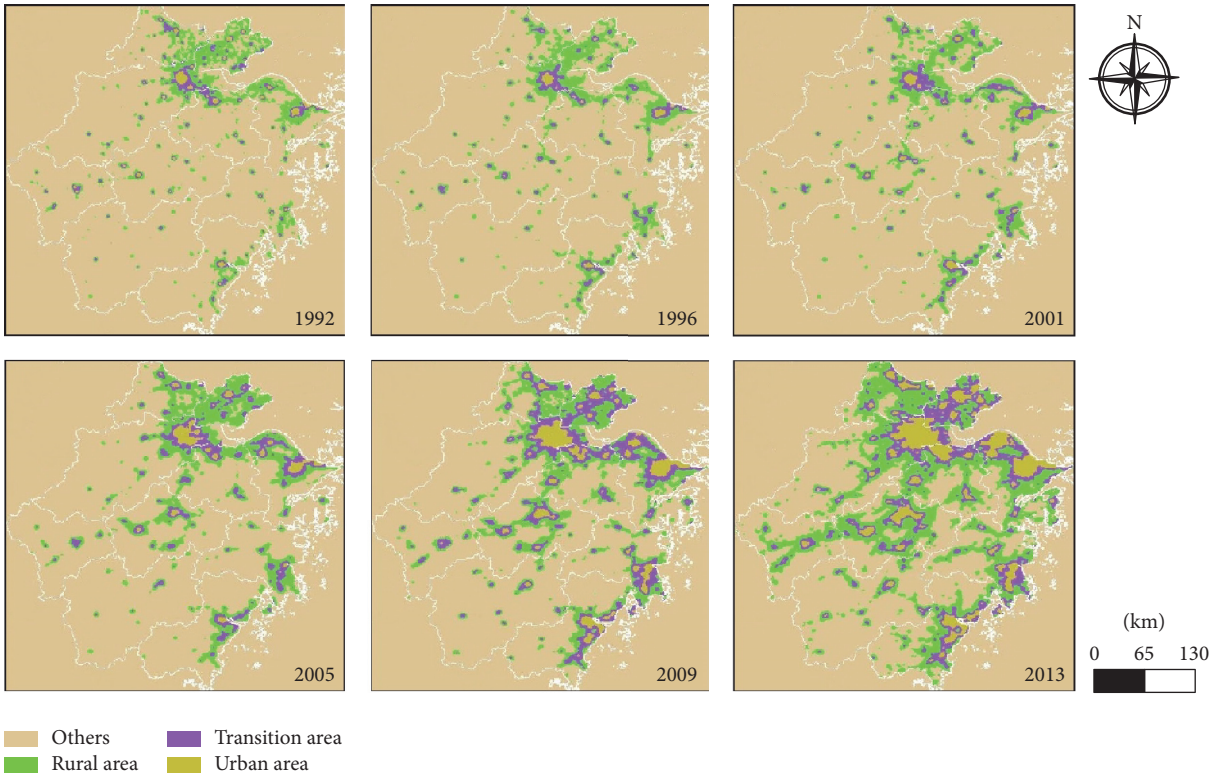

Figure 7: Spatial-temporal change of urbanization in Zhejiang province.

methods in data timeliness, spatial analysis, data processing, and so forth.

Based on the DMSP/OLS nighttime light data, the urbanization in Zhejiang province was analyzed from the perspective of geographic space. To reduce the differences between sensors, the invariant regions-method and regression method were selected to fully intercalibrate the data. The model of region light index (RLI) has now been established to make further research.

The results revealed that the RLI model has a strong relationship with urbanization indicators so it can be used to explain the development of urbanization in Zhejiang province. With the RLI model, the new "center-axes" pattern of urbanization was found. Meanwhile, the urbanization progress of Zhejiang has experienced a transformation from rapid development to steady improvement since 2000 and has been accompanied by a changing direction of urban expansion from coastal areas to inland areas. Based on the analysis above, the future of urbanization in Zhejiang should focus on the new "center-axes" pattern and pay more attention to the development of inland cities like Jinhua and Lishui, and enhanced cooperation is needed between cities to accelerate the economic society development.

It is a new attempt to analyze regional urbanization from geographical perspective; some valuable conclusions have been drawn based on the research. Nevertheless, this research only focuses on the regional level because of the limitation of relative statistics. Our hope is that, by using the DMSP/OLS nighttime light data, more researches that evaluate the urbanization and spatial-temporal changes over time can be made on the city level which is of great importance to the development, policy making, and planning of cities.

Disclosure

Pingbin Jin permanent address is School of Earth Science, Zhejiang University, Room-410, Yugu Road 38, Xihu District, Hangzhou 310027, China.

Competing Interests

The authors declare that there is no conflict of interests regarding the publication of this paper.

Acknowledgments

This paper is supported by the Zhejiang Provincial Natural Science Foundation (no. LY15G030004) and the research projects of the social science and humanity on Young Fund of the Ministry of Education (no. 12YJAZH042).

References

[1] X. Xueqiang, Z. Yixing, and N. Yuemin, *Urban Geography*, Higer Education Press, Beijing, China, 2009.

[2] L. Qiang, C. Yulin, and L. Jingming, "Analysis of urbanization in China," *Chinese Social Science*, vol. 7, pp. 82–100, 2012.

[3] L. Yansui and Y. Ren, "Characteristics and formation of urbanization in China," *Acta Geographica Sinica*, vol. 8, pp. 1011–1020, 2012.

[4] Y. Yang and H. Chunyang, "The analysis of hierarchical threshold value method to extract land use in urban area based on the DMSP/OLS stable night time light," *Journal of Image and Graphics*, vol. 4, pp. 666–674, 2011.

[5] Y. Zhou, L. Li, and F. Liao, "Analysis the spatial-temporal pattern of urbanization of chengdu metropolitan region using nighttime light image," *Region and City*, vol. 3, pp. 28–32, 2015.

[6] W. Lei, L. Congcong, and Y. Qing, "Mapping of urban expansion in China of 1990–2010," *Chinese Science Bulletin*, vol. 57, no. 16, pp. 1388–1399, 2012.

[7] J. Y. Liu, M. L. Liu, H. Tian et al., "Spatial and temporal patterns of China's cropland during 1990–2000: an analysis based on Landsat TM data," *Remote Sensing of Environment*, vol. 98, no. 4, pp. 442–456, 2005.

[8] X. Wenting, W. Bingfang, and Y. Changzhen, "Analysis of annual land cover data in China of 2000 with SPOT-VGT data," *Journal of Remote Sensing*, vol. 9, no. 2, pp. 204–214, 2005.

[9] T. R. Loveland, B. C. Reed, J. F. Brown et al., "Development of a global land cover characteristics database and IGBP DISCover from 1 km AVHRR data," *International Journal of Remote Sensing*, vol. 21, no. 6-7, pp. 1303–1330, 2000.

[10] L. Zhuo, J. Zheng, X. Zhang, J. Li, and L. Liu, "An improved method of night-time light saturation reduction based on EVI," *International Journal of Remote Sensing*, vol. 36, no. 16, pp. 4114–4130, 2015.

[11] Y. Liu, Y. Wang, J. Peng et al., "Correlations between urbanization and vegetation degradation across the world's metropolises using DMSP/OLS nighttime light data," *Remote Sensing*, vol. 7, no. 2, pp. 2067–2088, 2015.

[12] Y. Xuchao, G. Dawei, D. Mingjun et al., "Modeling population density using multi-sensor remote sensing data and DEM:a case study of Zhejiang province," *Resources and Environment in the Yangtze Basin*, vol. 22, no. 6, pp. 729–734, 2013.

[13] C. D. Elvidge, K. E. Baugh, E. A. Kihn, H. W. Kroehl, E. R. Davis, and C. W. Davis, "Relation between satellite observed visible-near infrared emissions, population, economic activity and electric power consumption," *International Journal of Remote Sensing*, vol. 18, no. 6, pp. 1373–1379, 1997.

[14] T. Li, C. He, Y. Yang, and Z. Liu, "Understanding electricity consumption changes in Chinese mainland from 1995 to 2008 by using DMSP/OLS stable nighttime light time series data," *Acta Geographica Sinica*, vol. 66, no. 10, pp. 1403–1412, 2011.

[15] W. Jiansheng, N. Yan, P. Jian et al., "Research on energy consumption dynamic among prefecture-level cities in China based on DMSP/OLS nighttime light," *Geographical Research*, vol. 33, no. 4, pp. 625–634, 2014.

[16] T. A. Croft, "Nighttime images of the earth from space," *Scientific American*, vol. 239, no. 1, pp. 86–98, 1978.

[17] M. Henderson, E. T. Yeh, P. Gong, C. Elvidge, and K. Baugh, "Validation of urban boundaries derived from global night-time satellite imagery," *International Journal of Remote Sensing*, vol. 24, no. 3, pp. 595–609, 2003.

[18] H. Chunyang, S. Peijun, L. Jinggang et al., "Analysis of reconstruction of urbanization in china in the 1990s using the DMSP/OLS night time data and statistical data," *Chinese Science Bulletin*, vol. 24, no. 3, pp. 595–609, 2003.

[19] Z. F. Liu, C. Y. He, and Y. Yang, "Mapping urban areas by performing systematic correction for DMSP/OLS nighttime lights time series in China from 1992 to 2008," in *Proceedings of the IEEE International Geoscience and Remote Sensing Symposium Proceedings (IGARSS '11)*, pp. 1858–1861, Vancouver, Canada, 2011.

[20] K. Yi, H. Tani, Q. Li et al., "Mapping and evaluating the urbanization process in northeast China using DMSP/OLS nighttime light data," *Sensors*, vol. 14, no. 2, pp. 3207–3226, 2014.

[21] T. Ma, Y. K. Zhou, C. H. Zhou, S. Haynie, T. Pei, and T. Xu, "Night-time light derived estimation of spatio-temporal characteristics of urbanization dynamics using DMSP/OLS satellite data," *Remote Sensing of Environment*, vol. 158, pp. 453–464, 2015.

[22] C. D. Elvidge, D. Ziskin, K. E. Baugh et al., "A fifteen year record of global natural gas flaring derived from satellite data," *Energies*, vol. 2, no. 3, pp. 595–622, 2009.

[23] J. S. Wu, S. B. He, J. Peng, W. Li, and X. Zhong, "Intercalibration of DMSP-OLS night-time light data by the invariant region method," *International Journal of Remote Sensing*, vol. 34, no. 20, pp. 7356–7368, 2013.

[24] M. L. Imhoff, W. T. Lawrence, D. C. Stutzer, and C. D. Elvidge, "A technique for using composite DMSP/OLS 'city lights' satellite data to map urban area," *Remote Sensing of Environment*, vol. 61, no. 3, pp. 361–370, 1997.

[25] S. Song, W. Bailing, W. Jianping et al., "Method for deriving urban built-up area using night-light data: assessment and application," *International Geoscience and Remote Sensing Symposium*, no. 4, pp. 169–176, 2011.

[26] C. Small, C. D. Elvidge, D. Balk, and M. Montgomery, "Spatial scaling of stable night lights," *Remote Sensing of Environment*, vol. 115, no. 2, pp. 269–280, 2011.

[27] W. Yang, F. Chuanglin, and W. Zhenbo, "The study on comprehensive evaluation and urbanization division at county level in China," *Geographical Research*, vol. 7, pp. 1305–1316, 2012.